DISSOLUTION KINETICS OF C-S-H GEL AND DURABILITY OF MORTAR

Ana Trapote-Barreira

Directors: Josep M. Soler Matamala

Jordi Cama i Robert

Doctoral Program in Civil Engineering

Institute of Environmental Assessment and Water Research

(IDAEA),CSIC

Technical University of Catalonia (UPC)

HYDROGEOLOGY GROUP
TECHNICAL UNIVERSITY OF CATALONIA

A mis padres, Dora y Florencio
A mi hermano César
A Arnim

ABSTRACT

The use of concrete in disposal facilities to contain low- and intermediate-level nuclear waste requires that the durability of this material is optimal for the lifetime of these repositories. One of the most important processes that put such durability at risk is the attack of concrete by water with low mineral content and neutral pH. For instance, in the El Cabril disposal facility (Southern Spain) the existence of water flow across the concrete of the wall cells can provoke the dissolution of concrete and originate alterations in the microstructure of the concrete, such as decalcification and dissolution of the cement phases, increased porosity and loss of barrier properties. Therefore, to yield reliable estimations of the durability of cement-based materials we need to increase our knowledge of the reactivity of these materials. Within this context, in this Thesis, the dissolution kinetics of the calcium silicate hydrate (C-S-H) -the main binding phase in all cement-based systems- and the processes responsible for mortar alteration have been studied.

In the first stage of this study, flow-through experiments were carried out to study the dissolution kinetics of C-S-H gel under CO_2-free atmosphere at room temperature (23 ± 2 ºC). The flow of demineralized water caused the dissolution of C-S-H and changes in the composition of the solutions. It was observed that the C-S-H gel dissolved incongruently when the Ca/Si ratio was high and congruently as the Ca/Si ratio decreased to the tobermorite-like stoichiometric Ca/Si ratio of ≈ 0.83. A dissolution rate law for C-S-H gel with Ca/Si ratio equal to 0.83 was proposed based on the dissolution rates normalized to the final BET surface area. Additionally, reactive transport modeling of the changes in aqueous chemistry allowed the fitting of the rate constants for C-S-H with Ca/Si ratio ranging from 1.7 to 0.83. Solid examination by scanning electron microscopy (SEM-EDX) and electron microprobe analyser (EPMA) showed some variability of the Ca/Si ratios of the analyzed particles, suggesting the existence of compositional domains with variable Ca/Si ratios. ^{29}Si nuclear magnetic resonance (^{29}Si MAS-NMR) spectra showed an increase in polymerization of the reacted C-S-H, associated with the decrease in Ca/Si ratio, and also the formation of Si-rich domains in some cases, mainly under slow flow conditions. Additionally, the changes in the microstructure of the dissolving C-S-H gel were characterized by small angle neutron scattering (SANS). The SANS data were fitted using a fractal model. The SANS specific surface area (S_T) tended to increase with time up to 31 days. Thereafter, it diminished as the C-S-H gel dissolved. The rest of the

fitted parameters (particle diameter (Do), fractal exponents (D_V and D_S), etc.) reflect the changes in the nanostructure of the dissolving C-S-H gel.

In the second stage, two types of experiments have been performed to study the alteration of the El Cabril mortar which is composed of 64% I42.5R/SR cement and 36 % fly ash.

Column experiments using mortar fragments of ≈ 2 mm in diameter were performed to study mortar alteration by flowing water at room temperature. Dissolution of the mortar released Ca, Si, Al, S, and Fe from the main mortar components (C-S-H gel, portlandite, fly ash, ettringite, monocarboaluminate, and Si-hydrogarnet). Variation of the chemical composition and the inspection of the mortar fragments by means of visual inspection, SEM and X-ray fluorescence (XRF), before and after the experiments, allowed interpretation of the dissolution and precipitation reactions. The aqueous chemistry data was modeled using the CrunchFlow reactive transport code in which the obtained dissolution rate law for the C-S-H gel and the associated kinetic parameters were incorporated.

Evaporation experiments with mortar samples, under controlled N_2 atmosphere, temperature and relative humidity, were performed at the laboratory scale to study the effect of the evaporation-induced water flow through the walls of the disposal cell at El Cabril on the microstructure of the mortar. The mortar specimens were visually inspected and SEM-EDX examined. Mortar samples were used to determine the retention curve and obtain hydraulic parameters to be used in the thermohydraulic modeling. First, variation in the water flux and temperature along the evaporation experiments was modeled with the multiphase flow and heat transport code CodeBright. Secondly, the multicomponent reactive transport code Retraso coupled to CodeBright was used to simulate the variation of solution composition along the samples during the experiments. The previously obtained C-S-H gel dissolution rate law and associated kinetic parameters were included in the model.

RESUMEN

El uso de hormigón en instalaciones de almacenamiento de residuos radiactivos de baja y media actividad requiere que la durabilidad de este material sea óptima durante el tiempo de vida de estos depósitos. Uno de los procesos más importantes que puede poner en riesgo su durabilidad es el ataque del hormigón por agua de bajo contenido mineral y pH neutro. Por ejemplo, en la instalación de almacenamiento de El Cabril (sur de España) la existencia de un flujo de agua a través del hormigón de la pared de las celdas puede provocar la disolución de hormigón y originar alteraciones en la microestructura del hormigón, como la descalcificación y la disolución de las fases de cemento, aumentando la porosidad y la pérdida de propiedades barrera. Por lo tanto, para obtener estimaciones fiables de la durabilidad de los materiales base cemento es necesario incrementar nuestro conocimiento de la reactividad de estos materiales. Dentro de este contexto, en esta Tesis, se han estudiado la cinética de disolución del silicato cálcico hidratado (gel C-S-H) -principal fase de unión en todos los sistemas base cemento- y los procesos responsables de la alteración de mortero.

En la primera etapa de este estudio, se realizaron experimentos de flujo continuo con el objetivo de estudiar la cinética de disolución de gel C-S-H en atmósfera sin CO_2 a temperatura ambiente (23 ± 2 ºC). El flujo de agua desmineralizada causó la disolución del gel C-S-H además de cambios en la composición de las soluciones. Se observó que el gel C-S-H disuelve incongruentemente cuando la relación Ca/Si es alta y congruentemente a medida que la relación Ca/Si disminuyó hacia la estequiometria de una tobermorita cuya relación Ca/Si es de ≈ 0.83. Se propuso una ley de velocidad de disolución para el gel C-S-H con una relación de Ca/Si de 0.83 basada en las velocidades de disolución normalizadas con el área superficial final determinada por BET. Adicionalmente, el modelado de los cambios en la química acuosa con el tiempo mediante transporte reactivo permitió el ajuste de las constantes de velocidad para el gel C-S-H con una relación de Ca/Si que varía entre 1.7 y 0.83. El análisis del sólido mediante microscopio electrónico de barrido (SEM-EDX) y microsonda electrónica de barrido (EPMA) mostró cierta variabilidad de las relaciones Ca/Si de las partículas analizadas, sugiriendo la existencia de dominios de composición con relaciones Ca/Si variables. Los espectros de resonancia magnética nuclear (^{29}Si MAS-RMN) mostraron un aumento en la polimerización del gel C-S-H reaccionado, asociado con una disminución de la relación Ca/Si, y también la formación de dominios ricos en Si en algunos casos, sobre todo en condiciones de flujo lento. Además, se han caracterizado los cambios en la microestructura del gel C-S-H disuelto por dispersión de

neutrones a bajo ángulo (SANS). Los datos SANS se ajustaron utilizando un modelo fractal. El área superficial específica de SANS (S_T) tiendió a aumentar con el tiempo hasta 31 días. Después disminuyó por efecto de la disolución del gel C-S-H. Los demás parámetros obtenidos del ajuste (diámetro de las partículas (D_o), exponentes fractales (D_V y D_S), etc.) reflejan los cambios en la nanoestructura del gel C-S-H disuelto.

En la segunda etapa, se realizaron dos tipos de experimentos para estudiar la alteración del mortero de El Cabril compuesto por un 64% de cemento I42.5R/SR y un 36% de cenizas volantes.

Por un lado, se realizaron experimentos en columna utilizando fragmentos de mortero de ≈ 2 mm de diámetro para estudiar la alteración de mortero. A través de las columnas se hizo pasar agua mediante una bomba peristáltica y los experimentos se realizaron en atmósfera sin CO_2 a temperatura ambiente (23 ± 2 ºC). La disolución del mortero liberó Ca, Si, Al, S y Fe de las principales fases (gel C-S-H, portlandita, cenizas volantes, etringita, monocarboaluminato, y Si-hidrogranate). La variación de la composición química y la inspección de los fragmentos de mortero por medio de la inspección visual, SEM y fluorescencia de rayos X (XRF), antes y después de los experimentos, permitieron interpretar que reacciones de disolución y precipitación habían tenido lugar. Los datos de la química acuosa se modelaron utilizando el código de transporte reactivo CrunchFlow en el cual fueron incorporados la ley de velocidad de disolución obtenida anteriormente y los parámetros cinéticos asociados al gel C-S-H.

Por otro lado, se realizaron experimentos de evaporación con probetas de mortero a escala de laboratorio, bajo condiciones controladas de atmósfera de N_2, temperatura y humedad relativa, para estudiar el efecto que el flujo de agua -inducido por evaporación- a través de las paredes de la celda de almacenamiento en El Cabril ejerce sobre la microestructura del mortero. Las probetas de mortero fueron inspeccionadas de forma visual y examinadas mediante SEM-EDX. Se utilizaron muestras de mortero para determinar la curva de retención y obtener parámetros hidráulicos aptos para ser utilizados en el modelo termohidráulico. En primer lugar, la variación en el flujo de agua y la temperatura a lo largo de los experimentos de evaporación fue modelada con el código de transporte multifase CodeBright de flujo y calor. En segundo lugar, el código Retraso de transporte reactivo multicomponente acoplado a CodeBright fue usado para simular la variación de la composición de la solución a lo largo de las probetas de mortero. La ley de velocidad de disolución obtenida previamente para el gel C-S-H y los parámetros cinéticos asociados se incluyeron en el modelo.

RESUM

L'ús de formigó en instal·lacions d'emmagatzematge de residus radioactius de baixa i mitjana activitat requereix que la durabilitat d'aquest material sigui òptima durant el temps de vida d'aquests dipòsits. Un dels processos més importants que pot posar en risc la seva durabilitat és l'atac del formigó per aigua de baix contingut mineral i pH neutre. Per exemple, en la instal·lació d'emmagatzematge d'El Cabril (sud d'Espanya) l'existència d'un flux d'aigua a través del formigó de la paret de les cel·les pot provocar la dissolució de formigó i originar alteracions en la microestructura del formigó, tals com la descalcificació i la dissolució de les fases del ciment, augmentant així la porositat i la pèrdua de propietats barrera. Per tant, per obtenir estimacions fiables de la durabilitat dels materials base de ciment cal incrementar el nostre coneixement de la reactivitat d'aquests materials. En aquest context, en aquesta Tesi s'han estudiat la cinètica de la dissolució del silicat càlcic hidratat (gel C-S-H) -principal fase d'unió en tots els sistemes base de ciment -i els processos responsables de l'alteració de morter.

En la primera etapa d'aquest estudi, es van realitzar experiments de flux continu amb l'objectiu d'estudiar la cinètica de dissolució del gel C-S-H en condicions atmosfèriques sense CO_2 a temperatura ambient (23 ± 2 º C). El flux d'aigua desmineralitzada va causar la dissolució del gel C-S-H i canvis en la composició de les solucions. Es va observar que el gel C-S-H va dissoldre incongruentment quan la relació Ca/Si era alta i congruentment a mesura que la relació Ca/Si va disminuir cap al valor de l'estequiometria d'una tobermorita de 0.83. Es va proposar una llei de velocitat de dissolució del gel C-S-H amb una relació de Ca/Si de ≈ 0.83 basada en velocitats de dissolució normalitzades amb l'àrea superficial final determinada per BET. Addicionalment, la modelització dels canvis en la química aquosa amb el temps mitjançant transport reactiu permet l'ajust de les constants de velocitat del gel C-S-H amb una relació Ca/Si que varia entre 1.7 i 0.83. L'anàlisi del sòlid mitjançant microscopi electrònic d'escombrat (SEM-EDX) i microsonda electrònica d'escombrat (EPMA) va mostrar certa variabilitat de les relacions Ca/Si de les partícules analitzades, suggerint l'existència de dominis de composició amb relacions Ca/Si variables. Els espectres de ressonància magnètica nuclear (^{29}Si MAS-RMN) van mostrar un augment en la polimerització del gel CSH reaccionat, associat amb el descens de la relació Ca/Si, i també la formació de dominis rics en Si en alguns casos, sobretot en condicions de flux lent. A més a més, es van caracteritzar els canvis en la microestructura del gel C-S-H dissolt per dispersió de neutrons a angle baix (SANS). Les dades de SANS es van ajustar utilitzant un model fractal. L'àrea superficial específica de SANS (S_T) va tendir a

augmentar amb el temps fins a 31 dies. Després va disminuir per efecte de la dissolució del gel C-S-H. Els altres paràmetres obtinguts de l'ajust (diàmetre de les partícules (Do), exponents fractals (D_V i D_S) , etc.) reflecteixen els canvis en la nanoestructura del gel C-S-H dissolt.

En la segona etapa, es van realitzar dos tipus d'experiments per estudiar l'alteració del morter d'El Cabril compost per un 64% de ciment I42.5R/SR i 36% de cendres volants.

D'una banda, es van realitzar experiments en columna utilitzant fragments de morter de ≈ 2 mm de diàmetre per estudiar l'alteració de morter. A través de les columnes es va fer passar aigua mitjançant una bomba peristàltica i els experiments es van realitzar en atmosfera sense CO_2 a temperatura ambient (23 ± 2 ºC). La dissolució del morter va alliberar Ca , Si , Al, S, i Fe de les principals fases (gel CSH, portlandita, cendres volants, etringita, monocarboaluminat, i Si-hidrogranat). La variació de la composició química i la inspecció dels fragments de morter a partir de la inspecció visual, SEM i fluorescència de raig X (XRF), abans i després dels experiments, va permetre interpretar que reaccions de dissolució i precipitació de fases. Les dades de la química aquosa es van modelar utilitzant el codi de transport reactiu CrunchFlow en el qual s'hi van incorporar la llei de velocitat de dissolució i els paràmetres cinètics associats al gel C-S-H, obtinguts anteriorment.

D'altra banda, es van realitzar experiments d'evaporació amb provetes de morter a escala de laboratori, sota condicions controlades d'atmosfera de N_2, temperatura i humitat relativa, amb l'objectiu d'estudiar l'efecte que el flux d'aigua induït per evaporació a través de les parets de la cel·la d'emmagatzematge d'El Cabril exerceix sobre la microestructura del morter. Les provetes de morter es van inspeccionar visualment i es van examinar mitjançant SEM-EDX. Amb mostres de morter es van determinar la corba de retenció i paràmetres hidràulics per ser utilitzats en el model termohidràulic. En primer lloc, la variació de flux d'aigua i la temperatura al llarg dels experiments d'evaporació es van modelitzar amb el codi de transport multifase CodeBright de flux i de calor. En segon lloc, el codi Retraso de transport reactiu multicomponent acoblat a CodeBright va ser usat per simular la variació de la composició de la solució al llarg de les provetes de morter. La llei de velocitat de dissolució del gel C-S-H obtinguda prèviament i els paràmetres cinètics associats es van incloure en el model.

AGRADECIMIENTOS

En primer lugar, me gustaría agradecer a mis directores de tesis, el Dr. Jordi Cama y el Dr. Josep Soler, por darme la oportunidad de realizar esta tesis y por toda la ayuda, apoyo, dedicación y confianza que han depositado en mí durante todos estos años. Gracias a mi tutor de tesis el Dr. Ignasi Casanova.

Sin lugar a duda, mil gracias al Dr. Carlos Ayora y al Dr. Maarten Saaltink por su inestimable ayuda y disponibilidad en la elaboración del modelo RETRASO. Gracias por tener siempre tiempo para sentaros conmigo y resolver todas las dudas y problemas que han ido surgiendo. Sin vuestra ayuda no hubiera podido acabar.

También quiero agradecer a la Dra. Lucía Fernández, una de las primeras personas que conocí al empezar esta andadura llamada tesis, su apoyo y cariño durante todos estos años. Gracias por tu contribución desinteresada, tanto científica como personal, a esta tesis.

Vielen Dank an Dr. Barbara Lothenbach und ihre Mitarbeiter für die Gastfreundschaft, Unterstützung und Hingabe, die mir während meiner Aufenthalte an der EMPA (Schweiz) entegengebracht wurden. In den kritischsten Momenten waren mir Deine Hilfe und Dein Rat, die immer Herzlichkeit und Nähe ausstrahlten, unersetzlich. Merci également à Dr. Gwenn Le Sâout pour son aide dans l'acquisition des spectres NMR de ^{29}Si-MAS. Thank you very much Dr. Mohsen Ben-Haha for his help in the study of C-S-H gel by SEM.

Gracias a Enresa por la financiación de esta tesis.

Thank you very much to Dr. Andrew Allen and Dr. Lioner Porcar. I have had the opportunity to work and learn with great experts the SANS technique. I also would like to acknowledge Dr. Colin Walker for the constructive comments that increased the quality of the thesis.

Agradezco también toda la ayuda prestada por los técnicos de los Serveis Científics Tècnics de la Universidad de Barcelona (Maite Romero, Toni Padró, Ana Domínguez, Eva Prats, Javier García-Veigas y Xavier Llovet). Gracias a ellos ha sido posible obtener los resultados que se presentan en esta tesis. Muchísimas gracias a Josep Elvira, no sólo por toda la ayuda prestada a la hora de interpretar resultados de DRX, sino también por todo el ánimo y motivación. Gracias

al Dr. Salvador Galí y el Dr. Salvador Martínez (Facultad de Geología, Universidad de Barcelona) por su ayuda en la síntesis y caracterización del C_3S.

Muchísimas gracias a todos mis compañeros y amigos de la etapa en el Jaume Almera (Mapi, Clara; Vanessa, Carmen, Cristina, Jorge, Patricia, Marco, Michael, Fulvio y Noemi) por hacer que el principio de esta tesis fuera mucho más fácil. Gracias también a todos aquellos compañeros del IDAEA (Katrien, Laura, Meritxell, Esther, Silvia, Rotman, Ana, Estanis, Alejandro, Mar, Violeta, Quim, Quique, Bayaraa y David) por vuestros ánimos, cafés, cervecitas, y sobre todo, por esas terapias de grupo.

En último lugar y no menos importante, quiero agradecer también a mi familia todo el apoyado y cariño. Gracias a mis padres, Dora y Florencio, por todo el ánimo que me han dado y que tanto he necesitado en los últimos años. A mi madre por ser el mejor ejemplo a seguir. A mi padre por su ayuda y su saber hacer a la hora de reparar cajas de guantes y preparar columnas. Sin vosotros esto no habría sido posible. A mi hermano, César, por tu apoyo, ánimo y empatía. Gracias por todo el tiempo y esfuerzo que has empleado en programar un algoritmo evolutivo para ajustar mis modelos. Es un placer aprender contigo. An meinen Partner Arnim, für seine Unterstützung, Geduld und Zuneigung. Danke für Dein Verständnis für die Schwierigkeiten die mit dem ganzen Prozeß verbunden waren, aber niemand weiß besser als Du, was es heißt, eine Doktorarbeit zu machen. Danke, daß Du an mich geglaubt hast.

Table of contents

PART I. C-S-H gel dissolution

List of figures

List of tables

CHAPTER 1

Introduction

1.1. Background

The El Cabril disposal facility (Southern Spain) is a vault-type surface disposal repository for the storage of low- and intermediate-level nuclear waste. The concept of this multibarrier surface disposal system consists of waste packages (220-liter drums) placed inside concrete containers (disposal unit). Mortar is injected into containers to fill all available space between the drums. The containers are placed inside 24x10x10 m^3 concrete vaults (Fig. 1.1).

Figure 1.1. *El Cabril disposal facility.*

Hydrated Portland cement is one of the fundamental materials for this kind of construction because of its high-quality performance in many environments and well known chemical-barrier behavior. The barrier behavior is due to (i) the pH of about 13 of the pore solution which limits the solubility of many radionuclides (Olson et al., 1997; Harris et al., 2002), and (ii) the high surface area for the sorption of the radionuclides (Harris et al., 2002; Sugiyama, 2008).

However, cement paste may be attacked by water with a low mineral content and approximately neutral pH (Faucon et al., 1998). The dissolution and decalcification reactions can promote the destruction of the microstructure of the material. This dissolution may affect all the phases present in the cement, being portlandite ($Ca(OH)_2$) the first phase to dissolve. Afterwards, the next phase to dissolve is the calcium silicate hydrate (C-S-H gel). In this manner, a series of reaction fronts are formed. These reactions cause changes in the barrier properties of the cement. Obtaining information about the process of degradation of the cement and concrete, and more specifically regarding the C-S-H gel, will eventually allow a more rigorous assessment of the service life of the disposal facility. This time is directly related to the time necessary for the radioactivity to reach natural background levels, which is typically around 300–400 years for the case of low- and intermediate-level nuclear waste.

1.2. Statement of the problem

Since the summer of 2003 water has been collected in the water collection system of some cells at El Cabril. The volume of flow shows a seasonal behavior; water is accumulated in the second part of the summer and during a longer period of time in winter. The initial volume was a few milliliters per day but this value was increasing until near 400 mL per day at the end of August of the same year. In the period from November of 2003 to March of 2004 the phenomenon was repeated and 83 liters were recollected. In the summer and winter periods of 2004 the collected volumes were 28 and 169 liters, respectively (Fig. 1.2).

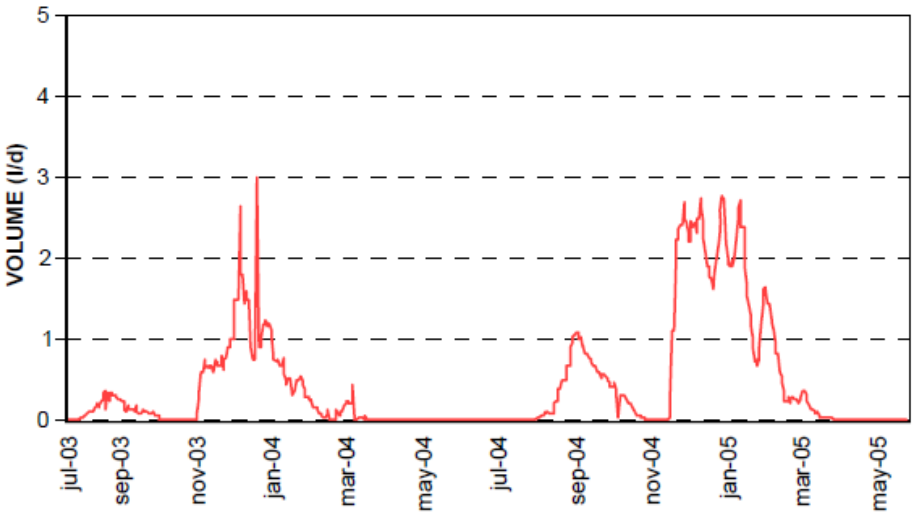

Figure 1.2. *Water collected in vault number 16.*

The recollected water is alkaline, with a pH near 10. The major ions in solution are OH^-, SO_4^{2-}, K^+ and Na^+. The concentrations of these ions initially showed a seasonal behavior, but later on the concentrations remained approximately constant during the different periods of the year.

The Hydrogeology group of the UPC (Polytechnic University of Catalonia) carried out studies about the source and the inflow mechanisms of this water (Saaltink et al., 2005; Zuloaga et al., 2006). From these studies, a first reactive transport model was developed. It was concluded that the source of collected water is groundwater and the air gap between containers and vault walls produced seasonal differences of temperature of a few degrees, causing water vapor diffusion from the walls to the concrete containers in summertime or vice versa in winter (Saaltink et al., 2005). The existence of this flow across the concrete of the cells can provoke the dissolution of concrete. The chemical and mechanical alterations may affect the durability of the material and the barrier properties (Fig. 1.3).

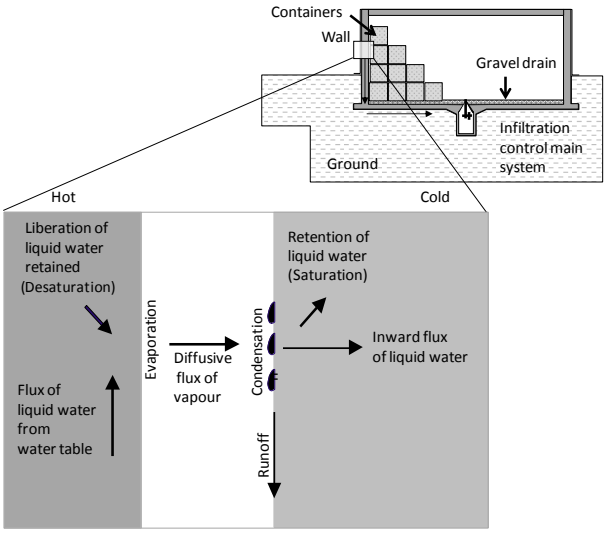

Figure 1.3. *Conceptual model of water flow in the wall and the concrete containe. After Saaltink et al. (2005).*

Subsequent reactive transport modeling of this system using the Retraso-CodeBright code (Ayora et al., 2007; Zuloaga et al., 2009) emphasizes a significant lack of data in the literature regarding the dissolution kinetics of C-S-H gel, which had a significant impact on model results.

This limitation in the understanding of the chemistry of the Portland cement, the lack of experimental data and the unknown kinetic reaction rate laws induce great uncertainties in any calculations regarding the durability of concrete during long periods of time.

1.3. Objectives

1.3.1 General objective

This project concerns the study of processes relevant for the durability of the concrete, and more specifically those processes more relevant at El Cabril.

1.3.2 Specific objectives

The present work covers three specific objectives.

The first objective is to determine the dissolution kinetics of the C-S-H gel by means of flow-through experiments. These experiments take place in cells which are designed to allow the reaction between powdered C-S-H and water. The release of aqueous Ca and Si from the

dissolving C-S-H and pH are monitored during the reaction. It is possible to measure the variation of the molar Ca/Si ratio of the C-S-H with time, to calculate dissolution rates, to assess the effect of the solution saturation state on the rates and to obtain a C-S-H dissolution rate law. C-S-H microstructural changes during dissolution were analyzed using several techniques (XRD (X-ray Diffraction), ^{29}Si-NMR, SEM, EPMA, and SANS). The first six techniques were applied at IDAEA (Institute of Environmental Sciences and Water Research, Barcelona-Spain) and EMPA (Swiss Federal Laboratories for Materials Science and Technology, Zurich-Switzerland). SANS measurements were conducted at ILL (Institut Laue-Langevin, Grenoble-France) and NIST (National Institute of Standards and Technology, Gaithersburg- USA).

The second objective focuses on applicability of the C-S-H reaction rate laws in a context of flux in porous media under controlled conditions. Hence, column experiments with ground mortar are carried out with a forced advective flow to accelerate water-solid interaction. The geochemical variation is modeled using the CrunchFlow reactive transport code (Steefel, 2009).

The third specific objective is to assess the extent of alteration in the concrete walls at El Cabril caused by evaporation-induced water flow. Evaporation essays were performed under conditions similar to those at the inner side of the walls of the disposal cells. The geochemical changes of the mortar test cylinders were modeled using the Retraso-CodeBright code (Olivella, 1996; Saaltink et al., 2004).

1.4. Thesis outline

The thesis is composed of six chapters including introduction and conclusions. All the chapters are based on manuscripts that are published or in preparation for publication (Trapote et al., 2013; Trapote et al., 2014). The thesis is divided into two parts. The first one corresponds to the first objective and the second one covers the second and third objectives.

Part I (Chapters 2 and 3) deals with kinetics of the C-S-H gel dissolution. Chapter 2 describes the conducted experimental methodology, based on flow-through experiments run under N_2 atmosphere, and the characterization of the solid samples by SEM-EDX and ^{29}Si-NMR. A C-S-H dissolution rate law is proposed based on reactive transport modeling of the experiments using CrunchFlow. Chapter 3 deals with the study of the associated structural changes in the C-S-H by means of SANS technique.

In Part II, Chapter 4 deals with the influence of C-S-H dissolution on the properties of mortar and concrete. Chapter 4 describes the experimental methodology for column experiments filled with ground mortar and run under advective-flux conditions. Geochemical variations in the solution and mortar are assessed by comparing with the chemistry of the unaltered samples. The CrunchFlow code is used to simulate the geochemical variation along the columns using the C-S-H dissolution rate law previously obtained. Chapter 5 is devoted to study the evaporation-induced processes. Chemical variation along a cylindrical mortar sample during the experiment is assessed by comparing to the unaltered sample. Quantification of the evaporation-induced processes is performed by reactive transport modeling.

Chapter 6 is a summary of the main conclusions and contributions of this thesis.

1.5. State of the art

In the first part, the theoretical background concerning the composition and structure of the C-S-H gel as the main phase of the hydrated cement is described. In the second part of the state of the art, the theoretical background related to the SANS technique to characterize C-S-H gel is described. Finally, included is a brief description of the cement composition, porosity, reactions involved in the degradation of the cement microstructure, transport mechanisms and a compilation of the previous studies on cement reactivity and hydration.

1.5.1 An overview of calcium silicate hydrate (C-S-H gel)

1.5.1.1 Composition of C-S-H gel

Calcium silicate hydrate (C-S-H) gel is the main binding phase in all Portland cement-based materials. High resolution techniques such as Transmission Electron Microscopy (TEM) or EPMA, where C-S-H can be analysed free of admixture with other phases, show that the C-S-H present in hardened pastes of C_3S or neat Portland cements generally has a mean Ca/Si ratio of about 1.75, with a range of values within a given paste from around 1.2 to 2.1 (Richardson, 1999). Higher values of Ca/Si in the literature could be explained by mixtures of C-S-H with portlandite ($Ca(OH)_2$, in cement chemistry notation, C= CaO, S= SiO_2, H= H_2O) (Chen et al., 2004). Richardson and Groves (1992) state that for aged pastes the range of Ca/Si ratio is approximately 1.6-1.85 with a mean value of 1.78 (Taylor, 1997).

1.5.1.2 Structure of C-S-H gel

C-S-H gel is often described as a poorly crystalline or nearly X-ray amorphous phase. The XRD patterns show that no long-range order exists in their structures. It is generally accepted that C-S-H has a disordered layer structure formed by silicate chains of varying lengths held together by layers of calcium (Gaitero et al., 2008). Experimentally, it is observed that these silicate chains are formed of both dimeric silicate units and polymeric units. Polymeric species are chains having lengths of 2, 5, 8 . . . (3n-1) tetrahedra, where n is integer for individual structural units (Richardson, 2008). With age, polymeric units form at the expense of existing dimers although the dimers remain in the pastes when the reactions are essentially completed.

The most accepted structure for C-S-H, which explains better the experimental observations, considers that C-S-H has a broad similarity with the crystalline calcium silicate hydrates 1.4 nm tobermorite and jennite (Richardson, 2008; Richardson, 2004). Their structures are described below.

1.4 nm Tobermorite

The crystal structure of 1.4 nm tobermorite has a central Ca-O sheet that has silicate chains on both sides. The silicate chains have dreierketten structure and so are linked in a manner that they repeat at intervals of three tetrahedra. Every third tetrahedron is a bridging tetrahedron, which could be absent to yield the (3n-1) chain lengths.

Two of these tetrahedra, the paired tetrahedral, share two oxygen atoms with the central Ca-O sheet, while the third, the bridging tetrahedra, shares only one. The interlayer spaces contain water molecules and additional Ca^{2+} ions to balance the negative charge of the composite layer (Chen et al., 2004). The chemical composition of the complex layer is $[Ca_5Si_6O_{16}(OH)_2 \cdot 7(H_2O)]$ (Bonaccorsi et al., 2005) and the Ca/Si ratio is 0.83 being a higher value in less crystalline forms. The structure is illustrated in Figure 1.4a.

Jennite

Jennite is a crystalline calcium silicate hydrate whose structure is based on layers. Acording to Chen et al. (2004), as with 1.4 nm tobermorite, the structure is based on layers in which a central Ca–O sheet is flanked on both sides by rows of single dreierketten, together with interlayer Ca atoms and water molecules. An important difference between 1.4 nm tobermorite and jennite is that every other dreierkette is replaced by a row of OH groups. This substitution causes a considerable corrugation of the Ca–O layers in jennite, which have the

empirical formula Ca_2O_5; some of the O atoms in this layer are shared with dreierketten, the paired tetrahedra of which are inset within the corrugations, whereas others form parts of water molecules and OH groups. These OH groups are balanced entirely by Ca, thus creating Ca–OH bonds; there are no Si–OH bonds in well-crystallized jennite. The chemical formula of jennite is $Ca_9(Si_6O_{18})(OH)_6 \cdot 8H_2O$ (Richardson et al., 2008), and the Ca/Si ratio of jennite is 1.5 which can increase in less crystalline forms. The structure is shown in Figure 1.4b.

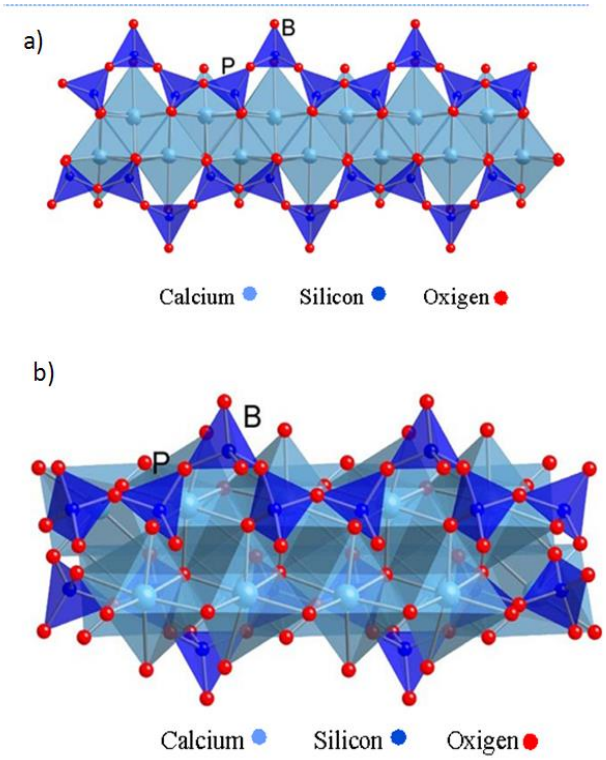

Figure 1.4. *Schematic diagram showing (a) 1.4 nm tobermorite structure (after Richardson, 2008) and (b) jennite structure (after Richardson, 2004). P and B denote "paired" tetrahedra and "bridging" tetrahedra, respectively.*

1.5.1.3 Structural models of C-S-H gel

The no long-range order existent in the C-S-H structure makes the term 'crystal structure' inapplicable, the term 'nanostrucure' is more appropriate for describing the structure at this level (Taylor, 1997). Up to date a large number of models have been developed to explain the observed silicate nanostructure, although not all of them can explain the observed experimental distribution of 3n-1 silicate anions. Most of these models were described by Richardson (2008) and are summarized in Table 1.1.

Table 1.1 *Summary of C-S-H models (after Richardson, 2008).*

Year	Author	Based on the structure of:	Silicate anion structure	Comments
1952	Bernal et al.	Tobermorite	Infinite	The model is not consistent with the experimentally observed distribution of silicate anions.i.e. 3n-1, where n is integer for individual structural units.
1954	Bernal	Tobermorite	Monomer	The model is not consistent with the experimentally observed distribution of silicate anions.i.e. 3n-1, where n is integer for individual structural units.
1956	Taylor and Howison	Tobermorite	3n-1	The Ca/Si ratio of the structure above 0.83 is explained by the removal of some "bridging" Si tetrahedraand replacement by interlayer Ca^{2+} ions.
1960-1962	Kurezyk and Schwiete	Ca(OH)2	infinite	Layers of tobermorite are sandwiched between layers of calcium hydroxide.
1967	Shpynova et al.	Tobermorite	Monomer	The model is not consistent with the experimentally observed distribution of silicate anions.i.e. 3n-1, where n is integer for individual structural units.
1980-1987	Stade and co-workers	Ca(OH)2,1.4nm Tobermorite and jennite	Dimer and polysilicate	Extension of Kurezyk and Schwiete's model (1960) with the particularity that this model considers dimers to fit the composition studied.
1984	Grudemo et al.	Tobermorite	Monomer	The model is not consistent with the experimentally observed distribution of silicate anions.i.e. 3n-1, where n is integer for individual structural units.
1986	Taylor	Tobermorite, jennite, Ca(OH)2	3n-1	The structure is based on 1.4 nm tobermorite and jennite. This model is so-called T/J model.
1987	Glasser et al.	Tobermorite and jennite	Dimer	Derived from Stade et al. (1980) dimeric model.
1992-1993	Richardson and Groves	Tobermorite	3n-1	The model includes tobermorite, jennite and portlandite-based structures that co-exist.
1993	Taylor	Tobermorite and jennite	3n-1	T/J model with some modifications (e.g. variable protonation and substituents).
1996	Cong and Kirkpatrick	Tobermorite	3n-1	It is a "defect tobermorite" model that is equivalent to Richardson and Groves's model (1992).
1997-1999	Grutzeck	Tobermorite, sorosilicate	Long-chain, dimer	Model with two based phases: T-based phase with low Ca/Si ratio and a sorosilicate based-phase with high Ca/Si.
1998	Nonat and Lecoq	Tobermorite	3n-1	Similar to Richardson and Groves model (1992) in the T units and Kurezyk and Schwiete and Stade and co-workers in the interlayer region.
2004	Chen, Thomas, Taylor and Jennings	Tobermorite and jennite	3n-1	Similar to Richardson and Groves model (1992) in the T units.
2004	Nonat	Tobermorite and jennite	3n-1	Update of Nonat and Lecoq (1998) model with jennite-based structure.

Table 1.1 shows that the models can be grouped into two categories: one where the silicate anion structure is entirely monomeric, and the other where a dreierketten based model, derived from the linear silicate chain present in 1.4 nm tobermorite and jennite. Also, the models are divided upon the type of structure used to describe the C-S-H. In this case, the so-called tobermorite/jennite (T/J) model considers the C-S-H as an assembly of tobermorite regions followed by jennite domains. The tobermorite-calcium hydroxide (T/CH) models consider solid solutions of tobermorite layers sandwiching calcium hydroxide to achieve a higher Ca/Si ratio.

The models proposed by Bernal (1954), Shpynova et al. (1967) and Grudemo (1984) fall in the first category, in which the hydrated calcium silicates are formed by monomeric silicate anions ($[SiO_2(OH)_2]^{2-}$) and do not consider the (3n-1) distribution of silicate anions. This model was used to explain the anomalous XRD peak intensities for $Ca(OH)_2$ in hardened cements, being derived from the structure of $Ca(OH)_2$ (Richardson, 2008).

The first dreierketten-based model to account for the C-S-H gel structure was originally proposed by Bernal et al. (1952) from XRD studies of hydrated C_3S pastes and diluted suspensions of C-S-H. It was concluded that the two types of formed C-S-H phases were similar and were called C-S-H(I) and C-S-H(II), having low and high Ca/Si ratios, respectively. C-S-H(I) had a layer and fibrous structure and showed similarities to tobermorite.

Kurczyk and Schwiete (1962) studied C_3S and C_2S-β pastes and proposed a model for the C-S-H structure that formed in both studied systems, which they referred to as a 'tobermorite-like phase'. Their model considers the tobermorite-like layers and included Si-OH groups and infinite silicate chain lengths. To explain the Ca/Si ratios observed (between 1.80 and 1.92) they postulated that the structure has excess of Ca^{2+} and OH^- ions in an interlayer region together with water molecules. A similar model was proposed by Kantros et al. (1962) in which the layers of tobermorite are sandwiched between layers of calcium hydroxide (Kantros' model).

Later, Stade and Wieker (1980) suggested that amorphous C-S-H phases present in cement paste are built up from CaO_x polyhedra sandwiched between two silicate layers. These three-layer sequences are separated by an intermediate layer containing H_2O, Ca^{2+} and OH^-. They expressed their model in two forms, one purely dimeric, and the other incorporating both dimer and polysilicate chains (Fig. 1.5), where y represents the studied composition. These authors and later Grutzeck (1989), by means of ^{29}Si-NMR spectra, described the transition between the two phases of C-S-H gel, tobermorite-type structure with long chains to a jennite-type structure containing shorter chains and dimeric silicate groups with a Ca/Si ratio of 1.0.

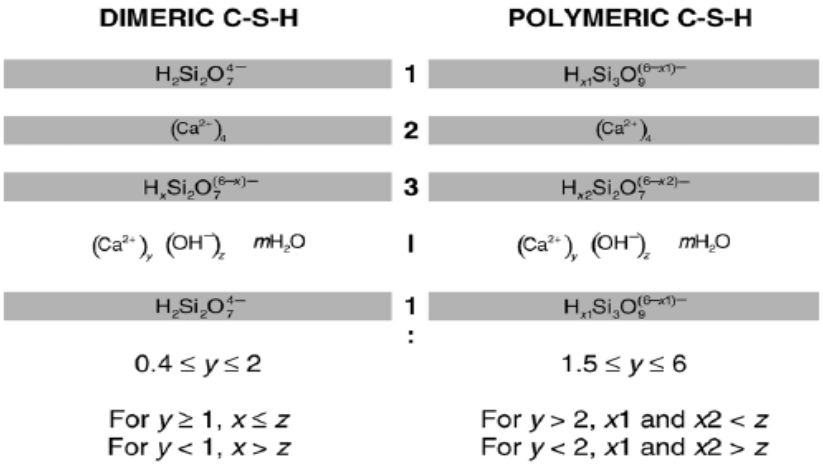

Figure 1.5. *Schematic representation of C-S-H- gel structures. After Stade and Wieker's model (1980).*

Taylor (1986) proposes a model that considers that C-S-H exists as C-S-H(I) that it is structurally similar to 1.4 nm tobermorite and C-S-H(II) similar to jennite. These structures are composed of structural units derived from imperfect tobermorite and jennite, respectively. Accordingly, the Ca/Si ratio of C-S-H(I) varies from 0.67 to 1.5 by omission of a part of the bridging tetrahedra or variations in the contents of interlayer Ca and protons attached to Si-O units. C-S-H(II) has Ca/Si ratios between 1.5 to 2.2. Taylor (1993) described a transition phase between both C-S-H gels taking place at around a Ca/Si ratio of 1.5. This transition phase was also observed by Klur et al. (1998). Hence, the observed composition (Ca/Si = 1.7-1.8) and structure of the C-S-H gel in hardened C_3S or Ordinary Portland Cement (OPC) pastes might be achieved by an intimate mix of these structural units having a mainly jennite-type structure. Currently this model (the T/J model) is the most accepted one for its plausibility in morphological terms, it is incompatible with two basic characteristics of real C-S-H: the Ca/Si ratio and C-S-H density (Pellenq et al., 2009).

Glasser et al. (1987) proposed a compositional model for C-S-H derived from the dimeric model proposed by Stade and Wieker (1980). Their thermodynamic treatment was strictly only applicable to precipitated gels with Ca/Si ratio between 1.0 and 1.4.

EDX analysis of C-S-H in hardened Portland cement pastes reveals a Ca/Si ratio that varies from approximately 1.2 to 2.3 with a mean value of 1.7. To account for this variability, Richardson and Groves (1992) proposed a model based on isolated silicate chains of variable length and OH^- content and intergrown with $Ca(OH)_2$. This model included a two-fold classification to clarify C-S-H chemistry that could be interpreted from either the T/J (tobermorite/jennite-like structure) or T/CH (tobermorite-'solid solution' $Ca(OH)_2$) viewpoints (Richardson, 2004). On the T/CH model the structure is a layer of CH sandwiched between silicate layers of tobermorite-like (solid solutions) structure whilst on the T/J model the main layer is formed of jennite-based structural units (as Si–O–Ca–OH) assembled with tobermorite regions. The model also considers the possibility that tobermorite, jennite and CH occur in the same system and the maximum flexibility in the possible degree of protonation of the silica chains (Richardson, 2008).

The so-called layer-structure model (Richardson and Groves 1992) has been widely accepted, but other researchers such as Cong and Kirkpatrick (1996) and Fujii and Kondo (1981) argue that the occurrence of jennite-type C-S-H(II) is extremely difficult to synthesize and subsequently characterize and this is why they proposed a 'defect tobermorite-like' model for C-S-H, which exists as a solid solution between tobermorite and $Ca(OH)_2$.

Grutzeck (1999) proposed another two-phase C-S-H model that embraces the idea that C-S-H consists of intergrowths of sorosilicate-like and tobermorite-like C-S-H, which describes the observed data better than the existing C-S-H models. Sorosilicate is not a silicate layer structure; it is comprised of columns of dimers $(Si_2O_7)^{6-}$ ions surrounded by chains of octahedrally coordinated CaO which hold the structure together. Also, the sorosilicates normally contain rather large cavities in 2D that form channels in 3D that can host water molecules, Ca^{2+}, OH^- and possibly other ions as well.

Nonat and Lecoq (1998) proposed another different model based on equilibrium data obtained from both $CaO–SiO_2$ mixes and fully hydrated C_3S samples in solution in which the lime concentration is maintained constant. The model is also based on a tobermorite-like structure and applicable to a whole range of Ca/Si (from 0.66 to 2). However, this model does not assume a disordered structure and the layers would not contain jennite-like regions. To reach high Ca/Si values the model assumes that most of the interlayer crystallographic sites of the tobermorite model are occupied by calcium ions balanced by OH- in interlayer positions (Richardson, 2008). Klur et al. (1998) obtained clear evidences of a transition phase at Ca/Si ratio of 1.5 and propose three types of C-S-H gel: C-S-H (α) for Ca/Si ratio below 1, C-S-H (β) for Ca/Si ratio between 1 and 1.5 and C-S-H (γ) for Ca/Si ratio larger than 1.5.

Later, Nonat (2004) proposed a model based on the preceding structural model. According with this model, the main layer of C-S-H consists of a silicate dimeric unit charge balanced by two calcium ions and the two free extremities bear two protons, $Ca_2H_2Si_2O_7$. Two successive dimeric units may be bridged by a silicate tetrahedron and $Ca(OH)_2$ units may be accommodated in place of missing bridging tetrahedra.

Kalliopi (2004) compiled the latter models of cement gel structure that describe the nanostructure of C-S-H gel and its porosity. These models were proposed by Powers and Brownyard (1948), Feldman and Sereda (1970), Wittmann (1977) and Jennings and Tennis (1994). The first two are based on a layered structure for the C-S-H gel, while another are based on a colloidal model (Fig. 1.6).

Powers and Brownyard (1948) proposed a model commonly known as Power Model supported by water adsorption test. According to the model, C-S-H gel is composed of particles with a layered structure of thin sheets, made of two or three layers randomly arranged and bonded together by surface forces. The C-S-H layers are separated by a maximum average distance of 3 nm and a minimum average distance of 0.4 nm. The model theorized that the loss of water is irreversible. Feldman and Sereda (1970) proposed that the sheets composing the C-S-H gel do not have an ordered layered structure creating a interlayer space with different

shapes and sizes (between 0.5 and 2.5 nm), and these layers may come together by means of Van der Waals forces. Water can be adsorbed in the solid surface or being like interlayer water associated with the C-S-H structure. They also suggest the irreversibility of loss of water during the adsorption and desorption processes.

On the other hand, Wittmann (1977) proposed the so-called Munich model, which is based on concepts of colloidal science. This model describes the C-S-H gel structure as a three dimensional network of amorphous colloidal particles, called a xerogel. The particles are held together by chemical bonds as well as Van der Waals bonds. Finally, the Jennings-Tennis model (Jennings and Tennis, 1994) is made up of basic building blocks formed of spheres that group together to form globules of 5 nm in diameter. The internal structure of the spheres is layered similarly to the Taylor model. The model considers two types of C-S-H gel, one with lower density (LD) and the other with higher density (HD). The structure is fractal and the model defines the size, density and packing efficiency of each of the mentioned structures (Chatterjee, 2004).

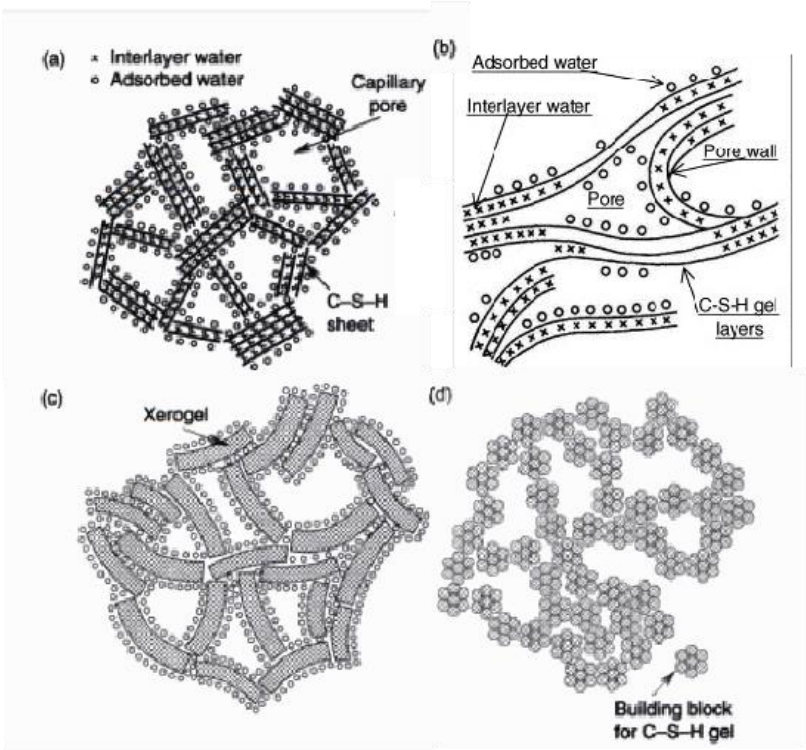

Figure 1.6. Schematic representation of C-S-H models (after Kalliopi, 2004). a) Powers and Brownyard (1948); b) Feldman and Sereda (1970); c) Wittmann (1977); d) Jennings and Tennis (1994).

1.5.1.4 Morphology of C-S-H gel

There are two types of hydration products (Taplin, 1959): the 'inner' products (Ip) which lie within the original boundaries of the clinker particles, and the 'outer' products (Op) which lie 'outside' the original grain boundaries". Later, Thomas et al. (2004), by means of SANS identified and classified these two types of C-S-H as HD and LD, respectively.

Inner product (Ip C-S-H) has a compact and homogeneous morphology at the fine-scale. The pores in Ip product are smaller than 10 nm and it appears to consist of aggregates of small globular particles 4-6 nm in diameter. The Op C-S-H present in hardened C_3S or OPC pastes has a fibrillar and directional morphology. This morphology is a function of space constraint: when it forms in large pore spaces, the fibrils form with a high length to width aspect ratio (which will be referred to as coarse fibrillar); in smaller spaces, it retains a directional aspect but forms in a more space-efficient manner (fine fibrillar). The space between the fibrils of Op C-S-H forms a three-dimensional interconnected pore network commonly known as the capillary porosity. The Op present in a hardened C_3S paste presents a coarse fibril about 100 nm wide, which appears to consist of a large number of long thin particles aligned along their length. But the Op C-S-H present in neat PC pastes typically has a finer morphology (Taylor, 1993; Richardson, 2004).

1.5.1.5 Synthesis of C-S-H gel

There are several successful methods to synthesize C-S-H gel that differ basically in the selected starting materials and in the Ca/Si ratio and structure obtained in the synthesized C-S-H (Fuji and Kondo, 1981; Cong and Kirpatrik, 1996; Nonat and Lecoq, 1988; Chen et al., 2004).

It is possible to obtain a disordered variety of C-S-H gel, like that present in hydrated cement and concrete, from the hydration of tricalcium silicate and dicalcium silicate (Garrault and Nonat, 2001). The hydration reactions of the cement can be considered a complex process of dissolution-precipitation of the phases present in the cement. In the particular case of hydration of C_3S or C_2S, system development is simple in comparison with that of cement, because the system presents only two components, the C-S-H gel and CH, although some grains of non-hydrated C_3S or C_2S could be present depending on the degree of hydration (Costolla et al., 2008). After a few hours of hydration, the aqueous ionic phase formed is saturated in CH and then starts to nucleate and precipitate. The grains of C_3S start to be surrounded by a layer of C-S-H gel that grows with time. Both Ip and Op products form. The difference between this gel and the gel present in the cement is in how CH precipitates. In cement, CH grows with a variable shape and is deposited throughout the matrix, while in C_3S hydration CH grows in

clusters that nucleate in the capillary pores and on the semi-hydrated C_3S grains, randomly stopping or decelerating the reaction (Gallucci and Scrivener, 2007).

C_3S is prepared according to the conventional solid-phase reaction from reagent-grade $CaCO_3$ and high-purity silica gel (reaction 1.1). The mixture is heated at high temperatures, e.g. slightly exceeding 1420 ºC (Harris et al., 2002) or 1500 ºC for 24 hours (Rodger et al., 1988). However, Thomas et al. (2004) synthesized C_3S using a 3:1 mixture by mass of CaO and SiO_2 powder at 1430 ºC without liberation of CO_2 (reaction 1.2).

$$3CaCO_3 + SiO_2 \overset{\Delta T}{\rightarrow} Ca_3SiO_5 + 3CO_2 \qquad \textit{Reaction 1.1}$$

$$3CaO + SiO_2 \overset{\Delta T}{\rightarrow} Ca_3SiO_5 \qquad \textit{Reaction 1.2}$$

The process is repeated 3 times. In the first step most of the CO_2 is liberated. To facilitate the overall process, the sample is not pressed into discs. At the second and third burnings, samples are quenched to room temperature, ground to powder, and then pressed into discs to enhance homogeneity. The final product is ground to powder with different particle sizes, e.g. 45 μm (Chen et al., 2004) or ca. 10 μm (Garrault et al., 2006). It is possible to monitor the whole process by XRD to ensure the reaction is complete.

Hydrated C_3S pastes are prepared with deionized water (reaction 1.3), with a water-to-solid mass ratio of 0.5 at room temperature to obtain C-S-H gel according to the following idealized reaction (Chen et al., 2004).

$$2Ca_3SiO_5 + 7H_2O \rightarrow Ca_3Si_2O_3(OH)_8 + 3Ca(OH)_2 \qquad \textit{Reaction 1.3}$$

Samples are manually mixed and poured in vials. All the processes are carried out under a CO_2-free atmosphere in a glove box. According to Chen et al. (2004) and Thomas et al. (2004), after 3 days the hardened pastes are demolded and stored in a CH-saturated solution. Pastes are hydrated for approximately 8 months at 22 ± 1ºC (Chen et al., 2004) or from 3.5 to 6 months (Thomas et al., 2004). Once hydration is completed the samples are dried by D-drying (vacuum drying to the equilibrium vapor pressure above ice at –79˚C (194 K) (Chen et al, 2004) or pouring propanol upon the paste and dried in vacuum desiccators (Rodger et al., 1988).

Using the stoichiometry of C-S-H proposed by Kulik and Kersten (2001), the hydration of C_3S can be written as

$$2Ca_3SiO_5 + 4H_2O \rightarrow SiO_2 \cdot 1.67Ca_3(OH)_2 \cdot H_2O + 1.33Ca(OH)_2 \qquad \textit{Reaction 1.4}$$

This is the reaction assumed in the present work. The Ca/Si ratio of the C-S-H is 1.67 that is close to the mean value measured in the C-S-H gel present in the cement pastes.

Likewise, C-S-H gel can also be obtained from hydration of highly reactive C_2S-β (reaction 1.5; Cong and Kirkpatrick, 1996):

$$2Ca_2SiO_4 + 5H_2O \rightarrow Ca_3Si_2O_3(OH)_8 + Ca(OH)_2 \qquad \textit{Reaction 1.5}$$

After C_3S hydration, a hardened paste containing two products (C-S-H gel and CH) is produced (reactions 1.3 or 1.4). The C-S-H gel shows a more disordered structure than C-S-H(I) and C-S-H(II). Based on these observations and the measured variations in Ca/Si ratio, together with selected area electron diffraction patterns, thermogravimetric curves and density measurements, Chen et al. (2004) concluded that the structure of the obtained C-S-H gel is a mixture of tobermorite and jennite-like structures where that of jennite is dominant.

Determination of the content of CH and residual C_3S by XRD and microanalyses using Electron Microprobe and TEM indicates a Ca/Si ratio of C-S-H gel of 1.7-1.8 (Taylor, 1986; Richardson, 1999; Costoya, 2008), which is the Ca/Si ratio of C-S-H in fresh Portland cement paste.

There are some other routes to synthetize C-S-H (Table 1.2): (1) from the reaction of silica and calcium hydroxide (portlandite) solution (Atkinson et al., 1989; Martínez-Ramírez and Blanco-Varela, 2008; Garrault-Gauffinet et al., 1999; Lesko, 2001; Plassard et al., 2004; Chen et al., 2004; Greenberg and Chang, 1965; Sugiyama, 2008; Fujii and Kondo, 1981) to obtain an imperfect version of 1.4 nm tobermorite (C-S-H(I)) with Ca/Si ratio from 0.41 to 1.85 (Cong and Kirkpatrick, 1996). This synthesis is also used by Labbez (2007) to obtain a C-S-H of Ca/Si ratio = 0.66. (2) Mechanochemical and hydrothermal methods are very useful to obtain C-S-H with a wide range of Ca/Si ratios between 0.2 and 2 (Mitsuda et al., 1986; Ishida et al., 1992a; Ishida et al., 1992b; Okada, 1994; Sasaki et al., 1996; Saito, 1997; Singh et al., 2002; Black et al., 2006; Black et al., 2008;).

Table 1.2 *Methods and starting materials to synthesize C-S-H with different Ca/Si ratio (after Chen et al., 2004).*

Method of preparation	Author(s)	Starting materials	Ca/Si at CH saturation	Solubility curve at high Ca concentration
Double decomposition	Bessey	$Na_2SiO_3 + Ca(NO_3)_2$	1.5	-
	Taylor	$Na_2SiO_3 + Ca(NO_3)_2$	1.5	A
	Fujii & Kondo	$Na_2SiO_3 + Ca(NO_3)_2$	1.5	Below A
	Current study	$Na_2SiO_3 + Ca(NO_3)_2$	1.5	C"
	Roller & Ervin	Na_2SiO_3 + CH	1.45	C"
Lime and silica suspensions	Baylis	$CaO + SiO_2$	1.5	-
	van der Burgh	$CaO + SiO_2$	1.4	-
	Shaw & MacIntire	$CaO + SiO_2$	1.4	-
	Le Chatelier	$CH + SiO_2$	1.7	-
	Flint & Wells	$CH + SiO_2$	1.7	C'
	Kalousek	$CH + SiO_2$	1.3 or 1.75[a]	C
	Cong & Kirkpatrick	$CH + SiO_2$	1.6	-
	Greenberg & Chang	$CH + SiO_2$, 50 °C	1.75	C"
Anhydrous calcium silicates	Kühl & Mann	CaO/SiO_2 melt	1.5	-
	Cong & Kirkpatrick	Reactive C_2S	1.6	-
	Thorvaldson & Vigfusson	C_2S, C_3S	1.45	-
	Nonat & Lecoq	C_3S	1.5	-
	Cirilli	C_3S	1.4	-
	Taylor	C_3S (2 points)	1.6	-
	Greenberg & Chang	Mature C_3S paste	1.75	A,C",C
	Current study	Mature C_3S paste	1.8	C

[a] Although the lower value is often cited, XRD showed evidence near 20 mM Ca for a single-phase C–S–H sample with Ca/Si = 1.7–1.8. Some of the Ca/Si ratios determined from the initial and final concentrations in solution also suggest values higher than 1.3.

1.5.1.6 C-S-H solubility

To predict the long-term behavior of cement-based systems in contact with an aqueous phase is essential to know the solubility of the C-S-H gel. The thermodynamic modeling of C-S-H solubility started with the use of empirical or semi-empirical models and evolved to the application of solid-solution models. Different models for the solubility of C-S-H gel have been proposed, mostly based on solubility data of the $CaO\text{-}SiO_2\text{-}H_2O$ system. The present section is based on the literature review of thermodynamic description of the solubility of C-S-H gel in hydrated Portland cement (Soler, 2007).

Jennings (1986) and Gartner and Jennings (1987) compiled experimental C-S-H solubility data and made a diagram ($[SiO_2]$vs.[CaO]). All the measurements were matched using two curves, A and B, which were calculated according to an equilibrium formation initially developed by Fujii and Kondo (1981). The lower curve A was interpreted as corresponding to a tobermorite-like phase (C-S-H(I). The Ca/Si ratio of the C-S-H ranged from 0.8 to 1.3. The upper curve B was interpreted as corresponding to a mixture of tobermorite-like and jennite-like phases (C-S-H(I)-C-S-H(II)) (Fig. 1.7).

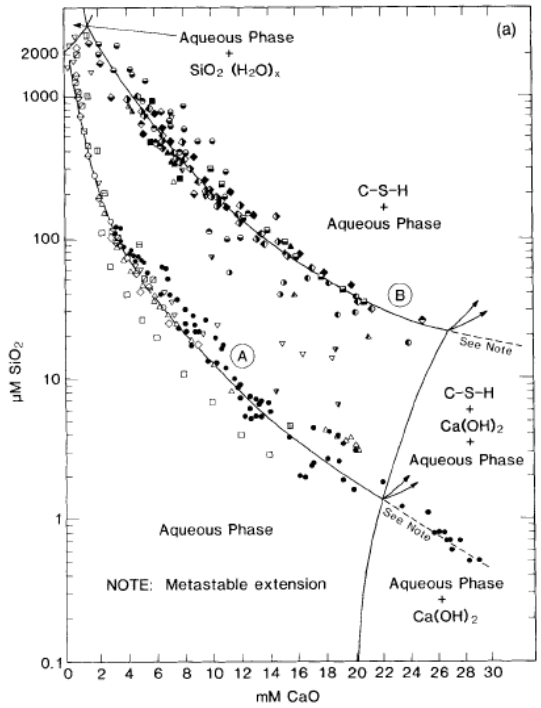

Figure 1.7. *C-S-H solubility data on a [SiO_2] vs. [CaO] plot. After Jennings (1986).*

Reardon (1990, 1992) formulated an empirical solubility model based on the experimental data compiled by Jennings (1986) to obtain the curve A. The model is applicable over a Ca/Si range from 0.9 to 1.7. The basis of the model is the empirical fitting of the solubility of C-S-H as a function of the solution composition.

Atkinson et al. (1989) formulated a non-ideal solid solution model to describe the solubility of C-S-H based on experimental data from their own data and data from Greenberg and Chang (1965), whose experimental data indicate that the phase diagram (Figs. 1.8 and Fig. 1.9) can be split into three subsidiary regions: (i) Ca/Si $\geq$ 1.8, (ii) 0.8 $\leq$ Ca/Si $\leq$ 1.8, and (iii) Ca/Si $\leq$ 0.8. This zone corresponds to a different solid solution (a different C-S-H).

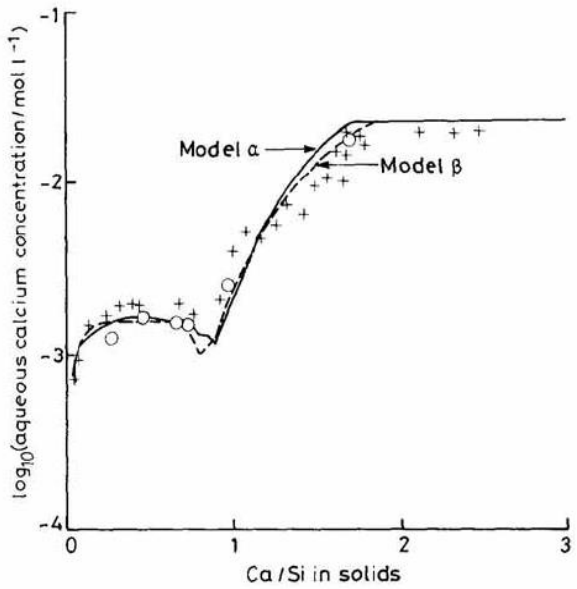

Figure 1.8. *Total calcium in aqueous solution in equilibrium with solids in the CaO – SiO_2 – H_2O system at 25°C as a function of the Ca/Si atom ratio in the solids. The curves are computed from thermodynamic modeling and the points correspond to experimental data. The curve labelled Model β is a variant of the same model. After Atkinson et al. (1989).*

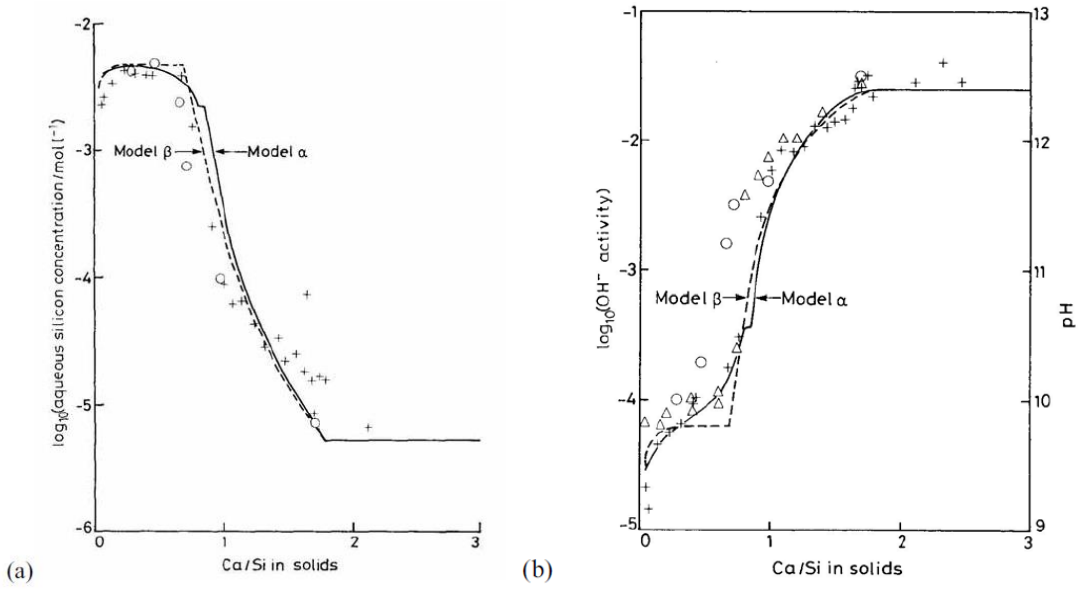

Figure 1.9. *Total silica (a) and pH (b) in aqueous solution in equilibrium with solids in the CaO – SiO_2 – H_2O system at 25°C as a function of the Ca/Si atom ratio in the solids. The curves are computed from thermodynamic modeling and the points correspond to experimental data. The curve labelled Model β is a variant of the same model. After Atkinson et al. (1989).*

Also, Berner (1988, 1990, 1992) formulated an empirical model based on thermodynamic considerations of non-ideal solid solutions and was used to predict the behaviour of cement structures which degrade in groundwater, including the chemical evolution of their pore water. This model reproduces a lot of solubility data for the C-S-H-water system in a satisfactory manner and in a whole range of possible C-S-H-gel compositions. It takes into account the incongruent solubility behaviour of C-S-H-gel, thermodynamic properties and their solubility products, which depend on the Ca/Si ratio of the C-S-H**.**

Later, Kersten (1996) proposed a non-ideal binary solid solution $Ca(OH)_2$-$CaHSiO_{3.5}\cdot 1.5H_2O$ to describe C-S-H solubility, based on the experimental data from Greenberg and Chang (1965) and Fujii and Kondo (1981).

Börjesson et al. (1997) formulated a non-ideal solid solution model based on C-S-H solubility data from Kalousek (1952). The end-members are $Ca(OH)_2$ and CaH_2SiO_4 for $1 < Ca/Si \leq 1.43$. For $1.43 < Ca/Si \leq 1.7$, equilibrium with respect to portlandite is forced in the model.

Afterward, Rahman et al. (1999) formulated a non-ideal solid solution model very similar to the model proposed by Börjesson et al. (1997), based also on C-S-H solubility data from Kalousek (1952). The end-members of this solid solution are $Ca(OH)_2$ and CaH_2SiO_4. For $1 < Ca/Si \leq 1.5$, only the $Ca(OH)_2$–CaH_2SiO_4 solid solution is applied. For $Ca/Si > 1.5$ equilibrium with respect to portlandite is forced in the model due to the saturation concentration of total Ca in solution for portlandite. The solubility results predicted by the proposed model are comparable with experimental data.

Later, Kulik and Kersten (2001) described the solubility of C-S-H system with two ideal C-S-H(I) (SiO_2-tobermorite) and C-S-H(II) (tobermorite-jennite) binary solid solution phases. Equilibrium with respect to portlandite is also added for Ca/Si > 1.7-1.8. The experimental data from Greenberg and Chang (1965) was used to calibrate the model, which is applicable to a wide range of Ca/Si ratios of the C-S-H. Figure 1.10 shows a comparison between model and experimental data.

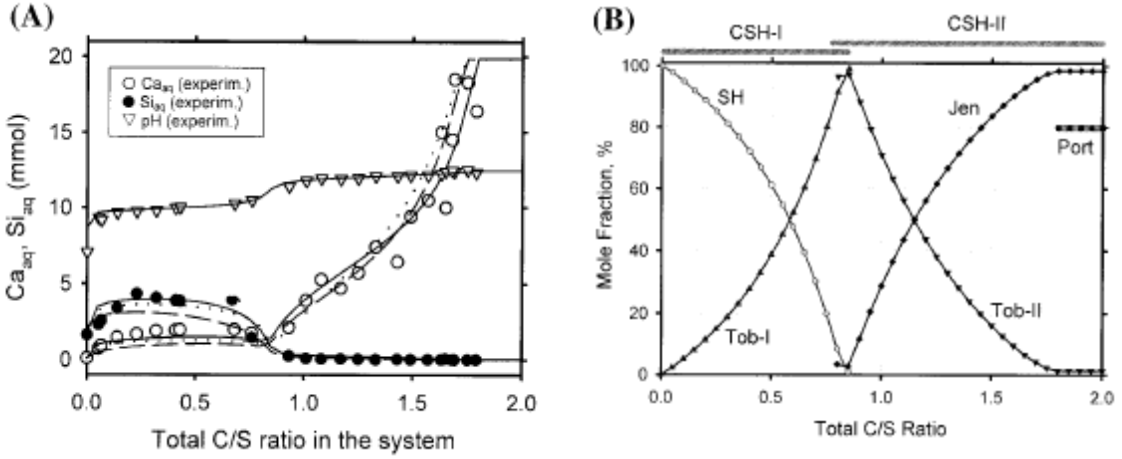

Figure 1.10. *(a) Ca concentration, Si concentration and pH vs. Ca/Si ratio of the solid. Points are experimental data (Greenberg and Chang, 1965). Lines correspond to model calculations. Dotted and dashed lines correspond to different variants of the model. (b) Mole fractions of the end-members of the two solid solutions as a function of the Ca/Si ratio of C-S-H. The presence of portlandite is indicated by a horizontal line (out of scale). After Kulik and Kersten (2001).*

The model included an explicit dependence of temperature (log K = a + b/T + c lnT) argued to be valid from 0 to 50 °C.

Harris et al. (2002) studied the leaching of synthetic C-S-H gels in demineralised water in static dissolutions. The results demonstrated that the initial stages of the dissolution of C-S-H gels in demineralised water are apparently incongruent decreasing the pH between 12.5 to 10.5, followed by an approach to congruent behavior where the pH remains constant around 10.5. In the same year, Gérard et al. (2002) elaborated a solubility diagram, with the data compiled by Berner (1992), representing the Ca/Si ratio of the hydrated phases against Ca in solution. In the diagram the author differentiates three stages: dissolution of portlandite up to 20 mmol/L of aqueous Ca; gel decalcification and leach of alkalis (between 2 and 20 mmol/L of aqueous Ca). Finally, dissolution of the gel (below 2 mmol/L of aqueous Ca), which becomes rich in Si.

Carey and Lichtner (2006, 2007) proposed a non-ideal binary solid solution (SiO_2 – $Ca(OH)_2$) to describe the solubility of C-S-H gel. The two end-members are SiO_2 and $Ca(OH)_2$. The model was calibrated using the experimental data from Chen et al. (2004).

Recently, using a multi-site (sublattice) concept, Kulik (2011) revised the 2001 ideal solid solution model of C-S-H to make it consistent with the Richardson–Groves structural model of C-S-H and with the modern interpretation of spectroscopic (^{29}Si MAS NMR) and solubility data. According to the author, consideration of two site substitutions, (1) coupled

H_2OCa^{2+} for $SiO_2H_2^{2+}$ replacement in bridging tetrahedral and adjacent interlayer sites, and (2) substitution of interstitial $Ca(OH)_2$ for a vacancy, leads to a new C-S-HQ model of (A,B)(C,D)X type composed of two tobermorite-like and two jennite-like end members. Because this ideal sublattice SS model cannot fit solubility data well at $0.8 < Ca/Si < 1.1$, a simpler C-S-H3T model is constructed from a polymeric TobH $(CaO)_2(SiO_2)_3(H_2O)_5$, a dimeric T2C $(CaO)_3(SiO_2)_2(H_2O)_5$, and an ordered pentameric T5C $(CaO)_{2.5}(SiO_2)_{2.5}(H_2O)_5$ tobermorite-like end members. This solid solution model, limited to the range $0.67 < Ca/Si < 1.5$, has a correct built-in dependence of the mean silicate chain length on Ca/Si and yields quite realistic fits to the solubility data, providing a basis for extensions with foreign cations whose sites in the defect-tobermorite structure of C-S-H are known. To account for C-S-H compositions with $Ca/Si > 1.5$, C-S-HQ end members were downscaled to one tetrahedral site and used within the simple mixing model. Despite some loss of structural consistency, the solubility and mean silicate chain length data can be reproduced well with this downscaled C-S-HQ model, capable of temperature corrections and dependencies of density and water content in fully-hydrated C-S-H on Ca/Si ratio.

In this Thesis, the Kulik and Kersten (2001) model will be applied in the study of the kinetics of C-S-H dissolution since it provides the necessary C-S-H gel thermodynamic parameters (e.g., solubility data of the discrete C-S-H gel composition, logK-T dependence, etc.)

1.5.2 SANS/USANS theoretical background

In recent years, considerable research on cement degradation has been conducted to understand the relevant mechanisms governing this complex process. To satisfy such demanding research different methodologies and techniques have been applied. A common methodology used for its simplicity are the laboratory leaching experiments (i.e., closed systems) to study the effect of decalcification on the C-S-H microstructure and cement mechanical properties (Carde et al., 1996; Thomas et al., 1998, 2004; Ulm et al., 1999; Allen and Thomas, 2007; Gonzalez-Teresa et al., 2010). Among the techniques used to study the cement and concrete structures, SANS and Ultra-small Angle Neutron Scattering (USANS) are particularly useful for investigating porous structures like C-S-H gel, given that the amorphous nature of C-S-H renders diffraction ineffective. In addition, specimens can be studied in their natural saturated state, thus avoiding complications associated with drying the C-S-H gel (Allen et al., 2007).

1.5.2.1 SANS technique

SANS is a technique of choice for the characterization of structures in the nanoscale size range (Hammouda, 1995). This covers structures from the near Angstrom to the near micrometer sizes. The small angles are typically from 0.2° to 20 ° and cover two orders of magnitude in two steps. A low-Q configuration covers the first order of magnitude (0.2° to 2°) and a high-Q configuration covers the second one (2° to 20°). A coherent collimated beam of neutrons passes through a thin specimen (2 mm thickness) where distance between the detector and the sample is bigger than the distance between the dispersive centres (Fig. 1.11).

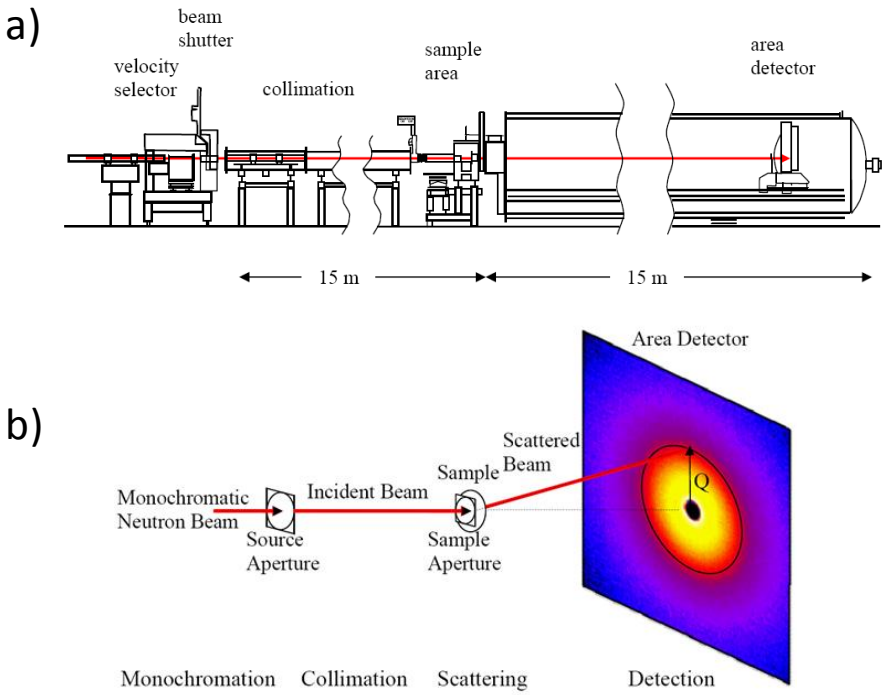

Figure 1.11. *Schematics of the SANS technique (it is not to scale) and (b) schematics of a 30 m SANS instrument at NIST. After Hammouda (2010).*

This fact provokes that a small fraction of the beam may be elastically scattered out of the incident beam direction by a small angle due to interfaces between the microstructural inhomegeneities within the sample (outer-product C-S-H gel particles and other features like CH crystals including pores) (Bumrongjaroen et al., 2009; Thomas et al., 1998b). The scattering variable is defined as $Q = (4\pi/\lambda) \sin(\theta/2)$ where λ is the neutron wavelength and θ is the scattering angle. At small angles, Q is considered to be $Q = 2\pi\theta/\lambda$.

The scattered neutron intensity (I (Q)) is registered, which is essentially a Fourier transform of the microstructure, as a function of the scattering angle θ, and plotted against the scattering vector Q (Fig. 1.12)

$$I(Q) = \frac{N}{V} P(Q)S(Q) \qquad \textit{Eq. 1.1}$$

where *N/V* is the number density of the scatter centres, *P(Q)* is the form factor that describes the scattering from a single particle, which strongly depends on its size and shape, and *S(Q)* is the structure factor containing all of the information about the spatial arrangement of the particles relative to an arbitrary origin, i.e. the correlations (Allen, 1991).

SANS thus provides a quantitative estimate of the fractal aspects of the microstructure, such as particle size, shape, surface area, and fractal properties. In general, the scattering from fine microstructure features occurs at relatively large scattering angles or Q values (SANS) and the coarse features occur at small Q (USANS). The upper-limit in Q for obtaining data from hydrating cement is about 2 nm^{-1}, due to the decrease in SANS intensity with increasing Q (Thomas et al., 2010). The fractal model (Allen and Thomas, 2007) (Eq. 1.9) is applied over the SANS Q range (Q> 0.035nm^{-1}). The model does not fit well to SANS data for Q < 0.035nm^{-1} because other non-fractal microstructure component dominates the scattering at length scales above 0.1 μm like micrometer-scale $Ca(OH)_2$ (Allen and Thomas, 2007).

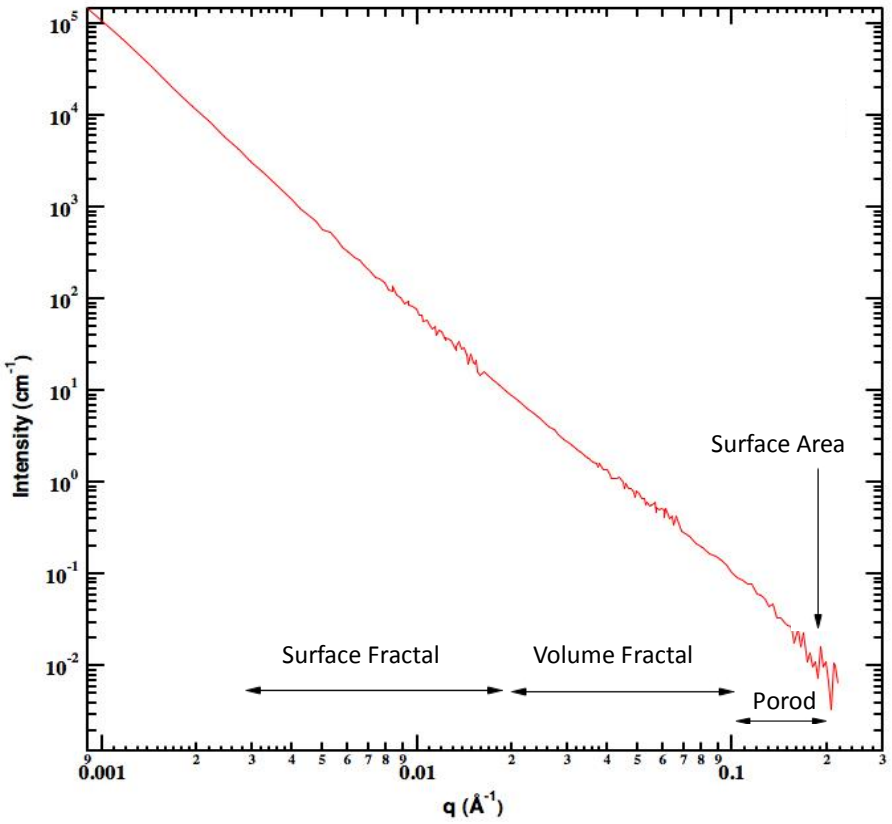

Figure 1.12. *Experimental SANS I(Q) data versus Q for the unreacted C-S-H gel of this study.*

1.5.2.2 The concept of a fractal

In Euclidean geometry, forms are grouped into lines, surfaces and volumes. Each of them has a characteristic number of dimensions to describe it: lines have one dimension, surfaces have two dimensions and volumes have three dimensions. Also they are considered to be smooth and well defined (Winslow 1985).

Irregular forms occurring in nature cannot be described by simple Euclidean ones. For example, the irregularities present in the surface of a hydrated cement grain. These irregularities observed to higher magnification reveal that they are composed at the same time of a series of additional, irregular features. When these irregularities continue to all levels of magnification and appear to be exactly or approximately similar to a larger viewer at a lesser magnification (concept of self-similarity), it is considered fractal geometry. The fractal geometry is divided into the same categories as Euclidean geometry: lines, surfaces and volumes with the difference that the dimensions can have non-integer numbers. Then, an irregular surface (fractal surface) with a fractal dimension of 2.4 is more irregular than one with a dimension of 2.2 and of course more irregular than an Euclidean smooth surface.

However, the self-similarity present in the fractals needs not to be extended over all ranges of magnification. There are scale limits of fractality above or below which the self-similarity ceases and where geometry may be considered to be Euclidean.

1.5.2.3 Models to interpret the C-S-H gel structure

Previous SANS studies combined with other structure-characterization results (e.g., from Transmission Electron Microscopy (TEM)) show that C-S-H gel has fractal-scaling characteristics (Allen, 1991). It is described as aggregates of nanometric particles that package in a fractal manner (the distribution of microscopic details is similar to that of macroscopic ones) (Fig. 1.13). In physic-chemical studies two main types of fractals are essentially encountered: mass fractal and surface fractal (Zarzycki, 1987).

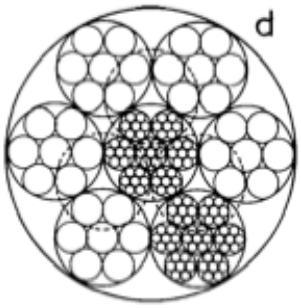

Figure 1.13. *Fractal multiple cluster like an example of fractal structure where the big sphere is filled with 13 small spheres. At the same time, the small spheres are also filled with 13 minispheres. After Zarzycki (1987).*

The mass of the fractal structure (or volume fractal) is typically represented by colloidal aggregates of individual particles size, which form clusters of size R. The mass of these fractal particles and the surface area increase more slowly with R than for a dense solid particle. However, the density decreases with R (Jennings et al., 2007; Zarzycki, 1987) being a typical behavior for a fractal structure. The surface fractals are characterized by a roughness of the interface (Fig. 1.14).

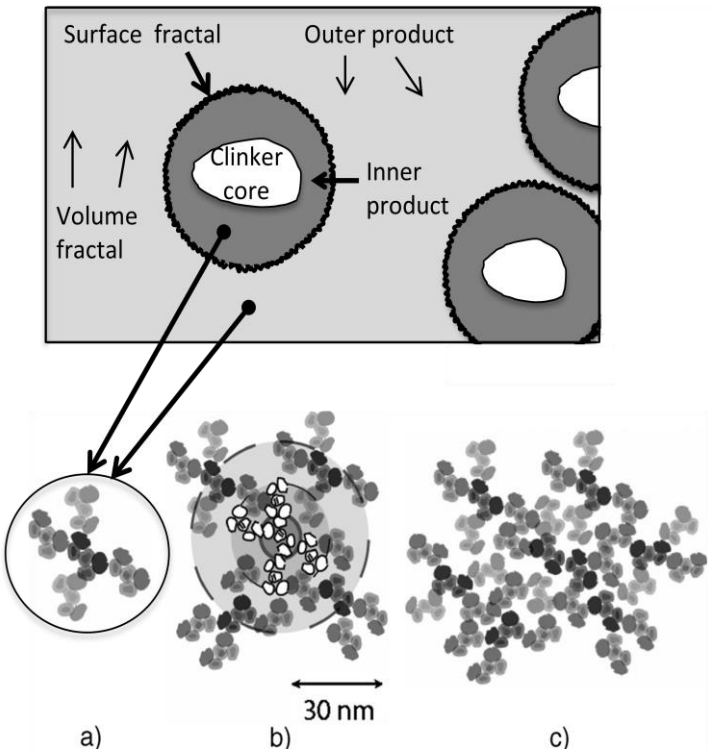

Figure 1.14. *a) Smallest fractal unit of ~ 5 nm globules of C-S-H. b) the fractal structure has grown with a reduced packing density. c) uniform structure of C-S-H gel. After Jennings et al., (2007).*

For an object with fractal geometry, SANS-USANS can be used to determine the fractal dimension and the nature of fractal morphology at large scale and these can be quantified through application of a fractal microstructure model (Allen et al., 1987; Jennings, 2000). This model considers spheroidal C-S-H particles with fixed aspect ratios that can be varied from 0.5 (oblade) to 2 (prolate). But the size and the shape of the particles is a matter of active research. Based on these observations and on a previous Jennings-Tennis model (1994), Jennings (2000) described a "colloid" model, so-called Colloidal Model I (CM-I), to explain the nanostructure of C-S-H (1 to 100 nm) from SANS measurements of density, pore size distribution and surface area (SSA). The model predicts that the smallest unit of C-S-H is a small tobermorite-like or jennite-like particle that has a radius of 1.2 nm (BBB-Basic Building Blocks). These fundamental units are packed together irregularly into structures called globules with a radius of 2.5 nm approximately (Jennings, 2000) (Fig. 1.15). The existence of these gel globules of 5 nm in diameter was confirmed by TEM images in the inner C-S-H gel product (Allen, 1991). The density of the smallest units is fixed to values close to 2.8 g cm^{-3} and the density of the globules is between 2.0 to 2.4 g cm^{-3} depending on the "intra-globular" water content. Later, Jennings et al. (2007) showed more exact calculations for the size of the smallest units, which are 4.4 nm in diameter. This fractal structure is bounded internally by a coarse system of capillary pores.

At larger scale, the globules pack together to form a dense volume fractal structure with two distinct densities: LD and a HD C-S-H gel that differ only in the porosity (Fig. 1.15). The density for the LD ranges from 1.440 to 2.013 g cm^{-3} and from 1.750 to 2.195 g cm^{-3} for the HD. The model CM-I makes good estimations of the surface area of the C-S-H units. The model assumes that the 5 nm gel globules are the fundamental building blocks of an aggregated Op product phase, that the Ip product is more compacted and gives very little scattering and the large features such as anhydrous clinker cores and CH add a Q^{-4} Porod scattering component. CM-I was recently refined (Colloid Model II (CM-II) (Jennings, 2008)) incorporating new values of density (2.6 g cm^{-3}), composition ($C_{1.7}$-S-$H_{1.8}$) (Allen and Thomas, 2007) and globule size (4.2 nm) (Jennings, 2008). However, several questions remain unanswered about the C-S-H nanostructure. For example, it is still unclear how tobermorite-like structure crystals can reorganize to form the basic building blocks of the colloidal models. Another open question is why HD C-S-H seems to be invisible to SANS measurement. Finally, there is a lack of knowledge concerning the effect of the colloidal packing on the appearance and disappearance of short-range ordering.

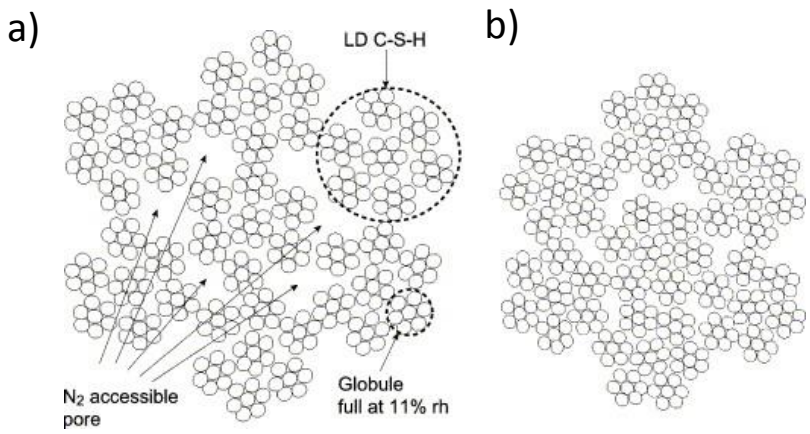

Figure 1.15. *Schematic representation of the C-S-H gel: low-density (LD) C-S-H (a) and high-density (HD) C-S-H (b). After Jennings (2000).*

1.5.2.4 SANS data analysis

The neutron scattering produced by the interaction with the structure can be mathematically explained by non-integral power laws with respect to the scattering vector Q (Allen, 1991).

Power laws

Three different scattering models or approximations for interpreting the data within the whole Q range, obtaining microstructural parameters of interest by means of standard plots and characteristics slopes and intercepts, are briefly described here. They are the Guinier approximation for well-defined discrete inhomogeneities, the Porod scattering Law for determining the surface area (S_v) and the volume-fractal structure and surface-fractal structure model to determine the volume fractal exponent (D_v) and the volume fractal scaling exponent (D_s).

- *Guinier Law*

The Guinier law applied at the low Q range (0.8-1.2 nm^{-1}) where $QR_g \leq 1$ for diluted systems. In this range, scattering from much larger particles like C-S-H gel particles is measured, for which it is possible to calculate the size of individual scattering objects (Guinier and Fournet, 1955). The intensity of scattering is related with the radius of gyration (R_g), associated with the size and shape of the particles. For the particular case of spheres or radius R, R_g is related with the radius of individual particles by means of $R = (5/3)^{1/2}R_g$, yielding:

$$I(Q) = I(0)\exp\left(-\frac{R_g^2 Q^2}{3}\right) \qquad \textit{Eq. 1.2}$$

The presence of a linear stage in the limits of low Q for Ln I(Q) vs. Q^2 informs about the existence of scattering centers with well-defined sizes. Otherwise, the absence of this linear zone informs of the polidispersity in size of the scattering centers.

- *Surface-fractal and Volume-Fractal (or mass fractals) structure.*

The analysis of intensity versus Q at higher values of Q means to check how the matter of the scattering centres fulls the volume. The surface fractal regime is associated with deposition of hydration products (C-S-H Op) onto the originally smooth surface of the cement clinker grains. While this structure co-exists with the volume-fractal, the scattering associated with it is only observable at lower Q, below 0.002 nm^{-1}. The surface fractal dimension, D_S, may be determined from the gradient of a log-log plot of I against Q where is characterized by non-integral power law ($d\Sigma/d\Omega \sim Q^{-(6-Ds)}$) and may vary between $2 < D_S < 3$ for non-smooth surfaces.

A steeper power law of $Q^{-3.2}$ is observed for $Q < 0.15$ nm^{-1} and this is believed to be associated with surface fractal behavior, arising from the deposition of C-S-H gel on the clinker/pore boundary and roughening as water intrudes to form the Ip (Thomas et al., 2004). Ds value close to 2 implies a smooth surface (Mazumder et al., 2002).

The surface-fractal component is associated with two surface area values: a smooth surface area S_o (m^2cm^{-3}) and rough surface area per unit paste volume (S_{SF}; m^2cm^{-3}) that are related as:

$$S_{sf} = S_0 \exp\left(\frac{\xi_s}{R_c}\right)^{D_s-2} \qquad \textit{Eq. 1.3}$$

where R_c is the correlation-hole radius (Å), that is the minimum center-to-center distance between particles, and ξ_S is the correlation length (Å).

The volume-fractal regime is a relatively high Q range (0.002 - 0.01 nm^{-1}). The scattering is produced by packing of primary C-S-H gel particles. It is characterized by the non-integral power law $d\Sigma/d\Omega \sim Q^{-Dv}$, for $1 < D_V < 3$ (usually 2 to 3) in the case of C-S-H gel. In the case of LD and HD C-S-H gel (Figs. 1.14 and 1.15), the fractal exponent can be calculated considering that the spheres are filled with 13 globules (Fig. 1.13). Then, D is defined as D = lim ($\mathrm{Ln}N(\lambda)/\mathrm{Ln}(1/\lambda)$) where $N(\lambda)$ is the number of the parts which divides the sphere, and l is

the globule that it is possible to observe in the diameter of the big sphere. Hence, D equals to 2.33 (Zarzycky et al. 1987) and is close to the value 2.5-2.7 reported by Thomas et al. (2008).

The amount of cement paste volume that may be occupied by the volume-fractal C-S-H morphology ($\phi_{C\text{-}S\text{-}H}$; LD C-S-H gel without the gel pores) and the gel pores is given by ϕ_{MAX}

$$\phi_{MAX} = \phi_{C-S-H}\left(\frac{\xi_V}{R_c}\right)^{3-D_V} \qquad \textit{Eq. 1.4}$$

where ξ_V is the correlation length(Å). The ratio $\phi_{C\text{-}S\text{-}H}/\phi_{MAX}$ provides a measure of the overall C-S-H particle packing density.

The volume-fractal component is quantified in terms of the surface area of the volume-fractal component per unit volume of paste (S_{VF}), which is defined as $S_{VF} = S_T\text{-}S_{SF}$ (Allen et al., 2007; Livingston, 2009).

- *Porod Law*

The Porod law applied at the Q range from 0.01 to 0.02 nm^{-1}, i.e. the Porod Regime. The total internal surface area, S_T, can be determined. The equation of intensity for this region of Q's can be expressed as:

$$I = \frac{Cp}{Q^4} + BGD \qquad \textit{Eq. 1.5}$$

$$C_p = 2\pi|\Delta\rho|^2 S_T \qquad \textit{Eq. 1.6}$$

$$|\Delta\rho|^2 = \left(\rho_{C-S-H} - \rho_{H_2O}\right)^2 \qquad \textit{Eq. 1.7}$$

where C_p is the Porod constant ($Å^{-5}$) that is the constant of proportionality for the Porod scattering, *BGD* is the background intensity caused by incoherent flat background scattering and $\Delta\rho^2$ is the scattering contrast. The scattering contrast is the parameter that measures the intrinsic strength of the neutron scattering interaction between the two phases: C-S-H gel and H_2O. For the system C-S-H gel and CH, the surface area is that between the C-S-H gel and the pore H_2O with small contributions of CH.

The $\rho_{C\text{-}S\text{-}H}$ and ρ_{H2O} are the neutron scattering length densities of C-S-H and water, respectively, that give an idea of the scattering capacity of a compound. This parameter is calculated from the density and the chemical composition of each phase using published tables

for the bound coherent scattering length (b_i) of the different atoms of the compound with the following expression (Thomas et al., 1998a):

$$\rho_b = \rho N_A \frac{\Sigma b_i x_i}{M} \qquad \textit{Eq. 1.8}$$

where ρ (g cm^{-3}) is the density of the compound, N_A is the Avogadro number, M (g mol^{-1}) is the molecular weight, b_i (cm^{-1}) is bound coherent scattering length (each atom's capacity to scatter neutrons) and x_i is the stoichiometric index. For the C-S-H gel phase the composition and the density are not known *a priory* because it is not known how much water should be included in the structure. For this, the contrast matchpoint method (Thomas et al., 2010) and the exchanges between H_2O and D_2O are used.

The linear fit of the data in the Porod regime plotted as IQ vs.Q^4 yields C_p as the intercept at $Q^4 = 0$ and BGD as the slope of the fitting. Large features, such as anhydrous clinker cores and $Ca(OH)_2$ crystals, simply add a Q^{-4} Porod scattering component. The Porod approximation is applied for coherent data (background substracted) to obtain a direct measurement of the total internal surface area (S_T) as C_p is obtained (Thomas et al., 1998a).

SANS model to characterize the C-S-H gel structure

The full fractal model combines a mass or volume fractal scattering term, attributed to the Op between the grains, and a surface-fractal scattering term, attributed to Op deposited at the clinker grain boundaries and on inert surfaces, such as those of micrometer scale $Ca(OH)_2$ crystallites. Nonetheless, the surface fractal may include some inner product formed topochemically (Fig. 1.14). The full expression of the model is (Bumrongjaroen et al., 2009):

$$I(Q) = \emptyset_{C-S-H} V_P \Delta\rho^2 \left\{ \frac{\eta R_C^3}{\beta R_0^3} \left(\frac{\xi_V}{R_C}\right)^{D_V} \times \frac{sin[(D_V-1)arctan(q\xi_V)]}{(D_V-1)q\xi_V[1+(q\xi_V)^2]^{\frac{(D_V-1)}{2}}} + (1-\eta)^2 \right\} F^2(q) + \frac{\pi \xi_S^4 \Delta\rho^2 S_0 \Gamma(5-D_S) sin[(3-D_S)arctan(q\xi_S)]}{[1+(q\xi_S)^2]^{\frac{(5-D_S)}{2}} q\xi_S} + BGD$$

Eq. 1.9

where the most important parameters are summarized in Table 1.3.

Table 1.3 *Parameter definitions for the fractal microstructure model (Eq.1.9).*

Parameters	
$\phi_{C\text{-}S\text{-}H}$	Volume fraction of solid C-S-H gel globules within the entire specimen volume penetrated by the neutron beam. It is essentially a measure of the amount of LD C-S-H (without gel pores) in the paste.
V_P	Volume of a single C-S-H globules. ($Vp= 4\pi\beta R_0^3/3$) where β is the particle aspect ratio.
R_C	Correlation-hole radius. Is the minimum center-to-center distance between C-S-H globules.
R_0	The radius of the building block C-S-H gel globules.
η	Local packing fraction for nearest neighbour C-S-H gel globules.
D_V	Volume fractal scaling exponent. An intensive property of matter that offers a quantitative measure of the volume fractal.
D_S	Surface fractal scaling exponent. An intensive property of matter that offers a quantitative measure of the degree of surface roughness.
ξ_V	Upper-limit length scales (correlation lengths) over which volume fractal scaling apply. Is the maximum size up-to which a volume can be viewed as a fractal.
ξ_S	Upper-limit length scales (correlation lengths) over which surface fractal scaling apply. Is the maximum size up-to which a surface can be viewed as a fractal.
S_0	Smooth geometric surface area on which the surface fractal microstructure is deposited.
$\Gamma(x)$	Mathematical Gamma function.
$F^2(q)$	Single-particle form factor for C-S-H gel globule.
$\Delta\rho^2$	Neutron scattering contrast factor. In this paper, the contrast factors of interest are those between solid C-S-H and H_2O, solid C-S-D and D_2O, solid C-S-H/D and H_2O/D_2O with same given H/D ratios in each, CH and H_2O, CH and D_2O, CH and H_2O/D_2O with any given H/D ratio.
BGD	Background intensity.

With the appropriate scattering contrast, the C-S-H and $Ca(OH)_2$ contributions to the scattering can be separated to apply the model to each component. The model incorporates a significant number (9) of adjustable parameters (Eq. 1.9). However, different terms dominate at different parts of the scattering curve, and hence only around three parameters are needed to determine the fit in any one region (Bumrongjaroen et al., 2009). A first term gives the volume-fractal and single-globule scattering (Q range between 0.003 and 0.020 Å) and a second term covers the surface fractal scattering (Q range between 0.020 and 0.1 Å).

Model fitting in the regime of volume fractal structure yields the volume fraction of scatterers ($\phi_{C\text{-}S\text{-}H}$), the radius of the building block particles (R_0), the volume fractal exponent (D_V), the volume-fractal correlation length and BGD, which was subtracted by Porod scattering

fits and is simply used to refine this subtraction when necessary. The model allows setting but not varying the particle aspect ratio (β), the scattering contrast factor and volume filling (η) because the fit does not converge to a stable result if η, BGD and R_0 vary simultaneously (Thomas et al., 2008). In the regime of surface fractal (low Q) the model allows to fit the smooth surface area (S_o), the surface fractal exponent (D_V) and the surface-fractal correlation length, and set but not vary the scattering contrast factor. Other three microstructure parameters of interest can be derived from the previous ones: the upper-limit volume fraction (ϕ_{MAX}) that gives a measure of how much of the cement paste volume may be occupied by the volume-fractal C-S-H morphology, the fractally rough surface area (S_{SF}) and the surface fractal of the volume-fractal morphology (S_{VF}).

Curve fitting of the obtained SANS data, assuming C-S-H fractal structure, can be performed using the Irena-package (Ilavsky and Jemian, 2009).

1.5.3 Cement properties and experimental studies on cement reactivity

1.5.3.1 Cement composition

Ordinary Portland Cement

The cement is composed basically by C_3S (alite ≈ 58%), C_2S (belite ≈ 13%), C_3A (tricalcium aluminate ≈ 8%) and C_4AF ≈ 7%. During hydration, the silicates and aluminate phases that compose the Portland cement react with water and generate hydration products. With time these products generate a hard mass (setting) and the mechanical resistance increases. In general, hydrated cement consists of 40-50 wt.% C-S-H gel, 20-25 wt.% CH, 10-20 wt.% AFt (ettringite) and AFm (monosulfate), 10-20 wt.% pore solution and 0-5 wt.% minor components (NaOH, KOH, $Mg(OH)_2$) (Berner, 1992; Taylor, 1997).

C_3S, the most unstable silicate present in the cement, and the C_2S-β, less reactive than C_3S, react with water to produce C-S-H gel and CH. The C-S-H gel configures the pore structure of the hydrated cement and agglutinates the rest of the phases. The Ca/Si ratio of the C-S-H gel is 1.75 in average, but if the paste contents any addition of fly ash or silica fume (both are pozzolans), metakaolin or slag, the Ca/Si ratio decreases to values below 1 (Richardson et al., 1999) or close to 1.4 (De Weerdt et al., 2011).

C_3A reacts with water and gypsum to produce ettringite (AFt, $3CaO.Al_2O_3.3CaSO_4.32H_2O$), whose crystals have prismatic or acicular morphology. Ettringite is poorly soluble in water (Alexander et al., 2013). After 24 hours of hydration, as calcium sulphate is consumed, ettringite transforms into calcium monosulfoaluminate (AFm, $3CaO.Al_2O_3.CaSO_4.12H_2O$) (Garcia Vílchez, 2004), which has hexagonal crystals. At 25 °C the presence of carbonate stabilises AFm and displaces OH^- and SO_4^{2-}. However, in the presence of portlandite, the reaction results in changes in the amount of both portlandite and ettringite (Matschei et al., 2007). At approximately 50 °C, thermodynamic calculations predicted the conversion of ettringite and monocarbonate to monosulphate (Lothenbach et al., 2008b). C_4AF (ferrite) reacts with water to produce iron oxide, hydrogarnet and portlandite and also with sulphate to generate ettringite.

CH constitutes the 20-25 wt.% of the hydrated cement paste. CH is a crystalline phase with a well-defined composition that precipitates heterogeneously in the cement paste in hexagonal or prismatic crystals.

Mineral additions to Ordinary Portland Cement

The use of mineral additions (e.g., gypsum, fly ash or limestone) is common to improve durability, mechanical properties and workability of cement, as well as to reduce the impact of CO_2 produced in the decalcification process. Gypsum is mainly added to regulate the cement early hydration so that setting is delayed and workability improved.

Addition of fly ash alters the composition of the pore solution due to puzzolanic reactions with CH, decreasing the content of Ca in the pore solution. As fly ash is added to cement, the content of CH lowers as it is consumed by fly ash hydration. The pore solution of fly-ash-containing cements has lower pH and alkali concentrations than OPC and OPC-limestone mixes. Also, fly ash brings additional alumina, which reduce the sulphate to alumina ratio and therefore increases the impact of limestone powder (De Weerdt et al., 2011). An observed effect of the lower Ca/Si ratio and lower pH on the C-S-H gel structure is that C-S-H becomes more polymerized: Q^2, and eventually Q^3, is the dominant peak in the ^{29}Si NMR spectra (Matsuyama and Young, 2000).

Without limestone powder, C_3A and C_4AF react with gypsum to form ettringite, which can react with remaining C_3A and C_4AF to form monosulphate or hydroxyl-AFm solid solution (De Weerdt et al. 2011). With limestone, AFt and AFm-carbonate can be formed.

1.5.3.2 Porosity

Hydrated cement is a porous material filled with pore solution of pH around 13. The pore solution is in equilibrium with the C-S-H gel, being an open thermodynamic system. The equilibrium is a function of the external media, the relative humidity and/or the penetration of the external agents (Lagerblad, 2001).

Porosity (macroporosity and capillary porosity) in cement-based materials is created during hydration. Macropores are due to captured air during the mix, creating spherically shape pores with a size ranging between 10 and 200 μm, but can be as large as 2 to 3 mm. Macropores remain dry (in non-fully saturated cement) and therefore are not involved in ion transport, but are important in mechanical strength. Capillary porosity is the free space generated when the hydration products replace the space initially filled by water and cement. The size is directly proportional to the w/c ratio and the grade of hydration. Capillary porosity is known as macroporous porosity when the pore size is between 10 and 0.05 μm, mesoporous when it is between 0.05 and 0.01 μm, and microporous when the size is less than 0.01 μm. The latter porosity is interconnected filled with alkaline solution, and responsible of ion transport. Permeability, sorptivity, mechanical resistance, diffusion or ionic interchange, in fact, are function of the pore size and pore connectivity of the capillary porosity. In mortar pastes, one of the zones with major capillary porosity (15-30 %) is the zone between the aggregates and the cement (wall effect), that is known as an interfacial transition zone. Around aggregates the amount of cement grains is low. An increment of the w/c ratio is originated generating a zone with high porosity, CH and ettringite around the aggregates. Bourdette et al. (1995) indicated that this zone can be percolated increasing the porous system connectivity and thus the permeability.

The C-S-H gel shows an inherent porosity within its structure, known as interlayer porosity. The pores are also known as gel pores with spaces from 5 to 25 Å between gel layers. Gleize et al. (2003) showed that the gel porosity is refined when the gel is formed by calcium hydroxide and silica fume (or fly ash) instead of the conventional hydration of C_3S and C_2S.

Finally, hollow-shell pores form when the Op precipitate, generating a shell of precipitate, in which exists an empty space. These pores can be partially or completely empty (Kjellsen et al., 1997).

1.5.3.3 Degradation of microstructure of cement-based materials

Cement microstructure is essential to understand the physicochemical properties of the cement-based materials and the processes involved in the cement degradation. For example, cement microstructure plays a fundamental role as a barrier to storage radioactive as the porous structure generates a high surface in which sorption of the radionuclides takes place (Harris et al 2002; Sugiyama, 2008), and the high porewater pH limits radionuclide solubility (Olson et al., 1997; Harris et al., 2002). Cements and concretes can be attacked and, as a result, exhibit a reduced service life (Glasser el at., 2008). Therefore, whatever evolution of the microstructure submitted to degradation affects the durability of these materials.

The porewater of cementitious materials is in equilibrium with the phases present in the hydrated cement and contains mainly K, Na, Ca, Si, S, Fe and Al in solution and is characterized by a high pH values. Replacement of the porewater will perturb the local equilibrium, causing dissolution and precipitation reactions (Faucon et al., 1998). Cement paste degradation is therefore induced by a combination of diffusion-transport effects and chemical reactions and the degradation kinetics depends thus upon the kinetics of each of these two phenomena (Faucon et al., 1997). The final result is a process of chemical changes and dissolution of the phases present in cement increasing the porosity and the degree of penetration (Fig. 1.16; Lagerblad, 2001). The first phase to dissolve is CH because of its high solubility, and its dissolution delimits the front of degradation. After CH dissolution, dissolution of other hydrated compounds like C-S-H gel, AFt (ettringite) or AFm (i.e. monosulfoaluminates) takes place, depending on their solubility (Rémond et al., 2002). Dissolution creates a front of dissolution/precipitation and zonation in the degraded material (Faucon et al., 1997). Berner (1992) shows that the C-S-H gel has different Ca/Si ratio values from 1.7, for the unaltered zone, to lower values, for the degraded zone. The dissolution of a phase influences the rest as it changes the equilibrium conditions of the porewater. Thus the process of dissolution in the cement occurs when a concentration gradient of ions such as Ca^{2+} and OH^- exists in the aqueous phase from poorly degraded zones to the more degraded zones (Lagerblad, 2001). If the leaching persists the zone directly in contact with water can be completely depleted in CH. The concrete surface is deteriorated to hydrous silica gel without presence of calcium (Duchesne et al., 2013). The ^{29}Si-NMR results show that C-S-H gel polymerises to greater chain length and the Ca/Si ratio lowers (Lagerblad, 2001).

The main process that takes places during leaching is decalcification of the system. Leaching is an acid-base reaction where input water (low pH) neutralizes the pore solution. Also, components of the input water like carbonate, chloride, sulfate, etc. can penetrate in the system and react with the phases present in the cement. The remaining non-hydrated products

start to hydrate during the leaching and consequently Ca is released and C-S-H gel is formed (Lagerblad, 2001).

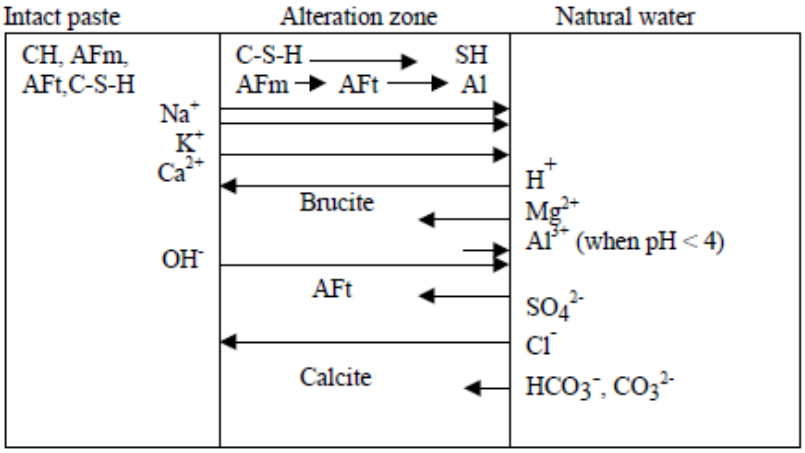

Figure 1.16. *Ionic movement across the cement paste by leaching effect. After Lagerblad (2001).*

1.5.3.4 Transport mechanisms in cement-based materials

The main leaching mechanism is ionic diffusion (Lagerblad, 2001). Other transport mechanisms, such as water movement (advection caused by a flow of the aqueous solution), advection phenomenon due to capillary suction, and chemical reactions, i.e. dissolution and precipitation, take place in the cement degradation. Diffusion is related to Fick's Law and flow through capillary pores in saturated concrete is bound to Darcy's Law.

The diffusion coefficient (D_i) is a proportionality constant (m^2/s) and it can be affected by the degree of saturation of the material, ambient temperature or the pore structure of the material (Glasser et al., 2008). Diffusion mainly occurs in the open connected capillary pores in the water phase. The structural changes in the paste, promoted by chemical reactions during the leaching, affect the porosity of cement and its transport properties (Glasser et al., 2008). Formation of new phases can lead to porosity reduction and contributes to reduce the transport properties. Dissolution of the existing phases can open the pore structure, increasing permeability and diffusivity and decreasing sorptivity, as well as loss of mechanical strength (Dow and Glasser, 2003). The sorptivity coefficient (k) is essential to predict the service life of concrete as a structural material and to improve its performance (Martys and Ferraris, 1997).

The presence of aggregates in the system increases tortuosity, which generates a decrease in diffusion. Added particles of limestone or fly ash react with CH, resulting in a

greater amount of hydrated products in the porous phase, increasing tortuosity and generating a dense matrix (Cruz et al., 2011).

1.5.3.5 Studies of cement degradation

In the last twenty five years, numerous studies of the reactivity of hydrated cement are found in the literature. The studies are classified into three categories according to the objective of the research: leaching of cement pastes, reactive transport modeling and thermodynamics of cement hydration processes.

Leaching of cement pastes

Adenot and Buil (1992) performed leaching experiments with ordinary Portland cement (OPC) specimens and deonized water. It was observed the formation of an uncorroded central core surrounded by three corroded zones with progressive decrease of Ca/Si ratio. The outermost zone no longer contained any portlandite. To account for the observed zoning degradation, a model based on solubility data by Berner (1988, 1992) was proposed by considering Ca diffusion and local chemical equilibrium

$$e_D = \sqrt{D_{ap} \cdot t} \qquad \textit{Eq. 1.10}$$

where e_D is the degraded depth zone, D_{ap} is the apparent diffusion coefficient and *t* is time.

Buil et al. (1992) proposed a mass balance equation of calcium to describe the Ca leaching experiments

$$\frac{\partial(C_{Ca}\phi)}{\partial t} = -div\left(-D(\phi)\ grad\ (C_{Ca})\right) - \frac{\partial S_{Ca}}{\partial t} \qquad \textit{Eq. 1.11}$$

where S_{Ca} is the solid calcium concentration, C_{Ca} is the liquid calcium concentration, D is the calcium effective diffusivity in porous material and ϕ is the porosity.

Revertegat et al. (1992) studied the effect of pH on the durability of cement pastes to conclude that the degree of C-S-H gel decalcification was related to the pH gradient and the ionic character of the pore solution. Also, a model to deal with the progressive decrease in the solid C-S-H gel Ca/Si ratio was proposed in which leaching of calcium was expressed as

$$\chi = a \cdot \sqrt{t} \qquad \textit{Eq. 1.12}$$

where χ is the depth of the degradation process, *a* is an experimental constant and *t* is time.

Delagrave et al. (1997) proposed an empirical relation between the calcium concentration of the pore solution with the calcium concentration of the cementitious skeleton. The equilibrium between the solid calcium phases and the calcium concentration of the pore solution is characterized by a curve with two steps. From a physical point of view, and agreeing with Adenot and Buil (1992), this phenomenon is driven by diffusion of the calcium ions from the reaction sites. Alteration of cement is due to dissolution of a layered system composed of an unaltered core delineated by total dissolution of CH, different zones separated by dissolution or precipitation fronts (AFm, Aft), and progressive decalcification of C-S-H gel, which induces silicate polymerization. Carde et al. (1997) observed that alteration of the structure of the gel is due to an increase in the length of the silicate chains with its decalcification and dissolution, and stabilization of the C-S-H gel structure occurs at Ca/Si ratio of 0.8.

Faucon et al. (1997, 1998) studied the leaching in cement paste by means of static dissolution experiments and controlling the Ca/Si ratio in the C-S-H, which continuously decreased between the intact and degraded zones. Calcium concentration gradient continuously decreased from the unaltered zone to the surface of the material, due to CH dissolution before and leaching of C-S-H gel later. C-S-H of low Ca/Si precipitated during degradation and dissolved by contact with the aggressive solution. This gradient caused the development of a degraded zone in the cement paste and diffusion of calcium in the interstitial solution toward the attacking solution. The decrease in the concentration of calcium in this zone induced secondary precipitations (AFm, ettringite and calcite) in the innermost part of the degraded zone, and dissolution in the outermost part of the degraded zone. Trivalent iron and aluminum, released from crystallized hydrates during dissolution, are partially incorporated into the C-S-H gel, enhancing the stability of these C-S-H gels (low Ca/Si ratio gels). It was observed that two different regimes (diffusion versus surface dissolution) occurred during demineralized-solution induced degradation of cement pastes, and it was deduced that the kinetics of degradation is proportional to the square root of time when the rate of superficial layer dissolution is negligible (diffusion regime). This situation would persist only if the solubility of the C-S-H in the superficial layer is low.

Mainguy et al. (2000) proposed a numerical solution for the non-linearity of the mass balance equation that describes the leaching of cement reported in Buil et al. (1992). It was based on a finite volume method. Another model was proposed by Gérard et al. (2002) using the solubility data by Berner (1988, 1992), based also on the criteria of diffusion and local equilibrium. Ca concentration as a variable of state is considered and Newton-Raphson approximation incorporates the non-linearity. However, none of the both models take into account reprecipitation of phases during the degradation process.

Moranville et al. (2004) and Maltais et al. (2004) proposed a more complex model by coupling the interaction between the ions of the aqueous phase and the solid phases, present in the cement paste, and considering the effect of the differences in concentration between the porous solution and the external solution. It was assumed that the porous solution was saturated, the process was controlled by diffusion, and chemical equilibrium persisted in the system. This proposed reactive transport model considered that species can dissolve and precipitate simultaneously. Haga et al. (2005) leached OPC in deionized water to study the effect of pore volume on the progress of dissolution. Experimental data was modeled using a basic mass conservation formula and considering one-dimensional diffusion of Ca and equilibrium between the solid and the liquid phase. It was concluded that leaching of portlandite generated porosity.

Kamali et al. (2008) degraded cement pastes using continuously renewed water as a function of temperature, water/cement ratio, percentage of silica fume content and pH. The experimental data was modeled using a simplified model earlier proposed by Revertegat et al. (1992)

$$L_d = a \cdot t^{1/n} \qquad \textit{Eq. 1.13}$$

where L_d is the leached depth (mm), t (days), n = 2 for degraded in absence of electric field and n = 1 on presence of electric field, a is a constant parameter determined as

$$a = b \cdot \prod_{i=1}^{n} f(i) \qquad \textit{Eq.1.14}$$

where b is a constant value, $f(i)$ are the functions that correspond to the influence of one of the various parameters i considered. These functions are built by means of linear regressions from the experimental data. Also, Yang et al. (2012) performed leaching experiments in cement pastes following the model by Revertegat et al. (1992) to model the evolution of the hardness in leached cement. De Larrad et al. (2010) argued that the non-linearity of the mass balance equation of calcium to describe the leaching proposed by Buil et al. (1992) is mainly due to the diffusivity which depends on the porosity, itself depending on the solid calcium concentration, and on the non-linearity between S_{Ca} and C_{Ca}.

Since the calcium leaching kinetics in water is slow, some studies used different strategies to accelerate the leaching process by using acidized solutions instead of deionised water (Carde et al., 1997; Heukamp et al., 2001; Thomas et al., 2004; Kamali et al., 2008). Ammonium nitrate solution was selected to be representative of an aggressive solution. Thomas et al. (2004) argued that NH_4NO_3 leaching preferentially removes calcium from the C-S-H even at very low Ca/Si. The preservation of the Si structure allows very low Ca/Si ratios (near 0.1) to

be reached while maintaining the integrity of the specimen. Other solutions with organic acids (acetic, propionic, butyric or isobutyric acids) were also used, observing that the alteration of the cement paste occurs by an almost complete decalcification, the disappearance of the crystallized or amorphous hydrated phases and the probable formation of a silica gel containing aluminum and iron, which acts to limit the kinetics of further alteration (Bertron et al., 2005). A different option to accelerate the calcium leaching process was application of a potential gradient across the mortar specimen (Saito et al., 2000).

Reactive transport modeling

Van der Lee and De Windt (2001) proposed a reactive transport model which considers the geochemically complex systems in a hydrodynamic context and accounting for unsaturated flow and transport processes in the gas phase. Samson et al. (2007) performed multiionic transport model for saturated/unsaturated cementitious materials to account for degradation of cement-based materials exposed to aggressive environments. The classical Fick's diffusion mechanism was contemplated, as well as the electrical coupling between the various ions and the chemical activity effect. Advection phenomenon due to capillary suction and chemical reactions typical to cement-based materials were also included. As Moranville et al. (2004), the model considers that the species can dissolve and precipitate.

Galíndez and Molinero (2010) developed a model to simulate degradation of cement injected in a granite fracture under assumptions of local equilibrium and diffusion of ions as transport process. Soler and Mäder (2010) and Soler (2013) simulated concrete-rock interactions between an hyperalkaline solution and a granite rock and a high-pH solution and a clay-rich rock, respectively, using the CrunchFlow code (Steefel, 2009).

Thermodynamics of the cement hydration processes

Thermodynamic modelling has been applied to study the hydration processes of Portland cement (Lothenbach and Winnefeld, 2006; Lothenbach and Wieland, 2006; Lothenbach et al., 2007, 2008; Gruskovnjak et al., 2008). Application of thermodynamics to cement hydration has been shown to be successful if used with an understanding of its underlying principles and limitations and gives important parameters used to assess the kinetics of reactions (Damidot et al., 2011). Winnefeld and Lothenbach (2010) investigated by experimental means and thermodynamic modeling the hydration mechanisms of calcium sulfoaluminate cements (CSA cements). The authors used the thermodinamic model GEMS (Kulik et al., 2004) with the cement chemical composition, the dissolution kinetics of the clinker

phases and the thermodynamic equilibria for the solid phases involved. Lothenbach et al. (2010) modeled successfully the ingress of sulfates in mortar by assuming interaction of mortar with sulfate solutions and coupling the thermodynamic model with transport codes. Leemann et al. (2010) studied the deterioration of the concrete surface by acid attack after two years of exposure caused by a nitrifying biofilm covering the concrete. The thermodynamic modeling of the changes induced in concretes was carried out. Good agreement with the experimental results was observed and was explained the observed profiles of porosity and chemical composition. Ben Haha et al. (2012) investigated the effect of Al_2O_3 in the slag on the hydration properties of alkali activated slag varying the Al_2O_3 content. Thermodynamic calculations indicate that the Al_2O_3 content of the slag is not expected to have a significant influence on the volume of the hydrated samples. Le Saoût et al. (2013) used GEMS to predict the composition of the liquid and the solid phase as function of hydration time for OPC with two additions calcium sulfoaluminate and an amorphous calcium aluminate. Kunther et al. (2013) investigated the influence of bicarbonate ions on the deterioration of cementitious material exposed to sodium sulfate solution and to solutions containing simultaneously sodium sulfate and sodium bicarbonate. Thermodynamic modeling of the changes caused by the interaction predicts that ettringite becomes unstable in the presence of bicarbonate ions and gypsum does not form. Zajac et al. (2014) studied the hydration of three limestone cements containing different amounts of $CaSO_4$ as well as industrially produced cements with different quantities of $CaCO_3$ in order to assess the influence of calcium sulphate and calcium carbonate on hydration.

References

Adenot, F., and Buil, M. (1992). Modelling of the corrosion of the cement paste by deionized water. *Cement and Concrete Research*, 22(2), 489-496.

Alexander, M. G., Bertron, A., and De Belie, N. (Eds.). (2013). Performance of Cement-based Materials in Aggressive Aqueous Environments (Vol. 10). Springer.

Allen, A. J., and Thomas, J. J. (2007). Analysis of C–S–H gel and cement paste by small-angle neutron scattering. *Cement and concrete research*, *37*(3), 319-324.

Allen, A. J., Thomas, J. J., and Jennings, H. M. (2007). Composition and density of nanoscale calcium–silicate–hydrate in cement. *Nature materials*, *6*(4), 311-316.

Allen, A. J. (1991). Time-resolved phenomena in cements, clays and porous rocks. *Journal of Applied Crystallography*, *24*(5), 624-634.

Allen, A. J., Oberthur, R. C., Pearson, D., Schofield, P., and Wilding, C. R. (1987). Development of the fine porosity and gel structure of hydrating cement systems. *Philosophical Magazine B*, 56(3), 263-288.

Atkinson, A., Hearne J. A., and Knights C. F. (1989). Aqueous Chemistry and Thermodynamic Modelling of CaO-SiO_2-H_2O Gels. *Journal of Chemical Society Dalton Transaction*, 12, 2371-2379.

Ayora, C., Soler, J. M., Saaltink, M. W., Carrera, J. (2007). Modelo de transporte reactivo sobre la lixiviación del hormigón por agua subterránea en la celda 16 de El Cabril. ENRESA.

Bernal, J. D., Jeffery, J. W., Taylor, H. F. W. (1952). Crystallographic research on the hydration of Portland cement. A first report on investigations in progress. *Magazine of Concrete Research*, 4(11), 49-54.

Berner, U. R. (1992). Evolution of pore water chemistry during degradation of cement in a radioactive waste repository environment. *Waste Management*, 12(2), 201-219.

Berner, U. R. (1990). Thermodynamic Description of the Evolution of Pore Water Chemistry and Uranium Speciation during the Degradation of Cement. PSI-Bericht Nr.62.

Berner, U. R. (1988). Modelling the incongruent dissolution of hydrated cement minerals. *Radiochimica Acta*, 44(45), 387-393.

Bertron, A., Duchesne, J., and Escadeillas, G. (2005). Accelerated tests of hardened cement pastes alteration by organic acids: analysis of the pH effect. *Cement and Concrete Research*, 35(1), 155-166.

Black, L., Garbev, K., Gee, I. (2008). Surface carbonation of synthetic CSH samples: A comparison between fresh and aged CSH using X-ray photoelectron spectroscopy. *Cement and Concrete Research*, 38(6), 745-750.

Black, L., Garbev, K., Beuchle, G., Stemmermann, P., Schild, D. (2006). X-ray photoelectron spectroscopic investigation of nanocrystalline calcium silicate hydrates synthesised by reactive milling. *Cement and Concrete Research*, 36(6), 1023-1031.

Bonaccorsi, E., Merlino, S., and Kampf, A. R. (2005). The crystal structure of tobermorite 14 Å (plombierite), a C–S–H phase. *Journal of the American Ceramic Society*, 88(3), 505-512.

Börjesson, S., Emrén, A., Ekberg, C. (1997). A thermodynamic model for the calcium silicate hydrate gel, modelled as a non-ideal binary solid solution. *Cement and Concrete Research*, 27(11), 1649-1657.

Bourdette, B., Ringot, E., and Ollivier, J. P. (1995). Modelling of the transition zone porosity. *Cement and Concrete Research*, 25(4), 741-751.

Buil, M., Revertegat, E., and Oliver, J. (1992). Model of the attack of pure water or undersaturated lime solutions on cement. ASTM Special Technical Publication, (1123), 227-241.

Bumrongjaroen, W., Livingston, R. A., Neumann, D. A., and Allen, A. J. (2009). Characterization of fly ash reactivity in hydrating cement by neutron scattering. *Journal of Materials Research*, 24(07), 2435-2448.

Carde, C., François, R., and Torrenti, J. M. (1996). Leaching of both calcium hydroxide and C-S-H from cement paste: Modeling the mechanical behavior. *Cement and Concrete Research*, 26(8), 1257-1268.

Carey, J. W., and Lichtner, P. C. (2007). Calcium Silicate Hydrate (C-S-H) Solid Solution Model Applied to Cement Degradation using the Continuum Reactive Transport Model FLOTRAN. In:Mobasher B. and Skalny J., Eds., Transport Properties and Concrete Quality:Materials Science of Concrete, Special Volume,pp.73-106.American Ceramic Society.

Carey, J. W., and Lichtner, P. C. (2006). Calcium Silicate Hydrate Solid Solution Model Applied to Cement Degradation using the Continuum Reactive Transport Model FLOTRAN. Report LA-UR-06-0636.

Carde, C., and François, R. (1997). Effect of the leaching of calcium hydroxide from cement paste on mechanical and physical properties. *Cement and Concrete Research*, 27(4), 539-550.

Chatterjee A. (2004). Shrinkage and Strength Characterizations of Concrete Containing Supplementary Cementing Materials, Department of Civil and Environmental Engineering Morgantown, West Virginia.

Chen, J. J., Thomas, J. J., Taylor, H. F., Jennings, H. M. (2004). Solubility and structure of calcium silicate hydrate. *Cement and Concrete Research*, 34(9), 1499-1519.

Cong, X., and Kirkpatrick, R. J. (1996). ^{29}Si MAS NMR Study of the Structure of Calcium Silicate Hydrate. *Advanced Cement Based Materials*, 3(3), 144-156.

Costoya, M. M. (2008). Effect of Particle size on the hydration kinetics and microstructural development of tricalcium silicate. École Polytechnique Fédérale de Lausanne-Suisse. Doctoral These.

Cruz, J. M., Payá, J., Lalinde, L. F., and Fita, I. C. (2011). Evaluación de las propiedades eléctricas de morteros de cemento con puzolanas. *Materiales de construcción*, 61(301), 7-26.

Delagrave, A., Gérard, B., and Marchand, J. (1997). Modelling the calcium leaching mechanisms in hydrated cement pastes. Mechanics of Chemical Degradation of Cement-Based Systems. Chapman and Hall, London, 30-37.

De Larrard, T., Benboudjema, F., Colliat, J. B., Torrenti, J. M., and Deleruyelle, F. (2010). Concrete calcium leaching at variable temperature: experimental data and numerical model inverse identification. *Computational Materials Science*, 49(1), 35-45.

De Weerdt, K., Haha, M. B., Le Saout, G., Kjellsen, K. O., Justnes, H., and Lothenbach, B. (2011). Hydration mechanisms of ternary Portland cements containing limestone powder and fly ash. *Cement and Concrete Research*, 41(3), 279-291.

Dow, C., and Glasser, F. P. (2003). Calcium carbonate efflorescence on Portland cement and building materials. *Cement and Concrete Research*, 33(1), 147-154.

Duchesne, J., and Bertron, A. (2013). Leaching of Cementitious Materials by Pure Water and Strong Acids (HCl and HNO_3). In Performance of Cement-Based Materials in Aggressive Aqueous Environments (pp. 91-112). Springer Netherlands.

Faucon, P., Adenot, F., Jacquinot, J. F., Petit, J. C., Cabrillac, R., Jorda, M. (1998). Long-term behaviour of cement pastes used for nuclear waste disposal: review of physico-chemical mechanisms of water degradation. *Cement and Concrete Research*, 28(6), 847-857.

Faucon, P., Adenot, F., Jorda, M., and Cabrillac, R. (1997). Behaviour of crystallised phases of Portland cement upon water attack. *Materials and Structures*, 30(8), 480-485.

Feldman, R. F., and Sereda, P. J. (1970). A new model for hydrated Portland cement and its practical implications. *Engineering Journal of Canada*, 53(8-9), 53-59.

Fujii, W., and K. Kondo. (1981). Heterogeneous Equilibrium of Calcium Silicate Hydrate in water at 30ºC. *Journal of the Chemical Society, Dalton Transactions*, 2, 645-651.

Gaitero, J. J., Campillo, I., and Guerrero, A. (2008). Reduction of the calcium leaching rate of cement paste by addition of silica nanoparticles. *Cement and Concrete Research*, 38(8), 1112-1118.

Galíndez, J. M., and Molinero, J. (2010). Assessment of the long-term stability of cementitious barriers of radioactive waste repositories by using digital-image-based microstructure generation and reactive transport modelling. *Cement and Concrete Research*, 40(8), 1278-1289.

Gallucci E., Scrivener, K. (2007). Crystallisation of calcium hydroxide in early age model and ordinary cementitious systems. *Cement and Concrete Research*, 37(4), 492-501.

García Vílchez E. (2004) Estabilitat de la Dolomita en el Medi de la Pasta Pòrtland: Aplicació a la Fabricació de Formigons amb Àrids Dolomítics. Ph.D. Thesis, University of Barcelona.

Garrault-Gauffinet, S., and Nonat, A. (1999). Experimental investigation of calcium silicate hydrate (CSH) nucleation. *Journal of Crystal Growth*, 200(3), 565-574.

Garrault, S., Behr, T., and Nonat, A. (2006). Formation of the C-S-H Layer during early Hydration of Tricalcium Silicate Grains. *Journal Physics Chemistry B*, 110(1), 270-275.

Garrault, S., and Nonat, A. (2001). Hydrate layer formation on Tricalcium and Dicalcium Silicate surface:Experimental study and numerical simulations. *Langmuir*, 17, 8131-8138.

Gartner, E. M., and Jennings, H. M. (1987). Thermodynamics of calcium silicate hydrates. *Journal of the American Ceramic Society*, 70(10), 743-749.

Gérard, B., and Le Bellego, C. 2002. Simplified modeling of Ca leaching of concrete in various environments. *Material and structure*, 35, 632-640.

Glasser, F. P., Marchand J., Samson E. (2008) Durability of concrete- Degradation phenomena involving detrimental chemical reactions. *Cement and Concrete Research*, 38(2), 226-246.

Glasser, F. P., Lachwski, E. E., and Macphee, D. E. (1987). Compositional Model for Calcium Silicate Hydrate (C-S-H) Gels, Their Solubilities, and Free Energies of Formation. *Journal of the American Ceramic Society*, 70(7), 481-485.

Gleize, P. J. P., Müller, A., and Roman, H. R. (2003). Microstructural investigation of a silica fume–cement–lime mortar. *Cement and Concrete Composites*, 25(2), 171-175.

Gonzalez-Teresa R., Morales-Florez V., Manzano H., Dolado J.S. (2010). Structural models of randomly packed tobermorite-like spherical particles: A simple computational approach. *Mater Construction*. 60(298), 7-15.

Greenberg, S. A., and Chang, T. N. (1965). Investigation of the Colloidal Hydrated Calcium Silicates. II. Solubility Relationships in the Calcium Oxide-Silica-Water System at 25°. *The Journal of Physical Chemistry*, 64(9), pp 1151–1157.

Gruskovnjak, A., Lothenbach, B., Winnefeld, F., Figi, R., Ko, S. C., Adler, M., and Mäder, U. (2008). Hydration mechanisms of super sulphated slag cement. *Cement and Concrete Research*, 38(7), 983-992.

Grutzeck, M. W. (1999). A new model for the formation of calcium silicate hydrate (C-S-H). *Material Research Innovations*, 3(3), 160-170.

Grutzeck, M., Benesi, A., and Fanning, B. (1989). Silicon-29 Magic Angle Spinning Nuclear Magnetic Resonance Study of Calcium Silicate Hydrates. *Journal of the American Ceramic Society*, 72(4), 665-668.

Guinier, A., and Fournet, G. (1955). Small Angle Scattering. International Tables for X-ray Crystallography, 324-30.

Haha, M. B., Lothenbach, B., Le Saout, G., and Winnefeld, F. (2012). Influence of slag chemistry on the hydration of alkali-activated blast-furnace slag—Part II: Effect of Al_2O_3. *Cement and Concrete Research*, 42(1), 74-83.

Haga, K., Sutou, S., Hironaga, M., Tanaka, S., and Nagasaki, S. (2005). Effects of porosity on leaching of Ca from hardened ordinary Portland cement paste. *Cement and Concrete Research*, 35(9), 1764-1775.

Hammouda, B. (2010). SANS from polymers—review of the recent literature. *Journal of Macromolecular Science®*, Part C: *Polymer Reviews*, 50(1), 14-39.

Hammouda, B., and Bauer, B. J. (1995). Compressibility of two polymer blend mixtures. *Macromolecules*, 28(13), 4505-4508.

Harris, A. W., Manning, M. C., Tearle, W. M., Tweed, C. J. (2002). Testing of models of the dissolution of cements—leaching of synthetic CSH gels. *Cement and Concrete Research*, 32(5), 731-746.

Heukamp, F. H., Ulm, F. J., and Germaine, J. T. (2001). Mechanical properties of calcium-leached cement pastes: triaxial stress states and the influence of the pore pressures. *Cement and Concrete Research*, 31(5), 767-774.

Ilavsky, J., and Jemian, P. R. (2009). Irena: tool suite for modeling and analysis of small-angle scattering. *Journal of Applied Crystallography*, 42(2), 347-353.

Ishida, H., Mabuchi, K., Sasaki, K., and Mitsuda, T. (1992a). Low-Temperature Synthesis of Ca_2SiO_4 from Hillebrandite. *Journal of the American Ceramic Society*, 75, 2427-2432.

Ishida, H., Sasaki, K., Mizuno, A., Okada, Y., and Mitsuda, T. (1992). Highly Reactive β-Dicalcium Silicate: IV, Ball-Milling and Static Hydration at Room Temperature. *Journal of the American Ceramic Society*, 75(10), 2779-2784.

Jennings, H. M. (2008). Refinements to colloid model of C-S-H in cement: CM-II. *Cement and Concrete Research*, 38(3), 275-289.

Jennings, H. M., Thomas, J. J., Gevrenov, J. S., Constantinides, G., and Ulm, F. J. (2007). A multi-technique investigation of the nanoporosity of cement paste. *Cement and Concrete Research*, 37(3), 329-336.

Jennings, H. M. (2000). A model for the microstructure of calcium silicate hydrate in cement paste. *Cement and Concrete Research*, 30(1), 101-116.

Jennings, H.M., Tennis, P.D. (1994). Model for the developing microstructure in Portland cement pastes. *Journal of the American Ceramic Society*, 77(12), 3161-3172.

Jennings, H. M. (1986). Aqueous solubility relationships for two types of calcium silicate. *Journal of the American Ceramic Society*, 69(8), 614-618.

Kalliopi, K. A. (2004). Pore structure of cement-based materials:testing, interpretation and requirements.. CRC Pr I Llc. Modern Concrete Technology Series.

Kalousek, G. L. (1952). Application of differential thermal analysis in a study of the system lime-silica-water. *Proc.third Int. Symp. on Chemistry of Cement*, 296-311.

Kamali, S., Moranville, M., and Leclercq, S. (2008). Material and environmental parameter effects on the leaching of cement pastes: experiments and modelling. *Cement and Concrete Research*, 38(4), 575-585.

Kantro, D. L., Brunauer, S., and Weise, C. H. (1962). Development of surface in the hydration of calcium silicates. II. Extension of investigations to earlier and later stages of hydration. *The Journal of Physical Chemistry*, 66(10), 1804-1809.

Kersten, M. (1996). Aqueous solubility diagrams for cementitious waste stabilization. *Environmental Science and Technology*, 30(7), 2286-2293.

Kjellsen, K. O., Lagerblad, B., and Jennings, H. M. (1997). Hollow-shell formation–an important mode in the hydration of Portland cement. *Journal of Materials Science*, 32(11), 2921-2927.

Klur, I., Pollet, B., Virlet, J., and Nonat A. (1998). C-S-H Structure Evolution with Calcium Content by Multinuclear NMR. In Nuclear magnetic resonance spectroscopy of cement-based materials. Springer Berlin Heidelberg. 119-141

Kulik, D. A. (2011). Improving the structural consistency of C-S-H solid solution thermodynamic models. *Cement and Concrete Research*, 41(5), 477-495.

Kulik D., Berner U., and Curti E., (2003). Modelling geochemical equilibrium partitioning with the GEMS-PSI Code, in: B. Smith, B. Gschwend (Eds.), Paul Scherrer Institut Scientific Report, *Nuclear Energy and Safety*, vol. IV, 2004, pp. 109–122.

Kulik, D. A., and Kersten, M. (2001). Aqueous solubility diagrams for cementitious waste stabilization systems: II, end-member stoichiometries of ideal calcium silicate hydrates solid solutions. *Journal of the American Ceramic Society*, 84(12), 3017-3026.

Kunther, W., Lothenbach, B., and Scrivener, K. (2013). Influence of bicarbonate ions on the deterioration of mortar bars in sulfate solutions. *Cement and Concrete Research*, 44, 77-86.

Kurczyk, H. G., Schwiete, H. E. (1962). Concerning the hydration products of C_3S and β-C_2S. *In Proc 4th Int. Symp. Chem. Cem*, 1, 349-358.

Labbez, C., Nonat, A., Pochard, I., and Jönsson, B. (2007). Experimental and theoretical evidence of overcharging of calcium silicate hydrate. *Journal of Colloid and Interface Science*, 309(2), 303-307.

Lagerblad, B. (2001). Leaching performance of concrete based on studies of samples from old concrete constructions. (Vol.1) Swedish Nuclear Fuel and Waste Management Co., Stockholm (Sweden).

Leemann, A., Lothenbach, B., and Hoffmann, C. (2010). Biologically induced concrete deterioration in a wastewater treatment plant assessed by combining microstructural analysis with thermodynamic modeling. *Cement and Concrete Research*, 40(8), 1157-1164.

Le Saoût, G., Lothenbach, B., Hori, A., Higuchi, T., and Winnefeld, F. (2013). Hydration of Portland cement with additions of calcium sulfoaluminates. *Cement and Concrete Research*, 43, 81-94.

Lesko, S., Lesniewska, E., Nonat, A., Mutin, J. C., and Goudonnet, J. P. (2001). Investigation by atomic force microscopy of forces at the origin of cement cohesion. *Ultramicroscopy*, 86(1), 11-21.

Livingston, R. A., Bumrongjaroen, W., and Allen, A. J. (2009). The Fractal Ratio as a Metric of Nanostructure Development in Hydrating Cement Paste. In Nanotechnology in Construction 3 (pp. 101-106). Springer Berlin Heidelberg.

Lothenbach, B., Bary, B., Le Bescop, P., Schmidt, T., & Leterrier, N. (2010). Sulfate ingress in Portland cement. *Cement and Concrete Research*, 40(8), 1211-1225.

Lothenbach, B., Le Saoût, G., Gallucci, E., and Scrivener, K. (2008). Influence of limestone on the hydration of Portland cements. *Cement and Concrete Research*, 38(6), 848-860.

Lothenbach, B., Matschei, T., Möschner, G., and Glasser, F. P. (2008b). Thermodynamic modelling of the effect of temperature on the hydration and porosity of Portland cement. *Cement and Concrete Research*, 38(1), 1-18.

Lothenbach, B., and Gruskovnjak, A. (2007). Hydration of alkali-activated slag: thermodynamic modelling. *Advances in Cement Research*, 19(2), 81.

Lothenbach, B., and Winnefeld, F. (2006). Thermodynamic modelling of the hydration of Portland cement. *Cement and Concrete Research*, 36(2), 209-226.

Lothenbach, B., and Wieland, E. (2006). A thermodynamic approach to the hydration of sulphate-resisting Portland cement. *Waste Management*, 26(7), 706-719.

Mainguy, M., Tognazzi, C., Torrenti, J. M., and Adenot, F. (2000). Modelling of leaching in pure cement paste and mortar. *Cement and Concrete Research*, 30(1), 83-90.

Maltais, Y., Samson, E., and Marchand, J. (2004). Predicting the durability of Portland cement systems in aggressive environments—laboratory validation. *Cement and Concrete Research*, 34(9), 1579-1589.

Martínez-Ramírez, S., and Blanco-Varela, M. T. (2008). Caracterización estructural y microestructural de geles C-S-H. X Congreso Nacional de Materiales (Donostia - San Sebastián).

Martys N.S., Ferraris C.F. (1997). Capillary transport in mortars and concrete. *Cement and Concrete Research*, 27 (5) 747–760.

Matschei, T., Lothenbach, B., and Glasser, F. P. (2007). The AFm phase in Portland cement. *Cement and Concrete Research*, 37(2), 118-130.

Matsuyama, H., and Young, J. F. (2000). Effects of pH on precipitation of quasi-crystalline calcium silicate hydrate in aqueous solution. *Advances in Cement Research*, 12(1), 29-33.

Mitsuda, T., Kobayakawa, S., and Toraya, H. (1986). Characterization of Hydrothermally Formed C-S-H. *8th International Congress on the Chemistry of Cement*, 3, 173-178.

Moranville, M., Kamali, S., and Guillon, E. (2004). Physicochemical equilibria of cement-based materials in aggressive environments—experiment and modeling. *Cement and Concrete Research*, 34(9), 1569-1578.

Nonat, A. (2004). The structure and stoichimetry of C-S-H. *Cement and Concrete Research*, 34(9), 1521-1528.

Nonat, A., and Lecoq, X. (1988). The structure, stoichiometry and properties of C-S-H prepared by C_3S hydration under controlled conditions. *Nuclear Magnetic Resonance Spectroscopy of Cement-Based Materials*, 197-207.

Okada, Y. (1994). ^{29}Si NMR Spectroscopy of Silicate Anions in Hydrothermally Formed C-S-H. *Journal of the American Ceramic Society*, 77(3), 765-768.

Olivella, S., Gens, A., Carrera, J., Alonso, E. E. (1996). Numerical formulation for a simulator (CODE_BRIGHT) for the coupled analysis of saline media. *Engineering computations*, 13(7), 87-112.

Olson, R. A., Neubauer, C. M., Jennings, H. M. (1997). Damage to the pore structure of hardened Portland cement paste by mercury intrusion. *Journal of the American Ceramic Society*, 80(9), 2454-2458.

Plassard, C., Lesniewska E., Pochard I., and Nonat A. (2004). Investigation of the surface structure and elastic properties of calcium silicate hydrates at the nanoscale. *Ultramicroscopy*, 331-338.

Pellenq, R. J. M., Kushima, A., Shahsavari, R., Van Vliet, K. J., Buehler, M. J., Yip, S., Ulm, F. J. (2009). A realistic molecular model of cement hydrates. *Proceedings of the National Academy of Sciences*, 106(38), 16102-16107.

Powers, T. C., and Brownyard, T. L. (1948). Studies of the physical properties of hardened Portland cement paste. Bull. 22, Res. Lab. of Portland Cement Association, Skokie, IL, U.S, reprinted from *J. Am. Concrete Inst*. (Proc.), Vol. 43 (1947), p. 101-132, p. 249-336, p. 469-505, p. 549-602, p. 669-712, p. 845-880, p. 933-992.

Rahman, Md. M., Nagasaki, S., and Tanaka, S. (1999). A model for dissolution of CaO-SiO_2-H_2O gel at Ca/Si>1. *Cement and Concrete Research*, 29(7), 1091-1097.

Reardon, E. J. (1992). Problems and approaches to the prediction of the chemical. *Waste Management*, 12(2), 221-239.

Reardon, E. J. (1990). An ion interaction model for the determination of chemical. *Cement and Concrete Research*, 20(2), 175-192.

Rémond, S., Pimienta, P., and Bentz, D. P. (2002). Effects of the incorporation of Municipal Solid Waste Incineration fly ash in cement pastes and mortars:: I. Experimental study. *Cement and Concrete Research*, 32(2), 303-311.

Revertegat, E., Richet, C., and Gegout, P. (1992). Effect of pH on the durability of cement pastes. *Cement and Concrete Research*, 22(2), 259-272.

Richardson, I.G. (2008). The calcium silicate hydrates. *Cement and Concrete Research*, 38(2), 137-158.

Richardson, I.G. (2004) Tobermorite/jennite- and tobermorite/calcium hydroxide-based models for the structure of C-S-H: applicability to hardened pastes of tricalcium silicate, h-dicalcium silicate, Portland cement, and blends of Portland cement with blast-furnace slag, metakaol. *Cement and Concrete Research*, 34 (9), 1733-1777.

Richardson, I. G. (1999). The nature of C-S-H in hardened cements. *Cement and Concrete Research*, 29(8), 1131-1147.

Richardson, I. G., and Groves, G. W. (1992). Models for the composition and structure of calcium silicate hydrate (C- S- H) gel in hardened tricalcium silicate pastes. *Cement and Concrete Research*, 22(6), 1001-1010.

Rodger, S. A., Groves, G. W., Clayden, N. J., and Dobson, C. M. (1988). Hydration of tricalcium silicate followed by ^{29}Si NMR with cross-polarization. *Journal of the American Ceramic Society*, 71(2), 91-96.

Saaltink, M., Sánchez-Vila, X., Carrera, J. (2005). Estudio cualitativo sobre la posibilidad que el agua recogida en la celda 16 proceda de un proceso de condensación, Octubre 2005. UPC Barcelona.

Saaltink, M. W., Batlle, F., Ayora, C., Carrera, J., Olivella, S. (2004). RETRASO, a code for modeling reactive transport in saturated and unsaturated porous media. *Geologica Acta*, 2(3), 235-251.

Saito, H., and Deguchi, A. (2000). Leaching tests on different mortars using accelerated electrochemical method. *Cement and Concrete Research*, 30(11), 1815-1825.

Saito, F. (1997). Mechanochemical synthesis of hydrated calcium silicates by room temperature grinding. *Solid State Ionics*, 101-103 (Part-1), 37-43.

Samson, E., and Marchand, J. (2007). Modeling the transport of ions in unsaturated cement-based materials. *Computers and Structures*, 85(23), 1740-1756.

Sasaki, K., T. Masuda, H. Ishida, and T. Mitsuda. (1996). Synthesis of Calcium Silicate Hydrate with Ca/Si=2 by Mechanochemical Treatment. *Journal of the American Ceramic Society*, 80(2), 472-476.

Singh, N. B., Rai, S., and Singh, N. (2002). Highly Reactive β-Dicalcium Silicate. *Journal of the American Ceramic Society*, 85(9), 2171-2176.

Soler, J. M. (2013). Reactive transport modeling of concrete-clay interaction during 15 years at the Tournemire Underground Rock Laboratory. *European Journal of Mineralogy*, 25(4), 639-654.

Soler, J.M, and Mäder, U. K. (2010). Cement-rock interaction: Infiltration of a high-pH solution into a fractured granite core. *Geologica Acta*, 8(3), 221-233.

Soler, J. M. (2007). Thermodynamic description of the solubility of the C-S-H gels in hydrated Portland cement. Literature review. Posiva Working Report 2007-88.

Stade, H., and Wieker, W. (1980). On the structure of ill-crystallized calcium hydrogen silicates. I. Formation and properties of an ill-crystallized calcium hydrogen disilicate phase. *Zeitschrift fur Anorganische und Allgemeine Chemie*, 470(11), 69-83.

Steefel, C. I. (2009). CrunchFlow software for modeling multicomponent reactive flow and transport. User's manual. Earth Sciences Division. Lawrence Berkeley, National Laboratory, Berkeley, CA. October, 12-91.

Sugiyama, D. (2008). Chemical alteration of calcium silicate hydrate (C–S–H) in sodium chloride solution. *Cement and Concrete Research*, 38(11), 1270-1275.

Taplin, J. H. (1959). A method to following the hydrate reaction in Portland Cement Paste. *Australian Journal Application of Science*, 10(3), 329-345.

Taylor, H. F.W. (1997). Cement chemistry. Thomas Telford.

Taylor, H. F.W. (1993). Nanostructure of C-S-H: Current Status. *Advanced Cement Based Materials*, 1(1), 38-46.

Taylor, H. F.W. (1986). Proposed structure of calcium silicate hydrate gel. *Journal of the American Ceramic Society*, 69 (6) 464-467.

Thomas, J. J., Jennings, H. M., and Allen, A. J. (2010). Relationships between Composition and Density of Tobermorite, Jennite, and Nanoscale CaO− SiO_2− H_2O. *The Journal of Physical Chemistry C*, 114(17), 7594-7601.

Thomas, J. J., Allen, A. J., and Jennings, H. M. (2008). Structural changes to the calcium–silicate–hydrate gel phase of hydrated cement with age, drying, and resaturation. *Journal of the American Ceramic Society*, 91(10), 3362-3369.

Thomas, J. J., Chen, J. J., Allen, A. J., and Jennings, H. M. (2004). Effects of decalcification on the microstructure and the surface area of cement and tricalcium silicate pastes. *Cement and Concrete Research*, 34 (12), 2297-2307.

Thomas, J. J., Jennings, H. M., and Allen, A. J. (1998a). The surface area of cement paste as measured by neutron scattering: evidence for two C-S-H morphologies. *Cement and concrete research*, 28(6), 897-905.

Thomas, J. J., Jennings, H. M., and Allen, A. J. (1998b). Determination of the Neutron Scattering Contrast of Hydrated Portland Cement Paste using H_2O/D_2O Exchange. *Advanced Cement Based Materials*, 7(3), 119-122.

Trapote-Barreira, A., Porcar, L., Cama, J., Soler, J. M., Allen A.J. (2014). Structural changes in C-S-H gel during dissolution: small-angle neutron scattering and Si-NMR characterization. *Cement and Concrete Research, (Submitted).*

Trapote-Barreira, A., Cama, J., and Soler, J. M. (2014). Dissolution kinetics of C–S–H gel. Flow-through experiments. *Physics and Chemistry of the Earth*, 70-71, 17-31.

Ulm, F. J., Torrenti, J. M., and Adenot, F. (1999). Chemoporoplasticity of calcium leaching in concrete. *Journal of Engineering Mechanics*, 125(10), 1200-1211.

Van Der Lee, J., and De Windt, L. (2001). Present state and future directions of modeling of geochemistry in hydrogeological systems. *Journal of Contaminant Hydrology*, 47(2), 265-282.

Winnefeld, F., and Lothenbach, B. (2010). Hydration of calcium sulfoaluminate cements—experimental findings and thermodynamic modelling. *Cement and Concrete Research*, 40(8), 1239-1247.

Winslow, D. N. (1985). The fractal nature of the surface of cement paste. *Cement and Concrete Research*, 15(5), 817-824.

Wittmann, F. (1977). Grundlagen eines Modells zur Beschreibung charakteristischer Eigenschaften des Betons. *Deutscher Ausschuss für Stahlbeton*, Heft 290, Berlin.

Yang, H., Jiang, L., Zhang, Y., Pu, Q., and Xu, Y. (2012). Predicting the calcium leaching behavior of cement pastes in aggressive environments. *Construction and Building Materials*, 29, 88-96.

Zajac, M., Rossberg, A., Le Saoût, G., and Lothenbach, B. (2014). Influence of limestone and anhydrite on the hydration of Portland cements. *Cement and Concrete Composites*, 46, 99-108.

Zarzycki, J. (1987). Fractal properties of gels. *Journal of Non-Crystalline Solids*, 95, 173-184.

Zuloaga, P., Ordonez, M., Saaltink, M. W., Castellote, M. (2009). Capillarity in Concrete Disposal Vaults and Its Influence in the Behavior of Isolation Barriers at El Cabril Low and Intermediate Level Radioactive Waste Disposal Facility in Spain-9015. In WM 2009 Conference, March 1-5.

Zuloaga, P., Andrade, C., Saaltink, M. W. (2006). Long term water flow scenario in low-level waste disposal vaults, with particular regard to concrete structures in El Cabril, Cordoba, Spain. *In Journal de Physique IV (Proceedings)* (Vol. 136, pp. 49-59). EDP sciences.

PART I. C-S-H gel dissolution

CHAPTER 2

Dissolution kinetics of C-S-H gel

This chapter focuses on the C-S-H gel dissolution kinetics. It consists of two parts. The first part describes the protocols to synthesize C_3S to obtain C-S-H gel, the characterization of the C-S-H gel, the experimental methodology to study the dissolution kinetics by means of flow-through experiments and the modeling of the experimental results using the reactive transport code CrunchFlow (Steefel, 2009). The second part presents the interpretation of the changes in aqueous chemistry and C-S-H gel structure to derive and propose a C-S-H gel dissolution rate law.

2.1. Introduction

C-S-H can be synthesized by hydration of C_3S as it occurs in OPC. Hydrated C_3S pastes are prepared with deionized water at a mass water-to-solid ratio of about 0.5 at room temperature and under CO_2-free atmosphere (Chen et al., 2004). Using the stoichiometry of C-S-H proposed by Kulik and Kersten (2001), the hydration of C_3S can be written as

$$Ca_3SiO_5 + 4H_2O \rightarrow SiO_2 \cdot 1.67Ca(OH)_2 \cdot H_2O + 1.33Ca(OH)_2$$

C_3S 67wt% C-S-H 33wt% CH

Reaction 2.1

To predict the long-term behavior of cement-based systems in contact with an aqueous phase it is essential to know the solubility of the C-S-H gel. C-S-H solubility initially considered empirical or semi-empirical descriptions of C-S-H gel and evolved to the application of solid-solution models. For the purpose of this experimental study, the model by Kulik and Kersten (2001) was adopted.

Flow-through experiments are used to study the dissolution kinetics of C-S-H gel. The flow of demineralized water causes the dissolution of C-S-H and changes in the composition of the solutions. The changes in Ca and Si concentrations and pH have been monitored during the reaction, allowing the measurement of the variation in the atomic Ca/Si ratio of the solution, the calculation of dissolution rates, the assessment of the effect of the solution saturation state on the rates and the derivation of a C-S-H dissolution rate law. Additionally, C-S-H compositional and microstructural changes during dissolution have been analyzed using several techniques (XRD, SEM, EPMA and ^{29}Si MAS-NMR).

2.2. Materials and Methods

The scheme depicted in Figure 2.1 summarizes the experimental tasks performed in this study to obtain C-S-H gel and its characterization, before (unreacted) and after the experiments (reacted). In the first stage C-S-H was synthesized by hydration of C_3S. It the second stage, flow-through experiments were carried out to determine the dissolution kinetics of the C-S-H gel under two different flow-rate ranges. Changes in solution chemistry and microstructural characterization of the solids are shown below.

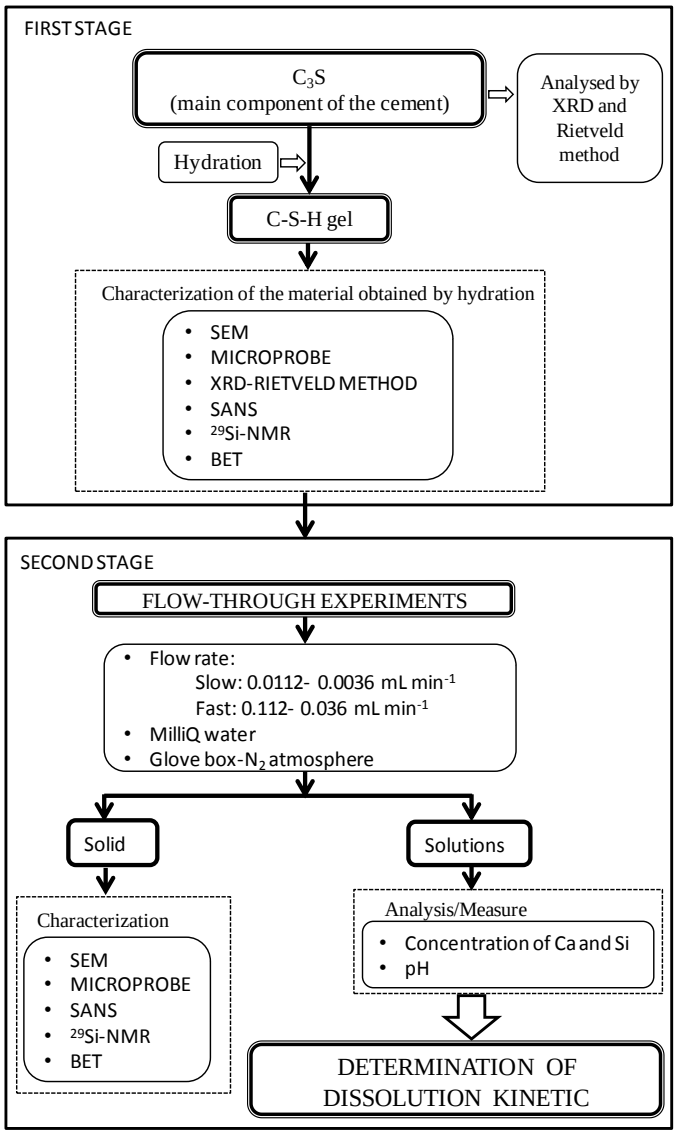

Figure 2.1. *Scheme of the tasks carried out to obtain and characterize the C-S-H gel.*

2.2.1. C-S-H gel

C-S-H gel was prepared by C_3S hydration. Synthesis of pure C_3S was performed together with Dr. Salvador Martínez and Dr. Salvador Galí at the Department of Crystallography, Mineralogy and Mineral Deposits of the Faculty of Geology at the University of Barcelona. The basis of the synthesis is similar to that described in Chapter 1. Firing a stoichiometric mixture of reagent-grade CaO and high-purity silica gel with a solid ratio of 3:1 at temperature around 1350 ºC for 72 hours (electrical oven). Reagent-grade CaO was obtained by decarbonising $CaCO_3$ for two hours at 950 ºC. XRD was used to confirm that all CaO had reacted to form C_3S. Before the second and third firings, the sample was quickly

cooled to room temperature in a water bath to avoid formation of C_2S which is less reactive than C_3S during hydration. After cooling, the sample was ground and compacted to discs to enhance homogeneity. Commercial C_3S was also purchased from Mineral Research Processing (France). According to the specifications it was also synthesized by burning $CaCO_3$ and silica gel at high temperature.

Purity of the final products was determined by XRD using Cu Kα radiation over a 2θ range from 0 to 60 degrees and quantified by Rietveld analysis (Young, 1995). XRD patterns of both samples showed that the C_3S presents triclinic T1 polymorphism (Figure 2.2). Rietveld analysis showed that the content of synthesized C_3S was 98.35 % with 0.02 % of residual quartz, 0.80 % of calcite and 0.83 % of portlandite; commercial C_3S consisted of 97 % of C_3S, 1 % of SiO_2, 1 % of calcite and 1 % of portlandite.

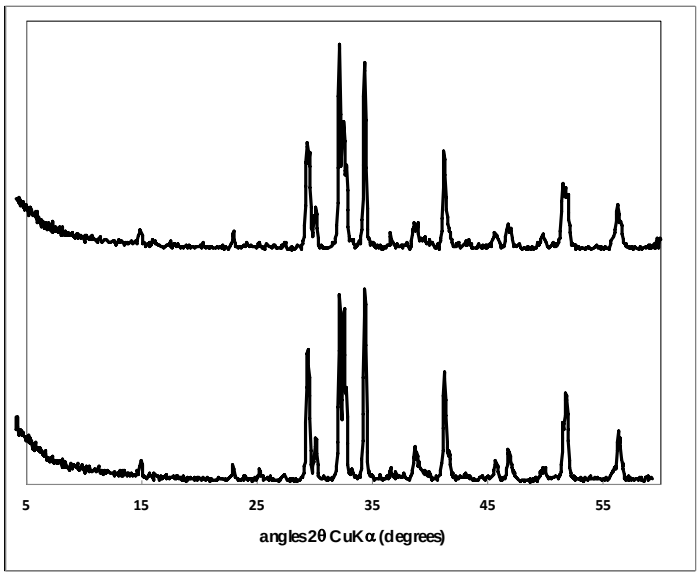

Figure 2.2. *X-Ray diffraction patterns of the synthesized and purchased C_3S samples.*

Both C_3S samples were ground in a ball agate mortar to a particle size smaller than 10 μm. Grinding was controlled by continuous performance of laser granulometry analyses using the LS 13320 laser diffraction size analyser (Beckman Coulter) (Scientific and Technical Services of Barcelona University) after ultrasonic disaggregation in ethanol for 5 min to prevent particle hydration. Grinding was stopped when the particle size distribution did not change significantly. In both C_3S samples the particle size distribution fell between 2 and 15 μm. For the purchased C_3S sample 90% of the particles were smaller than 10 μm, presenting two main size populations: one around 0.3 μm and the other around 3 μm. In the case of

synthesized C_3S 90% of the particles were also smaller than 10 μm with two main size populations (0.3 μm and 7 μm) (Figure 2.3).

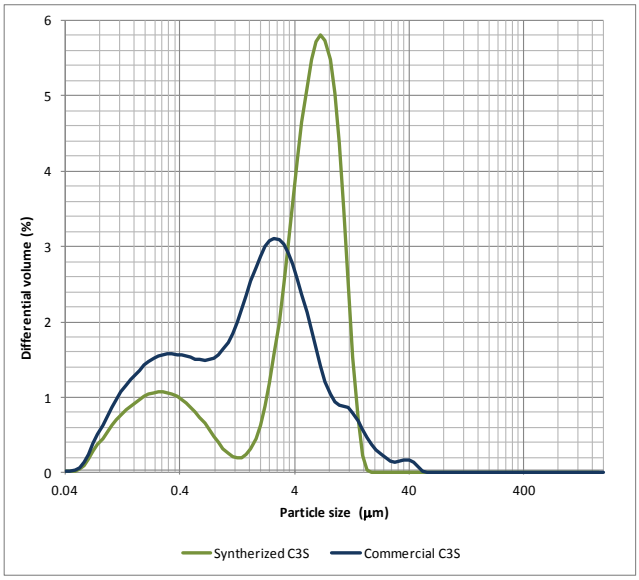

Figure 2.3. *Particle size distribution of the synthesized and purchased C_3S samples.*

The morphology of the particles was examined by Scanning electron Microscopy (SEM) using a JEOL JMS-840 electron microscope (Scientific and Technical Services of Barcelona University) (Figure 2.4). Particles showed rounded shapes and formed clusters (or agglomerates). The particle size ranged from 2 to 15 μm.

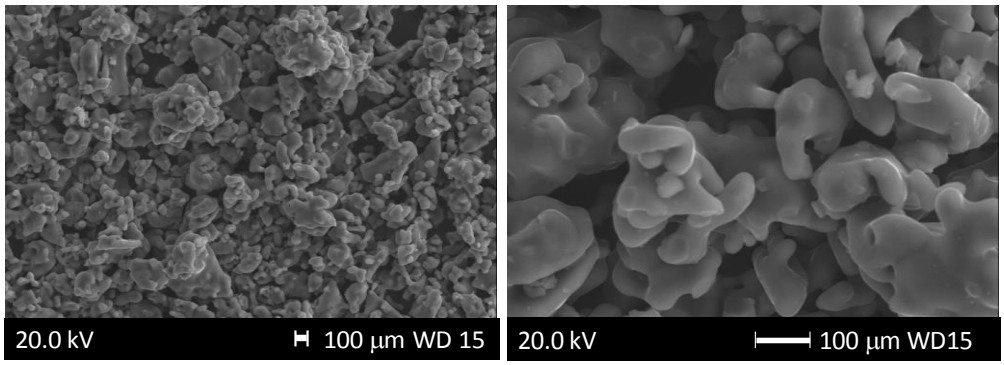

Figure 2.4. *SEM images of the initial C_3S.*

2.2.2. Hydration of C_3S

C_3S hydration was carried out using Milli-Q water (18.2 MΩ·cm at 25 °C) and a water/solid ratio of 0.5 in a N_2 filled glove box to avoid carbonation of the hydration products.

In the CO_2-free glove box, the Milli-Q water used to hydrate the C_3S was gently purged with a low flux of N_2 for 5 minutes to further avoid carbonation. Both C_3S samples, synthesized and purchased, were manually mixed. When both mixtures were considered to be homogeneous, mixing was stopped. Thereafter, the containers with the mixtures were covered with caps to prevent water evaporation and stored. The samples were stored for 28 days in the glove box at room temperature.

After 28 days, hydration was stopped using isopropanol. The pastes were retrieved from the containers, cut into small pieces and wet abundantly with isopropanol. When it was totally evaporated, and the mixtures were dried, the retrieved pastes were crushed in an agate mortar and sieved through a 25 μm sieve. All these manipulations were performed inside the glove box.

The powdered samples were examined by XRD and analyzed using the Rietveld method to quantify the amount of formed C-S-H and remaining C_3S. The XRD patterns showed the presence of C_3S (27%) indicating that hydration was not complete. C-S-H only accounted for about 43 % of the mass of the samples.

The Ca/Si ratio of the particles was analyzed by EPMA using a Cameca SX-50 device (4 WD spectrometers + 1 EDS) with an accelerating voltage of 20 kV and a beam current of 15 nA. The sample was embedded into epoxy resin, dried and cured in vacuum to extract the air and further polished and coated with a thin layer of graphite. The backscattered electron images show particles that are totally hydrated (C-S-H gel with a Ca/Si = 1.65) (Figure 2.5 a), and others that consist of partially hydrated C_3S zones (cores) (Ca/Si ≈ 3) with some zones rich in portlandite (Ca/Si >> 3) (Figure 2.5 b).

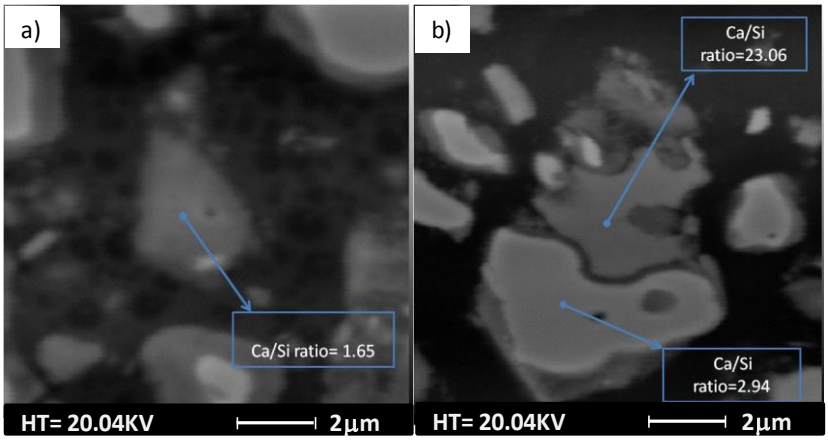

Figure 2.5. *Backscattered images that show the Ca/Si ratios in the hydrated C_3S samples: a) grain of C-S-H with a Ca/Si ratio of 1.65 and b) grain with a region of non-well hydrated C_3S (Ca/Si ratio of 2.94) and a zone of CH (Ca/Si ratio of 23.06).*

In order to obtain a complete C_3S hydration, a second hydration was carried out with the purchased C_3S. In this case, grinding was improved using isopropanol to obtain finer particles. 90% of the particles were smaller than 8 µm with only one main size (≈ 1.9 µm) (Figure 2.6).

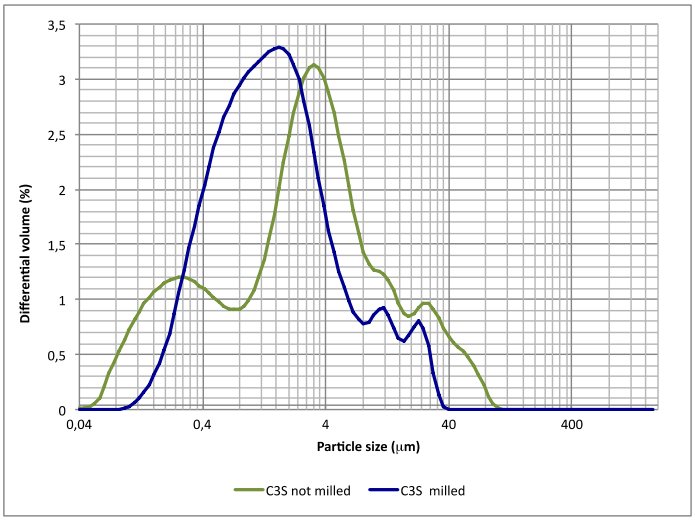

Figure 2.6. *Particle size distribution of the purchased C_3S sample.*

The samples were stored for 120 d in the glove box at room temperature (23 ± 2ºC). C_3S hydration was monitored by examining the samples after 45, 62, 83, 99 and 120 d by XRD and Rietveld analysis to quantify the amount of formed C-S-H and remaining C_3S. After 120 days, the reaction was stopped since XRD (with a detection limit below 1% wt.) could not

detect the presence of C_3S. 1.5 wt % content of quartz was detected. The sample was then ground inside the glove box in a N_2 atmosphere. Laser granulometry was performed after ultrasonic disaggregation in ethanol for 5 min to prevent particle hydration and agglomeration. 97 % of the particles were smaller than 100 μm, presenting a main size population with a peak around 20 μm and another small population around 5 μm (less than 25% of the sample).

Semi-quantitative analysis of the Ca/Si ratio of the C-S-H gel sample was performed by SEM-EDX using FEI NovaNanoSEM 230 Scanning Electron Microscope (Electron Microscopy Center of EMPA-Switzerland) employing an acceleration voltage of 15-20kV. The sample was not polished and was coated with a thin layer of graphite. Quantitative analysis was made with EPMA using Electron Microprobe CAMECA SX-50 instrument (4 WD spectrometers + 1 EDS) (Microprobe Unit of the University of Barcelona) under a 20 kV accelerating potential and 20 nA beam current. The sample for EPMA was embedded into epoxy resin, dried and cured in vacuum to extract the air and further polished and coated with a thin layer of graphite. Working at 20 kV should be adequate to ensure satisfactory analysis for Ca and produce an electron beam-sample interaction volume sufficiently small that single phases (e.g., C_3S, C-S-H and CH) can be analysed on areas of about 2 microns in size (Taylor, 1997). SEM and EPMA analysis results (atomic % values) did not add to 100%; they only added up to 60% - 75%. Factors affecting this lack of mass balance include the porosity of the analyzed region, retention of organic liquids used in preparing the polished sections, presence of carbonaceous residues formed under the action of the electron beam and superficial carbonation (Taylor and Newbury, 1984). However, it has been argued by Taylor (1997) that the measured Ca/Si ratios are still reliable. Section 1.01(a)(i)Figure 2.7 shows SEM and secondary electrons EPMA images of the hydrated C_3S.

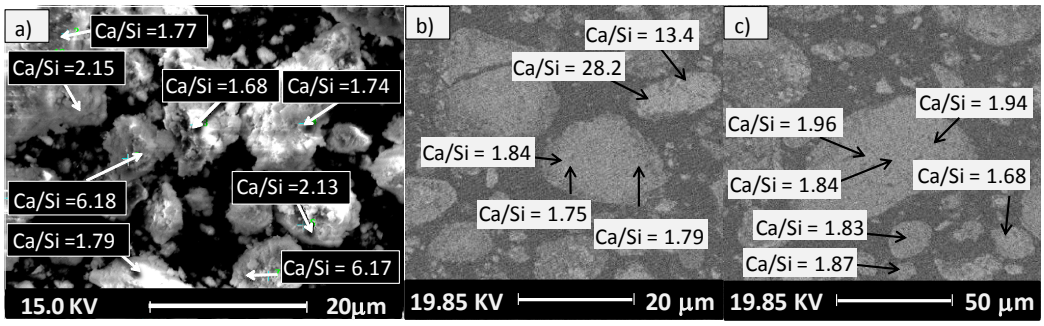

Figure 2.7. *a) SEM image of the initial C-S-H gel and b and c) Backscattered electron images of the initial C-S-H gel showing the EPMA multiple points.*

The analytical results indicate that three different ranges of Ca/Si ratio exist in the measured particles: (1) Ca/Si ratio between 1.68 and ca. 1.8, assigned to C-S-H gel; (2) Ca/Si ratio between ca. 1.8 and 2.34, corresponding to C-S-H gel particles with precipitated portlandite between the grains; (3) Ca/Si ratio larger than 6, indicating a large proportion of portlandite.

Rietveld analysis of the hydrated C-S-H paste showed that it is composed of 67 wt % C-S-H, 27.5 wt% portlandite, 1.5 wt% quartz and 4 wt% calcite, the latter probably due to some sample carbonation. This is in agreement with the amount of C-S-H and portlandite expected from the C_3S hydration reaction (67 wt % C-S-H and 33 wt % portlandite). Therefore, the C-S-H gel sample obtained in the second C_3S hydration (fully hydrated) was used in all the flow-through experiments of this study. The specific surface area of the sample was determined by the BET method (Brunauer et al. 1938) with a Micromeritics ASAP 2000 surface area analyzer using 5-point N_2 adsorption isotherms. The BET specific surface area was found to be 11.7 ± 1.7 $m^2\ g^{-1}$, which is similar to determined values for ordinary Portland cement after 28 days of hydration (Odler, 2003). No attempt to remove microparticles (< 1μm) resulting from grinding attached to grain surfaces was made. In long-term flow-through experiments, it is not necessary to pre-treat the samples since the possible effect of the particle size is corrected by normalizing the rates to the final specific surface area. The BET surface area of the samples retrieved after the experiments ranged from 14.5 ± 1.5 to 142 ± 14 $m^2\ g^{-1}$. The increase in BET surface area after the experiments could be attributable to an increase in pore space that facilitates N_2 penetration (Odler, 2003).

2.2.3. Flow-through experiments

Flow-through experiments were carried out to determine the C-S-H dissolution kinetics. Measurement of the changes in solution chemistry and microstructural characterization of the solids were carried out. Stirred and non-stirred Plexiglas reaction cells of 40 mL in volume, with two chambers separated by a fine mesh (5μm), were used. The powder samples were placed on the fine mesh (upper chamber). In the two stirred experiments the sample was in contact with a small teflon stir bar, a bigger teflon stir bar was placed in the lower chamber (Fig. 2.8). The flow rate was controlled by a peristaltic pump and ranged from 0.036 to 0.112 mL min^{-1} in a first set of experiments. A second set of experiments was performed by lowering the flow rate, which ranged from 0.0036 to 0.0112 mL min^{-1}. Residence times ranged from 6 to 185 h, respectively. Input and output solutions circulated through 0.45μm nylon and teflon membranes placed at the bottom and top of the reactor, respectively. The input solution was N_2-bubbled Milli-Q water (pH 7).

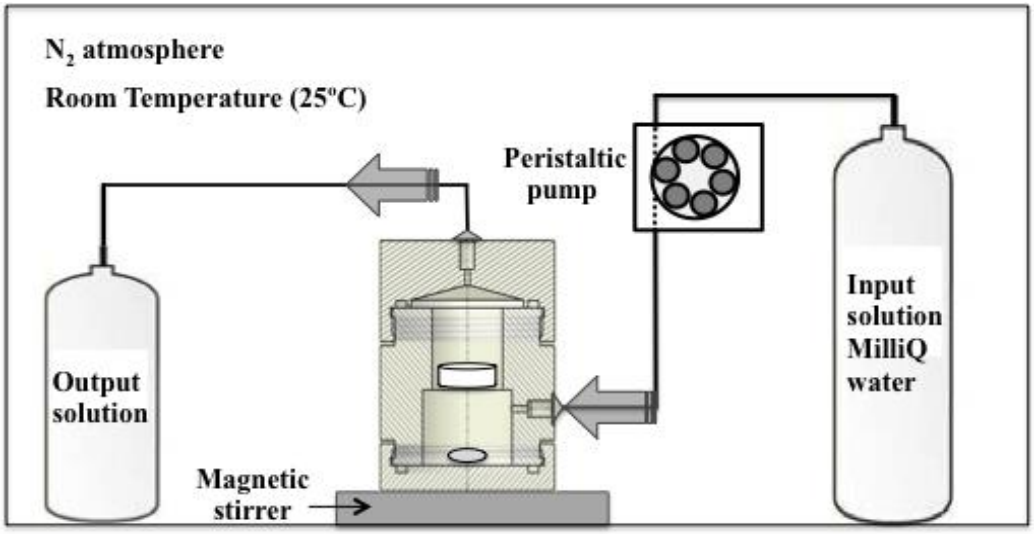

Figure 2.8. *Schematic representation of the flow-through experiments carried out under CO_2-free conditions (N_2 atmosphere) inside a glove box.*

All the experiments were carried out at room temperature in a glove box under N_2 controlled atmosphere to avoid carbonation of the samples. The N_2 gas (99% purity) was first bubbled through a NaOH 12 M solution before entering the glove box. The CO_2 content inside the glove box was indirectly controlled with an O_2 detector. During the experiments O_2 concentration ranged between 0.1 to 0.4% O_2, which according to the CO_2 content of atmospheric air corresponded to 2-8 ppm of CO_2.

Different experiments were stopped at different times. In some experiments, steady state was reached (dCa/dt and dSi/dt = 0). Steady-state conditions were considered to be attained when differences in the Si and Ca concentrations in output solutions were within ± 10 and ± 15 % in consecutive leachate samples for at least 200 hours. After the steady-state conditions were reached, steady-state C-S-H dissolution rates were calculated. Other experiments were stopped before reaching steady state with the aim of determining Ca/Si ratios in the solid at early stages. Output solutions were collected during the experimental runs. The saturation indexes of the steady-state output solutions (SI) was calculated at 25 °C using the PhreeqC code (Parkhurst and Appelo, 1999) and MINTEQ database (Allison et al., 1991) and CEM07 DATABASE (Matschei et al., 2007; Lothenbach et al., 2008). C-S-H solubility data from Kulik and Kersten (2001) was also included.

After the experiments, the retrieved solid samples were dried with isopropanol and kept in closed vials to be stored in the glove box at room temperature until examination by SEM, EPMA, BET and ^{29}Si MAS-NMR.

2.2.4. Calculation of the C-S-H gel dissolution rate

Based on a simple mass balance equation, the dissolution rate (mol $m^{-2}s^{-1}$), *R*, in a well-mixed flow-through experiment is given by (e.g Lasaga, 1998):

$$R = -\frac{dc_i}{dt} \cdot \frac{V}{m \cdot S \cdot v_i} - q\frac{(c_i - c_i^0)}{m \cdot S \cdot v_i} \quad \text{Eq. 2.1}$$

where, c_i^0 and c_i (mol m^{-3}) are concentrations of element i in the inflowing and outflowing solution, v_i is the stoichiometric coefficient of element *i* in the mineral, *V* is the volume of the reaction cell (m^3), q ($m^3 \cdot s^{-1}$) is the fluid volumetric flux through the reactor, *m* is the mass of mineral (g), and *S* (m^2 g^{-1}) is the specific (BET measured) surface area of the mineral. Reaction rates were normalized to the final surface area (steady state is achieved in the last stage of some of the experiments). Note that in our formalism, the rate is defined to be negative for dissolution and positive for precipitation.

The dissolution rate at steady state ($dc_i/dt = 0$) is readily calculated from the last term of the previous equation and is given by

$$R = -q\frac{(c_i - c_i^0)}{m \cdot S \cdot v_i} \quad \text{Eq. 2.2}$$

The error associated with the calculated dissolution rates (*ΔR*) was estimated using the Gaussian error propagation method (Barrante 1974):

$$\Delta R = \sqrt{\left(\frac{(c_i - c_i^0)}{A \cdot v_i}\right)^2 \cdot \Delta q^2 + \left(\frac{q \cdot (c_i - c_i^0)}{A^2 \cdot v_i}\right)^2 \cdot \Delta A^2 + \left(\frac{q}{A \cdot v_i}\right)^2 \cdot (\Delta c_i^2 + \Delta(c_i^0)^2)} \quad \text{Eq. 2.3}$$

Usually, the propagated error in the calculated rates is dominated by the uncertainty originated in the BET surface area measurements (± 15%).

2.2.5. Solid sample analyses

SEM imaging of unreacted and reacted C-S-H gel powders was performed on C-coated samples using a JEOL JSM-840 instrument and a field-emission SEM Hitachi H-4100FE instrument.

Small fractions of unreacted and reacted C-S-H powder samples were mounted in resin and polished for electron microprobe (EPMA) analyses, which were performed on multiple points using a CAMECA SX50 microprobe under a 20 kV accelerating potential and 20 nA beam current. The composition was dominated by Si and Ca. From the microprobe analyses, the Ca/Si atomic ratio can be calculated.

^{29}Si MAS-NMR spectra of approximately 2 mg of unreacted and reacted powdered samples were recorded on a Bruker Avance 400 NMR spectrometer (field strength of 9.4 T, Bruker Biospin AG, Fällanden, Switzerland) at 79.49 MHz applying 4.5 kHz spinning rates were applied on a 7 mm CP MAS probe using ZrO_2 rotors. Single-pulse experiments were carried out by applying 30 ° pulses of 2.9 ms with 1H decoupling of 31.3 kHz (TPPM15) and recycle delays of 20 s. The ^{29}Si chemical shift was referenced externally relative to tetramethylsilane at 0.0 ppm. The observed ^{29}Si resonances were analyzed using the standard Q^n nomenclature (Taylor, 1997), where one Si tetrahedron is connected to n Si tetrahedra with n varying from 0 to 4. In the following ^{29}Si MAS-NMR spectra, the tetrahedral coordination is expressed by means of Q^0, Q^1, Q^2, Q^{2v}, Q^{2i}, Q^{2p} , Q^3-defect, Q^3-gel and Q^4-gel, denoting the chemical shift (ppm) of a silicon atom bonded to n bridging oxygens. Q^0 denotes an isolated monomer tetrahedron ($Si(OH)_4$), Q^1 is a chain-end tetrahedron, Q^2 is a chain-intermediate tetrahedron (silicate tetrahedra coordinated to the calcium ions). Bridging tetrahedra can be distinguished between Q^{2p}, which denotes a bridge tetrahedron bonded to two protons, and Q^{2i}, a bridge tetrahedron bonded to a proton and a calcium ion. Q^3-defect is a tetrahedron surrounded by three silica tetrahedra where two are Q^2 and the third is another Q^3-defect (linking two silicate chains in the interlayer space). A Q^2 tetrahedron linked to a Q^3-defect is a Q^{2v}. Q^3-gel (also called Q^3OH) is a tetrahedron connected to three Q^3 tetrahedra. Q^4-gel corresponds to silica gel (Si-rich domain in the C-S-H gel) where a tetrahedron is connected to four tetrahedra forming a 3D structure (^{29}Si MAS-NMR allows to distinguish differences between silica gel –amorphous– and quartz –crystalline–). Figure 2.9 shows a diagram of the C-S-H gel structure indicating the type of signal attributed to each type of tetrahedron.

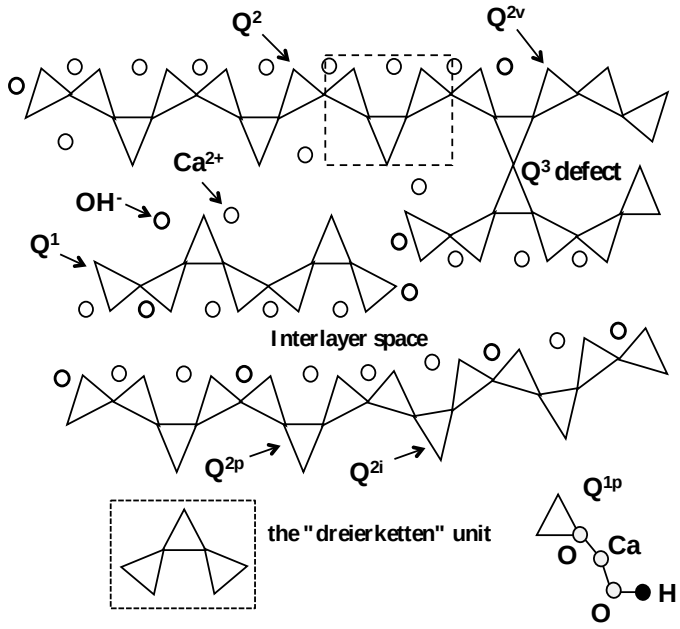

Figure 2.9. *Schematic representation of C-S-H gel and the assignment of the peaks in the ^{29}Si MAS- NMR (Gwenn Le Sâout; personal communication).*

The relative proportions of silicon associated with the Q^n units were determined by the deconvolution of the spectra using the Dmfit program (Massiot et al., 2002).

2.2.6. Solution analyses

The input and output solution pH was measured at 25ºC using a Thermo Orion Ag/AgCl electrode. Calibration was made with Crison © standard buffer solutions of pH 7.00 (K and N phosphate) and pH 9.21 (borax). The uncertainty was ± 0.05 pH units. After the pH measurements, output solutions were acidified to pH 3 to prevent precipitation of calcium carbonate in the solutions.

Total concentrations of Ca and Si of the output solutions were analyzed by Inductively Coupled Plasma Atomic Emission Spectroscopy (ICP-AES, thermo Jarrel-Ash with CID detector and a Perkin Elmer Optima 3200RL). The accuracy of ICP-AES measurements is estimated to be around 3%. The detection limit of the analysis for Ca and Si concentration was 0.5 ppm.

2.2.7. Reactive transport modeling

Modeling was performed to allow the calculation of the dissolution rate constants (*k*) for the different C-S-H compositions. The experimental variation of the output concentrations with time was modeled using the CrunchFlow reactive transport code (Steefel, 2009). CrunchFlow solves numerically the advection-dispersion-reaction equations

$$\frac{\delta\left(\phi\left(C_i^{mob}+C_i^{inmob}\right)\right)}{\delta t}=\nabla\cdot\left(D\nabla C_i^{mob}\right)-\nabla\cdot\left(qC_i^{mob}\right)+R_i \qquad \text{Eq. 2.4}$$

$$(i=1,2,\ldots,N_{tot})$$

where φ is porosity, C_i^{mob} is the total concentration of mobile component or primary species *i* in solution (mol m^{-3}), C_i^{inmob} is the total concentration of immobile component *i* in solution (sorbed by surface complexation or ion exchange; mol m^{-3}), *D* is the combined dispersion-diffusion coefficient (m^2 s^{-1}), *q* is Darcy velocity (m^3 m^{-2} s^{-1}), R_i is the total reaction rate affecting component *i (*mol m^{-3} s^{-1}), *t* is time (s) and N_{tot} is the total number of independent aqueous chemical components (primary species). The expression of the total reaction rate for component *i*, R_i, is

$$R_i=-\sum_m \upsilon_{im}R_m \qquad \text{Eq. 2.5}$$

where R_m (mol m^{-3}_{bulk} s^{-1}) is the rate of precipitation ($R_m > 0$) or dissolution ($R_m < 0$) of solid phase *m* per unit volume of rock, and ν_{im} is the number of moles of *i* per mole of mineral *m*. Since the C-S-H gel dissolution reaction is described using a kinetic rate law, the dissolution rate constants of the discrete compositions defined from the C-S-H solid solution are obtained by fitting the model to the experimental variation of the output concentrations with time in the flow-through experiments. In the simulations, the reaction rate law that has been used is of the form

$$R_m=-A_m k_m(1-\Omega) \qquad \text{Eq. 2.6}$$

where R_m is the reaction rate for a given mineral (mol m^{-3} s^{-1}), A_m is the mineral surface area (m^2 m^{-3}), k_m is the reaction rate constant (mol m^{-2} s^{-1}) and (1-Ω) is the term

describing the dependence of the rate on the solution saturation state. Ω is the ionic activity product (IAP) of the solution with respect to the mineral divided by K_{eq} (equilibrium constant for that mineral reaction). This (1-Ω) term corresponds to a formulation of the rate law based on Transition State Theory (TST) for a single elementary reaction controlling the reaction mechanism (Lasaga, 1998). Data for steady-state dissolution (see below) are consistent with this simple formulation.

The flow-through experiments were modelled using a 1 D representation of the reaction cell. The length of the flow-through cell was discretized in three nodes, and grid spacing was 1 cm. Dispersivity was set to 1 m, which ensured homogeneous solution composition in the 3 nodes (well-mixed conditions).

The initial mineralogical composition, porosity and flow rate used in the model for representative experiments are given in Table 2.1. Mass fraction was calculated based on the C-S-H and portlandite contents (67.2% and 32.8%, respectively) and the total mass; the mineral volumetric fractions were calculated using the density of C-S-H and CH (2.7580 and 2.2414 g cm^{-3}, respectively). Porosity values (volume of solid per volume of reaction cell) ranged from 98.83% to 99.42%. The initial BET surface area of the C-S-H gel was used to calculate the mineral surface area (m^2 m^{-3}). Additional calculations were also performed considering the small amounts of calcite (4%) and quartz (1.5%) in the system and their geometric surface areas. Results showed a negligible effect from these phases.

Table 2.1. *Model parameters used in the calculations.*

experiment	total mass (g)	mass (g)		volumetric fraction		residence time (h)	flow rate (m/h)
		C-S-H	CH	C-S-H	CH		
CSH-25_19	2.9976	2.016	0.984	0.018	0.011	57.8	5.04E-04
CSH-25_20	1.4961	1.008	0.492	0.009	0.005	58.7	5.04E-04
CSH-25_21	3.0034	1.008	0.492	0.009	0.005	182.5	1.62E-04
CSH-25_22	1.4975	2.016	0.984	0.018	0.011	179.8	1.62E-04
CSH-25_23	2.9855	2.016	0.984	0.018	0.011	57.8	5.04E-04
CSH-25_3	1.5027	1.008	0.492	0.009	0.005	18.2	1.62E-03
CSH-25_2	1.5011	1.008	0.492	0.009	0.005	18.2	1.62E-03
CSH-25_1	1.5031	1.008	0.492	0.009	0.005	18.2	1.62E-03

The composition of the injected solution is that of deionized water in a CO_2-free atmosphere (pH = 7). The initial solution in the reactor is at equilibrium with the C-S-H gel and portlandite with an initial pH of ca. 12.5. The C-S-H solid solution was discretized into 19 different stoichiometries, ranging from Ca/Si ratio = 1.67 to Ca/Si ratio = 0.83 (Table 2.2). All the chemical equilibria in solution are listed in Table 2.3. All the equilibrium constants

were taken from the database included in CrunchFlow, which is based on the EQ3/6 database (Wolery, 1990), except for the C-S-H phases calculated from the data in Kulik and Kersten (2001). Activity coefficients were calculated using the extended Debye-Hückel formulation (b-dot model) using parameters from the same database. The activity of water is taken to be unity.

Initial C-S-H (Ca/Si ratio = 1.67) surface area was calculated from the measured BET data and the initial mass of C-S-H. Surfaces of all the other compositions (C-S-H with Ca/Si < 1.67) are assumed to be the same as the initial surface area of C-S-H with Ca/Si = 1.67. The surface area of portlandite was fitted to reproduce the high initial Ca concentration. The rate constant for portlandite (k) is $10^{-5.4}$ mol m^{-2} s^{-1} as reported in Bullard et al. (2010). The rate constants for the discrete cementitious C-S-H phases were obtained by fitting the model to the experimental variation of the output Ca and Si concentrations.

Table 2.2. *Equilibrium constants (log K_{eq}) and stoichiometric coefficients for solid dissolution reactions. Reactions are written as the dissolution of 1 mol of the solid phase.*

		stoichiometric coefficients			
mineral	log K	Ca^{2+}	SiO_2	H^+	H_2O
CSH-167	2.9133E+01	1.67	1	-3.34	4.34
CSH-165	2.8724E+01	1.65	1	-3.3	4.3
CSH-160	2.7572E+01	1.60	1	-3.2	4.19
CSH-155	2.6443E+01	1.55	1	-3.1	4.08
CSH-150	2.5328E+01	1.50	1	-3	3.97
CSH-145	2.4222E+01	1.45	1	-2.9	3.86
CSH-140	2.3124E+01	1.40	1	-2.8	3.75
CSH-135	2.2034E+01	1.35	1	-2.7	3.64
CSH-130	2.0950E+01	1.30	1	-2.6	3.53
CSH-125	1.9873E+01	1.25	1	-2.5	3.42
CSH-120	1.8801E+01	1.20	1	-2.4	3.31
CSH-115	1.7736E+01	1.15	1	-2.3	3.19
CSH-110	1.6678E+01	1.10	1	-2.2	3.08
CSH-105	1.5627E+01	1.05	1	-2.1	2.97
CSH-100	1.4583E+01	1.00	1	-2	2.86
CSH-095	1.3550E+01	0.95	1	-1.9	2.75
CSH-090	1.2529E+01	0.90	1	-1.8	2.64
CSH-085	1.1531E+01	0.85	1	-1.7	2.53
CSH-083	1.1150E+01	0.83	1	-1.66	2.49
Portlandite	2.2800E+01	1.00	0	-2	2
SiO_2 (am)	-2.7200E+00	0	1	0	0
Quartz	-4.0056E+00	0	1	0	0

Table 2.3. *Equilibrium constants (log K_{eq}) and stoichiometric coefficients for equilibria in solution. Reactions are written as the destruction of 1 mol of the species in the first column.*

		stoichiometric coefficients			
species	Log K	Ca^{2+}	SiO_2	H^+	H_2O
$CaOH^+$	1.2850E+01	1	0	-1	1
$H_2SiO_4^{2-}$	2.2960E+01	0	1	-2	2
$HSiO_3^-$	9.9422E+00	0	1	-1	1
OH^-	1.3991E+01	0	0	-1	1

2.3. Results and discussion

2.3.1. C-S-H dissolution reaction

Table 2.4 shows the experimental conditions of the flow-through experiments run at room temperature (23 ± 2 ºC). Experiments were repeated with different durations (from 433 to 5754 h) to evaluate changes in the solid composition with time. Therefore, steady-state conditions were not always reached. Usually, steady state was attained after 1200-1500 h, always exceeding 200 h. The output pH was both measured and calculated by charge balance fixing the measured Ca and Si concentrations using the PhreeqC code (Parkhurst and Appelo, 1999) and the CEM07 database (Matschei et al., 2007; Lothenbach et al., 2008). As Ca was released from both the dissolution of CH and C-S-H gel, the output Ca concentration was not used to calculate the C-S-H dissolution rates. Dissolution rates were only calculated based on the Si output concentration and normalized to both the final mass (rates expressed mol g^{-1} s^{-1}) and the final surface area (rates expressed mol m^{-2} s^{-1}). Three sets of experiments were carried out according to the flow rate (Table 2.4). In the first set (flow rate ≈0.046 mL min^{-1}), to examine whether the C-S-H dissolution could be affected by stirring (solute transport control), three stirred flow-through experiments were carried out at different stirring rates (0 rpm in C-S-H_25-1, 600 rpm in C-S-H_25-2 and 1200 rpm in C-S-H_25-3;Table 2.4). In the three experiments, the evolution of pH and Ca and Si concentrations with time allowed distinction of three stages during the C-S-H dissolution (Fig. 2.10). The output Ca concentration was initially high and decreased sharply until ≈ 250 h (stage 1; Fig. 2.10a). Thereafter a gradual Ca decrease was observed (up to 1500 h, stage 2) until steady state was attained (up to 2000 h, stage 3). During stages 1 and 2, Si concentration increased until steady state was reached in stage 3 (Fig. 2.10b).

Table 2.4. *Experimental conditions and steady-state C-S-H gel dissolution rates. Initial BET area of the unreacted C-S-H gel is 11.7±1.7 $m^2 g^{-1}$*

experiment	time	flow rate	initial mass	initial CSH mass	final CSH mass	pH		Ca	Si	aqueous Ca/Si	BET area	RSi	RSi	log R|Si|	SI	ΔG (kcal mol^{-1})	SI
	(h)	(mL min^{-1})		(g)		measured	calculated	μM			($m^2 g^{-1}$)	(mol $g^{-1} s^{-1}$)	(mol $m^{-2} s^{-1}$)		CSH_083	CSH_083	quartz
FIRST SET		*0.046*															
C-S-H_25-1	2011	0.045	1.5031	1.0101	0.7698	10.31	10.50	626.96	501.15	**0.92**	52.7	**-4.9E-10**	**-9.3E-12**	**-11.0**	**-0.23**	**-0.31**	-0.33
C-S-H_25-2 (1)	2011	0.041	1.5011	1.0087	0.7031	10.42	10.82	712.26	505.36	**1.29**	48.9	**-4.9E-10**	**-1.0E-11**	**-11.0**	**-0.14**	**-0.19**	-0.41
C-S-H_25-3 (2)	2011	0.038	1.5027	1.0098	0.7401	10.53	11.00	708.67	666.16	**1.06**	50.9	**-6.0E-10**	**-1.2E-11**	**-10.9**	**-0.07**	**-0.10**	-0.20
C-S-H_25-4	2011	0.055	3.0707	2.0635	1.6986	10.49	10.85	779.07	613.46	**1.27**	42.9	**-3.0E-10**	**-7.0E-12**	**-11.2**	**-0.05**	**-0.07**	-0.33
C-S-H_25-5	493	0.043	1.5009	1.0086	0.9912	10.80	10.79	647.73	115.32	5.62	52.7	-8.4E-11	-1.6E-12	-11.8			-1.19
C-S-H_25-6	1755	0.055	1.5033	1.0010	0.8250	9.67	10.50	347.98	271.68	**1.28**	142.0	**-3.0E-10**	**-2.1E-12**	**-11.7**	**-0.83**	**-1.13**	-0.38
C-S-H_25-7	910	0.047	1.4998	1.0079	1.0040	11.12	11.13	377.29	2.74	137.79	46.1	-2.1E-12	-4.7E-14	-13.3			-2.60
C-S-H_25-8	1756	0.041	2.9951	2.0127	1.8747	10.21	10.02	694.91	388.89	1.80	61.7	-1.4E-10	-2.3E-12	-11.6			-0.57
C-S-H_25-9	1049	0.054	2.9934	2.0116	1.9861	10.74	10.67	375.55	6.09	61.62	63.3	-2.8E-12	-4.4E-14	-13.4			-2.25
C-S-H_25-10	433	0.041	2.9013	1.9497	1.9468	11.48	11.46	325.81	5.62	57.97	25.0	-2.0E-12	-7.9E-14	-13.1			-2.23
SECOND SET		*0.12*															
C-S-H_25-11	717	0.132	0.5007	0.3355	0.2168	9.92	10.18	126.69	144.35	**0.88**	77.9	**-1.6E-09**	**-2.1E-11**	**-10.7**	**-1.82**	**-2.48**	-0.29
C-S-H_25-12	717	0.130	0.5004	0.3353	0.2150	9.99	10.46	266.36	275.79	**0.97**	60.1	**-1.8E-09**	**-3.0E-11**	**-10.5**	**-1.03**	**-1.40**	-0.23
C-S-H_25-13	1755	0.123	1.5018	1.0092	0.3832	9.75	10.46	260.16	246.25	**1.06**	131.0	**-1.3E-09**	**-1.0E-11**	**-11.0**	**-1.08**	**-1.47**	-0.29
C-S-H_25-14	1049	0.126	1.5011	1.0087	0.2934	10.03	10.44	383.25	372.02	**1.03**	74.0	**-2.7E-09**	**-3.6E-11**	**-10.4**	**-0.67**	**-0.92**	-0.23
C-S-H_25-15	432	0.102	1.5097	1.0145	0.9973	11.00	10.99	726.17	31.16	23.06	54.2	-5.3E-11	-9.8E-13	-12.0			-1.85
C-S-H_25-16	570	0.120	2.9994	2.0153	1.8544	10.60	10.41	682.55	195.78	3.49	14.5	-2.1E-10	-1.5E-11	-10.8			-0.95
C-S-H_25-17	1049	0.118	2.9951	2.0127	1.8129	10.08	10.71	143.05	58.60	2.44	28.8	-6.4E-11	-2.2E-12	-11.7			-0.82
C-S-H_25-18	1617	0.097	2.998	2.0147	1.8247	10.68	10.63	636.37	12.69	50.63	15.9	-1.1E-11	-7.1E-13	-12.1			-2.18
THIRD SET		*0.008*															
C-S-H_25-19	4534	0.013	2.9976	2.0144	1.8842	9.36	10.9	830.68	806.13	**1.03**	54.6	**-9.5E-11**	**-1.7E-12**	**-11.8**	**-0.02**	**-0.03**	-0.17
C-S-H_25-20	4534	0.012	1.4961	1.0054	0.9282	10.12	10.9	597.79	733.16	**0.82**	62.9	**-1.6E-10**	**-2.6E-12**	**-11.6**	**-0.19**	**-0.26**	0.00
C-S-H_25-21	5754	0.005	3.0034	2.0183	1.9917	9.98	11.6	610.87	215.52	2.84	38.2	-8.0E-12	-2.1E-13	-12.7			-0.83
C-S-H_25-22	5754	0.004	1.4975	1.0063	0.9337	9.04	11.0	771.93	586.47	**1.32**	93.0	**-4.0E-11**	**-4.4E-13**	**-12.4**	**-0.04**	**-0.06**	-0.36
C-S-H_25-23	4534	0.012	2.9855	2.0063	1.8946	9.58	11.0	590.48	673.84	**0.88**	48.3	**-7.2E-11**	**-1.5E-12**	**-11.8**	**-0.21**	**-0.29**	-0.06
C-S-H_25-24	5754	0.005	1.5062	1.5062	1.4426	9.42	11.0	849.38	602.28	**1.41**	85.3	**-3.4E-11**	**-4.0E-13**	**-12.4**	**-0.07**	**-0.10**	-0.41

Bold indicates experiments that approached steady state and dissolution was congruent

Experiments in italics indicate equilibrium with respect to quartz

Calculated output pH using the PHREEQC code (see text)

R_{Si} is calculated according to the Si release (see text)

(1) stirred (600 rpm) and (2) stirred (1200 rpm)

Propagated error in the dissolution rate is approximately 15%

The high Ca concentration at the start of the experiments was mainly due to fast dissolution of CH (Haga et al., 2002; Galan et al., 2011). In contrast, at the start of the experiments the Si released from C-S-H dissolution was low due to a common-ion effect. Because fast portlandite dissolution results in large Ca concentrations, Si can only be present at very low concentrations (limited by the equilibrium with respect to C-S-H). As portlandite was consumed, released Si increased with time (stage 1). In stage 2, portlandite was mostly dissolved, and the C-S-H dissolution was incongruent, showing preferential Ca release and consequent gradual decrease in the aqueous Ca/Si ratio. In stage 3, C-S-H dissolution reached steady state, i.e., the output Ca and Si concentrations were constant with time for more than 500 h, and the Ca and Si output concentrations were similar within error (Fig. 2.10c).

The stoichiometric Ca/Si ratio is defined as the ratio between the output concentrations of Ca and Si. Variation in the Ca/Si ratio in solution with time in experiments C-S-H_25-1, C-S-H_25-2 and C-S-H_25-3 is shown in Figure 2.10d. Usually, the output Si concentration is lower than that of Ca until steady state is approached. In stage 1 the Ca/Si ratio is very high due to preferential dissolution of portlandite. In stage 2, as the portlandite content diminishes, a gradual decrease in Ca and increase in Si is observed, indicating an enhancement of the C-S-H gel dissolution rate, resulting in an increase in the Ca/Si ratio. At the third stage, concentration of Ca and Si reached steady state. The Ca/Si ratio in the aqueous phase tended to be constant (Ca/Si $\approx 0.9 \pm 0.1$), indicating congruent C-S-H dissolution of a tobermorite-like phase (Ca/Si ≈ 0.83).

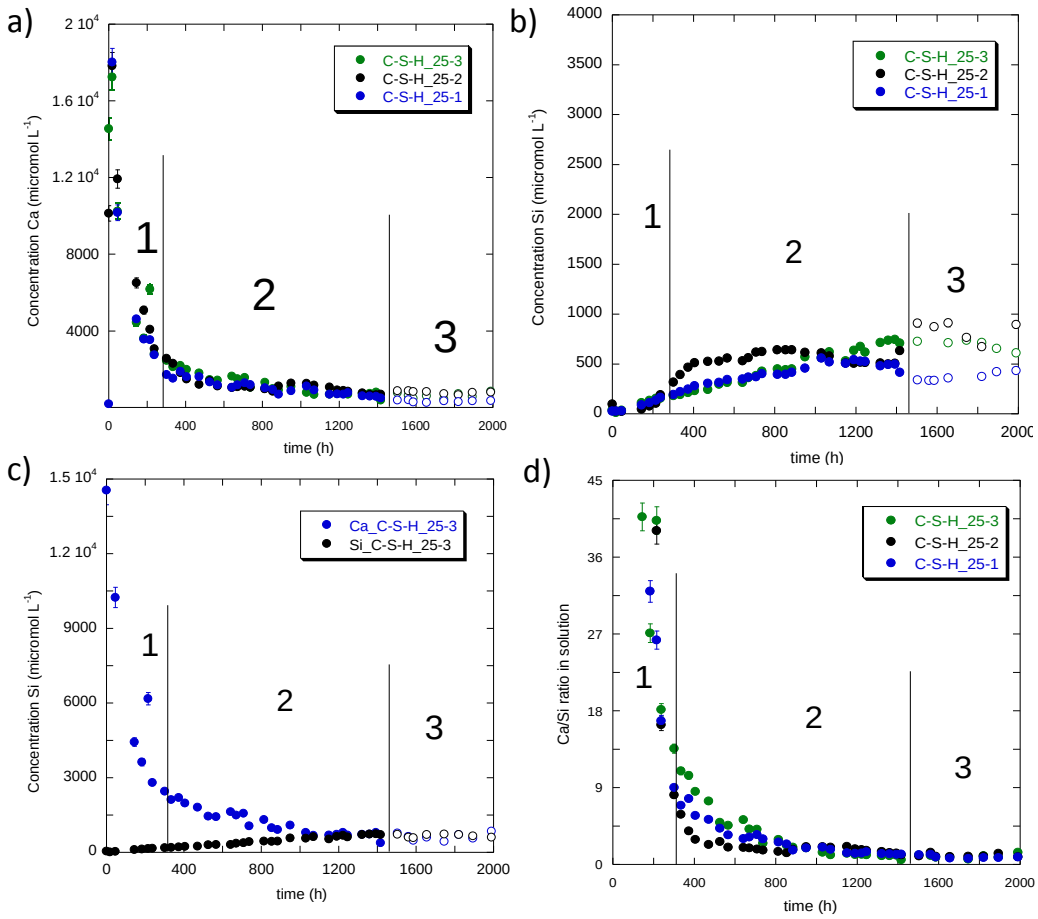

Figure 2.10. *Variation of the output (a)Ca and (b)Si concentrations with time in experiments C-S-H_25-1, C-S-H_25-2 and C-S-H_25-3; c) variation of Ca and Si concentration in experiment C-S-H_25-3;d) variation of the aqueous Ca/Si ratio in experiments C-S-H_25-1, C-S-H_25-2 and C-S-H_25-3. 1, 2 and 3 represent the three different stages mentioned in text. Empty symbols represent steady-state output concentrations.*

At the stage of congruent dissolution, the steady-state C-S-H gel dissolution rates were calculated based on the steady-state Si release (Eq. (2.2), Table 2.4). The average rate from the three experiments is - 1.02×10^{-11} ± 1.0×10^{-12} mol m^{-2} s^{-1} with a coefficient of variation (CV) of 10 %. This error is smaller than the uncertainty in the measurements (15%), which indicates that the dissolution reaction was not transport-controlled (not affected by the stirring). Based on this result, the rest of the experiments were performed using non-agitated cells to prevent possible stirring-induced abrasion of the particles that could affect the C-S-H dissolution rates (Metz and Ganor, 2001).

Figure 2.11a depicts the output pH variation with time in the three experiments. In stage 1, the initial pH of about 12 is caused by portlandite dissolution. pH decreases as portlandite is consumed and C-S-H dissolution becomes dominant (stage 2). Output pH

values below 10.5 are likely affected by undesired carbonation of the collected output solution prior to analysis as is suggested by the higher calculated pH values (PhreeqC, Fig. 2.11b). Solutions with high pH values (10-12.5) are highly sensitive to carbonation. However, the pH decrease will be larger in a solution with a pH of approx. 10.5. In stage 3, the output pH is fairly constant (around 10) indicating that C-S-H dissolution reaches steady state.

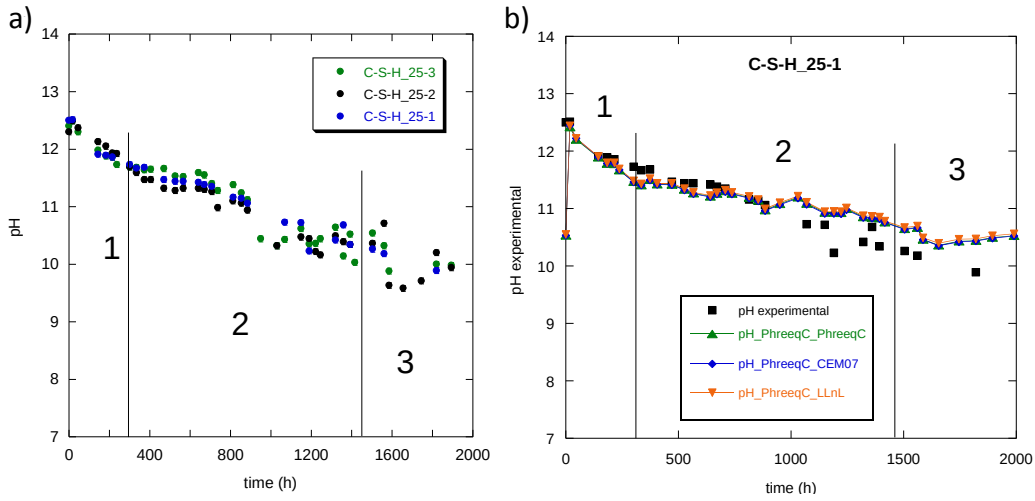

Figure 2.11. *(a) Output pH variation with time in experiments C-S-H_25-1, C-S-H_25-2 and C-S-H_25-3; (b) measured and calculated output pH variation in experiment C-S-H_25-3. Error bars are within the symbol size. The PhreeqC code was used to calculate the output pH (charge balance).*

These results (stage 3) indicate that (i) the C-S-H gel was the main dissolving phase and (ii) the dissolution reaction was stoichiometric with respect to a phase with a Ca/Si ratio similar to that of tobermorite. In this third stage the solid and aqueous Ca/Si ratios would be expected to be approximately the same. The results agree with those reported by Harris et al. (2002) and Carey and Lichtner (2006, 2007) who showed that the leaching of C-S-H gels in demineralized water could initially be described as an incongruent dissolution, tending gradually to a congruent dissolution.

The second and third sets of experiments were carried out by respectively increasing and decreasing the flow rate (≈ 0.12 and ≈ 0.008 mL min^{-1}) with respect to the first set (≈ 0.046 mL min^{-1}; Table 2.4). Faster flow yields lower output concentrations and slower flow yields higher output concentrations. With time, behaviour of output pH and output concentration of Ca and Si was similar to that observed in the first set of experiments with a mere change in the time to achieve steady state (longer time to steady state in slower-flow experiments; Fig. 2.12).

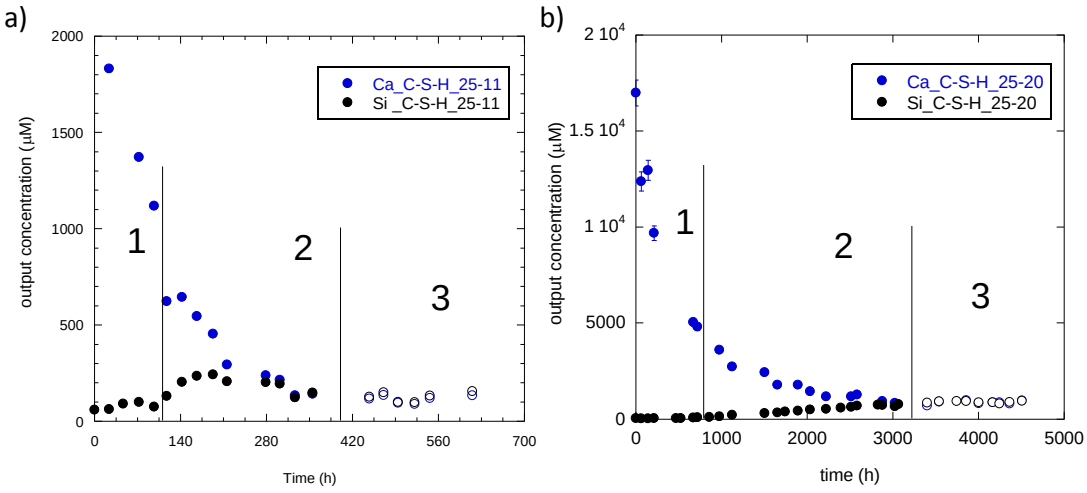

Figure 2.12. *Variation of the output concentrations with time in experiment C-S-H_25-11(≈ 0.132 mL min^{-1}) and C-S-H_25-20 (≈ 0.012 mL min^{-1}). Steady state was reached earlier in the experiment with faster flow rate.*

2.3.2. The C-S-H gel dissolution rate at steady state

In the experiments where the output solution concentrations did not reach steady state, the dissolution rate was calculated based on the output Si concentrations according to Eq. (2.1) at room temperature (23 ± 2˚C) and normalized to final mass and final surface area (Table 2.4). In these experiments, the aqueous Ca/Si ratio ranged from 1.8 to 137.8 (stage 2).

In the experiments where the steady state was attained, the dissolution rate of the C-S-H gel was also calculated based on Si release (Eq. 2.2). In this case, the aqueous Ca/Si ratio equals approximately the stoichiometric value expected for a congruent dissolution of the C-S-H gel with a tobermorite-like composition (Ca/Si ratio ≈ 0.83). The steady-state dissolution rates of the C-S-H gel ranged from -3.4x10^{-11} to -2.70x10^{-9} mol g^{-1} s^{-1} or -4.0x10^{-13} to -3.0x10^{-11} mol m^{-2} s^{-1} (see values in bold in Table 2.4).

Variation in SI with time in a representative experiment (e.g., C-S-H_25-1) is shown in Figure 2.13. A similar behavior is obtained in the different calculations. Initially, the solution is nearly saturated with respect to jennite (C-S-H_1.667) and portlandite, even slightly supersaturated, and undersaturated with respect to amorphous SiO_2 and quartz. With time SI decreases, the solution is becoming undersaturated with respect to C-S-H_1.67 and highly undersaturated at steady state. In turn, SI increases with respect to SiO_2 amorphous and quartz. Regarding the discrete cementitious composition between the two end-members jennite and tobermorite, the associated SI values showed an increase in undersaturation with

time. With respect to tobermorite (C-S-H_0.83), the calculated SI showed slight undersaturation during all the experiments.

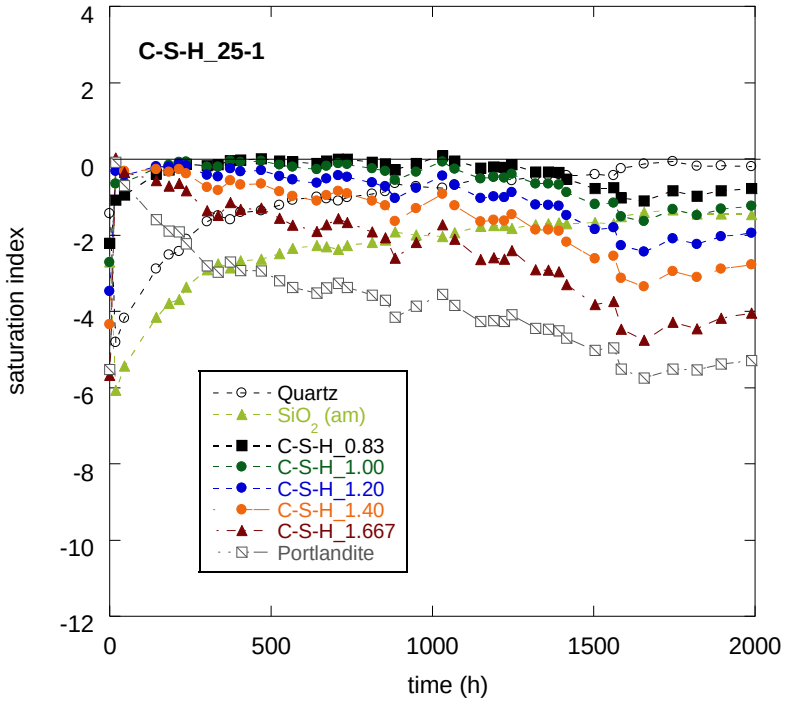

Figure 2.13. *SI variation with time in a representative experiment (C-S-H_25-1) using PhreeqC code with MINTEQ and CEM07 databases.*

The saturation state of the solution was calculated in terms of the Gibbs energy, ΔG, according to

$$\Delta G = 2.303RT \cdot SI \qquad and\ SI = \log \frac{IAP}{K_{eq}} \qquad \text{Eq. 2.7}$$

where *R* is the gas constant, *T* is the absolute temperature, *SI* is the saturation index of the solution with respect to C-S-H_0.83 and *IAP* is the ion activity product. Figure 2.14 plots the steady-state dissolution rates obtained in this study against ΔG.

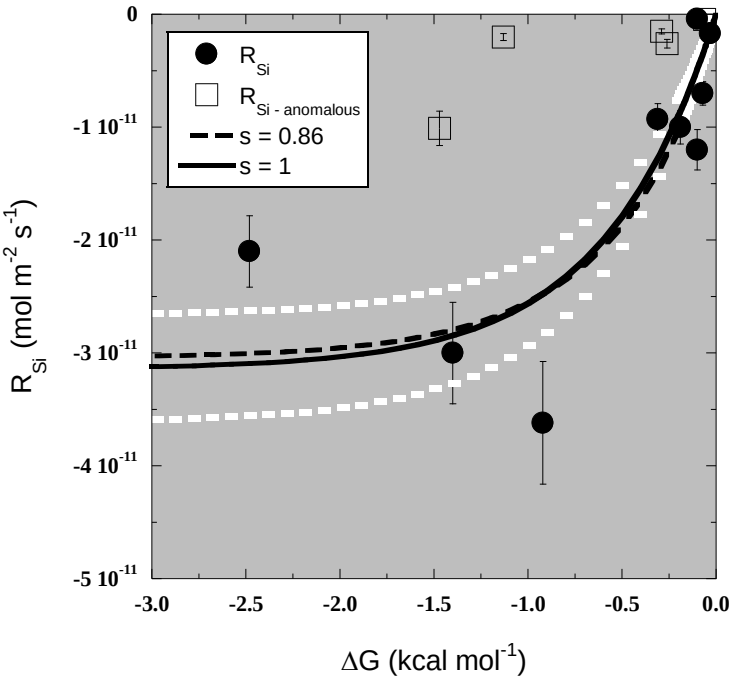

Figure 2.14. *Variation of the steady-state dissolution rates (C-S-H_0.83) with the solution saturation state in terms of the Gibbs energy, ΔG (22 ± 2°C). The solid and dotted lines are the best fitting curves using Eq. (2.8) in which the Temkin's number, σ, equals 1 or 0.86, respectively. The respective R^2 values are around 0.8. The two fitting curves lie within the area between the dashed white lines that corresponds to the 15% error associated to the rates. Rates in empty symbols are not accounted for the rate-ΔG fitting (see text).*

Two groups of rates represented by empty and solid symbols are depicted in Figure 2.14. The former includes experiments where dissolution rates are small and diminish in magnitude as ΔG increases to equilibrium (from ΔG ≈ -1.5 to 0 kcal mol^{-1}). In contrast, the rates included in the latter are faster and also decrease as equilibrium is approached (from ΔG ≈ -2.5 to 0 kcal mol^{-1}). Thus, it appears that over the same range of solution saturation states, pH (10.5 - 11) and temperature (23 ± 2°C), some of the steady-state dissolution rates were noticeably slower (empty symbols in Fig. 2.14). If, as it was shown above, the C-S-H dissolution rate is not transport controlled (dominated by diffusion), different dissolution rates should not be obtained at the same ΔG. The evolution of aqueous chemistries was similar in all and it cannot explain the slow rates. However, the output solution was at equilibrium with respect to quartz and close to equilibrium with respect to amorphous SiO_2 in two experiments showing large Q^4-gel peaks (C-S-H_25-20 and C-S-H_25-23, Table 2.6 and section 2.3.5 below). The NMR spectra of the reacted samples suggest the formation of Si-rich domains during C-S-H dissolution in most of the slow dissolution-rate experiments (see section 2.3.5). Hence, the steady-state rates calculated from these experiments were not taken into account the derive a dissolution rate law for the C-S-H_0.83 gel. However, the inhibitory effect that

formation of Si-rich domains might exert on the C-S-H dissolution rates has to be highlighted. Further studies should address this issue.

In order to account for the solution saturation effect on the C-S-H_0.83 gel dissolution rate, a transition state theory (TST)-derived rate law is proposed

$$Rate = k \cdot \left(1 - \exp\left(\frac{\Delta G}{\sigma RT}\right)\right) \quad \text{Eq. 2.8}$$

where k stands for the dissolution rate constant and σ is known as the Temkin's stoichiometric number (Cama et al., 2010). Likewise, Eq. (2.8) can be expressed in terms of the saturation state, Ω, that is used in the CrunchFlow code

$$Rate = k \cdot \left(1 - \Omega^{1/\sigma}\right) \quad \text{Eq. 2.9}$$

where $\Omega = IAP/K_{eq}$.

A reasonable fit to the experimental data at pH 10.50 to 11 and temperature 23 ± 2°C can be obtained with σ = 1 or σ = 0.86 (Fig. 2.14), yielding respective k values of 3.1 ± 0.4 $x10^{-11}$ and 3.0 ± 0.3 $x10^{-11}$ mol m^{-2} s^{-1}. Considering the similarity in the values of the fitted kinetic parameters, it is suggested to use the simplest TST-form (i.e., σ = 1) and the average rate constant k of 3.1 ± 0.4 $x10^{-11}$ mol m^{-2} s^{-1} for the rate law

$$Rate_{C-S-H\_0.83}\ (mol\ m^{-2}\ s^{-1}) = -3.1 \pm 0.4 \times 10^{-11} \cdot (1 - \Omega) \quad \text{Eq. 2.10}$$

Moreover, the TST-form of this rate law supports the use of Eq. (2.9) in the reactive transport modeling to derive the rate constants for the discrete C-S-H compositions used to represent the solid solution.

2.3.3. C-S-H dissolution rate at different Ca/Si ratio. Modeling

CrunchFlow simulations of the variation of Ca and Si output concentration and output pH with time in a representative experiment, C-S-H_25-3, are shown in Figure 2.15. Table 2.5 lists the derived rate constants associated to the variable C-S-H composition (Ca/Si ratio between 1.67 and 0.83) from fitting the model to experimental data. The rate constants ranged from $10^{-7.5}$ to 10^{-11}. The value of the coefficients decreases with decreasing Ca/Si ratio of the C-S-H gel.

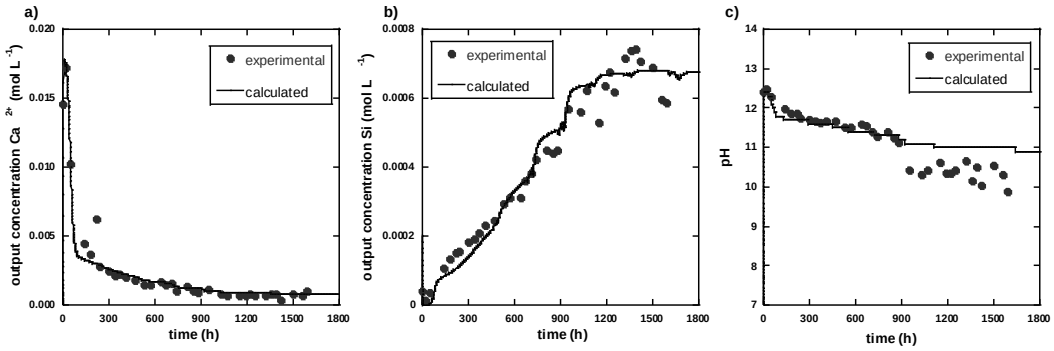

Figure 2.15. *Experimental and calculated variation of a) the output Ca concentration; b) the output Si concentration, and c) output pH in experiment C-S-H_25-3. Symbols correspond to experimental data and lines to model results.*

To obtain a reasonable fit between model and experimental output Ca concentration (Fig. 2.15a), the amount of portlandite and its reactive surface area are fitted to adjust the initial Ca concentrations (the first 200 hours). Thereafter, portlandite is mostly dissolved, and dissolution of the C-S-H dominates (Fig. 2.15b). The progress of the reaction is marked by release of Ca and Si, evolving to lower Ca/Si ratios. Microprobe analyses show higher solid Ca/Si ratios in C-S-H particles after shorter experiments and lower Ca/Si ratios in those where steady state was achieved. Fitted rate constants associated to discrete cementitious compositions with high Ca/Si ratios are larger than those related to compositions with low Ca/Si ratio. Regarding pH (Fig. 2.15c), a successful fit between model and experimental output pH is obtained up to 800 h. Thereafter, the experimental pH is lower than the calculated one. The reason of this apparent discrepancy is that these output solution samples underwent carbonation prior to pH measurement.

In the simulations, the volumetric fraction of portlandite and associated surface area varied between 0.0017 and 0.0018 and 0.07 and 0.09 m^2 g^{-1}, respectively (Table 2.5). The

obtained values of the dissolution rate constants of the different C-S-H gel compositions considered ($0.83 \leq$ Ca/Si ratio ≤ 1.67) to fit the experimental results of Ca and Si in solution range from about 10^{-8} to10^{-11} mol m^{-2} s^{-1}. The fastest rate coefficients are associated with the C-S-H_1.67 end-member with Ca/Si of 1.67 (jennite-like phase). The rates decrease by decreasing the Ca/Si ratio so that the end-member C-S-H_0.83 with Ca/Si of 0.83 (tobermorite-like phase) is the slowest (Table 2.5).

A polynomial fit to the derived rate constants from the three experiments (Table 2.5) yields a continuous function that can be more easily implemented in reactive transport modeling

$$Log\ k\ (mol\ m^{-2}\ s^{-1}) = 202.55\left(\frac{Ca}{Si}\right)^5 - 1283.97\left(\frac{Ca}{Si}\right)^4 + 3191.77\left(\frac{Ca}{Si}\right)^3 - 3883.10\left(\frac{Ca}{Si}\right)^2 + 2312.78\frac{Ca}{Si} - 550.97 \qquad \text{Eq. 2.11}$$

Since the form of the rate laws used in the modeling does not explicitly include the effect of pH (e.g. an $a_{H+}{}^n$ term), it is possible that the observed variation of the rate constants (k) with Ca/Si ratio of the solid is due (at least partially) to the lower pH associated with the smaller values of Ca/Si ratio. Two points should be mentioned: (1) most experimental results correspond to close-to-equilibrium conditions (region where the rate in not independent of ΔG) and therefore a pH effect cannot be clearly separated from a ΔG effect. (2) If a rate law of the form $R_m = -A_m\ k_m\ a_{H+}{}^n\ (1- \Omega)$ were used in the modeling of the experiments, it would not be possible to decouple k_m from $a_{H+}{}^n$, yielding infinite possible combinations of k_m and $a_{H+}{}^n$. Therefore, the simple form of the rate law (Eq. 2.6) was used. However, it is indeed possible that the variability in k reflects (at least partially) an actual dependency on pH.

Table 2.5. *Fitting parameters used in the simulations of the representative experiments.*

Parameters	Experiments			Polynomial form
	C-S-H_25-3	C-S-H_25-2	C-S-H_25-1	
Initial Mass (g)	1.5027	1.5011	1.5031	1.5
Experimental Flux (mL min^{-1})	0.04	0.04	0.04	0.04
Volumetric fraction of C-S-H gel	0.009			
C-S-H	Fitted parameters (log k, mol m^{-2} s^{-1})			
CSH-1667	-9.01	-7.50	-8.50	-8,4
CSH-165	-9.12	-7.50	-9.01	-8,47
CSH-160	-9.28	-7.50	-8.76	-8,53
CSH-155	-9.30	-7.60	-8.93	-8,53
CSH-150	-9.07	-7.67	-8.96	-8,56
CSH-145	-9.06	-7.80	-8.90	-8,67
CSH-14	-9.28	-7.80	-9.32	-8,89
CSH-135	-9.45	-9.00	-9.10	-9,2
CSH-130	-9.79	-9.10	-10.13	-9,58
CSH-125	-10.49	-9.00	-10.92	-9,98
CSH-120	-10.70	-9.10	-11.12	-10,36
CSH-115	-10.45	-10.4	-11.20	-10,67
CSH-110	-10.40	-10.5	-11.20	-10,88
CSH-105	-10.90	-10.9	-11.30	-10,97
CSH-10	-10.95	-10.9	-11.00	-10,95
CSH-095	-10.95	-10.9	-10.70	-10,86
CSH-090	-10.90	-10.9	-10.65	-10,79
CSH-085	-10.90	-11.0	-10.88	-10,87
CSH-083	-10.90	-11.1	-10.80	-10,99
CH volumetric fraction	0.0017	0.0018	0.0017	0.0017
CH surface area (m^2 g^{-1})	0.0800	0.0700	0.0900	0.0800

C-S-H_1.667 and C-S-H_0.83 are the jennite-like and tobermorite-like end-members of the solid solution.

The calculated initial volumetric fraction of portlandite (CH) was 0.005.

Variation of dissolution rates (R_{Si}) with pH for some representative experiments is shown in Figure 2.16. At ≈ pH 12.5 preferential dissolution of portlandite takes place, and C-S-H gel with Ca /Si ratio of 1.667 dissolves under close-to-equilibrium conditions. The values of the dissolution rate at this stage are around 10^{-14}-10^{-13} mol m^{-2} s^{-1} and the rate constant (k) is 10^{-8} mol m^{-2} s^{-1}. With time, the content of portlandite diminishes increasing the C-S-H gel dissolution. At the end of the experiments, when the pH is around 10.5 and the Ca/Si ratio of the gel is close to 0.83, the dissolution rate is about $9.3 \cdot 10^{-12}$-$1.0 \cdot 10^{-11}$ mol m^{-2} s^{-1} and the rate constant (k) becomes smaller (10^{-11} mol m^{-2} s^{-1}).

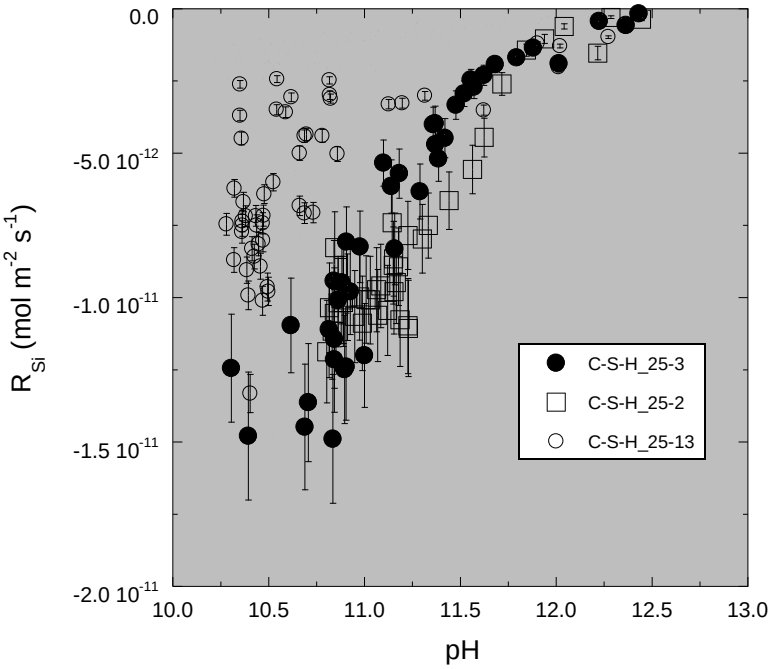

Figure 2.16. *Variation of the dissolution rates (C-S-H_0.83) with pH for 3 representative experiments.*

2.3.4. Morphology and composition of the C-S-H gel

2.3.4.1 Morphology of C-S-H gel (SEM-EDX measurements)

The SEM images show the aspect of unreacted C-S-H gel particles and reacted ones retrieved from experiment C-S-H_25-3 (Fig. 2.17). It is observed that the unreacted particles have irregular round shapes (Fig. 2.17a). EDX analyses revealed that some of the particles are CH as Ca was the only element detected (Fig. 2.17b). After dissolution (Fig. 2.17c), the C-S-H particles show similar morphology, and particles of CH are not detected.

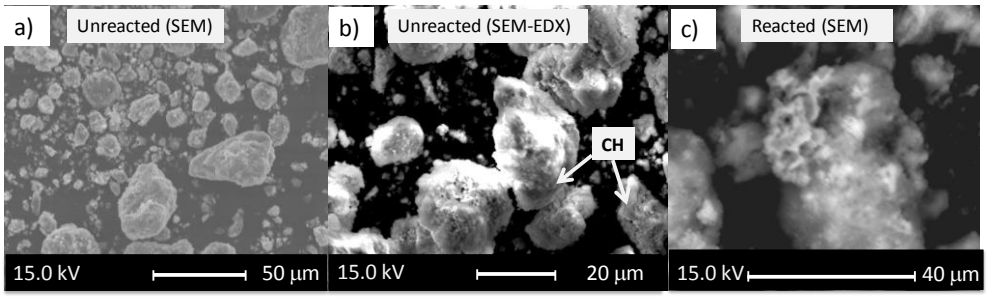

Figure 2.17. *SEM images of C-S-H samples: a) overall view of the unreacted C-S-H gel powder; b) close-up view of the portlandite (see arrows) and C-S-H particles and c) retrieved C-S-H gel sample in experiment C-S-H-25_3.*

2.3.4.2 Composition of the C-S-H gel (EPMA analyses)

EPMA analyses were performed on multiple points of the unreacted and reacted C-S-H samples and were used to calculate the solid Ca/Si ratio. Ca/Si ratio greater than 1.70 ± 0.10 suggest portlandite-rich regions, and Ca/Si ratios equal or smaller than 1.70 ± 0.10 indicate that the analyzed particles is exclusively formed of C-S-H (see Fig. 2.7). In principle, considering that these particles were retrieved after achieving steady-state, no portlandite should be found. However, some portlandite remained unreacted, likely due to the fact that some portandite-rich regions could remain coated by C-S-H-rich domains during dissolution. Also, the solid Ca/Si ratio of the C-S-H particles retrieved after the steady state should be close to 0.9 ± 0.1, which is the stoichiometric Ca/Si ratio of the tobermorite-like C-S-H and is inferred by the aqueous Ca/Si ratio of 0.9 ± 0.1. The observed compositional variability within the C-S-H particles could be caused by heterogeneous dissolution from the particle surface to the unreacted core. Figure 2.18 shows the backscattered electron images of some reacted particles retrieved after the steady state was achieved (experiments C-S-H_25-1, C-S-H_25-2 and C-S-H_25-23). The EPMA multipoint analysis shows that the solid Ca/Si ratio varies within a range in the analyzed particles. The values of the solid Ca/Si ratio of the particles indicate that the analyzed particles are exclusively formed of C-S-H with a solid Ca/Si ratio that varies from 0.44 and 1.60.

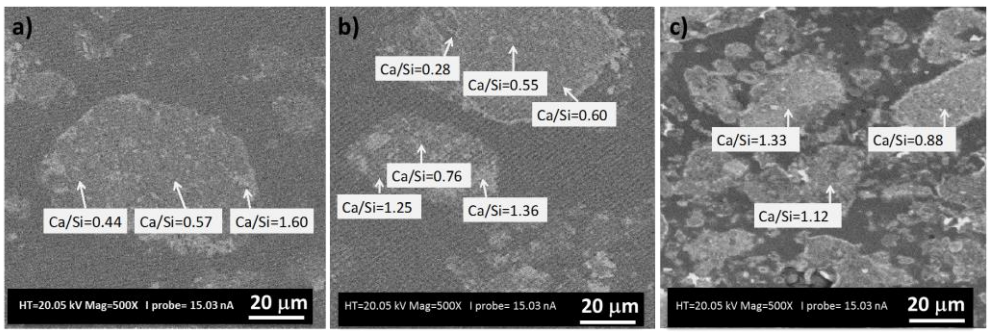

Figure 2.18. *Backscattered-electron images of the reacted C-S-H gel in experiments C-S-H_25-2 (a), C-S-H_25-1 (b) and C-S-H_25-23 (c).*

Measurements of the solid Ca/Si ratios were also performed on samples from experiments not reaching steady state (C-S-H_25-8 of ≈ 1756 h, C-S-H_25-9 of ≈ 1049 h, C-S-H_25-10 of 433 h, C-S-H_25-16 of 570 h and C-S-H_25-6 of 1755 h; Fig. 2.19). The analyses show that the solid Ca/Si ratio decreases with reaction time, as expected, since the Ca/Si ratio of the longer-reacted particles at steady state is lower (i.e., around 0.9 ± 0.1) than that of reacted particles that did not reach steady state.

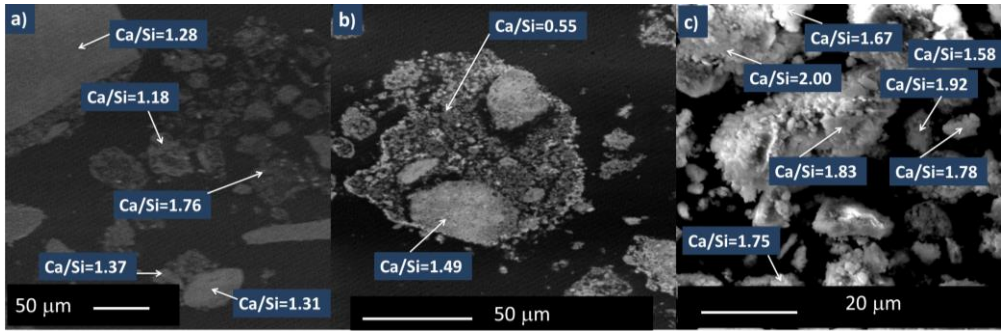

Figure 2.19. *Backscattered-electron (a,b) and secondary-electron (c) images of the reacted C-S-H sample in experiments (a) C-S-H_25-8 (1756 h), (b) C-S-H_25-9 (1049 h), and (c) C-S-H_25-10 (433 h). Numbered points correspond to the analyzed particle micro-regions.*

2.3.5 Structure of the C-S-H gel (^{29}Si MAS-NMR spectra)

Quantitative information on the connectivity of the silicate tetrahedra is provided by ^{29}Si MAS-NMR. The relative proportions of silicon associated with the Q^n units were determined by the deconvolution of the different peaks in the spectra using the Dmfit program and the Gaussian/Lorentzian model (Massiot et at., 2002). The results of the dipolar correlation model of C-S-H obtained by Klur et al. (1998) were used to improve the spectra interpretation. The model considers the following chemical shifts: Q^1 at -78.9 ppm, Q^{1p} at -76 ppm (for Ca/Si ratio > 1; Fernández et al., 2008), Q^{2p} at -82.1 ppm, Q^{2i} at -83.9 ppm (the difference between Q^{2p} and Q^{2i} is in the tetrahedron connection to protons with a resonance at

lower field than those connected to calcium atoms; Klur et al., 1998), Q^2 at -85.3 ppm, Q^3-defect at -91.5 ppm, Q^{2v} at -87.3 ppm, Q^3-gel at -93 ppm and Q^4-gel at -111.7 ppm.

Based on the intensity of the peaks, the mean chain length (MCL) of the C-S-H gel is calculated using the following expression (Chen et al., 2004)

$$MCL = \frac{2 \cdot (Q^1 + Q^2)}{Q^1} \quad \text{Eq. 2.12}$$

where Q^1 and Q^2 are the relative intensities of these deconvoluted peaks expressed in %. This expression is valid as Q^1 and Q^2 are the only peaks present in the spectra. The length of the chain can also be estimated from the Q^2/Q^1 ratio (Haga et al., 2002). In general, the Q^2/Q^1 ratio of the C-S-H gel in Portland cement is about 0.68, though Beaudoin et al. (2009) reported a Q^2/Q^1 ratio of 0.6 for a C-S-H gel sample with Ca/Si ratio of 1.6. This low Q^2/Q^1 ratio indicates that the sample has short chain lengths. A Q^1 intensity higher than Q^2 denotes high quantity of end-chain silicates in the sample. The polymerization of the C-S-H gel is expressed by the $Q^1/\Sigma Q^i$ (i = 1-3) ratio, which decreases as Ca/Si ratio decreases ($Q^1/\Sigma Q^i$ > 0.5 in C-S-H gels with Ca/Si ratio > 1.67; Cong and Kirpatrick, 1996).

Concerning the presence of other peaks in the spectra, due to changes in the C-S-H structure after dissolution, Fernández and Puertas (2003) suggest that the presence of Q^3 and Q^4 peaks precludes the utilization of expressions derived for MCL and propose an expression that accounts for the tetrahedral condensation ratio

$$\frac{\Sigma Q^2}{Q\text{Total}} \quad \text{Eq. 2.13}$$

where $Q_{Total} = \Sigma Q^n$ and Q^n stands for Q^1, Q^2 and Q^3 units.

Gaitero et al. (2008) explicitly included all peaks in a calculated average segment length (SL), which is a measure of the number of unit lengths (silicate tetrahedra) in all possible geometric combinations leading to chains of tetrahedral. SL is calculated according to

$$\langle SL \rangle = \frac{(2 \cdot (Q^1 + Q^2 + 1.5Q^2(Al) + 3Q^3 + 4Q^4))}{Q^1 + 3Q^3 + 4Q^4} \quad \text{Eq. 2.14}$$

where Q^i represents the area of the peak i. Q^2 (Al) is not present in the measurements reported here (no Al in the system).

A Q^3/Q^2 ratio of 0.5 indicates a crosslinked tobermorite structure with Ca/Si ratio near to 0.83 (Houston et al., 2009; Myers et al., 2013). The Q^3/Q^2 ratio is calculated according to

$$\frac{\left(Q^3 defect + Q^{2i} + Q^{2p}\right)}{Q^2} = \frac{1}{2} \qquad \text{Eq. 2.15}$$

2.3.5.1 Unreacted C-S-H gel

The ^{29}Si MAS-NMR spectrum of the unreacted C-S-H gel shows two peaks corresponding to Q^1 and Q^2 at -78.88 and -85.24 ppm, respectively (Fig. 2.20). Cong and Kirkpatrick (1996) and Haga et al. (2002) showed that the C-S-H gel structure is formed of dimers and short silicate chains. It was not possible to deconvolute between Q^1 and Q^{1p} in these samples. The obtained spectrum with the lack of Q^3 and Q^4 peaks indicates a non-three-dimensional silicate structure for the initial C-S-H gel. Presence of SiO_2 (quartz) is detected at nearly -107 ppm. This amount of SiO_2 could either be some remanent reactant or some byproduct of the ball milling process. Q^{2p} and Q^{2i} are also observed at -81.65 and -83.92 ppm, respectively. The MCL is calculated according to Chen et al. (2004) to be 3.35 (Table 2.6).

2.3.5.2 Reacted C-S-H gel

Representative ^{29}Si MAS-NMR spectra of the reacted C-S-H gel samples are shown in Figure 2.20. Table 2.6 lists the peak shifts and integral relative intensities (%). The spectrum of experiment CSH-25-18 is very similar to that of initial C-S-H gel (Fig. 2.20); Q^1 and Q^2 peaks prevail, indicating that the C-S-H gel structure is similar to that of the unreacted C-S-H gel, even after 1617 h. In fact, the high aqueous Ca/Si ratio indicates that portlandite and C-S-H still coexist (Table 2.6), and that the composition of the latter should be close to that of jennite-like C-S-H structure. In contrast, the spectra of the other reacted C-S-H gel samples show a decrease in Q^1 and Q^{2i} peaks, an increase in Q^2 peak, better resolved Q^{2p}, and the appearance of new peaks (Q^3-defect, Q^3-gel and Q^4-gel). According to Chen et al. (2004) the hydroxylated Q^3(OH) (Q^3-gel) (-101ppm) and Q^4-gel (-110 ppm) can be assigned to silica gel. Experimental solutions (Table 2.4) were undersaturated with respect to quartz, except those corresponding to the samples showing large Q^4-gel peaks (CSH-25-20 and CSH-25-23), which were at equilibrium with respect to quartz. It was not possible to model SiO_2 (quartz) precipitation in the experiments, since the solutions were at most at equilibrium with this

phase, suggesting that these silica-rich domains may be formed during incongruent dissolution (preferential release of Ca), rather than by precipitation from the bulk solution. However, precipitation cannot completely be discarded.

These C-S-H gel samples show a solid Ca/Si ratio fairly close to 0.9 (the expected solid Ca/Si ratio of tobermorite-like structure) that corresponds to steady-state samples. Q^3-gel and Q^4-gel appears at low Ca/Si ratios (below 0.8 (Cong and Kirkpatrick, 1996) and 0.6 (Beaudoin et al., 2009)). The presence of Q^3 defect, Q^3-gel and Q^4-gel peaks indicates the existence of bonds between chains, cross-linked chains and silicate polymerization. The observed increase in polymerization of the reacted C-S-H samples, as Ca/Si ratio decreases, indicates that the gel dissolution tends to condense the evolving C-S-H structure (Table 2.6). This observation agrees with the tendency of Q^2/Q^1 ratio, $Q^1/\Sigma Q^n$ ratio and <SL>. Experiments with the lowest aqueous Ca/Si ratio show the highest Q^2/Q^1 ratio and the lowest $Q^1/\Sigma Q^n$ ratio. Cong and Kirkpatrick (1996) reported $Q^1/\Sigma Q^n$ ratio values below 0.2 for a C-S-H with a Ca/Si ratio < 0.8. This suggests the C-S-H structure changes from short chains (high intensity of Q^1 peak in the jennite-like phase) to long chains (high intensity of Q^2 peak).These results are in agreement with those in the study by Grutzeck et al. (1989) who showed that lime-rich C-S-H consists of mixture of dimer and shorter chains and the silica-rich C-S-H consists of long chains of tetrahedra. Moreover, the decrease in $Q^1/\Sigma Q^n$ ratio with dissolution shows that silica gel may form at low solid Ca/Si ratio (Table 2.6). The value of average segment length, <SL>, increases as Ca/Si ratio decrease due to the formation of long chains (e.g long segments). When the ramifications take place in the structure, the value of <SL> decrease due to the chain length between cross-linkers (Q^3-gel or Q^4-gel tetrahedra) decrease and the structure evolves more dense. The obtained Q^3/Q^2 values near to 0.5 for some of the C-S-H samples indicate that the resulting structures are that of a tobermorite-like phase, except for the C-S-H_25-20 and C-S-H_25-23 samples that showed high contribution of a silica-rich C-S-H gel.

Table 2.6. *Chemical shift (ppm), relative peak intensity (%) and Q relations from ^{29}SiMAS-NMR spectra.*

	Experiments															
	C-S-H initial		**C-S-H_25-13**		**C-S-H_25-18**		**C-S-H_25-6**		**C-S-H_25-8**		**C-S-H-20**		**C-S-H-21**		**C-S-H-22**		**C-S-H-23**	
			t 1755 h		**t 1617 h**		**t 1755 h**		**t 1756 h**		**t 4534 h**		**t 5754 h**		**t 5754 h**		**t 4534 h**	
			aq Ca/Si =1.06		aq Ca/Si =50.63		aq Ca/Si =1.28		aq Ca/Si =1.80		aq Ca/Si =0.82		aq Ca/Si =2.84		aq Ca/Si =1.32		aq Ca/Si =0.88	
Q^n	Peaks (ppm)	%	Peaks (ppm)	%	Peaks (ppm)	%	Peaks (ppm)	%	Peaks (ppm)	%	Peaks (ppm)	%	Peaks (ppm)	%	Peaks (ppm)	%	Peaks (ppm)	%
Q^{1p}	-	-	-	-	-	-	-76.42	3.36	-76.21	1.97	-	0	-	0	-	0	-	0
Q^1	-78.88	**58.66**	-79.53	5.87	-78.98	**48.64**	-79.39	13.48	-79.42	13.73	-79.7	0.96	-79.25	14.29	-79.59	5.48	-79.61	2.27
Q^{2p}	-80.96	2.94	-82.49	11.06	-81.91	2.66	-83.02	**22.51**	-83.08	**22.56**	-82.84	0.36	-82.18	8.59	-82.21	6.29	-82.34	2.09
Q^{2i}	-83.92	7.91	-84.01	1.29	-83.95	12.72	-84.38	0.87	-84.42	0.43	-84.2	0.48	-83.95	15.82	-83.75	7.37	-83.66	1.47
Q^2	-85.26	**28.88**	-85.8	**43.46**	-85.21	**34.85**	-85.52	**48.67**	-85.48	**51.52**	-85.84	**16.33**	-85.47	**48.83**	-85.61	**43.15**	-85.76	**22.5**
Q^{2v}	-	0	-87.32	1.77	-	0	-86.95	0.49	-86.83	1.73	-87	1.24	-	0	-87.22	0.93	-86.98	0.86
Q^3 defect	-	0	-89.96	4.86	-	0	-90.66	3.2	-90.85	1.76	-91.5	13.07	-91.4	6.53	-90.93	12.39	-91.37	10.61
Q^3 gel	-	0	-94.7	**17.56**	-	0	-93.52	5.6	-93.23	4.73	-100.7	**27.25**	-93.81	5.42	-97.55	**17.41**	-99.83	**26.3**
Q^4 gel	-	0	-109	6.07	-	0	-	0	-	0	-111.1	**38.67**	-	0	-110.2	5.97	-110.6	**33.39**
Q^4 $SiO_{2(quartz)}$	-107.2	1.61	-107.3	8.06	-107.3	1.13	-107.2	1.82	-107.3	1.59	-107.3	1.64	-107.1	0.52	-107.1	1.03	-107.2	0.52
MCL		3.35		-		-		-		-		-		-		-		-
ΣQ^2		39.73		57.58		50.23		72.54		76.24		18.41		73.24		57.74		26.92
$\Sigma Q^2/Q_{total}$		0.40		0.63		0.51		0.74		0.77		0.19		0.74		0.58		0.27
Q^2/Q^1		0.68		9.81		1.03		4.31		4.86		19.18		5.13		10.54		11.86
Q^3/Q^2		-		0.43		-		0.55		0.51		0.927		0.63		0.62		0.66
$Q^1/\Sigma Q^n$ n=1 and 4		0.60		0.06		0.49		0.17		0.16		0.01		0.14		0.06		0.02
<SL>		3.35		3.15		4.07		5.33		6.24		2.12		4.92		2.96		2.21

<SL> (average segment length) is a generalization of the average chain length to the case containing also planar and three-dimensional structures (including also atoms with Q^3 and Q^4 type connectivities).

"aq" denotes aqueous; "t" denotes duration

Bold (integral relative intensity) indicates high signal.

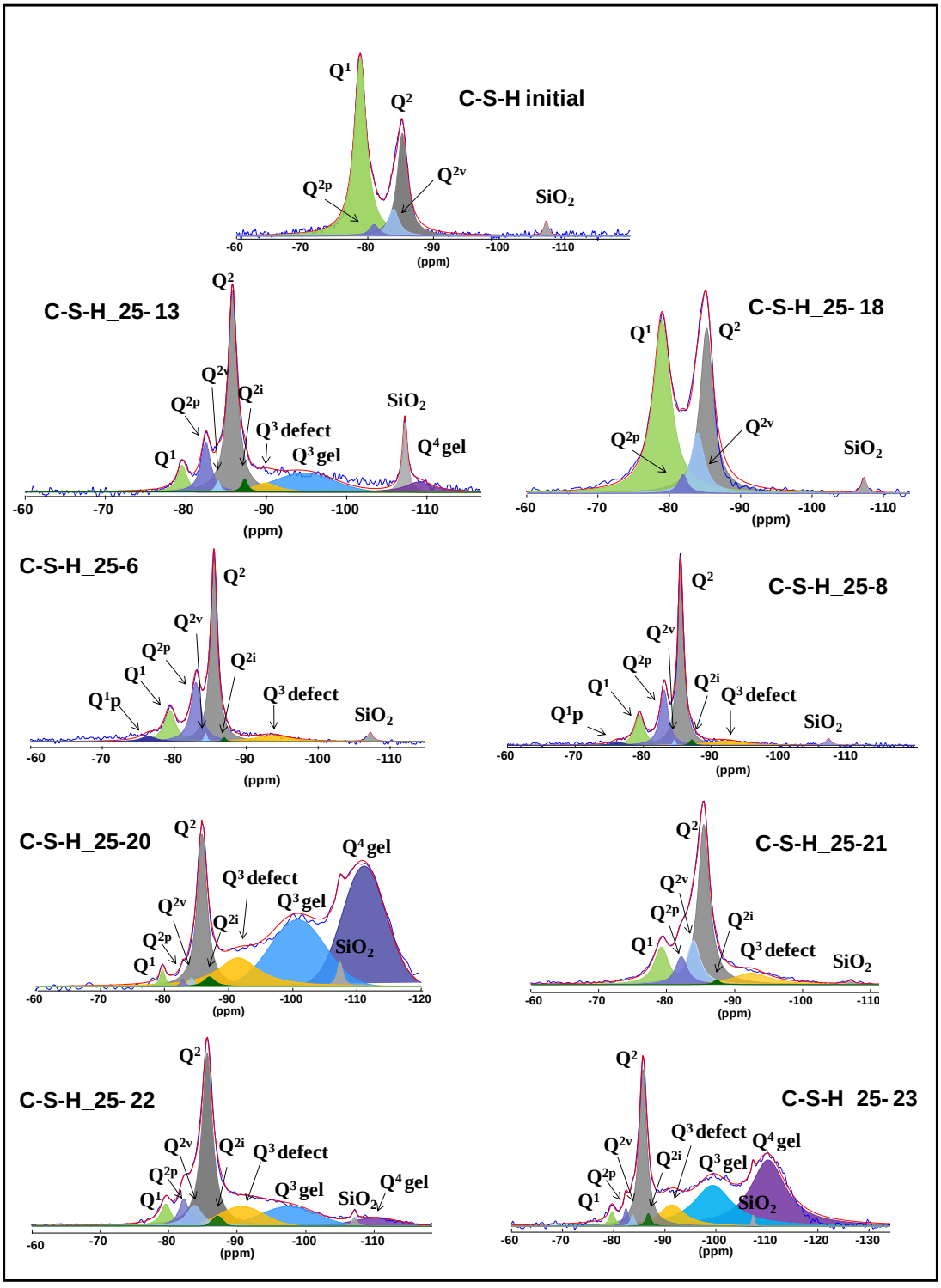

Figure 2.20. *Deconvolution of the ^{29}Si MAS-NMR spectra of the unreacted (initial) C-S-H sample and some reacted C-S-H samples (see experimental conditions in Table 2.4).*

2.4. Conclusions

To fully understand the process of cement degradation it is essential to understand the dissolution kinetics of C-S-H gel, which constitutes at least 60 % of fully hydrated Portland cement paste. In this study, the kinetics of the C-S-H gel dissolution has been studied at room temperature, conducting twenty-four flow-through experiments with variation of the flow rate and the C-S-H gel mass. Milli-Q water circulated through the C-S-H gel powdered samples (grain size between 5 and 100 μm). Therefore, no solutes, other than H^+, OH^-, Ca and Si, the two latter released by the gel, intervened in the reaction.

The presence of portlandite in the initial C-S-H gel sample after C_3S hydration affected C-S-H gel dissolution during the experimental runs. The evolution of pH, Ca and Si concentrations showed three distinct stages during the experiments. In the first stage, Ca concentration was much larger than Si, indicating preferential dissolution of portlandite and slow close-to-equilibrium dissolution of C-S-H. The initial Ca/Si ratio in solution was much larger than in the solid and the pH was around 12. In the second stage, as the portlandite content diminished, a gradual decrease in Ca and increase in Si was observed, indicating an increase in C-S-H gel dissolution. The aqueous Ca/Si ratio decreased to values below 10 and the ratio also decreased in the solid. pH decreased to values about 11.5 - 11. In the last stage, concentrations of Ca and Si and pH (≈ 11) reached steady state. At this stage the Ca/Si ratio in the solid and in the aqueous phase tended to a constant value of about 0.9 indicating that (i) the C-S-H gel was the main dissolving phase and (ii) the dissolution reaction evolved to the congruent dissolution of a phase with tobermorite stoichiometry (Ca/Si ratio = 0.83), which is consistent with current C-S-H solubility models (e.g. Kulik and Kersten, 2001).

In the experiments where steady state was attained and congruent dissolution occurred, the dissolution rate of the C-S-H gel phase with tobermorite stoichiometry (namely C-S-H_0.83 with Ca/Si ratio = 0.83) was calculated based on the Si release and at different solution saturation states. The dissolution rate of C-S-H_0.83 slows down as equilibrium is approached. Based on these results, a rate law accounting for the saturation effect on the C-S-H_0.83 dissolution rate (i.e., a rate-ΔG dependency), was obtained and is expressed as

$$Rate_{C-S-H\_0.83}(mol\ \ m^{-2}s^{-1}) = -2.6 \pm 0.7\ \mathrm{x}10^{-11} \cdot (1-\Omega)$$

where Ω is the saturation degree (ionic activity product divided by equilibrium constant). The form of this expression indicates that the simplest TST-derived rate law

suitably accounts for the C-S-H_0.83 dissolution kinetics. In accordance to these results, the experimental variation of the output concentrations with time were modeled with the CrunchFlow reactive transport code, assuming a dissolution rate law of the form $R = -A \cdot k \cdot (1-\Omega)$, where R is rate (mol m^{-3} s^{-1}), A is surface area (m^2 m^{-3}), and k is the rate constant (mol m^{-2} s^{-1}). The surface area of portlandite was calculated to reproduce the high initial Ca concentration, and the surface area of the C-S-H gel was based on the initial specific surface area. Results were consistent with rate constants of about 10^{-8} mol m^{-2} s^{-1} for the C-S-H with jennite stoichiometry (Ca/Si ratio = 1.67) to 10^{-11} mol m^{-2} s^{-1} for the C-S-H with tobermorite stoichiometry (Ca/Si ratio = 0.83), when normalizing to BET specific surface area. No pH effect is included in the rate law. Therefore, it is only applicable to the pH conditions of the study (pH 11 – 12.5), which is relevant in cement media. It is possible that the variability in the rate constants reflects (at least partially) at pH dependency.

Although an apparent change in morphology was not observed after dissolution, the specific surface area increased from about 12 to 14-142 m^2 g^{-1}. SEM-EDX and EPMA multipoint analyses showed that the solid Ca/Si ratio of the initial C-S-H particles was approximately 1.7 ± 0.1. Ca/Si ratio of 2.2 ± 0.2 corresponded to C-S-H gel particles with precipitated portlandite. Ca/Si ratios larger than 6 were an evidence of the presence of portlandite. The solid Ca/Si ratio of the C-S-H particles decreased to values about 0.9 ± 0.1 as dissolution progressed. The obtained Ca/Si ratios from the multipoint analyses indicate some compositional variability over the analyzed particles, suggesting the existence of compositional domains with variable Ca/Si ratio.

^{29}Si MAS NMR spectra showed that the reacted C-S-H structure evolves to longer chain length (high Q^2/Q^1 ratio and low $Q^1/\Sigma Q^n$ ratio) with the appearance of cross-linked chains (Q^3 defect peak). Also, Si-rich domains (high intensity of Q^3 and Q^4 signals) were identified in samples reacted under a slow flow regime. These domains are probably associated to the formation of leached diffusion layers over the course of the incongruent dissolution, although precipitation cannot completely be discarded.

The implementation of the proposed rate law for C-S-H gel dissolution in reactive transport codes could result in a substantial gain of reliability of the predictions of cement/concrete durability when advective flow through cementitious materials is expected (reaction control of the dissolution).

References

Adenot, F., Buil, M. (1992). Modelling of the corrosion of the cement paste by dionized water. *Cement and Concrete Research*, 22(2), 489-496.

Allen, A.J., Thomas, J.F., and Jennings, H.M. (2007). Composition and density of nanoscale calcium–silicate–hydrate in cement. *Nature Materials*. 6(4), 311-316.

Allison, J. D., Brown, D. S., and Kevin, J. (1991). MINTEQA2/PRODEFA2, a geochemical assessment model for environmental systems: Version 3.0 user's manual (p. 117). Athens, Georgia, USA: Environmental Research Laboratory, Office of Research and Development, US Environmental Protection Agency.

Atkinson, A., Hearne, J. A. and Knights, C. F. (1989). Aqueous chemistry and thermodynamic modelling of CaO-SiO_2-H_2O gels. *Journal of the Chemical Society, Dalton Transactions*, 12, 2371-2379.

Barrante J. R. (1974). Applied Mathematics for Physical Chemistry. Prentice-Hall. Englewood Cliffs, New Jersey.

Beaudoin, J. J., Raki, L., and Alizadeh, R. (2009). A ^{29}Si MAS-NMR study of modified C–S–H nanostructures. *Cement and Concrete Composites*, 31(8), 585-590.

Berner, U. R. (1992). Evolution of pore water chemistry during degradation of cement in a radioactive waste repository environment. *Waste Management* 12(2), 201-219.

Berner, U. R. (1990). A Thermodynamic Description of the Evolution of Pore Water Chemistry and Uranium Speciation during the Degradation of Cement. PSI-Bericht Nr. 62.

Berner, U. R. (1988). Modelling the incongruent dissolution of hydrated cement minerals. *Radiochimica Acta*, 44(45), 387-393.

Börjesson, S., Emrén, A., and Ekberg, C. (1997). A thermodynamic model for the calcium silicate hydrate gel, modelled as a non-ideal binary solid solution. *Cement and Concrete Research*, 27(11), 1649-1657.

Brunauer, S., Emmett, P. H., and Teller, E. (1938). Adsorption of gases in multimolecular layers. *Journal of the American Chemical Society*, 60(2), 309-319.

Bullard, J. W., and Flatt, R. J. (2010). New insights into the effect of calcium hydroxide precipitation on the kinetics of tricalcium silicate hydration. *Journal of the American Ceramic Society*, 93(7), 1894-1903.

Cama, J., Zhang, L., Soler, J. M., Giudici, G. D., Arvidson, R. S., and Lüttge, A. (2010). Fluorite dissolution at acidic pH: In situ AFM and ex situ VSI experiments and Monte Carlo simulations. *Geochimica et Cosmochimica Acta*, 74(15), 4298-4311.

Carey, J. W., and Lichtner, P. C. (2007). Calcium Silicate Hydrate (C-S-H) Solid Solution Model Applied to Cement Degradation using the Continuum Reactive Transport Model FLOTRAN. *In:Mobasher B. and Skalny J., Eds., Transport Properties and Concrete Quality:Materials Science of Concrete, Special Volume,pp.73-106.American Ceramic Society*.

Carey, J. W., and Lichtner, P. C. (2006). Calcium Silicate Hydrate Solid Solution Model Applied to Cement Degradation using the Continuum Reactive Transport Model FLOTRAN. *Report LA-UR-06-0636*.

Chen, J. J., Thomas, J. J., Taylor, H. F., and Jennings, H. M. (2004). Solubility and structure of calcium silicate hydrate. *Cement and Concrete Research*, 34(9), 1499-1519.

Cong, X., and Kirkpatrick, R. J. (1996). ^{29}Si MAS-NMR Study of the Structure of Calcium Silicate Hydrate. *Advanced Cement Based Materials*, 3(3), 144-156.

Fernández-Jiménez, A., Puertas, F., Sobrados, I., and Sanz, J. (2003). Structure of Calcium Silicate Hydrates Formed in Alkaline-Activated Slag: Influence of the Type of Alkaline Activator. *Journal of the American Ceramic Society*, 86(8), 1389-1394.

Fernández, L., Alonso, C., Andrade, C., and Hidalgo, A. (2008). The interaction of magnesium in hydration of C_3S and CSH formation using ^{29}Si MAS-NMR. *Journal of Materials Science*, 43(17), 5772-5783.

Gaitero, J. J., Campillo, I. and Guerrero, A. (2008). Reduction of the calcium leaching rate of cement paste by addition of silica nanoparticles. *Cement and Concrete Research*, 38(8), 1112-1118.

Galan, I., Glasser, F., Andrade, C., and Baza, D. (2011). Dissolution of portlandite. In 13th International Congress on the Chemistry of Cement, Number II (pp. 1-7).

Gartner, E. M., and Jennings, H. M. (1987). Thermodynamics of calcium silicate hydrates and their solutions. *Journal of the American Ceramic Society*, 70(10), 743-749.

Greenberg, S. A., and Chang, T. N. (1965). Investigation of the Colloidal Hydrated Calcium Silicates. II. Solubility Relationships in the Calcium Oxide-Silica-Water System at 25°C. *The Journal of Physical Chemistry*, 64 (9), 1151–1157.

Grutzeck, M. W. (1999). A new model for the formation of calcium silicate hydrate (CSH). *Material Research Innovate*, 3(3), 160-170.

Haga, K., Shibata, M., Hironaga, M., Tanaka, S. and Nagasaki, S. (2002). Silicate Anion Structural Change in Calcium Silicate Hydrate Gel on Dissolution of Hydrated Cement. *Journal of Nuclear Science and Technology*, 39 (5), 540-547.

Harris, A. W., Manning, M. C., Tearle, W. M., and Tweed, C. J. (2002). Testing of models of the dissolution of cements—leaching of synthetic CSH gels. *Cement and Concrete Research*, 32(5), 731-746.

Houston, J., Maxwell, R. S., and Carroll, S. A. (2009). Transformation of meta-stable calcium silicate hydrates to tobermorite: reaction kinetics and molecular structure from XRD and NMR spectroscopy. *Geochemical transactions*, 10(1), 1.

Jennings, H. M. (1986). Aqueous solubility relationships for two types of calcium silicate hydrate. *Journal of the American Ceramic Society*, 69(8), 614-618.

Kersten, M. (1996). Aqueous solubility diagrams for cementitious waste stabilization systems. 1. The C-S-H solid-solution system. *Environmental Science and Technology*, 30(7), 2286-2293.

Klur, I., Pollet, B., Virlet, J., and Nonat, A. (1998). CSH structure evolution with calcium content by multinuclear NMR. In Nuclear magnetic resonance spectroscopy of cement-based materials (pp. 119-141). Springer Berlin Heidelberg.

Kulik, D. A. (2011). Improving the structural consistency of CSH solid solution thermodynamic models. *Cement and Concrete Research*, 41(5), 477-495.

Kulik, D. A., and Kersten, M. (2001). Aqueous Solubility Diagrams for Cementitious Waste Stabilization Systems: II, End-Member Stoichiometries of Ideal Calcium Silicate Hydrate Solid Solutions. *Journal of the American Ceramic Society*, 84(12), 3017-3026.

Lasaga, A. C. (1998). Kinetic Theory in the Earth Sciences. Princeton University Press, Princeton.

Lothenbach, B., Matschei, T., Möschner, G., Glasser, F. (2008). Thermodynamic modelling of the effect of temperature on the hydration and porosity of Portland cement. *Cement and Concrete Research*, 38(1), 1-18.

Massiot, D. F. Fayon, M. Capron, I. King, S. Le Calvé, B. Alonso, J.-P. Durand, B. Bujoli, Z. Gan and G. Hoatson. (2002). Modelling one- and two- dimensional solid-state NMR spectra. *Magnetic Resonance in Chemistry*, 40(1), 70-6.

Matschei, T., Lothenbach, B., and Glasser, F. P. (2007). Thermodynamic properties of Portland cement hydrates in the system CaO-Al_2O_3-SiO_2-$CaSO_4$-$CaCO_3$-H_2O. *Cement and Concrete Research*, 37(10), 1379-1410.

Metz, V., and Ganor, J. (2001). Stirring effect on kaolinite dissolution rate. *Geochimica et Cosmochimica Acta*, 65(20), 3475-3490.

Myers, R. J., Bernal, S. A., San Nicolas, R., and Provis, J. L. (2013). Generalized Structural Description of Calcium–Sodium Aluminosilicate Hydrate Gels: The Cross-Linked Substituted Tobermorite Model. *Langmuir*, 29(17), 5294-5306.

Odler, I. (2003). The BET-specific surface area of hydrated Portland cement and related materials. *Cement and Concrete Research*, 33(12), 2049-2056.

Parkhurst, D. L., and Appelo, C. A. J. (1999). User's guide to PHREEQC (Version 2): A computer program for speciation, batch-reaction, one-dimensional transport, and inverse geochemical calculations.

Rahman, M. M., Nagasaki, S., and Tanaka, S. (1999). A model for dissolution of CaO-SiO_2-H_2O gel at Ca/Si > 1. *Cement and Concrete Research*, 29(7), 1091-1097.

Reardon, E. J. (1992). Problems and approaches to the prediction of the chemical composition in cement/water systems. *Waste Management*, 12(2), 221-239.

Reardon, E. J. (1990). An ion interaction model for the determination of chemical equilibria in cement/water systems. *Cement and Concrete Research*, 20(2), 175-192.

Revertegat, E., Richet C., and Gégout, P. (1992). Effect of pH on the durability of cement pastes. *Cement and Concrete Research*, 22(2), 259-272.

Richardson, I. G. (2004). Tobermorite/jennite-and tobermorite/calcium hydroxide-based models for the structure of CSH: applicability to hardened pastes of tricalcium silicate, β-dicalcium silicate, Portland cement, and blends of Portland cement with blast-furnace slag, metakaolin, or silica fume. *Cement and Concrete Research*, 34(9), 1733-1777.

Richardson, I. G. (1999). The nature of C-S-H in hardened cements. *Cement and Concrete Research*, 29(8), 1131-1147.

Richardson, I. G., and Groves, G. W. (1992). Models for the composition and structure of calcium silicate hydrate (C-S-H) gel in hardened cement pastes. *Cement and Concrete Research*, 22(6), 1001-1010.

Steefel, C.I. (2009). CrunchFlow. Software for Modeling Mul- ticomponent Reactive Flow and Transport. User's Manual. Earth Sciences Division, Berkeley (USA), Lawrence Berke- ley National Laboratory, 90pp.

Sugiyama, D. (2008). Chemical alteration of calcium silicate hydrate (C-S-H) in sodium chloride solution. *Cement and Concrete Research*, 38(11), 1270-1275.

Sugiyama, D., and Fujita, T. (2006). A thermodynamic model of dissolution and precipitation of calcium silicate hydrates. *Cement and Concrete Research*, 36(2), 227-237.

Taylor, H. F. W. (1997). Cement Chemistry. (2nd Edition) Thomas Telford Ltd, London.

Taylor, H. F.W. (1986). Proposed structure of calcium silicate hydrate gel. *Journal of the American Ceramic Society*, 69(6), 464-467.

Taylor, H. F. W., and Newbury, D. E. (1984). An electron microprobe study of a mature cement paste. *Cement and Concrete Research*, 14(4), 565-573.

Walker, C., Savage, D., Tyrer, M., Ragnasdottir, K.V. (2007). Non-ideal solid solution aqueous solution modeling of synthetic calcium silicate hydrates. *Cement and Concrete Research*, 37(4), 502-511.

Wolery, T. J., Jackson, K. J., Bourcier, W. L., Bruton, C. J., Viani, B. E., Knauss, K. G., and Delany, J. M. (1990). Current status of the EQ3/6 software package for geochemical modeling. Chemical modeling of aqueous systems II, 416, 104-116.

Young, R. A. (1995). The Rietveld Method, International Union of Crystallography Monographs on Crystallography 5. IUCr/Oxford University Press, Oxford.

CHAPTER 3

SANS characterization of the C-S-H gel dissolution

3.1 Introduction

SANS is particularly useful for investigating porous structures like C-S-H gel, given that the amorphous nature of C-S-H renders diffraction ineffective. In addition, specimens can be studied in their natural saturated state, thus avoiding complications associated with drying the C-S-H gel (Allen and Thomas, 2007). SANS data are effective in probing features in the 10 Å to 1000 Å (1 nm to 100 nm) size range (short-ranged crystalline order) that defines critical aspects of the solid C-S-H structure within the gel (Thomas et al., 2004), providing quantitative information about microstructural features (e.g., particle size, shape, surface area and fractal properties). SANS covers the range of scattering q values from 0.002 $Å^{-1}$ to 0.2 $Å^{-1}$, where $q = (4\pi/\lambda)\sin(\theta)$, λ is the neutron wavelength and 2θ is the scattering angle. SANS data permit determination of the fractal exponent and fractal morphology of the C-S-H gel over a large scale range, and this can be quantified through application of a fractal microstructure model (Winslow

1985; Allen et al., 1998; Jennings 2000; Allen and Thomas; 2007Allen et al., 2007; Thomas et al., 2012).

In this study powdered C-S-H gel samples were dissolved for up to 74 days in Milli-Q water (18.2 MΩ·cm at 25 ºC) using flow-through reactors, under a CO_2-free atmosphere at room temperature (23 °C ± 2 ºC). The evolution of C-S-H gel dissolution with time was monitored by the solution chemistry variation, which allows understanding the kinetics of dissolution of the C-S-H gel (Chapter 2). In parallel, the reacted C-S-H gel samples were characterized using the ^{29}Si MAS-NMR and SANS techniques to evaluate the changes in the dissolving solid C-S-H nanostructure (particle size, shape, surface area and fractal exponents). The SANS contrast matchpoint of the starting solid C-S-H was obtained from the measured change in the scattering contrast as a function of D_2O content. The content of both solid C-S-H and fine CH crystals in the initial composition of C-S-H gel was evaluated. This combined approach allowed investigation of the changes in structure of the C-S-H gel related to changes in solution composition with time. The advantage of this kinetic approach is that it yields a full understanding of the overall C-S-H gel dissolution reaction, and contributes to the assessment of cement durability.

3.2 Experimental methodology

The scheme depicted in Figure 3.1 summarizes the experimental tasks.

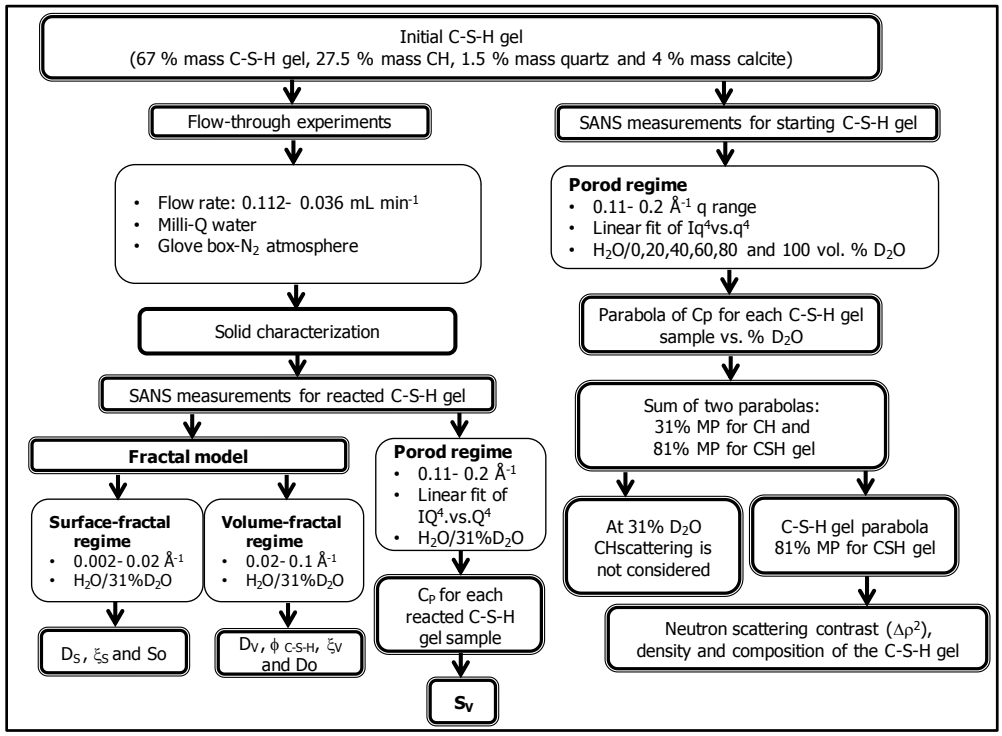

Figure 3.1. *Scheme that summarizes the experimental tasks performed in SANS characterization of C-S-H gel dissolution.*

3.2.1 Sample characterization

The C-S-H gel used to perform the flow-through experiments and SANS measurements is described in Chapter 2. The initial specific surface area of the C-S-H gel was measured using the 5-point BET (N_2) method. The BET surface area was 11.7 $m^2\ g^{-1}$.

3.2.2 Dissolution experiments

Powder samples of the starting hydrated paste with mass between 1.5 g and 3.0 g and powder particle size ≈ 10 μm were placed in the flow-through reactors under CO_2-free atmospheric conditions and room temperature (23 ± 2 °C; Table 3.1). See details of the setup in Chapter 2. Note that experiments C-S-H-4, C-S-H-6, C-S-H-7 and C-S-H-8 are the same experiments as C-S-H-25-10, C-S-H-25-9, C-S-H-25-18 and C-S-H-25-8 described in Chapter 2. These masses were sufficient to allow us to retrieve enough reacted sample to perform BET, ^{29}Si MAS-NMR, XRD and SANS measurements. Milli-Q water (18 MΩ·cm at 25 °C) reacted with the starting C-S-H gel, while being supplied at a constant flow rate over the course of the experiment. The flow rates were increased from 0.040 mL min^{-1} to 0.126 mL min^{-1} shortening

residence times from ≈ 16 h to 5 h. The output solutions were periodically collected. The evolution of the dissolution reaction with time was monitored by measuring the output solution pH and the output aqueous concentrations of Ca and Si, which were released from the dissolution of the C-S-H and portlandite. Variation of Ca/Si ratio with time was determined from the periodical variation in the Ca and Si output concentrations (Chapter 2). Experiments with different masses and flow rates were repeated with different time durations (from 16 d to 74 d) to evaluate changes in the solid composition with time. Therefore, steady-state conditions were not always reached. As explained in Chapter 2, based on a simple mass balance equation, the dissolution rate (mol m^{-2} s^{-1}), R, in a flow-through experiment is obtained from Eq. (2.1). Likewise, the dissolution rate in the experiments where the composition of the output solution reaches steady state is calculated from Eq. (2.2). In the experiments where the composition of the output solutions did not reach a constant value, the dissolution rate was calculated from the last output concentration. Dissolution rates (R_i) were only calculated based on the Si output concentrations and normalized to both the final mass (R_{Si} expressed in mol g^{-1} s^{-1}) and the final surface area (R_{Si} expressed in mol m^{-2} s^{-1}). The uncertainty associated with the calculated dissolution rates was estimated using the Gaussian uncertainty propagation method (Barrante, 1974) to be 15% (standard deviation).

Table. 3.1 *Experimental conditions for the flow-through experiments.*

Experiment	Time	Flow rate	Mass	
			(C-S-H gel + CH)	C-S-H gel
	(day)	(mL min^{-1})	(g)	
C-S-H-1	16	0.126	3.0000	2.0100
C-S-H-2	16	0.046	1.5000	1.0050
C-S-H-3	16	0.054	3.0000	2.0100
C-S-H-4	17	0.041	2.9013	1.9497
C-S-H-5	31	0.042	1.5039	1.0076
C-S-H-6	44	0.054	2.9934	2.0116
C-S-H-7	67	0.097	2.9980	2.0147
C-S-H-8	74	0.041	2.9951	2.0127

Experiments are ordered according to their duration.
C-S-H gel mass is 67 % of that of C-S-H+CH mass.
C-S-H-4, C-S-H-6, C-S-H-7 and C-S-H-8 experiments are the same as C-S-H-25-10, C-S-H-25-9, C-S-H-25-18 and C-S-H-25-8 from Chapter 2, respectively.

The powder samples from these experiments were retrieved after the dissolution reaction times specified in Table 3.1, and the measured final BET surface areas ranged from 14.5 m^2 g^{-1} to 63.3 m^2 g^{-1}, which represent an increase in the reactive surface area by a factor of between 1.5 and 6 relative to the initial BET surface area (Table 3.2). Initial and retrieved powders were dried with isopropanol under a CO_2-free atmosphere and examined by SEM in order to identify

the major residual phases (C-S-H and CH) and characterize their morphology, and by XRD and Rietveld Analysis to quantify their content. ^{29}Si MAS-NMR and SANS analyses were performed to determine the structural variation and examine the evolution of the surface area and morphology of the C-S-H gel within the powdered paste sample.

Table. 3.2 *Experimental results of the flow-through experiments.*

Experiment	Time	pH out	Ca out	Si out	aqueous Ca/Si	BET	Dissolution rate		Log R_{Si}
							R_{Si}		
	(day)		(μM)			(m^2 g^{-1})	(mol g^{-1} s^{-1})	(mol m^{-2} s^{-1})	
C-S-H-1	16	10.96	735.6	12.93	56.88	14.5	1.36E-11	9.35E-13	-12.0
C-S-H-2	16	11.29	1824.9	4.05	450.56	52.7	3.11E-12	5.91E-14	-13.2
C-S-H-3	16	11.52	1748.04	4.26	409.88	18.6	1.89E-12	1.02E-13	-13.0
C-S-H-4	17	11.48	325.81	5.62	57.97	25.0	2.00E-12	7.90E-14	-13.1
C-S-H-5	31	11.09	1290.31	229.6	5.62	46.1	1.63E-10	3.54E-12	-11.5
C-S-H-6	44	10.74	375.55	6.09	61.62	63.3	2.77E-12	4.40E-14	-13.4
C-S-H-7	67	10.68	636.37	12.69	50.63	15.9	1.07E-11	7.10E-13	-12.1
C-S-H-8	74	10.21	694.91	388.89	1.80	61.7	1.40E-10	2.30E-12	-11.6

Aqueous Ca/Si ratio is computed from the Ca and Si output concentration (Ca out and Si out).

BET represents the measured specific surface area after the experiments (associated uncertainty is approximately 10 % (1σ).

Dissolution rate is calculated according to Eqs. (2.1) and (2.2). LogR_{Si} is calculated from dissolution rate expressed in mol m^{-2} s^{-1}.

3.2.3 ^{29}Si MAS-NMR

The ^{29}Si MAS-NMR spectra of approximately 2 mg of unreacted and reacted powder samples that underwent different degrees of dissolution were recorded on a Bruker Avance 400 NMR spectrometer (field strength of 9.4 T, Bruker Biospin AG, Fällanden, Switzerland) following the procedure described in Chapter 2.

3.2.4 SANS

The SANS experiments were performed on powder samples of unreacted (starting) and reacted C-S-H gel, taken from the flow-through experiments at room temperature in a CO_2-free atmosphere using the NG7 30-m SANS Instrument (Barker et al., 2005) at the NIST Center for Neutron Research (NCNR), Gaithersburg, Maryland, USA. The SANS neutron wavelength, λ, was 8.09 Å and using three different configurations of the instrument, the overall measured q range extended from 0.001 $Å^{-1}$ to 0.22 $Å^{-1}$ (0.01 nm^{-1} to 2.2 nm^{-1}). This q range is sufficient to characterize morphological features of particles with a size ranging from ≈ 10 Å to ≈ 1000 Å. Scattered neutron intensities were recorded on a two-dimensional detector. These data were corrected for the background and empty-cell scattering and calibrated against a standard

attenuator. The 2D SANS data set was reduced to 1D by circular averaging to obtain the scattered intensity or scattering cross-section ($d\Sigma/d\Omega$) as a function of the magnitude of the scattering vector q (Bumrongjaroen et al., 2009). At small scattering angles (small q values) the largest features are probed, whereas the smaller features are probed at higher q values. Owing to a decrease in SANS intensity with increasing q, the q upper limit to obtain scattering data from hydrated cement is just over 0.2 $Å^{-1}$ (Thomas et al., 2010; Fig. 3.2).

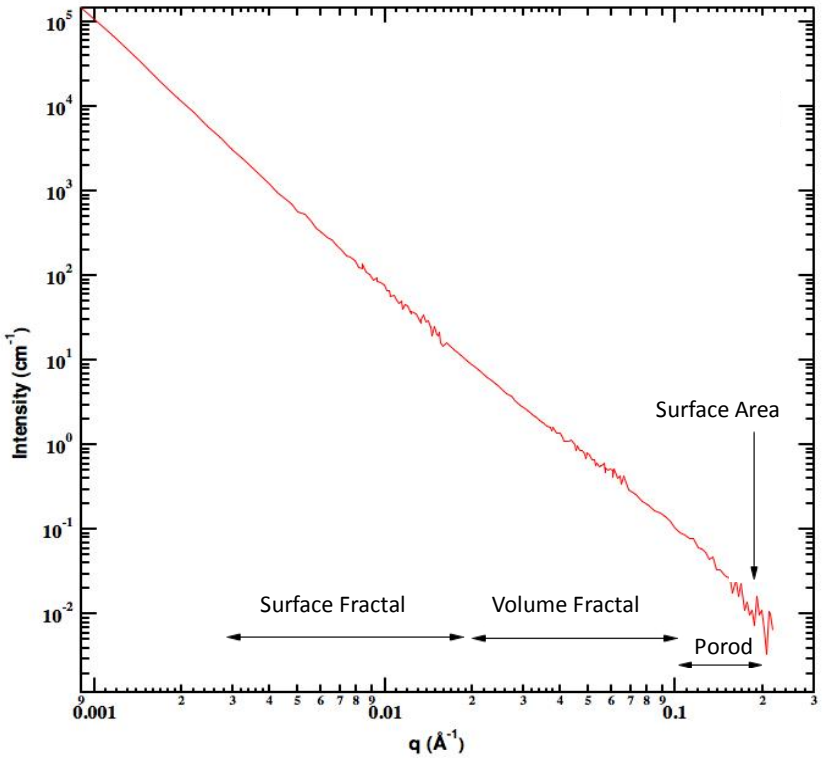

Figure 3.2. *Experimental SANS I(q) data versus q for the starting cement paste sample (prior to dissolution) of this study. As the scattering vector (or angle) increases, scattering occurs from smaller features in the microstructure. Data plotted as a line with erratic oscillations associated with the statistical uncertainties at each point.*

To fit the scattered intensity data, I(q), a fractal microstructure model of Allen et al. (2007) was applied over the SANS q range where $q > 0.0035$ $Å^{-1}$. Below this q other non-fractal components dominate the scattering like micrometer-scale $Ca(OH)_2$ (Allen et al., 2007). As given in Appendix II, the full expression of the model is:

$$(q) = \emptyset_{C-S-H} V_P \Delta\rho^2 \left\{ \frac{\eta R_C^3}{\beta R_0^3} \left(\frac{\xi_V}{R_C}\right)^{DV} \times \frac{sin[(D_V - 1)arctan(q\xi_V)]}{(D_V - 1)q\xi_V[1 + (q\xi_V)^2]^{\frac{(D_V-1)}{2}}} + (1-\eta)^2 \right\} F^2(q)$$
$$+ \frac{\pi \xi_S^4 \Delta\rho^2 S_0 \Gamma(5 - D_S) sin[(3 - D_S)arctan(q\xi_S)]}{[1 + (q\xi_S)^2]^{\frac{(5-D_S)}{2}} q\xi_S} + BGD$$

Eq. 3.1

where the various fit parameters are summarized in Table 3.3.

Table. 3.3 *Parameters definitions (Eq. 3.1) for the fractal microstructure model (Allen and Thomas, 2007). For full explanation see Table 1.3.*

Parameters	
$\phi_{C\text{-}S\text{-}H}$	Volume fraction of solid C-S-H gel globules within the entire specimen volume penetrated by the neutron beam. It is essentially a measure of the amount of LD C-S-H (without gel pores) in the paste.
V_P	Volume of a single C-S-H globules. ($Vp= 4\pi\beta R_0^3/3$) where β is the particle aspect ratio.
R_C	Correlation-hole radius (minimum center-to-center distance between particles.
R_O	The radius of the building block C-S-H gel globules.
η	Local packing fraction for nearest neighbor C-S-H gel globules.
D_V	Volume fractal scaling exponent.
D_S	Surface fractal scaling exponent.
ξ_V	Upper-limit length scales (correlation lengths) over which volume fractal scaling apply.
ξ_S	Upper-limit length scales (correlation lengths) over which surface fractal scaling apply.
S_O	Smooth geometric surface area on which the surface fractal microstructure is deposited.
$\Gamma(x)$	Mathematical Gamma function.
$F^2(q)$	Single-particle form factor for C-S-H gel globule.
$\Delta\rho^2$	Neutron scattering contrast.
BGD	Background intensity.

Eq. (3.1) consists of three component terms: volume fractal incorporating a single globule ($F^2(q)$) term, surface fractal and flat background scattering. Allen et al. (2007) have shown that the model results confirm that the volume-fractal nature of hydrated cement is mainly attributable to the C–S–H component. This model combines the volume-fractal and the surface-fractal scattering terms. The former is attributed to random agglomeration of the outer-product C-S-H nanoparticles between grains, and the latter to deposition of the outer-product C-S-H nanoparticles at the clinker grain boundaries and on inert surfaces such as the micrometer scale CH crystallites. Also, the surface fractal may include some inner product formed topochemically (Bumrongjaroen et al., 2009), that is, at the boundary of clinker phases (C_3S and C_2S). The *Irena* program package (Ilavsky and Jemian, 2009), together with the model by Allen

et al. (2007), was used to analyze the SANS scattering data to obtain the solid C-S-H structure parameters: D_o, D_V, ϕ_{CSH}, S_O, D_S, ξ_V and ξ_S, as well as the upper-limit volume fraction (ϕ_{MAX}), the fractally rough surface area (S_{SF}), which is define as $S_{SF}= S_O \cdot((\xi_S/Rc)^{(Ds-2)})$, and the surface area of the volume-fractal morphology ($S_{VF} =S_T-S_{SF}$). Note that ϕ_{MAX} is defined as a measure of the total volume fraction occupancy of the volume-fractal phase. It is necessarily a rough estimate based on $\phi_{MAX} = \phi_{C\text{-}S\text{-}H} \cdot((\xi v/Rc)^{(3-Dv)})$ and may be an over-estimate if the volume fractal structures actually grow into each other.

A set of six SANS experiments was carried out on the initial hydrated pastes prior to the dissolution measurements in order to obtain the contrast matchpoint (MP) of the starting solid C-S-H from the measured change in the scattering contrast as a function of D_2O content. 0.25 g of initial (unreacted) C-S-H gel sample was poured in 5 mL of mixed D_2O-H_2O solutions of 0 %, 20 %, 40 %, 60 %, 80 % and 100 % D_2O (by mole) under CO_2-free atmospheric conditions in a N_2-filled glove box to avoid C-S-H carbonation. The mixtures were stirred for 12 h to ensure full exchange of H_2O and D_2O. Thomas et al. (1998a) showed that in thin cement specimens full H_2O-D_2O exchange occurred within hours, in both the pore fluid and the C-S-H. The relative scattering contrast was obtained by calculating the Porod constant (C_p) after plotting the SANS scattering data as Iq^4 versus q^4 in the Porod regime (q ranges from 0.11 to 0.2 $Å^{-1}$). The C_p values can be obtained from the unconstrained intercepts of linear fits of Iq^4 versus q^4, and the flat background scattering, *BGD*, is obtained from the slopes as (Thomas et al., 1998a):

$$Iq^4 = Cp + BGD\ q^4 \qquad \textit{Eq. 3.2}$$

The highest C_p value obtained (0 % of D_2O water) was used to normalize the derived (lower) C_P values at higher D_2O water contents (Table 3.4). In a two-phase system, such as C-S-H and water, the relative scattering contrast is a parabola in relative scattering contrast vs. % D_2O with a minimum value of zero contrast at the MP (Thomas et al., 2004). The presence of an additional phase (e.g. CH) with a different contrast MP within the gel increases the minimum value in the C-S-H/D relative scattering contrast curve and displaces it with respect to D_2O content.

A second set of SANS experiments was performed on the reacted samples to study the changes in the C-S-H gel structure due to dissolution. According to the decreasing aqueous Ca/Si ratio and decreasing pH of the output solutions (Table 3.2), for the samples retrieved after 16 to 17 days, 31 to 44 days and 67 to 74 days, the C-S-H and CH coexisted but with a decreasing content of the latter with increasing dissolution time. It is known that the CH contrast

matchpoint occurs in a H_2O/D_2O fluid mixture of 31 % D_2O (Allen et al., 2007). Therefore, in a system with H_2O/D_2O fluid, C-S-H/D and CH, to obtain the relative scattering contrast of the C-S-H/D, solid samples must be mixed in a 31 % D_2O solution. 0.25 g each of unreacted or reacted samples from 16 to 74 days, were immersed in 5 mL of solution (31% D_2O) for 24 h to allow full exchange of H_2O and D_2O. Thereafter, sufficient amounts of wet powder samples were placed into 1 mm quartz optical cells to prevent sample drying during the measurements. The wet powders were allowed to settle for 2 h before the SANS experiments.

Table. 3.4 *C_p values (obtained from the Porod scattering region) and the relative scattering contrast factor for the initial hydrated C_3S paste with pore fluid.*

% D_2O	C_p (10^{-12} Å^{-5})	Relative scattering contrast of initial C-S-H gel
0	0.69 ± 0.03	1
20	0.36 ± 0.02	0.53
40	0.18 ± 0.02	0.26
60	0.04 ± 0.01	0.06
80	0.03 ± 0.01	0.04
100	0.10 ± 0.01	0.14

Initial hydrated C_3S paste is composed of 67 % mass of C-S-H, 27.5 % mass of portandite (CH), 1.5 % mass quartz and 4 % mass calcite

3.3 Results and discussion

3.3.1 C-S-H gel dissolution

The flow-through experiments were performed with different time durations (from 16 days to 74 days) to evaluate changes in the liquid and solid composition with time. Steady-state conditions were only reached in the longest experiments (Figs. 3.3a,b,d and e). The observed decrease in output Ca concentration and decrease in output pH with time, together with the increase in Si, indicate that portlandite and C-S-H gradually dissolved. The decrease in the aqueous Ca/Si ratio indicates that the high Ca concentration at the start of the experiments was mainly due to an initial dissolution of portlandite (Figs. 3.3 c and f). As portlandite was mostly dissolved, the C-S-H gel dissolution was incongruent, showing preferential Ca release and consequent gradual decrease in the aqueous Ca/Si ratio (Table 3.2). In the longest experiments, C-S-H dissolution reached steady state, i.e., the output Ca and Si concentrations were constant with time (Figs. 3.3 d and e), and the Ca and Si output concentrations were similar within the measurement uncertainties, yielding aqueous Ca/Si ratio of 1.8 ± 0.2 (congruent dissolution)

(Figs. 3.3 c and f). The results agree with those reported by Harris et al. (2002) and Carey et al. (2006, 2007) who showed that the leaching of C-S-H gels in demineralized water could initially be described as an incongruent dissolution, tending gradually to a congruent dissolution. Overall, the observed behavior suggests that after ≈ 70 days, the reacted samples merely consisted of C-S-H powder grain particles. This fact was corroborated by XRD analyses, which showed the samples to be only composed of C-S-H, as no portlandite XRD peaks were observed, thus indicating that portlandite was mostly exhausted. Moreover, the composition of the remaining C-S-H powder grain particles showed a solid Ca/Si ratio of 1.03±0.10 (1σ), which is close to that of a tobermorite-like phase (molar Ca/Si = 0.83) (Fig. 3.3f). BET measurements showed significant variation in reactive surface area during C-S-H gel dissolution, which has implications in the quantification of the C-S-H dissolution kinetics (Chapter 2). As the Ca/Si ratio decreased to a value close to a tobermorite stoichiometric value of 0.83, the C-S-H dissolution rate, based on the Si release (R_{Si}), increased from $4.50x10^{-14}$ mol m^{-2} s^{-1} (log R_{Si} = - 13.3) to $2.30x10^{-12}$ mol m^{-2} s^{-1} (log R_{Si} = - 11.5; Table 3.2). Figure 3.4 depicts the variation of log R_{Si} as a function of the Ca/Si aqueous ratio. It is observed that as the aqueous Ca/Si ratio diminishes to around 60, the dissolution rates are the same within the estimated uncertainty of 15 %. However, the rates increased as long as the C-S-H gel was the main dissolving phase, which implies a change from the initial C-S-H composition to that of a tobermorite-like phase.

Electron Microprobe CAMECA SX-50 instrument (4 WD spectrometers + 1 EDS) (Microprobe Unit of the University of Barcelona) under a 20 kV accelerating potential and 20 nA beam current was used to acquire SEM images and determine the C-S-H gel in the unreacted and the reacted samples. Comparison of SEM images and EPMA between the unreacted and the reacted samples shows that most of the portlandite dissolved during the experiments (Fig. 3.5).

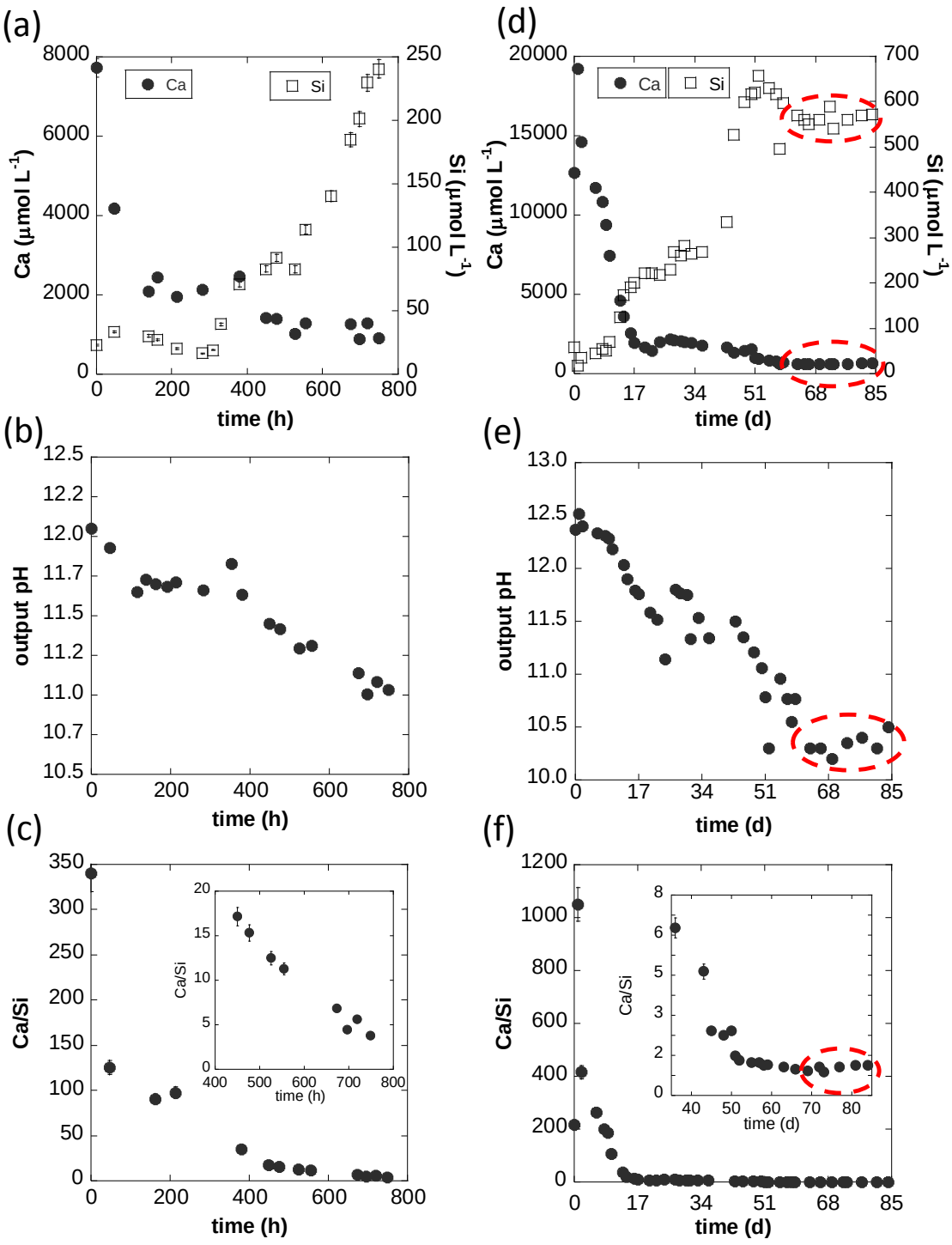

Figure 3.3. *Two representative experiments: left (experiment C-S-H-5): steady state was not approached (see text); variation of output concentration of Ca and Si (a), output pH (b) and aqueous Ca/Si ratio (c) with time. Right (experiment C-S-H-8): steady state was approached (see text); variation of output concentration of Ca and Si (d), output pH (e) and aqueous Ca/Si ratio (f) with time. Dashed red lines indicate steady state. Data scatter and vertical bars indicate statistical standard deviation uncertainties. Uncertainties associated to with measured concentrations and Ca/Si ratios are 3 % and 10 %, respectively. The insets in c) and f) show the variation of the aqueous Ca/Si ratio with time in the last 17 and 30 days, respectively.*

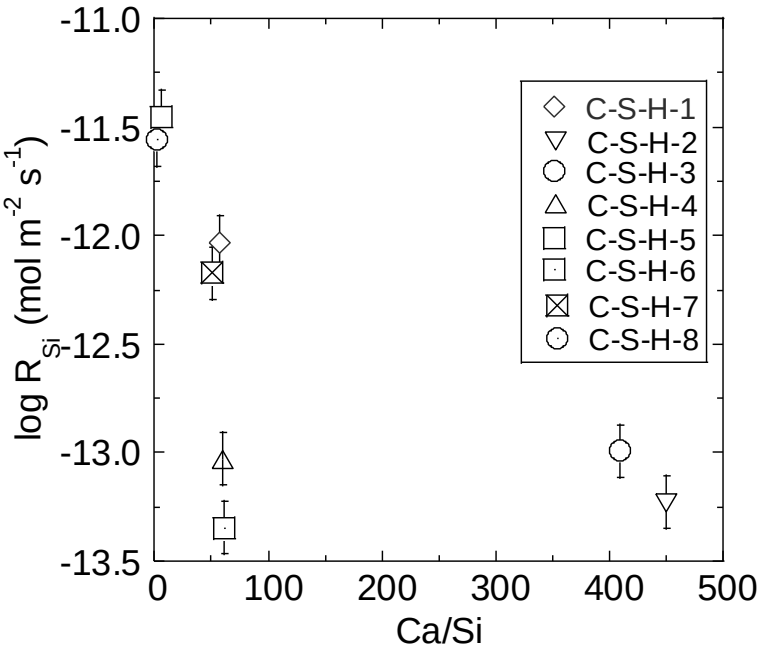

Figure 3.4. *Logarithm of the final state dissolution rates (R_{Si}) versus aqueous Ca/Si ratio (see results presented in Table 3.2). Vertical bars represent statistical standard deviation uncertainties. As the aqueous Ca/Si ratio diminishes from around 450 to around 60 (i.e., dissolution of portlandite is mainly taking place), the dissolution rates are the same within the estimated uncertainty of 15 %. And the rates increased as long as the C-S-H gel was the main dissolving phase.*

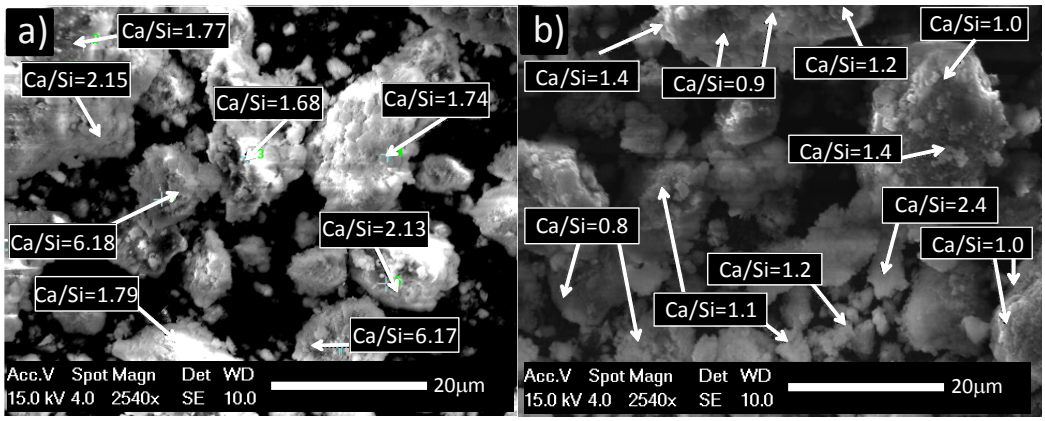

Figure 3.5. *Comparison between SEM images of unreacted and reacted samples (a) particles of C-S-H gel and $Ca(OH)_2$ in the initial (unreacted) sample (see Figure 2.7). The microprobe analysis shows that the Ca/Si ratio of the C-S-H particles is 1.74 ± 0.10; Ca/Si ratio higher than 2.5 indicates the presence of portlandite; (b) after 73 d of reaction most of the particles shown are C-S-H with a Ca/Si ratio of 1.02 ± 0.09.*

3.3.2 ^{29}Si MAS-NMR: C-S-H gel and portlandite

Q^2/Q^1 ratio indicated that the solid C-S-H polymerization increased with time (Q^1 intensity decreases and Q^2 intensity increases resulting in a Q^2/Q^1 ratio increase; Fig. 3.6). Likewise, Figure 3.7a shows that the Q^2/Q^1 ratio increased with decreasing aqueous Ca/Si ratio. Figure 3.7b shows pH and Q^2/Q^1 ratio as a function of time multiplied by flow rate and divided by sample mass. Overall, Figure 3.7b indicates that as pH decreased to a constant value (ca. 10.50), the Q^2/Q^1 ratio (C-S-H gel polymerization) tended to increase with dissolution. This is evidence that the partial dissolution of solid C-S-H leaves a residual structure that may be similar to a more ordered tobermorite structure. The attainment of similar aqueous and solid Ca/Si ratio values, respectively ($Ca/Si_{aqueous}$ = 1.80 ± 0.2 (1σ) and Ca/Si_{solid} = 1.03 ± 0.16 (1σ)), close to that of tobermorite (Ca/Si_{solid} ratio = 0.83) strongly supports this trend (Table 3.2, Fig. 3.5). This fact implies both a gradual change in solid C-S-H composition accompanied by a gradual change from non-stoichiometric C-S-H dissolution to stoichiometric dissolution.

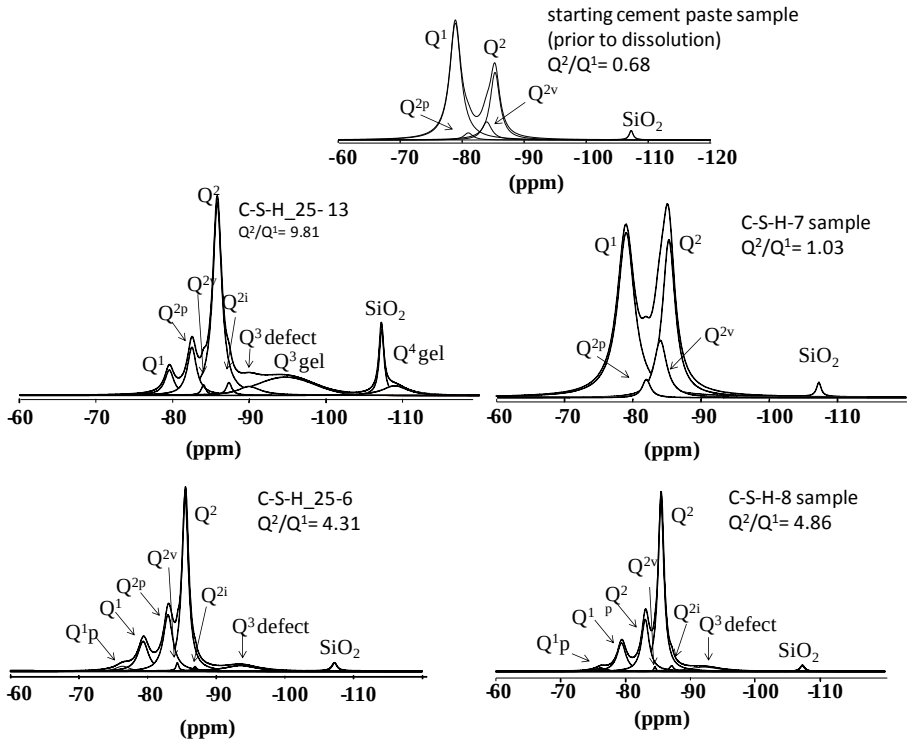

Figure 3.6. *Deconvolution of the ^{29}Si MAS-NMR spectra of the hydrated C_3S sample prior to dissolution and the reacted samples in experiment C-S-H-7 and C-S-H-8 and experiments C-S-H-25-6 and C-S-H-25-13 (Chapter 2) that underwent different degrees of dissolution. This figure is slightly modified from Figure 2.20 and shows the Q^2/Q^1 ratio values.*

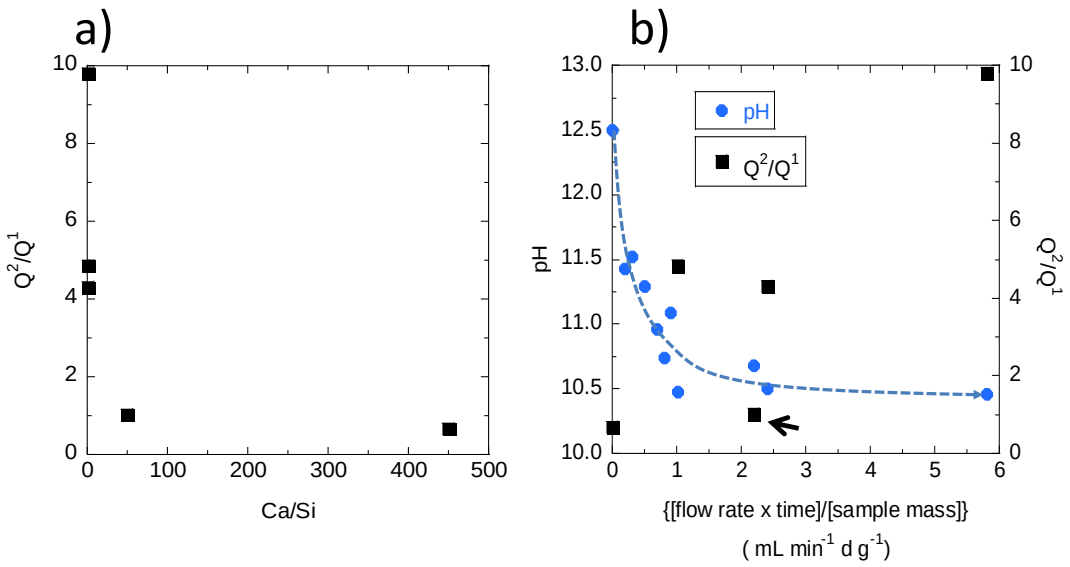

Figure 3.7. *Variation of (a) Q^2/Q^1 ratio as a function of aqueous Ca/Si ratio and (b) output pH and Q^2/Q^1 ratio as a function of flow rate x time / sample mass. Arrow indicates an outlier value of Q^2/Q^1 ratio (see text). The values of Q^2/Q^1 ratio were calculated from the values given in Table 2.6 (Chapter 2) and are shown in Figure 3.6.*

3.3.3 Neutron scattering contrast: initial C-S-H gel

It is necessary to determine the scattering contrast from the composition and density of the C-S-H gel to calculate the SANS surface area. As both, the composition and density of the gel are a *priori* unknown and needed to calculate the neutron scattering length density ($\rho_{C\text{-}S\text{-}H}$), the relative scattering contrast of the starting C-S-H was obtained from calculation of the Porod constants, which were normalized to that obtained at 100% H_2O (contrast variation method; Fig. 3.8). Using six specimens in varying H_2O/D_2O fluid mixtures the Porod constants were calculated from the linear fit of Iq^4 vs. q^4 according to Eq. (3.2) in the Porod regime data (0.11 $Å^{-1} < q < 0.2$ $Å^{-1}$), where the scattering is dominated by the nanoscale C-S-H gel-water interface (Allen et al., 2007; Table 3.4).

In a system with H_2O/D_2O fluid and solid C-S-H, the scattering intensity drops to zero at the contrast matchpoint (81 % D_2O; Fig. 3.8). This occurs when the solid scattering-length density ($\rho_{C\text{-}S\text{-}H/D}$) of C-S-H where the H content has partially exchanged for D content and the pore fluid density (ρ_{liquid}) with an identical H_2O/D_2O mix as in the C-S-H/D solid are the same, resulting in a zero scattering contrast (Fig. 3.8).

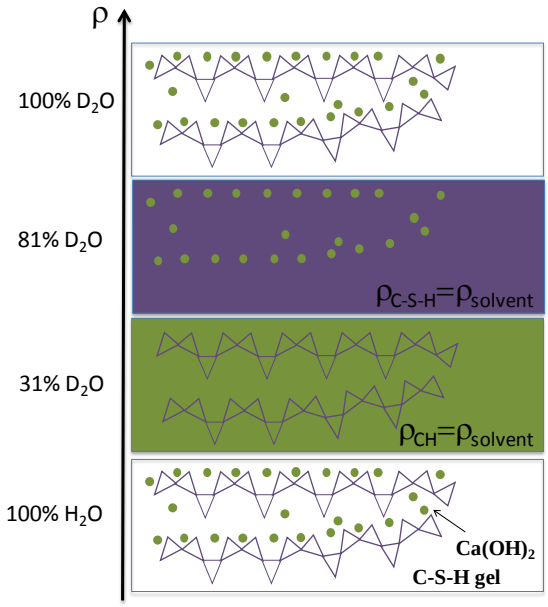

Figure 3.8. *Schematic representation of the contrast matchpoint of the system formed of C-S-H and CH with different D_2O molar fraction (%). Fluid mixtures of 100, 81 and 31 vol.% D_2O give scattering of C-S-H gel and CH, CH and C-S-H gel, respectively. Fluid mixture of 100 vol. % of H_2O gives scattering of C-S-H gel and CH and the CH scattering predominates.*

However, in a system with H_2O/D_2O, solid C-S-H/D and CH when $\rho_{liquid} = \rho_{C\text{-}S\text{-}H/D}$, the experimentally measured contrast never goes to zero because scattering contributions from nanoscale CH become non-negligible (Thomas et al., 1998b). Figure 3.9 shows the C-S-H gel non-zero contrast minimum, which indicates the presence of both solid C-S-H and fine CH crystals as expected from the initial composition of C-S-H gel (≈ 67 % mass solid C-S-H and ≈ 27.5 % mass CH).

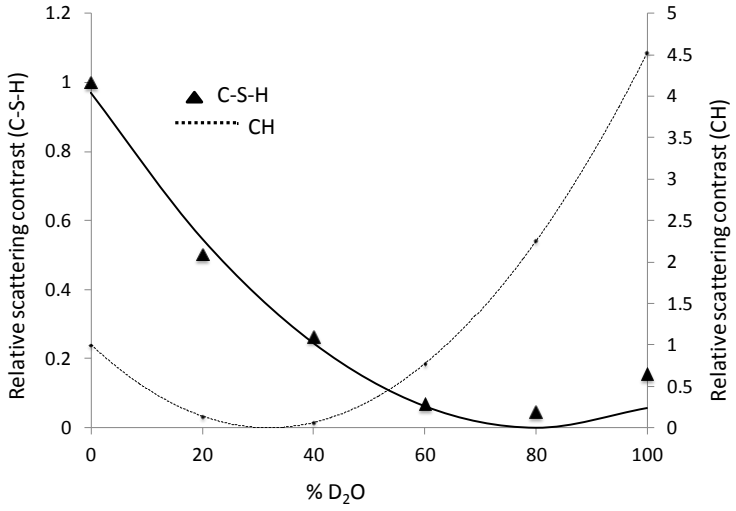

Figure 3.9. *Relative SANS intensity (scattering contrast) data versus molar D_2O content (triangles with experimental uncertainties smaller than the size of the symbols), together with the two-component parabola fit for the initial C-S-H gel sample (line) and calculated scattering curve of pure portlandite, $Ca(OH)_2$, (CH) (dotted line).*

When scattering contributions at high-q are from two solid phases (C-S-H and CH), the measured contrast curve can be fitted with two component parabolas, yielding a single parabola with a minimum value greater than zero. The first parabola accounts for CH with a 31 % (molar) D_2O matchpoint and the second one for C-S-H gel constrained only by requiring zero intensity at contrast match (Allen et al., 2007). The two fitting parameters are (1) the small fractional intensity contribution from nanoscale CH (f_{CH}), which is calculated from the known neutron scattering length density of CH, and (2) the contrast matchpoint of the C-S-H gel. The C-S-H gel mass density, the H/D ratio (from the H_2O/D_2O exchange), and the C-S-H gel composition are obtained from Allen et al. (2007).The calculated contrast curve for CH (ρ_{CH} = 1.643 x10^{14} m^{-2}) is shown in Figure 3.9 and the computed scattering contrast data are listed in Table 3.5.

Table. 3.5 *Calculated neutron scattering length density and contrast values for the CH.*

Molar % D_2O	Neutron scattering length density H_2O/D_2O (x 10^{14} m^{-2})	Neutron scattering contrast factor between CH and pore fluid (x 10^{28} m^{-4})	Relative scattering contrast factor between CH and pore fluid
0	-0.561	4.837	1
20	0.816	0.677	0.140
31	1.573	0.044	0
40	2.192	0.305	0.063
60	3.568	3.719	0.769
80	4.944	10.92	2.258
100	6.320	21.91	4.529

Neutron scattering contrast of CH was calculated based on the length density of $Ca(OH)_2$ (1.64·10^{14} m^{-2}).

The solid C-S-H/D contrast matchpoint with H_2O/D_2O fluid takes place with 81 % D_2O (Fig. 3.9). This value was obtained by subtracting the intensity contribution from nanoscale CH (f_{CH} = 1.66 %). To determine the correct C-S-H/H_2O scattering contrast, the measured relative scattering contrast data were fitted using different values of C-S-H chemical composition and density published in previous C-S-H hydration studies (Table 3.6). Early studies (Allen et al., 1987, 1989) using the $C_3S_2H_{2.5}$ composition and density of 2.15 g cm^3 obtained a reasonable match between the experimental contrast data and the predicted curve. Thomas et al. (1998b) obtained experimental contrast data and relative scattering contrast as a function of D_2O content, using four theoretical C-S-H gel formula (the previous one by Allen et al. (1987) and three new ones which were derived under three different conditions: D-dried, water-saturated and equilibrated to 11% RH). The best match was obtained with the latter one ($C_{1.7}SH_{2.1}$) and density of 2.18 g cm^3). Recently, Allen et al. (2007) suggested a new C-S-H composition and density ($C_{1.7}SH_{1.8}$ and 2.604 g cm^3) to be more precise as it was able to distinguish water within the C-S-H nanostructure, which includes water physically bound within the internal structure of the nanoparticles.

Table. 3.6 *Composition and density of the C-S-H gel according to the literature values.*

Bulk formula	Density ($g\ cm^{-3}$)	Contrast MP	Relative scattering contrast (100 % D_2O)	Reference
$C_3S_2H_{2.5}$	2.15	58.3	0.513	(Allen et al., 1987, 1989)
$C_{1.67}SH$	2.10	76.2	0.115	(Zarzycki, 1987)
$C_{1.5}SH_{2.5}$	2.15	72.7	0.141	(Thomas et al., 1998b)
$C_{1.7}SH_4$	1.90	57.7	0.600	(Thomas et al., 1998b)
$C_{1.7}SH_{2.1}$	2.18	66.2	0.260	(Thomas et al., 1998b)
$C_{1.7}SH_{1.8}$	2.604	81.0	0.045	(Allen et al., 2007)
The values of bulk formula and density used in this study are from Allen et al. (2007)				

An evaluation of the quality of the fit curves of the experimental data was made following Thomas et al. (1998b). Best fit parabola was obtained using the C-S-H gel chemical composition and density of $C_{1.7}SH_{1.8}$ and 2.604 g cm^{-3} reported by Allen et al. (2007) and is shown in Figure 3.9. For a H_2O saturated C-S-H gel specimen, the neutron scattering length density ($\rho_{C\text{-}S\text{-}H}$) and the neutron scattering contrast ($\Delta\rho^2$) are calculated as

$$|\Delta\rho|^2 = \left(\rho_{C-S-H} - \rho_{H_2O}\right)^2 \qquad \textit{Eq. 3.3}$$

where ρ_{H2O} is the neutron scattering length density of water. $\rho_{C\text{-}S\text{-}H}$ and $\Delta\rho^2$ values were $2.572x10^{14}$ m^{-2} and $9.83x10^{28}$ m^{-4}, respectively. Nonetheless, in the calculations the slightly

modified $\Delta\rho^2$ value of 9.64×10^{28} m^{-4} was used because it takes into account the presence of scattering from nanoscale CH at high q (Allen et al., 2007).

Once C-S-H composition, density and the scattering contrast were known, SANS measurements on initial and reacted C-S-H samples were performed at 31 % D_2O (CH match), and changes in the structure of the C-S-H could be quantified over a scale range from 10 Å to 10^4 Å (Allen et al., 2007).

3.3.4 SANS data: reacted C-S-H gel

Figure 3.10 shows the SANS data obtained in a H_2O/D_2O fluid mix with 31 % molar D_2O (0.001 $Å^{-1}$ < q < 0.22 $Å^{-1}$) for the starting (unreacted) C-S-H gel (Fig. 3.10a) and reacted C-S-H gel (Fig. 3.10b) samples in a log-log plot of I(q) versus q. Under these circumstances, the scattering contrast between CH and the pore fluid is matched out, and the scattering contrast is almost entirely that between solid C-S-H/D (with 31 % of the C-S-H bound H exchanged for D) and H_2O/D_2O with 31 % D_2O. Changes with time in the shape of the SANS data in this plot suggest that microstructural changes occurred in the reacted samples. SANS is particularly useful for measuring the surface area of cement paste because it is noninvasive and is performed on saturated specimens (Thomas et al., 1998b). For cement based materials, the surface area is dominated by that between the C-S-H gel and the pore H_2O (Allen et al., 2007), and with the CH matched out, the SANS Porod surface area should be entirely that between C-S-H/D and the H_2O/D_2O pore fluid. In a two-phase specimen, the specific surface area per unit specimen volume (S_T), between the two phases as determined from small angle scattering can be written as (Allen et al., 1987)

$$S_T = \frac{C_P}{2\pi|\Delta\rho|^2} \qquad \textit{Eq. 3.4}$$

where $\Delta\rho^2$ is the scattering contrast, and the Porod constant (C_p) for each reacted sample was obtained from a linear fit of Iq^4 vs. q^4 in a q range from 0.15 $Å^{-1}$ to 0.2 $Å^{-1}$ (Thomas et al., 1998a). A calculated specific surface area (SSA in m^2 g^{-1}) is computed by dividing S_T by the solid C-S-H density (2.604 g cm^{-3}).

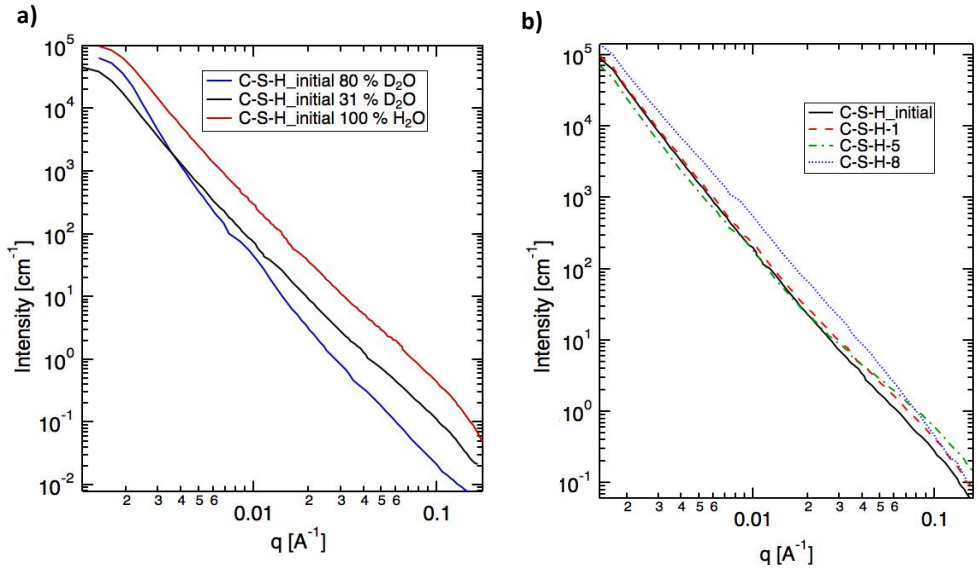

Figure 3.10. *SANS data for the initial (unreacted) C-S-H gel sample (a) and reacted C-S-H gel samples (b) in log-log plots of I(q) versus q. Data scatter representative of the standard deviation uncertainties (1 σ). In a) the SANS data given for the hydrated paste (prior to dissolution) immersed in a 100 % H_2O solution, 31 % and 80 % D_2O solutions illustrate that in a 31 % D_2O solution, the intensity is given by the C-S-H gel (same slope as that in 100 % H_2O solution), and in 80 % D_2O solution the intensity is given by CH (i.e., MP of C-S-H gel). In b) the SANS data for the C-S-H gel samples are rescaled to their predicted contrast in 100 % H_2O according to Allen et al. (2007).*

Table 3.7 lists the obtained values of C_p, S_T, *SSA* and the measured BET specific surface areas of the unreacted and reacted C-S-H gel samples, using the composition and density (2.604 g cm^{-3}) obtained by Allen et al. (2007). The derived S_T for the initial C-S-H sample is lower than 178 ± 4.8 m^2 cm^{-3}, which was obtained by Thomas et al. (1998a) with a density of 1.457 g cm^{-3}.

Table. 3.7 *Porod constant (C_p), Porod surface area (S_T), calculated total internal surface area (SSA) and specific surface area (BET) of the reacted C-S-H gel samples.*

Experiment	Time (day)	C_P (x 10^{-12} Å^{-5})	S_T (m^2 cm^{-3})	SSA (m^2 g^{-1})	BET
C-S-H_initial	0	0.49 ± 0.01	78.96 ± 1.70	30.32 ± 0.57	11.7
C-S-H-1	16	0.88 ± 0.08	126.1 ± 11.6	48.41 ± 4.47	14.5
C-S-H-2	16	0.68 ± 0.07	97.38 ± 10.7	37.39 ± 4.14	52.7
C-S-H-3	16	0.71 ± 0.08	101.5 ± 12.7	38.99 ± 4.88	18.6
C-S-H-4	17	0.59 ± 0.06	84.33 ± 9.38	32.38 ± 3.60	25.0
C-S-H-5	31	1.16 ± 0.07	150.2 ± 10.2	57.67 ± 3.91	46.1
C-S-H-6	44	1.01 ± 0.07	130.9 ± 9.10	50.26 ± 3.49	61.6
C-S-H-7	67	0.79 ± 0.07	98.66 ± 9.16	37.88 ± 3.51	15.9
C-S-H-8	84	0.70 ± 0.08	87.60 ± 9.22	33.64 ± 3.75	42.9
Estimated standard deviation measurement uncertainty is 10 % for BET (1 σ)					

Figure 3.11a depicts the variation of S_T, S_{SF} and S_{VF} with reacting time multiplied by flow rate and divided by sample mass. S_T increases significantly from 78.96 ± 1.70 m^2 cm^{-3} to

150.2 ± 10.2 m^2 cm^{-3} after 0.86 mL min^{-1} d g^{-1} (31 days), thereafter decreasing to 87.60 ± 9.22 m^2 cm^{-3} as dissolution continues. This behavior is consistent with that shown by Thomas et al. (2004) in which the total internal surface area of leached OPC first increased from 120 m^2 cm^{-3} to 200 m^2 cm^{-3} as the Ca/Si ratio decreased to 1, with the surface area thereafter decreasing as the Ca/Si ratio decreased below 1, due to thickening of the (now sheet-like) fundamental C-S-H units. S_{VF} shows similar tendency to that of S_T. The significant stochastic variation and a rather large S_{SF} suggest that the powdered nature of the samples may affect the obtained values in comparison to the values calculated from monolithic hydrated cement coupons used in previous studies (Thomas et al., 2004; Allen et al., 2007).

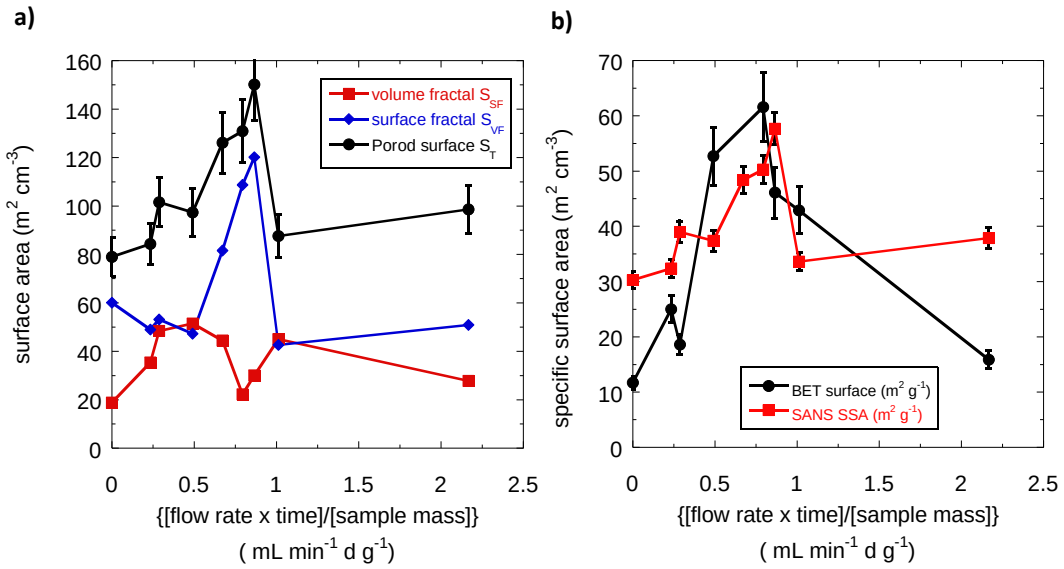

Figure 3.11. *Variation of surface area as a function of flow rate x time / sample mass: a) total surface area (S_T), surface fractal surface area (S_{SF}) and surface area of the volume-fractal morphology (S_{VF}) and b) calculated specific surface area (SSA) and measured BET specific surface area. Vertical bars represent standard deviations.*

A working assumption is that the density for the unreacted and reacted C-S-H gel is constant (2.604 g cm^{-3}), and the specific surface area (SSA) is calculated from the S_T values. The resulting SSA ranged from 30.32 ± 0.57 m^2 g^{-1} (initial C-S-H) to 57.67± 3.91 m^2 g^{-1} in the reacted C-S-H (Table 3.7, Fig. 3.11b). The C-S-H gel is often conceived by simplification to be formed by two components, a high-density (HD) inner-product and a low-density (LD) outer-product (Tennis and Jennings, 2000). Constantinides and Ulm (2004) argued that the C-S-H gel is formed of 30 vol. % HD C-S-H gel and 70 vol. % LD C-S-H gel. It is considered that the former product is a rough and dense disordered particulate matrix, and the latter is a less dense phase and SANS sensitive. The LD C-S-H gel is the component of the microstructure that remarkably contributes to the measured BET specific surface area (Morales-Florez et al., 2012). Figure 3.11 b depicts the measured BET specific surface area variation with time and compares

with the SSA variation. On the one hand, in terms of magnitude, the SSA and BET are fairly comparable, even though lower BET values could be systematically expected since nitrogen physisorption may not access the interlayer C-S-H porosity. It is found that SANS-based surface areas are remarkably consistent (Allen et al., 2007), providing the right criteria are used to extract the Porod constant. It is observed that the BET values tend to increase with time up to ≈ 40 days and decrease thereafter. This behaviour, which is similar to that of S_T, could be caused by an increase in LD product released as the HD C-S-H gel dissolves. This increase in LD product yields a large accessible surface area to nitrogen physisorption and neutron scattering. However, as more material is leached or dissolved away over longer times, the surface area declines. The trend of SSA and BET surface areas could also correspond to a change in the fundamental C-S-H gel units that evolve into a sheet-like morphology (Thomas et al., 2004).

3.3.5 Volume-fractal and surface-fractal structure

The measured SANS data intensity for the starting (unreacted) C-S-H gel and reacted C-S-H samples were rescaled to the predicted contrast in H_2O. The scattering contrast value for the unreacted C-S-H sample was 9.64×10^{28} m^{-4} (see section 3.3.3) and for the reacted C-S-H samples were those obtained by Thomas et al. (2004). Figures 3.12a and b shows the SANS data for the hydrated sample prior to dissolution and a hydrated sample after 44 days of flow-through dissolution, respectively, in log-log plots of $I(q)^4$ vs. q with the fitted flat background scattering removed. The neutron scattering contrast assumed was 9.64×10^{-28} m^{-4}. According to the fractal model (Allen et al., 2007), the scattering cross-section is separated into three component terms: volume fractal, surface fractal and Porod regime (Eq. 3.1). The surface fractal regime occurs at the q range from ≈ 0.002 $Å^{-1}$ to ≈ 0.02 $Å^{-1}$, and the volume-fractal regime ranges from ≈ 0.02 $Å^{-1}$ to ≈ 0.1 $Å^{-1}$. Primarily, surface-fractal and volume-fractal model components were used independently to fit the data in these q-ranges to guarantee a physical significance of the components. With a reasonable fit, all parameters (D_o, D_V, ϕ_{CSH}, S_O, D_S, ξ_V and ξ_S) were varied together assuming prolate gel globules with an aspect ratio (β) of 2 and then assuming oblate gel globules ($\beta = 0.5$). The obtained R_o values were converted to a sphere-equivalent radius and then are averaged (Allen et al 2007; Thomas et al., 2008).

There is a covariance between S_o and ξ_S that does not allow these parameters to be fitted independently to the data. Together they define the absolute intensity of the surface fractal scattering. ξ_S has a value beyond where there is true information content in the scattering data. To obtain a reasonable fit, ξ_S cannot be larger than a value between the mean clinker radius and the mean clinker diameter (as this would imply surface fractal scaling going beyond the

dimensions of the substrate upon which it is deposited). The mean size of the clinker grains is ≈1.9 μm and 90 % of the C-S-H gel sample has a particle size < 8 μm. The detected S_o-ξ_S covariance does not affect the overall rough surface-fractal surface area (S_{SF}). Best fits were obtained with the ξ_S value ranging from 700 Å to 9000 Å (Table 3.8). The best fractal model fits suggest changes in the microstructure of the reacted C-S-H gel during dissolution. This is also inferred from the variation of the fit parameters (Table 3.8).

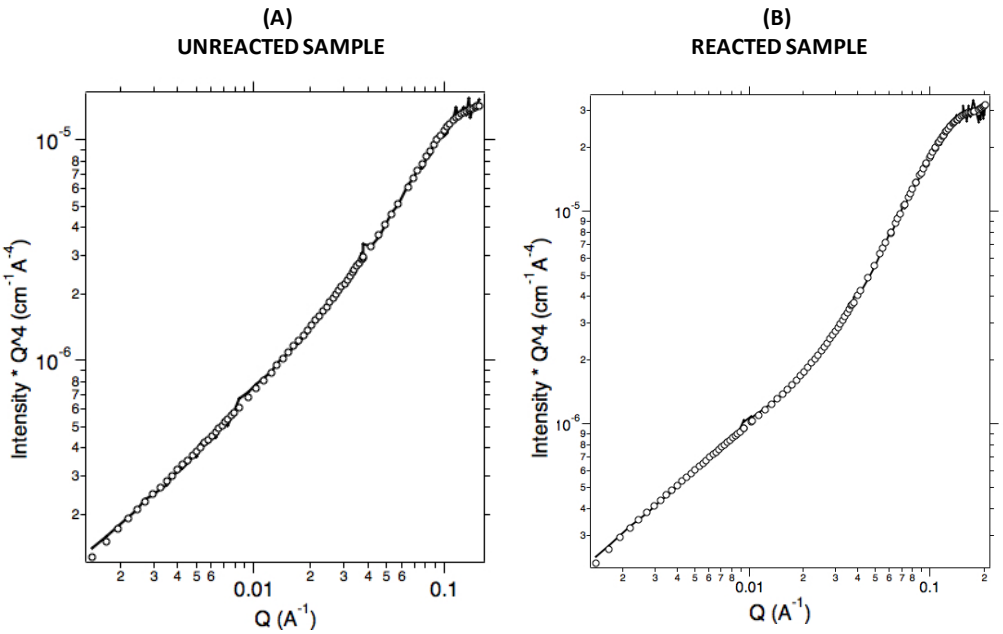

Figure 3.12. *Small-angle neutron scattering data (solid lines) and fits using the fractal model (Eq. (3); open circles) for hydrated sample prior to dissolution (a) and hydrated sample after 44 days of flow-through dissolution (experiment C-S-H-6) (b). There is an excellent agreement between the experimental and fractal model data.*

The fitted values obtained in the volume or mass-fractal component are the volume fraction of solid C-S-H ($\phi_{C\text{-}S\text{-}H}$), the volume or mass fractal dimension (D_V), the volume or mass fractal correlation length (ξ_V), and the mean radius of the volume fractal building block, R_o. Two additional terms, the local volume fraction (η) and the correlation hole radius (R_c), are sensitive to the nearest and next nearest neighbor globules and are necessary to create an acceptable fit where the volume fractal transitions at high q to single C-S-H particle scattering.

From the surface fractal component the surface fractal dimension (D_S), which varies from 2 to 3 for non-smooth surfaces, the surface fractal correlation length (ξ_S) and the smooth surface (S_o) are determined. S_o shows monotonic increased with dissolution. Three other parameters of interest are obtained assuming that the C-S-H gel globule nanoparticle diameter ($D_o = 2R_o = R_c$) is the building block particle size of the fractal morphology: the upper-limit volume fraction per unit sample volume of the whole volume-fractal morphology (ϕ_{MAX}), the

fractally-rough surface area (S_{SF}), and the surface area of the volume-fractal morphology (S_{VF}). They provide the relative amount of solid material within the two fractal morphologies. We note that the variation in S_o and S_{SF} are likely dominated by the finest grains in the powder samples, since these have the highest surface area, and are likely to be more affected (in proportion to their volume) by the dissolution process. The stochastic variability in fine powder grain content among the samples may not be sufficient to break the observed monotonic increase in S_o with dissolution, but the variability in surface fractal created by different amounts of fine grain material may be sufficient to produce the observed stochastic S_{SF}, assuming that stochastic variations are amplified in S_{SF}, compared to S_o.

For the initial C-S-H gel sample, the radius of the building block particles (D_o) obtained is 47.37 Å, and the D_V and D_S values are 2.369 and 2.729, respectively (Table 3.8). The resulting initial diameter value, D_o, is close to that for the fractal sphere (D_V = 2.33) calculated by Zarzycky et al. (1987). The D_o, D_V and D_S values for an unaltered C-S-H gel obtained by (Allen and Thomas, 2007) were 44.4 Å, 2.61 and 2.55, respectively. Thomas et al. (2004) obtained D_V values that range from 2.01 to 2.28 for C-S-H gel in white Portland cement pastes (WPC) with Ca/Si ratio ranging from 1.47 to 2.4.

In the reacted samples, D_o decreases from an initial value of 47.37 Å to 35.089 Å after 31 days. Thereafter, it increases to 72.72 Å (Table 3.8). Such a D_o increase is consistent with the roughly equiaxed particles that build the solid C-S-H structure changing their shape with dissolution into sheet-like structures of increasing thickness (Thomas et al. 2004). D_v decreases for 44 days from 2.369 to 1.538 (Fig. 3.13a, Table 3.8) and thereafter to increase to 2.038. A decrease in the volume fractal scaling factor suggests that the unreacted C-S-H gel, composed of equiaxed ≈ 5 nm C-S-H gel globule building blocks, transforms to sheet-like structures during dissolution (as the Ca/Si ratio decreases to nearly 1), which is in agreement with the ^{29}Si MAS-NMR results of this study and those reported by Thomas et al. (2004) and Allen and Thomas (2007). D_s tends to be constant, merely changing from 2.844 to 2.559 (D_s value of 2 indicates smooth surface) (Fig. 3.13a), which would indicate decrease in surface roughness during dissolution.

Table. 3.8 *Fit and derived microstructure parameters from the fractal model. Estimated uncertainties (standard deviation) for each value are given in parentheses. Fixed ξ_S values from 700 Å to 9000 Å yield S_0 uncertainties lower than 10 %.*

Parameter (Local packing parameter η set to 0.5)	C-S-H_initial	C-S-H-1	C-S-H-2	C-S-H-3	C-S-H-4	C-S-H-5	C-S-H-6	C-S-H-7	C-S-H-8
Duration (day)	0	16	16	16	17	31	44	67	84
$D_o=R_c$ (Å)$=2R_o$ [f]	47.37 (2.15)	43.37 (3.74)	41.89 (0.85)	44.26 (3.33)	45.21 (8.02)	35.08 (3.92)	33.25 (18.29)	41.43 (23.24)	72.72 (4.09)
R_o (Å) [f]	23. 68 (1.07)	21.68 (1.87)	20.94 (0.42)	22.13 (1.66)	22.60 (4.01)	17.54 (1.46)	16.62 (9.15)	20.72 (11.62)	36.36 (2.04)
$\phi_{C\text{-}S\text{-}H}$ (%) [f]	4.093 (0.289)	4.025 (1.245)	5.757 (0.759)	6.022 (0.802)	4.930 (1.404)	5.855 (1.107)	2.887 (0.737)	2.007 (2.409)	3.184 (0.866)
D_V [f]	2.369 (0.078)	2.132 (0.335)	2.045 (0.129)	2.244 (0.109)	1.955 (0.154)	1.907 (0.158)	1.538 (0.178)	1.821 (0.927)	2.038 (0.305)
ξ_V (Å) [f]	176 (52)	60 (25)	78 (26)	198 (73)	189 (130)	44 (10)	54 (65)	40 (46)	124 (111)
S_o ($m^2\,cm^{-3}$) [f]	0.412 (0.005)	0.471 (0.038)	0.676 (0.049)	0.711 (0.033)	0.671 (0.024)	2.011 (0.159)	2.163 (0.049)	5.725 (0.0752)	6.806 (0.906)
D_S [f]	2.729 (0.011)	2.844 (0.022)	2.813 (0.027)	2.794 (0.021)	2.749 (0.076)	2.807 (0.018)	2.611 (0.019)	2.559 (0.008)	2.7878 (0.013)
ξ_S (Å)	9000	9500	8800	9000	9000	1000	1500	700	800
Total S_T ($m^2\,cm^{-3}$) (measured by Porod law)	78.96 (1.70)	126.1 (11.6)	97.38 (10.7)	101.5 (12.7)	84.33 (9.38)	150.2 (10.2)	130.9 (9.10)	98.66 (9.16)	87.60 (9.22)
S_{SF} ($m^2\,cm^{-3}$) [d]	18.88	44.51	52.24	48.37	35.37	30.03	22.17	27.80	45.01
S_{VF} ($m^2\,cm^{-3}$) [d]	60.07	81.56	47.25	53.18	48.96	120.16	108.72	50.90	42.59
ϕ_{MAX} (%) [d]	9.37	5.27	10.43	18.71	21.97	4.60	5.94	1.94	5.31
$\phi_{MAX}/\phi_{C\text{-}S\text{-}H}$ (%) [d]	2.30	1.31	1.81	3.11	4.46	1.30	2.06	0.97	1.67
f and d denote fitted and derived, respectively.									

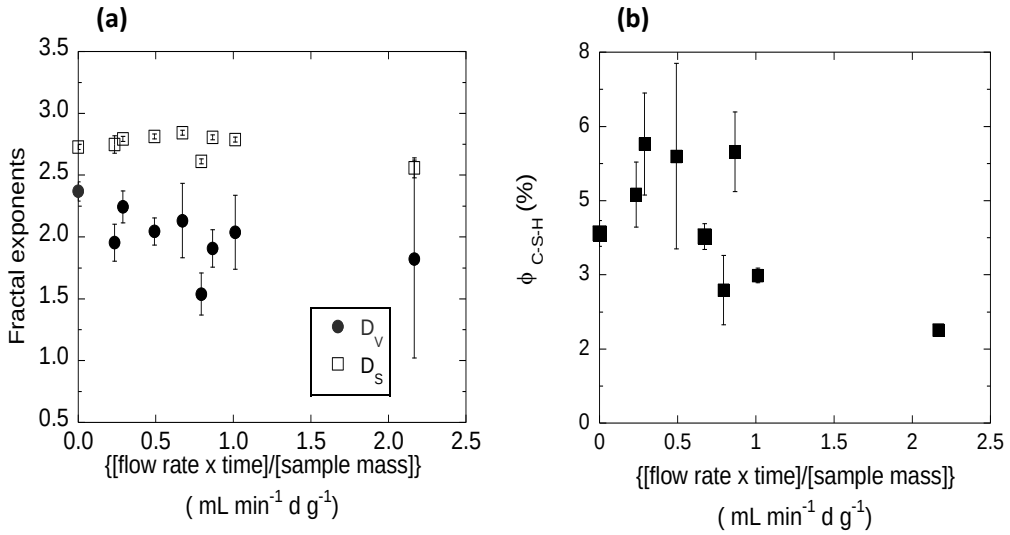

Figure 3.13. *SANS scattering data: fit fractal parameters as a function of time. Vertical bars, where visible, represent the computed or estimated standard deviation uncertainties in the fit results. a) Variation of fractal exponents with dissolution expressed as a function of flow rate x time / mass and b) variation of outer C-S-H volume fraction with dissolution expressed as a function of flow rate x time / sample mass.*

Considering that the starting C-S-H gel is composed of 67 % mass of C-S-H and the amount of LD C-S-H gel is 70 vol. % with an estimated porosity of minimally 36 % (Jennings et al., 2007), the expected volume fraction ($\phi_{C\text{-}S\text{-}H}$) of the starting C-S-H gel can be about 11 %. The obtained $\phi_{C\text{-}S\text{-}H}$ value of about 8 % would imply an initial porosity of 43 %, which is a reasonable estimation. The trend in the volume fraction ($\phi_{C\text{-}S\text{-}H}$) (Fig. 3.13b), which essentially is a measure of the amount of LD C-S-H gel (without gel pores) in the paste, is similar to the trend observed for the total internal surface area (S_T). As dissolution progresses, the HD C-S-H gel evolves into LD C-S-H gel, with a maximum after 31 days. Then, LD C-S-H gel continues to dissolve too leading to a volume fraction decrease.

3.4 Conclusions

It is illustrated that SANS measurements were applicable to study the evolution of the C-S-H structure during C-S-H dissolution. SANS data obtained at 31 % D_2O provided a scattering intensity dominated by the C-S-H structure. SANS data for the unreacted C-S-H gel indicated that the resulting contrast curve was consistent with a solid C-S-H phase with composition $C_{1.7}SH_{1.8}$ and density of 2.604 g cm^{-3} as suggested by Allen et al. (2007).

The SANS total internal surface (S_T) increased as the Ca/Si ratio decreased (for ≈ 31 days) and thereafter decreased when the Ca/Si ratio was ≈ 1. These observations agree with the measurements reported by Thomas et al. (2004) and suggest that the accessibility of HD C-S-H gel increases with dissolution, contributing to the S_T enhancement. The variation of surface area with time, i.e., when the Ca/Si ratio decreases to reach a tobermorite stoichiometric ratio, is similar for the measured specific surface area (BET) and comparable to the derived SANS surface area (SSA). This observed behavior suggests that, as C-S-H gel dissolves, the morphology of the HD C-S-H gel compound is being transformed to LD C-S-H, increasing the measured specific surface area. Therefore, the use of the BET surface area to normalize the C-S-H gel dissolution rates is fully justified.

The change of the C-S-H gel nanostructure (at the scale range from 10 Å to 1000 Å) during C-S-H gel dissolution was determined from the SANS experimental data fitted with the fractal model (Allen and Thomas, 2007), considering a fractal structure that is composed of a volume fractal structure, mainly LD C-S-H gel, and a surface fractal structure on the surface of the clinker grains. Using this model, fit parameters (D_0, D_V, D_S, ξ_V and $\phi_{MAX}/\phi_{C\text{-}S\text{-}H}$ ratio) were obtained that describe the changes in the nanostructure of the C-S-H gel during dissolution.

As dissolution progressed it was inferred that the roughly equiaxed C-S-H gel globules, which comprise the unreacted C-S-H gel structure, change their shape into a sheet-like morphology with progressively increasing thickness (D_o increase). This transformation was supported by the decrease in D_v values (≈ 2) which is expected for this structure (Thomas et al., 2004, Allen and Thomas, 2007). Surface roughness of the coarse features was inferred by the slight D_S increase. In addition, a decrease in ξ_V and increase in the $\phi_{MAX}/\phi_{C\text{-}S\text{-}H}$ ratio indicate a loss of structural compaction and density during dissolution.

The C-S-H gel evolution deduced from the SANS experiments is in agreement with the ^{29}Si MAS-NMR measurements that show an increase in polymerization with C-S-H gel dissolution, i.e., dissolution promotes the C-S-H gel structure transformation to a more ordered tobermorite structure.

References

Allen, A. J., Thomas, J. J., and Jennings, H. M. (2007). Composition and density of nanoscale calcium–silicate–hydrate in cement. *Nature Materials*, 6(4), 311-316.

Allen, A. J., and Thomas, J. J. (2007). Analysis of C–S–H gel and cement paste by small-angle neutron scattering. *Cement and Concrete Research*, 37(3), 319-324.

Allen, A. J., and Livingston, R. A. (1998). Relationship between differences in silica fume additives and fine-scale microstructural evolution in cement based materials. *Advanced cement based materials*, 8(3), 118-131.

Allen, A. J., Baston, A. H., and Wilding, C. R. (1989). Small angle neutron scattering studies of pore and gel structures, diffusivity, permeability and damage effects. *Materials Research Society Symposium Proceedings*, 137, 119 –125.

Allen, A. J., Oberthur, R. C., Pearson, D., Schofield, P., and Wilding, C. R. (1987). Development of the fine porosity and gel structure of hydrating cement systems. *Philosophical Magazine B*, 56(3), 263-288.

Barker, J.G., Glinka, C.J, Kim, M.H., Moyer, J.J., Drews, A.R. and Agamalian, M. (2005). Design and performance of a thermal-neutron double-crystal diffractometer for USANS at NIST. *Journal of applied crystallography*, 38(6), 1004–1011.

Barrante J. R. (1974). Applied Mathematics for Physical Chemistry. Prentice-Hall. Englewood Cliffs, New Jersey.

Bumrongjaroen, W., Livingston, R. A., Neumann, D. A., and Allen, A. J. (2009). Characterization of fly ash reactivity in hydrating cement by neutron scattering. *Journal of Materials Research*, 24(7), 2435-2448.

Carey, J. W., and Lichtner, P. C. (2007). Calcium silicate hydrate (CSH) solid solution model applied to cement degradation using the continuum reactive transport model FLOTRAN. *Transport properties and concrete quality: materials science of concrete, special volume*. 73-106.

Carey, J. W., and Lichtner, P. C. (2006) Calcium Silicate Hydrate Solid Solution Model Applied to Cement Degradation using the Continuum Reactive Transport Model FLOTRAN. Report LA-UR-06-0636.

Harris, A.W., Manning, M.C., Tearle, W.M., and Tweed, C.J. (2002). Testing of models of the dissolution of cements-leaching of synthetic CSH gels. *Cement and Concrete Research*, 32(5), 731-746.

Ilavsky, J., and Jemian, P. R. (2009). Irena: tool suite for modeling and analysis of small-angle scattering. *Journal of Applied Crystallography*, 42(2), 347-353.

Jennings, H. M., Thomas, J. J., Gevrenov, J. S., Constantinides, G., and Ulm, F. J. (2007). A multi-technique investigation of the nanoporosity of cement paste. *Cement and Concrete Research*, 37(3), 329-336.

Jennings, H. M. (2000). A model for the microstructure of calcium silicate hydrate in cement paste. *Cement and Concrete Research*, 30(1), 101-116.

Morales-Florez, V., Findling, N., and Brunet, F. (2012). Changes on the nanostructure of cementitius calcium silicate hydrates (C–S–H) induced by aqueous carbonation. *Journal of Materials Science*, 47(2), 764-771.

Tennis, P. D., and Jennings, H. M. (2000). A model for two types of calcium silicate hydrate in the microstructure of Portland cement pastes. *Cement and Concrete Research*, 30(6), 855-863.

Thomas, J. J., Allen, A. J., and Jennings, H. M. (2012). Density and water content of nanoscale solid C–S–H formed in alkali-activated slag (AAS) paste and implications for chemical shrinkage. *Cement and Concrete Research*, 42(2), 377-383

Thomas, J. J., Jennings, H. M., and Allen, A. J. (2010). Relationships between Composition and Density of Tobermorite, Jennite, and Nanoscale $CaO{-}\ SiO_2{-}\ H_2O$. *The Journal of Physical Chemistry C*, 114(17), 7594-7601.

Thomas, J. J., Allen, A. J., and Jennings, H. M. (2008). Structural changes to the calcium–silicate–hydrate gel phase of hydrated cement with age, drying, and resaturation. *Journal of the American Ceramic Society*, 91(10), 3362-3369.

Thomas, J. J., Chen, J. J., Allen, A. J., and Jennings, H. M. (2004). Effects of decalcification on the microstructure and surface area of cement and tricalcium silicate pastes. *Cement and Concrete Research*, 34(12), 2297-2307.

Thomas, J. J., Jennings, H. M., and Allen, A. J. (1998a). The surface area of cement paste as measured by neutron scattering: evidence for two CSH morphologies. *Cement and Concrete Research*, 28(6), 897-905.

Thomas, J. J., Jennings, H. M., and Allen, A. J. (1998b). Determination of the Neutron Scattering Contrast of Hydrated Portland Cement Paste using H_2O/D_2O Exchange. *Advanced Cement Based Materials*, 7(3), 119-122.

Constantinides, G., and Ulm, F. J. (2004). The effect of two types of CSH on the elasticity of cement-based materials: Results from nanoindentation and micromechanical modeling. *Cement and Concrete Research*, 34(1), 67-80.

Winslow, D.N. (1985). The fractal nature of the surface of cement paste. *Cement and Concrete Research*, 15(5), 817-824.

Zarzycki, J. (1987). Fractal properties of gels. *Journal of Non-Crystalline Solids*, *95*, 173-184.

PART II. Degradation of mortar

CHAPTER 4

Mortar column experiments

4.1. Introduction

The porewater of cementitious materials, which contains K, Na, Ca, Si, S, Fe and Al in solution is characterized by pH values ($\geq$ 13), is in equilibrium with the phases present in hydrated cement. Replacement of the porewater will perturb the local equilibrium, causing dissolution of the cementitious phases and precipitation of secondary phases. A brief description of cement composition is given in Chapter 1.

In this study, column experiments using ground mortar were performed to study mortar alteration by flowing water. The experimental results were interpreted, first, by means of analyses of solutions and inspection of the solids that intervened in the experiments and, secondly, using reactive transport modeling. The full approach made it possible to check the applicability of the previously obtained dissolution rate law for the C-S-H gel in the context of real Portland cement material and to enhance the current knowledge of mortar alteration.

In the research field that deals with the reactivity of cement-based materials (cement, mortar and concrete), the studies based on leaching of cement pastes are numerous (Adenot

and Buil, 1992; Revertegat et al., 1992; Mainguy et al., 2000; Gérard and Bellego, 2002; Haga et al., 2005; Kamali et al., 2008), and some of them present theoretical or multi-species reactive transport models that describe the leaching processes (Maltais et al., 2004; Moranville et al., 2004; Samson et al., 2007; Galíndez and Molinero, 2010; Soler and Mäder, 2010; Soler et al., 2011; Soler, 2012, 2013). In turn, the use of reactive transport modeling to account for the studied cement degradation requires reliable thermodynamic and kinetic databases. Several works that deal with the thermodynamics of cement-based materials are found in the literature (Berner et al., 1992; Reardon et al., 1992; Kulik and Kersten, 2001; Matschei et al., 2007; Lothenbach et al., 2008b; Schmidt et al., 2008; Damidot et al., 2011; Dilnesa et al., 2014). Lack of knowledge of dissolution rate laws of the cementitious phases yields uncertain cement degradation predictions (Zuloaga et al., 2009; Lothenbach, 2010). A brief description of the most representative studies on cement degradation is given in Chapter 1. Additionally, prominent research dealing with cement hydration processes and accompanying modeling is included.

This chapter is structured into two parts. The first part describes the experiments with mortar columns under forced advective flow. The second part shows the two-dimensional reactive transport calculations using CrunchFlow (Steefel, 2009) in which the dissolution rate law for the C-S-H gel (see Chapter 2) has been applied.

4.2. Materials and methods

The scheme depicted in Figure 4.1 summarizes the experimental tasks carried out in this study, which included characterization of the mortar, performance of column experiments and solid and solution analyses. Reactive transport calculations were performed to interpret the experimental results and check the applicability of the C-S-H dissolution rate law.

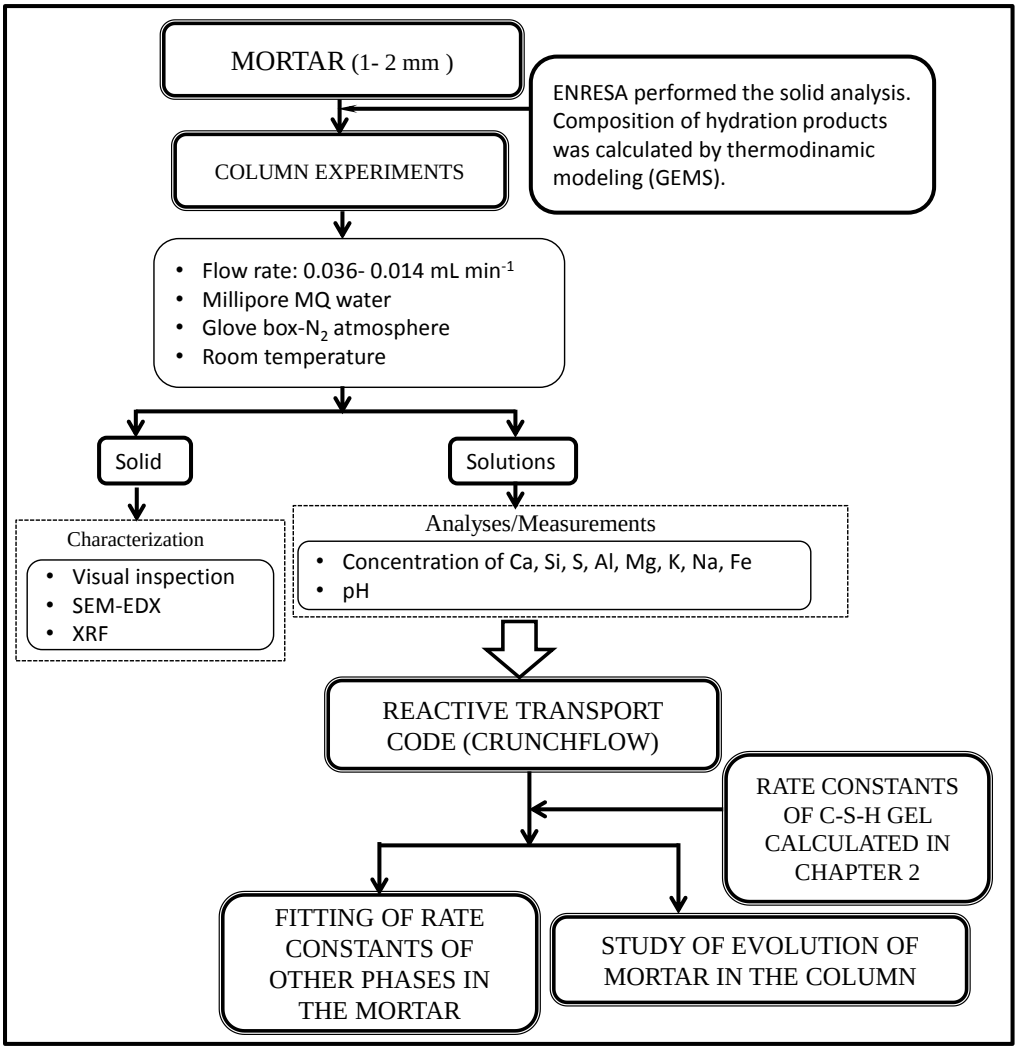

Figure 4.1. *Scheme of the main tasks carried out to study the degradation of mortar.*

4.2. 1 Characterization of the mortar

The experiments were carried out with cylindrical samples provided by Enresa as representative of the mortar used in El Cabril walls (see characteristics in Table 4.1). The I42.5R/SR cement is made up by adding 5% limestone ($CaCO_3$) to the clinker (95%) according to the UNE-80304 norm. Fly ash was added to this mixture (64% I42.5R/SR cement and 36 % fly ash). Sand and additives were finally added to obtain the mortar with the proportions shown in Table 4.1. Porosity was measured at the Eduardo Torroja Institute (CSIC) by mercury intrusion porosimetry at 28 days of hydration. The mortar was cured in a moisture room to ensure that hydration continued for as long as possible in order to reach maximum strength and durability, sufficient impermeability and reduced risk of cracking.

Table. 4.1 *Characteristics and dosing (wt. %) of the El Cabril mortar samples.*

Characteristics	Dimensions	11x10 cm
	Cured type	moisture room
	Total porosity (%)	14.9
	Median pore diameter (μm)	0.02
	Density (g mL^{-1})	2.0
Mortar Dosing (wt. %)	Cement I 42.5R/SR	20.0
	Water	13.7
	Sand (quartz)	54.6
	Fly Ash	11.2
	Additive (Rheobuild 1222)	0.5

X-ray fluorescence (XRF) to obtain the chemical composition of the cement and fly ash (Table 4.2). The clinker composition, expressed as oxides, was measured by X-ray fluorescence following the UNE 80-210-94 norm and the normative phase composition of the clinker was calculated following the UNE 80304 norm. The mineralogical composition of the clinker is shown in Table 4.3. One of the mortar samples was crushed into grains of 1 to 2 mm size. The specific surface area of the mortar grains was measured by BET, being the samples previously degassed for 10 h at 50 ºC. The BET specific surface area was 2.88 m^2 g^{-1}. The Blaine surface was calculated by the Blaine method that calculates the specific surface by means of the time that a fixed volume of air needs to pass through a bed of cement multiplied by a constant, which is determined by a known specific surface cement. D_{50} equal to 20.20 means that 50 wt. % of the sample is smaller than 20 μm.

Table. 4.2 *Chemical composition (wt. %) of the cement and fly ash of the El Cabril mortar, and physical characteristics of the cement. Error in XRF analysis is around 5%.*

	Cement I 42.5R/SR (wt. %)	**Fly Ash (wt. %)**
SiO_2	21.45	55.61
Al_2O_3	2.30	30.10
Fe_2O_3	4.85	6.56
CaO	68.40	1.74
MgO	0.77	2.01
CaO free	1.78	
SO_3	1.86	
K_2O	0.34	
Na_2O	0.09	
Alkali (Na_2O equivalent)	0.31	
Cl	0.01	
Density (g/cm^3)	3.13	
Blaine Surface (g/cm^2)	3685	
D_{50} (μm)	20.20	

Table. 4.3 *Mineralogical composition of the clinker (wt. %).*

Phases	Composition (wt. %)
C3S (alite)	78.7 ± 1%
C2S (belite)	2.1 ± 1%
C3A	0.0
C4AF (ferrite)	11.0 ± 0.1%
C2F	2.1 ± 0.1%

Composition in cement notation C: CaO, S: SiO_2, A: Al_2O_3, F: Fe_2O_3.

4.2. 2 Mortar hydration

The composition of the hydrate assemblage formed during the hydration of the OPC + fly ash mixtures was calculated based on the cement and fly ash composition (Table 4.2) using the GEM-Selektor (GEMS) software package (Lothenbach and Winnefeld, 2006; Lothenbach et al., 2008a; De Weerdt et al.; 2011; Wagner et al., 2012; Kulik et al., 2013). The hydration time of the products was 830 days. Reaction of fly ash was modelled according to (De Weerdt et al., 2011):

$$FA\ (reacted) = 36g \cdot (10 \cdot \ln(t + 4.5) - 15) \qquad \text{Eq. 4.1}$$

where *FA* is fly ash, *t* is time in days, and *g* is grams of fly ash.

Table 4.4 lists the calculated phases in the mortar. GEMS computes the equilibrium phase assemblage and speciation in a complex chemical system from its total bulk elemental composition. The chemical interactions involving pure solid phases, solid solutions, gas mixture, and aqueous electrolyte are considered simultaneously. The thermodynamic data for aqueous species, as well as for many solids, were taken from the PSI-GEMS thermodynamic database (Thoenen and Kulik, 2003 ; Hummel et al., 2002), whereas the solubility products for cement minerals were taken from the cemdata07 database (Lothenbach et al., 2008b; Matschei et al., 2007; Schmidt et al., 2008) completed with the recently determined solubility products of Fe-monocarbonate, Fe-monosulfate, and Si-hydrogarnet ($C_3(F,A)S_{0.84}H_{4.32}$ in cement notation; Dilnesa et al., 2011, 2012, 2014). The extent of aluminium substitution in Si-hydrogarnet was limited to 1:1 Al:Fe. Formation of $C_3AS_{0.41}H_{5.18}$ was excluded for its unlikely ocurrence at ambient temperature (Dilnesa et al., 2014).

The small amounts of remnant unhydrated phases (C_3S, C_2S, C_3A and C_4AF) were not taken into account when calculating the volume fractions of the different phases used in the reactive transport model of the column experiment. Owing to the high Ca concentration in the output solutions in the first hours during the dissolution experiments, portlandite (CH) was

also included in the model. Additionally, to make the composition of the mortar consistent with the presence of portlandite, it was assumed that the initial C-S-H gel had a Ca/Si ratio equal to 1.667. Initial composition of the mortar in the reactive transport calculations is given in Table 4.5. More details about the calculations of the initial composition are given in section 4.4.2.1.

Table. 4.4 *Phases initially present in the mortar (830 d) calculated using the GEMS code.*

Phase	Wet process	g/100g
FA (bulk composition)	$0.926SiO_2 \cdot 0.295Al_2O_3 \cdot 0.041Fe_2O_3 \cdot 0.031CaO \cdot 0.05MgO$	6.9007
C_3S	Ca_3SiO_5	0.8834
C_2S	Ca_2SiO_4	0.1744
C_3A	$Ca_3Al_2O_6$	3.58E-05
C_4AF	$Ca_4Al_2Fe_2O_{10}$	0.9624
C-S-H	$1.67Ca(OH)_2 \cdot SiO_2 \cdot H_2O$	30.3768
Ettringite (AFt)	$Ca_6[Al(OH)_6]_2(SO_4)_3 \cdot 26H_2O$	3.3195
Portlandite (CH)	$Ca(OH)_2$	0
Gypsum	$CaSO_4 \cdot 2H_2O$	0
Calcite	$CaCO_3$	0.0946
Monosulphate (AFm)	$4CaO \cdot Al_2O_3 \cdot SO_3 \cdot 12H_2O$	0
Brucite	$Mg(OH)_2$	0
Hydrotalcite	$Mg_6Al_2CO_3(OH)_{16} \cdot 4H_2O$	1.0899
Stratlingite	$Ca_2Al_2SiO_2(OH)_{10} \cdot 3H_2O$	0
Monocarbonate (Hc)	$Ca_4[Al(OH)_6]_2(CO_3) \cdot 6H_2O$	7.7035
Hemicarbonate(Mc)	$Ca_4[Al(OH)_6]_2(CO_3)_{1/2} \cdot 5H_2O$	0
Si-hydrogarnet	$C_3(A,F)S_{0.84}H_{4.32}$ $(Ca_3Al_2Fe_2(SiO_4)_{0.84}(OH)_{8.64})$	5.7445
Quartz (sand)	SiO_2	66.037
Solution		9.8734

Table. 4.5 *Average initial composition of the mortar in the reactive transport calculations.*

Phases of the mortar	Initial volumetric fraction	Initial area ($m^2 m^{-3}_{bulk}$)
Fly ash	0.04704*	$3.0\ 10^5$
CSH-1667	0.20709	$1.6\ 10^6$
Ettringite	0.02263	$1.2\ 10^5$
Hydrotalcite-OH	0.00743	$4.3\ 10^4$
Monocarboaluminate	0.05251	$3.3\ 10^5$
Si-hydrogarnet ($C_3(A,F)S_{0.84}H_{4.32}$)	0.03916	$3.3\ 10^5$
Portlandite	0.04750	$2.9\ 10^5$
Calcite	0.00064	$5.1\ 10^3$
Quartz	0.45020	$5.4\ 10^3$
Porosity	0.125	-
*Value calculated using Eq 4.1		

The porewater composition was calculated to be in equilibrium with the hydrated phases of the mortar (Table 4.6).

4.2. 3 Mortar column experiments

Three methacrylate (PMMA) columns of 2.6 cm in length and 3 cm in diameter -2.5 cm of inner diameter- were filled with approximately 25 g of mortar grains (grain size 1-2 mm; Fig. 4.2). 0.45 μm Teflon ® filters were placed at the inlet and outlet of the columns to prevent any microparticle circulation through the inlet and outlet tubing. An extra filter was placed at the inlet of the column to homogenize the influent solution. The porosity of the columns was calculated from the difference in weight between dry and water saturated columns. This porosity does not include the internal porosity of the mortar grains which were previously saturated with water. Hence, in the saturated columns, the porosity corresponding to the water between mortar grains was about 42.5%.

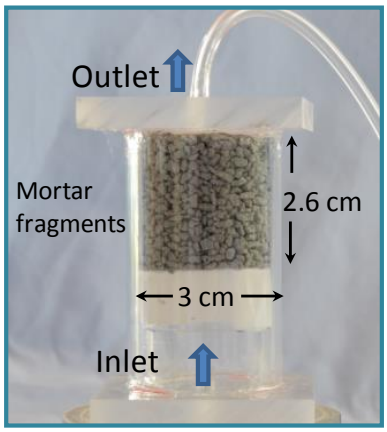

Figure 4.2. *Photograph of a mortar column.*

A peristaltic pump was used to inject Millipore MQ water from the inlet of the columns at constant flow rate, which was different in each column (0.014, 0.028 and 0.036 mL min^{-1}) and yielded residence times of 6.9, 3.5 and 2.7 h, respectively. The entire experimental setup (input and output solutions, peristaltic pump, columns and tubing) was enclosed in a glove box purged with pure N_2 (99% purity) at room temperature (23 ± 2 °C) (Fig. 4.3). Input Millipore MQ water was purged with N_2 inside the glove box to avoid carbonation. Oxygen concentration was continuously monitored by an oxygen partial pressure detector and varied from 0.1 to 0.4% O_2, being equivalent to 2-8 ppm of CO_2 according to the CO_2 content of atmospheric air. The output solutions were collected every two days and kept inside the glove box until analyzed.

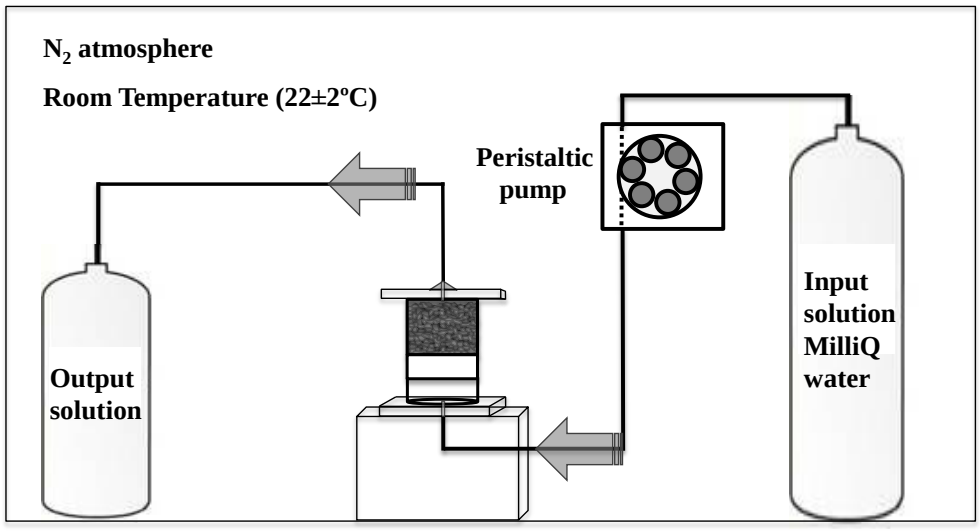

Figure 4.3. *Schematic representation of the mortar - column experimental setup.*

The three experiments lasted 3423 h and were carried out until steady state was reached. Steady state was considered to be attained when differences in the concentrations in output solutions were below 10% in consecutive leachate samples for at least 200 h.

Once the experiments were finished, isopropanol was circulated through the columns to remove the retained solution. Isopropanol was allowed to evaporate, and thereafter epoxy resin was pumped into the columns to fill the pore volume. After resin solidification, column slices at different lengths were produced by diamond disc cutting. The surfaces of the slices were polished avoiding contact with water to be examined optically and by SEM-EDS.

4.2. 4 Analysis of solutions

Input and output solution pH was measured at room temperature using a Thermo Orion Ag/AgCl electrode. Calibration was made with Crison © standard buffer solutions of pH 7.00 (K and N phosphate) and pH 9.21 (borax). The reported uncertainty is ± 0.05 pH units. After pH measurements, the output solutions were acidified to pH 3 to avoid any formation of calcium carbonate in the collected solutions.

Total concentrations of Ca, Na, K, Fe, S, Al, Mg, and Si in the input and output solutions were analyzed by Inductively Coupled Plasma Atomic Emission Spectroscopy (ICP-AES using a thermo Jarrel-Ash with CID detector and a Perkin Elmer Optima 3200RL. The accuracy of ICP-AES measurements was estimated to be around 3%. Detection limits for Ca, Na, K, Fe, S, Al, Mg and Si were 1.25 10^{-6} mol L^{-1}, 1.30 10^{-4} mol L^{-1}, $1.28 \cdot 10^{-6}$ mol L^{-1}, $3.58 \cdot 10^{-7}$ mol L^{-1}, $1.56 \cdot 10^{-6}$ mol L^{-1}, $1.85 \cdot 10^{-6}$ mol L^{-1}, $2.06 \cdot 10^{-6}$ mol L^{-1} and $4.48 \cdot 10^{-7}$ mol L^{-1}, respectively.

4.2. 5 Analysis of solids

Visual inspection of the surfaces was carried out using a Leica M125 stereomicroscope. The surfaces of carbon-coated slices were examined by Scanning Electron Microscopy (SEM) using a JEOL JSM-840 microscope and a Hitachi H-4100FE field-emission scanning microscope. X-ray fluorescence (XRF) analysis of the carbon-coated slices was carried out using a Bruker spectrometer model AXS-S2 Ranger.

4.3. Reactive transport modeling

4.3.1 Description of the reactive transport code

Reactive transport modeling was performed using CrunchFlow (Steefel, 2009). CrunchFlow includes the simulation of advective, dispersive and diffusive transport, non-isothermal transport-reaction, kinetically-controlled mineral dissolution and precipitation and reaction-induced porosity and permeability feedback to both diffusion and flow. Only a summary will be given here.

CrunchFlow solves numerically the advection-dispersion-reaction equations

$$\frac{\partial\left(\phi\left(C_i^{mob}+C_i^{inmob}\right)\right)}{\partial t}=\nabla\cdot\left(D\nabla C_i^{mob}\right)-\nabla\cdot\left(qC_i^{mob}\right)+R_i \qquad \text{Eq. 4.2}$$

$$(i=1,2,\ldots,N_{tot})$$

where ϕ is porosity, C_i^{mob} is the total concentration of mobile component or primary species i in solution (mol m^{-3}), C_i^{inmob} is the total concentration of immobile component i in solution (sorbed by surface complexation or ion exchange; mol m^{-3}), D is the combined diffusion-dispersion coefficient (m^2 s^{-1}), q is Darcy velocity (m^3 m^{-2} s^{-1}), R_i is the total reaction rate affecting component i (mol m^{-3} s^{-1}), t is time (s) and N_{tot} is the total number of independent aqueous chemical components (primary species).

The combined diffusion-dispersion coefficient D (m^2 s^{-1}) is defined as the sum of the mechanical or kinematic dispersion coefficient D^* and the effective diffusion coefficient D_e

$$D = D^* + D_e \quad \text{Eq. 4.3}$$

The kinematic dispersion coefficient is written as

$$D_{ij}^* = \alpha_T |q| + (\alpha_L - \alpha_T) \frac{q_i q_j}{|q|} \quad \text{Eq. 4.4}$$

where α_L and α_T are the longitudinal and transverse dispersivities, respectively, and q is the magnitude of the Darcy velocity. The model assumes that the principal direction of flow is aligned with the grid, i.e. D_{ij}^* is a diagonal matrix.

Effective diffusion coefficient (D_e; $m^2\ s^{-1}$) was calculated making use of the Archie's Law with a cementation exponent (m) equal to 3 for cement (Trotignon et al., 2007). This parameter specifies a porosity-dependent tortuosity according to

$$D_e = \phi^m D_0 \quad \text{Eq. 4.5}$$

where D_o is the molecular diffusion coefficient in pure water ($10^{-9}\ m^2\ s^{-1}$) and ϕ is the porosity.

The expression of the total reaction rate for component i, R_i, is

$$R_i = -\sum_m v_{im} R_m \quad \text{Eq. 4.6}$$

where R_m (mol $m^{-3}_{bulk}\ s^{-1}$) is the rate of precipitation ($R_m > 0$) or dissolution ($R_m < 0$) of solid phase m per unit volume of rock, and v_{im} is the number of moles of i per mole of mineral m. Since mineral reactions are described using kinetic rate laws, initial mineral surface areas and several reaction rate parameters have to be supplied by the user as input. In the simulations, the reaction rate laws that have been used for the phases present in the mortar are of the form

$$R_m = -A_m \sum_{terms} k_m \, a_{H^+}^{n_{H^+}} \left(\prod_i a_i^{n_i} \right) f_m(\Delta G) \qquad \text{Eq. 4.7}$$

where A_m is the mineral surface area ($m^2_m \, m^{-3}_{bulk}$), k_m is the reaction rate constant (mol $m^{-2} \, s^{-1}$) at the temperature of interest, $a_{H^+}^{n_{H^+}}$ is the term describing the effect of pH on the rate, $a_i^{n_i}$ is a term describing a catalytic/inhibitory effect by another species on the rate and $f_m(\Delta G)$ is the function describing the dependence of the rate on solution saturation state and is in the form

$$f_m(\Delta G) = (1 - (\Omega)^{m_2})^{m_1} \qquad \text{Eq. 4.8}$$

in which ΔG is the Gibbs energy of the reaction (J mol^{-1}), Ω is the ionic activity product (IAP) of the solution with respect to the mineral divided by K_{eq} (equilibrium constant for that mineral reaction), and m_1 and m_2 are empirical exponents. The summation term indicates that several parallel rate laws may be used to describe the dependence of the rate on pH or on other species. In the simulations, the reaction rate law for the C-S-H gel is in the form that was considered in Chapter 2

$$R_m = -A_m k_m (1 - \Omega) \qquad \text{Eq. 4.9}$$

There are two options to calculate changes in mineral surface area due to reaction: (1) When specifying bulk surface area ($m^2_m \, m^{-3}_{bulk}$) as input parameter changes are calculated according to

$$A = A^{initial} \left(\phi_m \Big/ \phi_m^{initial} \right)^{\frac{2}{3}} \left(\phi \Big/ \phi^{initial} \right)^{\frac{2}{3}} (dissolution) \qquad \text{Eq. 4.10}$$

$$A = A^{initial} \left(\phi \Big/ \phi^{initial} \right)^{\frac{2}{3}} (precipitation) \qquad \text{Eq. 4.11}$$

where ϕ refers to the porosity and ϕ_m refers to the individual mineral volume fraction. The inclusion of a 2/3 dependence on porosity is chiefly to ensure that as the porosity goes to 0, so too does the mineral surface area available for reaction. This formulation is used primarily for primary minerals (that is, minerals with initial volume fractions > 0). For secondary minerals which precipitate, the value of the initial bulk surface area specified is used as long as precipitation occurs—if this phase later dissolves, the above formulation is used, but with an arbitrary "initial volume fraction" of 0.01.

(2) When specifying specific surface area ($m^2\ g^{-1}$) as input parameter, reactive surface area is calculated according to

$$A_{bulk} = \phi_m A_{sp} \frac{MW_m}{V_m} \qquad \text{Eq. 4.12}$$

where MW_m and V_m are the molecular weight (g mol^{-1}) and molar volume ($m^3\ mol^{-1}$) of the solid phase, respectively. Additionally, for secondary phases (initial ϕ_m equal to 0) a "threshold mineral volume fraction" has to be specified, to be used when ϕ_m is smaller than the threshold value. This is the option used for the different C-S-H gel compositions.

4.3.2 Modeling of mortar dissolution under advective flux

4.3.2.1. Conceptual model

To simulate the experimental column data with the 2D CrunchFlow model several considerations had to be taken into account. The system was divided into two parts: immobile zone (mortar grains where solute transport takes place only by diffusion) and mobile zone (pore space where water circulates across the mortar grains). In order to take these considerations into account, the column model was designed with two concentric cylinders. An internal one with mortar and an external one filled with water to allow diffusion through the mortar and advection along the pore space (Fig. 4.4). For the immobile zone, the radius was considered to equal the radius of a mortar grain (7.5×10^{-4} m).

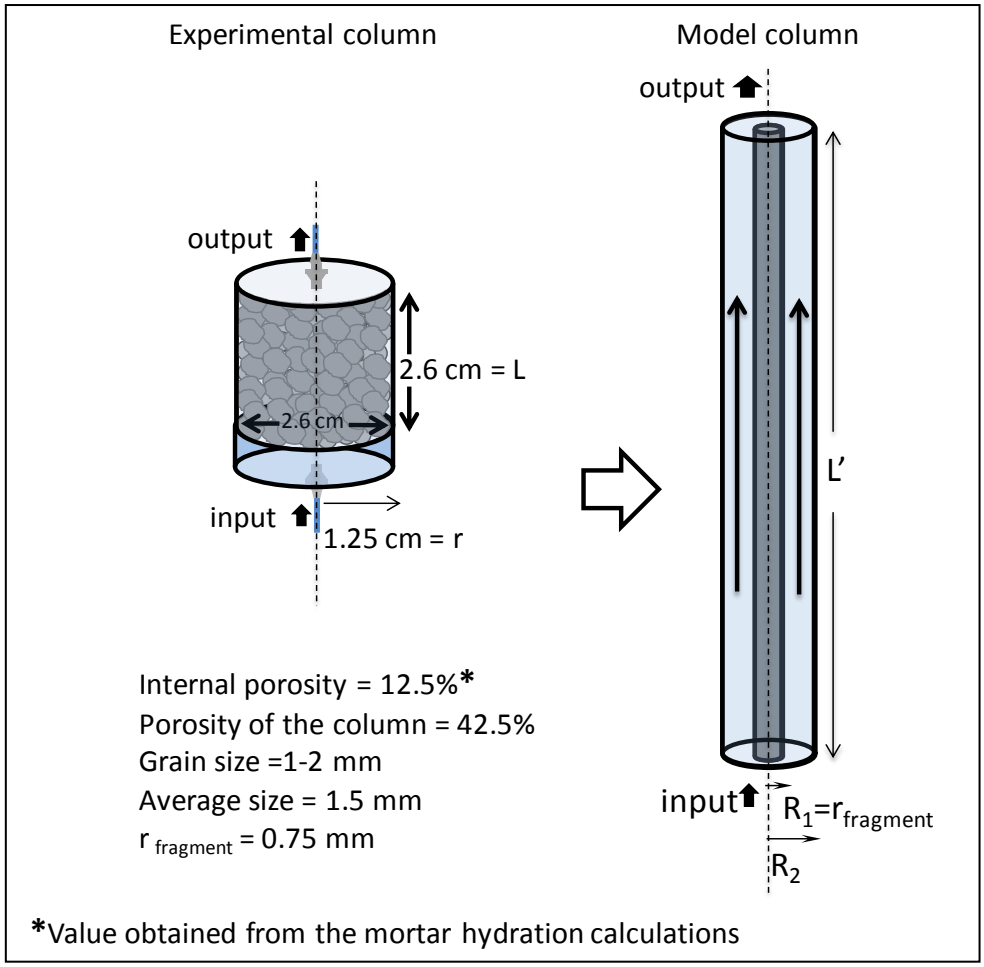

Figure 4.4. *Schematic representation of the experimental mortar column and the model setup.*

To calculate the dimensions of the model column (*L'* and R_2), the volume of both the experimental and model columns was considered to be the same

$$V_{TOT} = \pi \cdot r^2 \cdot L = \pi \cdot R_2^2 \cdot L' \qquad \text{Eq. 4.13}$$

where *r* and *L* are equal to 0.0125 m and 0.026 m, respectively. The volume for both columns equals $1.27 \cdot 10^{-5}$ m^3. R_2 was calculated by means of the porosity of the system (0.425)

$$\phi = \frac{V_{H_2O}}{(V_{H_2O} + V_{Mortar})} = \frac{\pi(R_2^2 - R_1^2)L'}{\pi R_2^2 L'} = \frac{(R_2^2 - R_1^2)}{R_2^2} \qquad \text{Eq. 4.14}$$

resulting in R_2 equal to $9.89 \cdot 10^{-4}$ m and *L'* equal to 4.13 m. The width of the mobile zone was 2.39×10^{-4} m (the difference between R_1 and R_2).

The contact area between grains and flowing water in the experiment (area per bulk volume) is given by

$$A_{g-w-exp} = \frac{A_g}{V_g}(1-\phi) = \frac{3}{R_1}(1-\phi) \qquad \text{Eq. 4.15}$$

where Ag is area of grains per bulk volume (m^2m^{-3}), Vg is volume of grains per bulk volume (m^3m^{-3}). Using the experimental value of R_1, and ϕ, $A_{g\text{-}w\text{-}exp}$ equals to 2300 m^2m^{-3}.

In the model, this contact area ($A_{g\text{-}w\text{-}model}$) is given by

$$A_{g-w-model} = \frac{2\pi R_1 L'}{\pi R_2^2 L'} = \frac{2R_1}{R_2^2} \qquad \text{Eq. 4.16}$$

which results in 1530 m^2m^{-3}.

Therefore, there is slightly less contact area in the simplified model than in actuality. However, the difference is small and the error in reactivities and diffusive transport should be relatively insignificant.

Figure 4.5 shows schematically the dimensions of the mesh which were calculated to represent the experimental column. This is a 2D mesh, with a cylindrical geometry around the y axis. The domain representing the mortar was divided into 10 and 25 nodes in the x and y directions, respectively, yielding a distance between nodes of $7.5 \cdot 10^{-5}$ m and 0.1652 m in the x and y directions, respectively. The mesh in the mobile zone consisted of 1 node in the x direction and 25 nodes in the y direction. Flow velocities in the mobile water zone were calculated to obtain the same flow residence times as in the experiments.

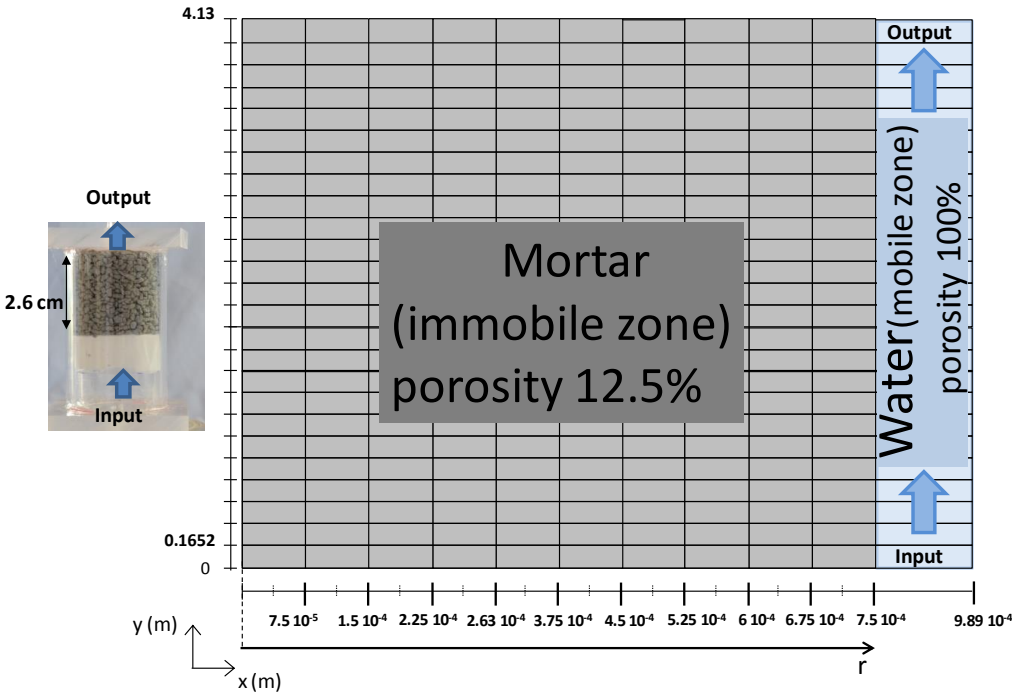

Figure 4.5. *Schematic representation of the numerical domain.*

The composition of the initial porewater was calculated with GEMS by considering the solution at equilibrium with respect to the phases present in the mortar (Table 4.6). Due to the fact that the experimental concentration of Ca during the first hours was higher than the concentration calculated by GEMS, portlandite and C-S-H gel with high Ca/Si ratio were also included in the system. This seems to indicate that the degree of hydration of the mortar was lower than predicted by GEMS. Feldman et al. (1990) found a similarly low degree of hydration in high-volume fly ash / cement pastes (fly ash/cement ratio of 1.27); considerable amounts of $Ca(OH)_2$ and fly ash remaining unreacted after 91 days of hydration. The concentrations for the rest of the different ions were constrained by equilibrium with the solid phases (Table 4.6), except for Na and K, whose concentrations were considered to be those calculated with GEMS. The composition of the injected solution was that of Millipore MQ water in a CO_2-free atmosphere (pH = 7).

Table. 4.6 *Considered composition of the initial porewater in the column.*

Component	Concentration (mol/L)	Equilibrium constraint
Ca^{2+}	$4.176\ 10^{-4}$	Portlandite
$SiO_{2(aq)}$	$2.852\ 10^{-4}$	CSH-1667
HCO^{3-}	$2.751\ 10^{-4}$	Calcite
SO_4^{2}-	$2.935\ 10^{-3}$	Ettringite
Al^{3+}	$5.806\ 10^{-4}$	Monocarboaluminate
Fe^{3+}	$3.310\ 10^{-7}$	Si-hydrogarnet ($C_3(A,F)S_{0.84}H_{4.32}$)
Mg^{2+}	$1.000\ 10^{-10}$	Hydrotalcite
Na^{+}	$4.575\ 10^{-2}$	-
K^{+}	0.118	-
pH	13.076	Charge balance

36 species in solution and 26 solid phases were taken into account in the calculations. All the equilibrium constants at 25ºC for aqueous species (Table 4.7) and calcite and quartz (Table 4.8) were taken from the database included in CrunchFlow, which is based on the EQ/6 database (Wolery et al, 1990). The log K_{eq} values for the C-S-H gel were obtained from the solid solution model in Kulik and Kersten (2001), and those for hydrotalcite-OH and monocarbonaluminate from Lothenbach et al. (2008). The log K_{eq} value and the molar volume for Si-hydrogarnet ($C_3(A,F)S_{0.84}H_{4.32}$) phase were calculated assuming an ideal solid solution between $C_3AS_{0.84}H_{4.32}$ and $C_3FS_{0.84}H_{4.32}$ from the CEMDATA2013 database (Dilnesa et al., 2014). The log K_{eq} values for portlandite and ettringite were obtained from Hummel et al. (2002) and cemdata07 database (Matchei et al., 2007; Lothenbach et al., 2008b), respectively. Activity coefficients were calculated using the extended Debye-Hückel formulation (b-dot model), with parameters from the same database. The activity of water was taken as unity.

The rate constant for portlandite (k) was $10^{-5.4}$ mol m^{-2} s^{-1} as reported in Bullard et al. (2010). The rate constants for quartz was obtained from Bandstra et al., (2008) and for calcite from Palandri and Kharaka (2004). Rate parameters are listed in Table 4.9 where the rates-pH dependence is specified. The C-S-H solid solution was discretized into 19 different stoichiometries, ranging from Ca/Si = 1.67 to Ca/Si = 0.83 (Table 4.8) as explained in Chapter 2. The dissolution rate constants of the discretized C-S-H gel were obtained in Chapter 2. For the rest of the minerals present in the mortar (ettringite, monocarboaluminate, Si-hydrogarnet, hydrotalcite-OH and fly ash) the rate constants were obtained from the fitting of the model to the experimental data. For the particular case of the fly ash, irreversible kinetics was assumed (no dependence on solution saturation state).The value of the rate constant for fly ash was fixed to be 10^{-12} mol m^{-2} s^{-1} to allow only minor variation in the fly ash content, as observed by SEM. Using this value, only 1.5 % of the fly ash volumetric fraction dissolves. Greater values generate non-realistic variations of its volumetric fraction. With a k value of 10^{-11} mol m^{-2} s^{-1} 15% of fly ash dissolves. With k values smaller than 10^{-12} mol m^{-2} s^{-1} dissolution is insignificant, but the Al and Fe output concentrations are underestimated.

Table. 4.7 *Equilibrium constants (log K_{eq}) and stoichiometric coefficients for equilibria in solution. Reactions are written as the destruction of 1 mol of the species in the first column.*

Species	log K	Stoichiometric Coefficient										
		Ca^{2+}	$SiO_{2(aq)}$	H^+	HCO_3^-	SO_4^{2-}	Al^{3+}	Fe^{3+}	Mg^{2+}	Na^+	K^+	H_2O
AlO_2^-	2.29E+01	0.00	0.00	-4.00	0.00	0.00	1.00	0.00	0.00	0.00	0.00	2.00
$Al(OH)_{3(aq)}$	1.64E+01	0.00	0.00	-3.00	0.00	0.00	1.00	0.00	0.00	0.00	0.00	3.00
$AlOH^{2+}$	4.96E+00	0.00	0.00	-1.00	0.00	0.00	1.00	0.00	0.00	0.00	0.00	1.00
$CO_{2(aq)}$	-6.34E+00	0.00	0.00	1.00	1.00	0.00	0.00	0.00	0.00	0.00	0.00	-1.00
CO_3^{2-}	1.03E+01	0.00	0.00	-1.00	1.00	0.00	0.00	0.00	0.00	0.00	0.00	0.00
$CaCO_{3(aq)}$	7.01E+00	1.00	0.00	-1.00	1.00	0.00	0.00	0.00	0.00	0.00	0.00	0.00
$CaHCO_3^+$	-1.04E+00	1.00	0.00	0.00	1.00	0.00	0.00	0.00	0.00	0.00	0.00	0.00
$CaOH^+$	1.29E+01	1.00	0.00	-1.00	0.00	0.00	0.00	0.00	0.00	0.00	0.00	1.00
$CaSO_{4(aq)}$	-2.10E+00	1.00	0.00	0.00	0.00	1.00	0.00	0.00	0.00	0.00	0.00	0.00
$Fe(OH)_2^+$	5.67E+00	0.00	0.00	-2.00	0.00	0.00	0.00	1.00	0.00	0.00	0.00	2.00
$Fe(OH)_{3(aq)}$	1.20E+01	0.00	0.00	-3.00	0.00	0.00	0.00	1.00	0.00	0.00	0.00	3.00
$Fe(OH)_4^-$	2.16E+01	0.00	0.00	-4.00	0.00	0.00	0.00	1.00	0.00	0.00	0.00	4.00
$FeCO_3^+$	6.18E-01	0.00	0.00	-1.00	1.00	0.00	0.00	1.00	0.00	0.00	0.00	0.00
$FeOH^{2+}$	2.19E+00	0.00	0.00	-1.00	0.00	0.00	0.00	1.00	0.00	0.00	0.00	1.00
$H_2SiO_4^{2-}$	2.30E+01	0.00	1.00	-2.00	0.00	0.00	0.00	0.00	0.00	0.00	0.00	2.00
$HSiO_3^-$	9.94E+00	0.00	1.00	-1.00	0.00	0.00	0.00	0.00	0.00	0.00	0.00	1.00
KSO_4^-	-8.75E-01	0.00	0.00	0.00	0.00	1.00	0.00	0.00	0.00	0.00	1.00	0.00
$MgCO_{3(aq)}$	7.36E+00	0.00	0.00	-1.00	1.00	0.00	0.00	0.00	1.00	0.00	0.00	0.00
$MgHCO_3^+$	-1.03E+00	0.00	0.00	0.00	1.00	0.00	0.00	0.00	1.00	0.00	0.00	0.00
$MgOH^+$	1.14E+01	0.00	0.00	-1.00	0.00	0.00	0.00	0.00	1.00	0.00	0.00	0.00
$MgSO_{4(aq)}$	-2.41E+00	0.00	0.00	0.00	0.00	1.00	0.00	0.00	1.00	0.00	0.00	0.00
$NaCO_3^-$	9.82E+00	0.00	0.00	-1.00	1.00	0.00	0.00	0.00	0.00	1.00	0.00	0.00
$NaHCO_{3(aq)}$	-1.56E-01	0.00	0.00	0.00	1.00	0.00	0.00	0.00	0.00	1.00	0.00	0.00
$NaSO_4^-$	-8.20E-01	0.00	0.00	0.00	0.00	1.00	0.00	0.00	0.00	1.00	0.00	0.00
OH^-	1.40E+01	0.00	0.00	-1.00	0.00	0.00	0.00	0.00	0.00	0.00	0.00	1.00

Table. 4.8 *Equilibrium constants (log K_{eq}) and stoichiometric coefficients for mineral reactions. Reactions are written as the dissolution of 1 mol of mineral.*

Mineral	log K	V molar (cm^3mol^{-1})	Stoichiometric coefficient										
			Ca^{2+}	$SiO_{2(aq)}$	H^+	HCO_3^-	SO_4^{2-}	Al^{3+}	Fe^{3+}	Mg^{2+}	Na^+	K^+	H_2O
CSH-1667	2.91E+01	73.10	1.67	1.00	-3.34	0.00	0.00	0.00	0.00	0.00	0.00	0.00	4.34
CSH-165	2.87E+01	72.66	1.65	1.00	-3.30	0.00	0.00	0.00	0.00	0.00	0.00	0.00	4.30
CSH-160	2.76E+01	71.38	1.60	1.00	-3.20	0.00	0.00	0.00	0.00	0.00	0.00	0.00	4.19
CSH-155	2.64E+01	70.11	1.55	1.00	-3.10	0.00	0.00	0.00	0.00	0.00	0.00	0.00	4.08
CSH-150	2.53E+01	68.83	1.50	1.00	-3.00	0.00	0.00	0.00	0.00	0.00	0.00	0.00	3.97
CSH-145	2.42E+01	67.55	1.45	1.00	-2.90	0.00	0.00	0.00	0.00	0.00	0.00	0.00	3.86
CSH-14	2.31E+01	66.27	1.40	1.00	-2.80	0.00	0.00	0.00	0.00	0.00	0.00	0.00	3.75
CSH-135	2.20E+01	64.99	1.35	1.00	-2.70	0.00	0.00	0.00	0.00	0.00	0.00	0.00	3.64
CSH-130	2.10E+01	63.71	1.30	1.00	-2.60	0.00	0.00	0.00	0.00	0.00	0.00	0.00	3.53
CSH-125	1.99E+01	62.43	1.25	1.00	-2.50	0.00	0.00	0.00	0.00	0.00	0.00	0.00	3.42
CSH-12	1.88E+01	61.16	1.20	1.00	-2.40	0.00	0.00	0.00	0.00	0.00	0.00	0.00	3.31
CSH-115	1.77E+01	59.88	1.15	1.00	-2.30	0.00	0.00	0.00	0.00	0.00	0.00	0.00	3.19
CSH-110	1.67E+01	58.60	1.10	1.00	-2.20	0.00	0.00	0.00	0.00	0.00	0.00	0.00	3.08
CSH-105	1.56E+01	57.32	1.05	1.00	-2.10	0.00	0.00	0.00	0.00	0.00	0.00	0.00	2.97
CSH-10	1.46E+01	56.04	1.00	1.00	-2.00	0.00	0.00	0.00	0.00	0.00	0.00	0.00	2.86
CSH-095	1.36E+01	54.77	0.95	1.00	-1.90	0.00	0.00	0.00	0.00	0.00	0.00	0.00	2.75
CSH-090	1.25E+01	53.49	0.90	1.00	-1.80	0.00	0.00	0.00	0.00	0.00	0.00	0.00	2.64
CSH-085	1.15E+01	52.21	0.85	1.00	-1.70	0.00	0.00	0.00	0.00	0.00	0.00	0.00	2.53
CSH-083	1.12E+01	51.70	0.83	1.00	-1.66	0.00	0.00	0.00	0.00	0.00	0.00	0.00	2.49
Calcite	1.85E+00	36.93	1.00	0.00	-1.00	1.00	0.00	0.00	0.00	0.00	0.00	0.00	0.00
Quartz	-4.01E+00	22.68	0.00	1.00	0.00	0.00	0.00	0.00	0.00	0.00	0.00	0.00	0.00
Ettringite	5.68E+01	707	6.00	0.00	-12.00	0.00	3.00	2.00	0.00	0.00	0.00	0.00	30.00
Hydrotalcite	7.37E+01	220	0.00	0.00	-14.00	0.00	0.00	2.00	0.00	4.00	0.00	0.00	5.00
monocarboaluminate	8.06E+01	263	4.00	0.00	-13.00	1.00	0.00	2.00	0.00	0.00	0.00	0.00	3.00
Si-hydrogarnet ($C_3(A,F)S_{0.84}H_{4.32}$)	7.09E+01	145	3.00	0.84	-12.00	0.00	0.00	1.00	1.00	0.00	0.00	0.00	0.32
Portlandite	2.28E+01	33.05	1.00	0.00	-2.00	0.00	0.00	0.00	0.00	0.00	0.00	0.00	2.00

Table. 4.9 *Rate constants (log k) and parameters of calcite (Palandri and Kharaka, 2004), quartz (Bandstra et al., 2008), portlandite (Bullard et al., 2010) and fly ash.*

Mineral	log k (mol m^{-2} s^{-1})	$a_{H^+}^{n_{H^+}}$	m_1	m_2
Calcite	-0.3	1	1.0	1.0
	-5.81	-	1.0	1.0
Quartz	-11.4	0.3	1.0	1.0
	-14.9	-0.4	1.0	1.0
Portlandite	-5.14	-	1.0	1.0
Fly ash	-12	-	1.0	1.0

Two parallel rates laws are used for calcite and quartz to describe the different pH dependences under acid and alkaline conditions (see Eq. 4.7).

4.4. Results and discussion

4.4.1 Aqueous chemistry

Variation with time of the output concentrations and output pH in the column experiments is depicted in Figure 4.6. The experimental conditions and steady-state results are summarized in Table 4.10. Overall, in the three experiments the temporal variation of the output concentrations and pH was similar. An initially high release of Ca was observed. The concentration of Ca sharply diminished for 1000 h to achieve steady state. The high concentration of Ca at early times can only be explained if some portlandite that did not react with the fly ash remained in the system. Si was slowly released mainly from the C-S-H dissolution as Ca decreased to approach steady state. The Al concentration initially increased to slightly decrease and reach steady state. The Fe concentration remained approximately constant. The Mg concentration was progressively increasing to reach steady state. Na concentration decreased abruptly. K concentration tended to decrease for 1000 h down to very small values. S increased initially to thereafter decrease and achieve steady state. Output pH decreased to reach steady state at an approximate value of 9.

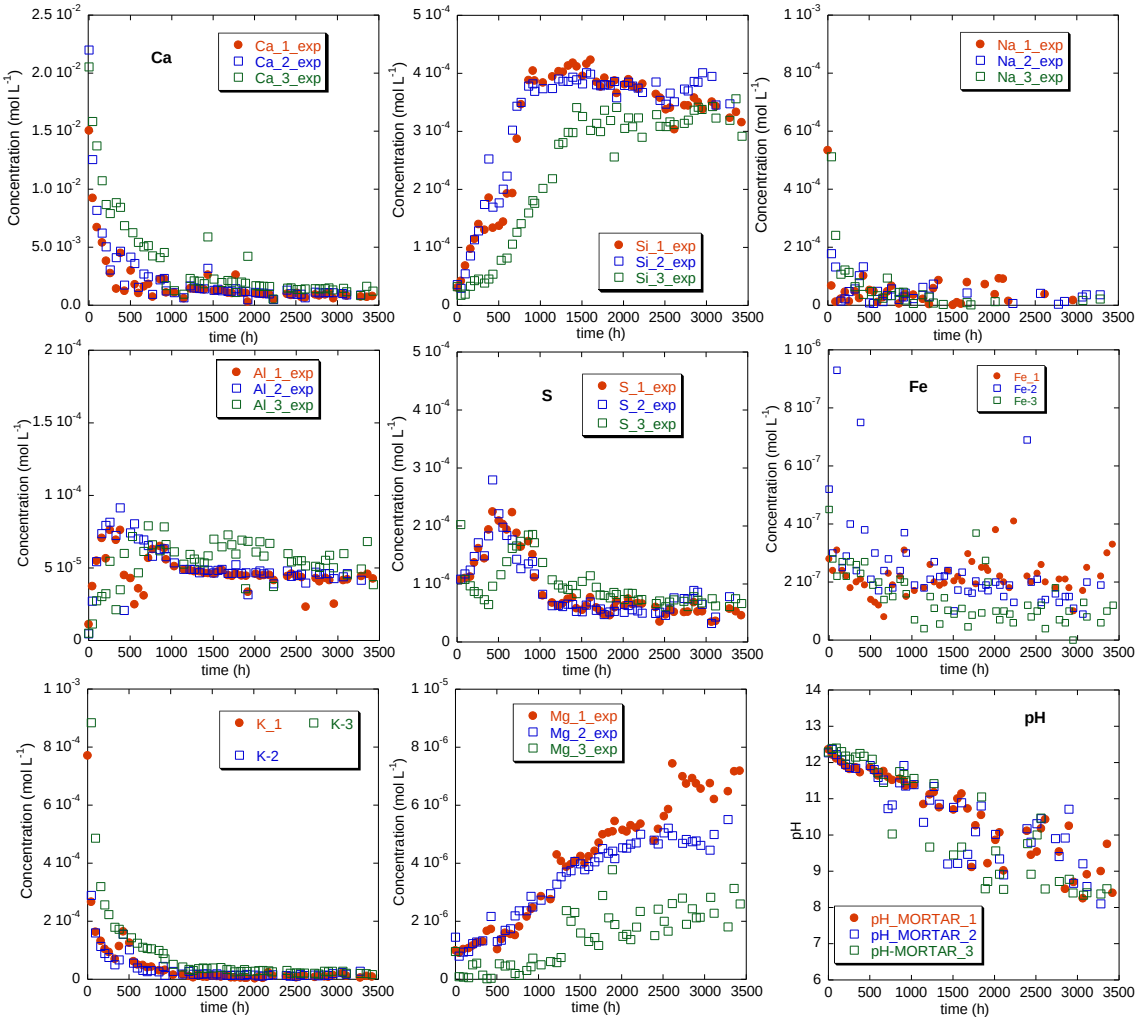

Figure 4.6. *Variation of the output concentrations and output pH with time in the three column experiments.*

Table. 4.10 *Experimental conditions and steady-state results of the column experiments.*

Experiment	Mortar_1	Mortar_2	Mortar_3
Time (days)	143	143	143
Flow rate (mL min^{-1})	0.036	0.028	0.014
pH out	9.75 ± 0.75	9.97 ± 0.81	9.92 ± 0.77
Ca out (μM)	792.12 ± 23.76	882.34 ± 26.47	1221.42 ± 36.64
Si out (μM)	315.86 ± 9.47	347.77 ± 10.43	291.61 ± 8.74
Na out (μM)	(*)	36.54 ± 1.09	(*)
K out (μM)	9.09 ± 0.27	28.16 ± 0.84	16.38 ± 0.49
S out (μM)	45.74 ± 1.37	78.06 ± 2.34	66.37 ± 1.99
Al out (μM)	42.58 ± 1.27	41.51 ± 1.24	38.53 ± 1.15
Mg out (μM)	7.19 ± 0.21	5.51 ± 0.16	2.60± 0.08
Fe out (μM)	0.33 ± 0.01	0.19 ± 0.006	0.12 ± 0.004
(*) below detection limit			
The weight of the mortar grains was ≈10 g in the three columns			

4.4.2 Mortar grains

Figures 4.7a and 4.7b show one of the columns before and after the experiment. After the experiments, the existence of some dark material was mostly observed at the inlet, between the column wall and the grains (Fig. 4.7c).

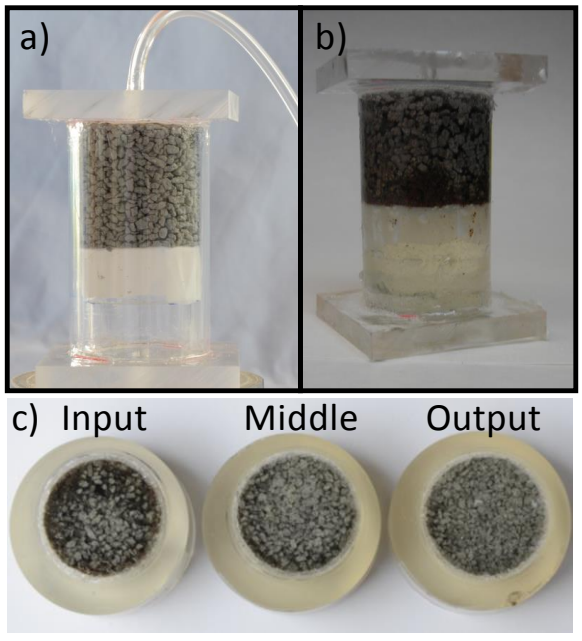

Figure 4.7. *Photographs of a column experiment: a) before, b) after the experiment, and c) slices cut at different column length after the experiment.*

Two zones along the length of the column could be distinguished: near the inlet with dark precipitates and near the outlet where no alteration of the grains was visually observed. From a detailed visual inspection, it was observed that the dark precipitates between the grains were mainly residing close to the column wall (Fig. 4.8).

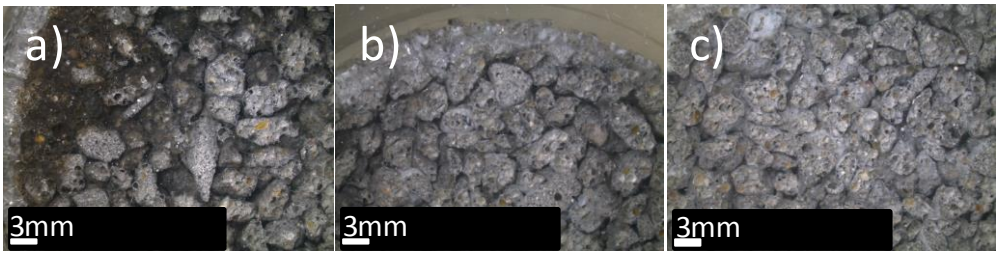

Figure 4.8. *Photographs of reacted mortar using the Leica M125 stereomicroscope: a) at the inlet of the column (≈ 0.86 cm) deposition of dark precipitate was observed near the column wall. No precipitate was observed at the middle of the column (≈ 1.72 cm) (b) nor at the top (≈ 2.60 cm) (c).*

Qualitative XRF analysis of the polished surface of the column slices showed that differences in the Fe concentration at different lengths of the column could be observed (Fig 4.9). In the inlet of the column (Figs. 4.9a and b), zonation is observed as being the highest concentration of Fe close to the column wall corresponding with the dark precipitates (red and orange zones). In the middle of the column no high concentration of Fe is observed (blue and green zones; Fig 4.9c).

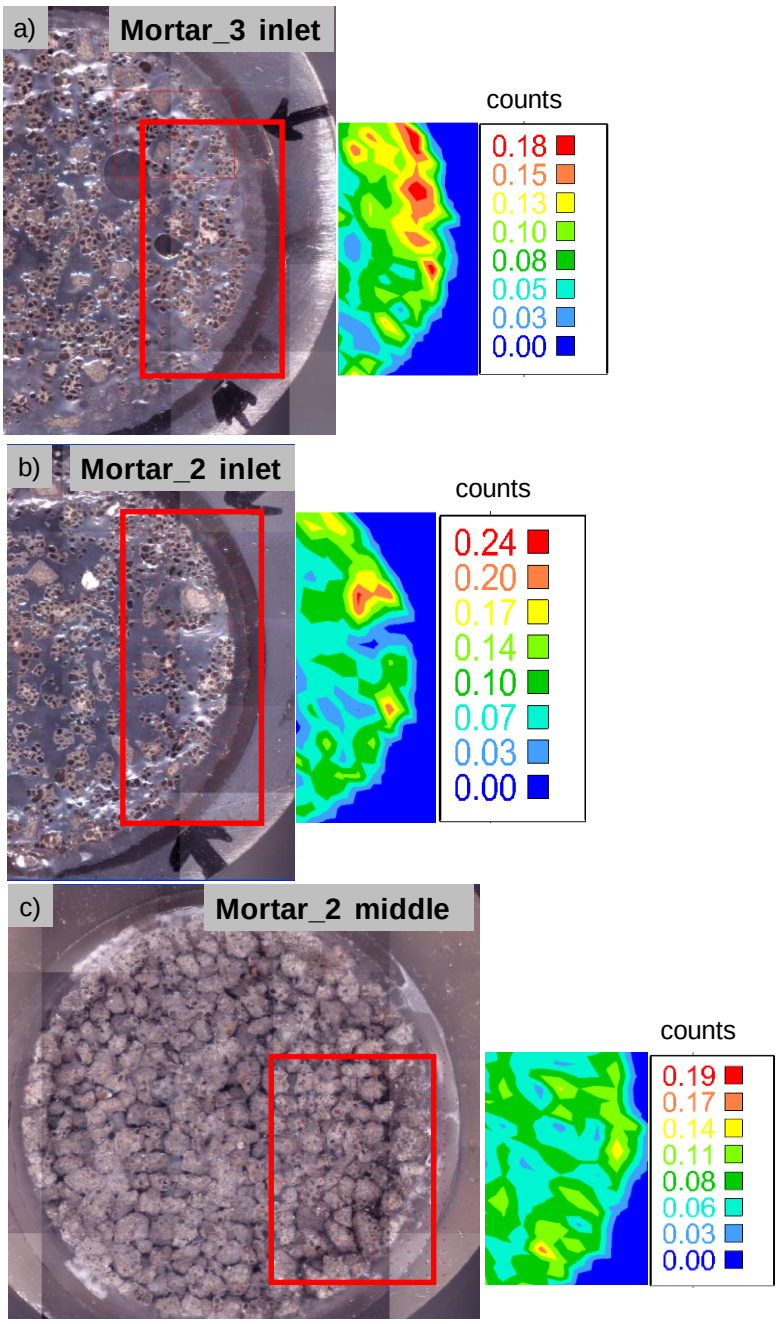

Figure 4.9. *Photographs and XRF analysis of the column slices for a) inlet of the experiment Mortar_3; b) inlet of the experiment Mortar_2 and c) middle of the experiment Mortar_2.*

The polished surface of the bottom slice of the column (input) was examined by SEM-EDX (Fig. 4.10). The images showed the presence of uniform distribution of quartz grains in a cement matrix (Fig. 4.10a). In the cement matrix, unreacted fly ash particles (small spheres) were observed. The dark precipitates were found to be iron-rich compounds deposited on the surface of the quartz grains (Fig. 4.10b).

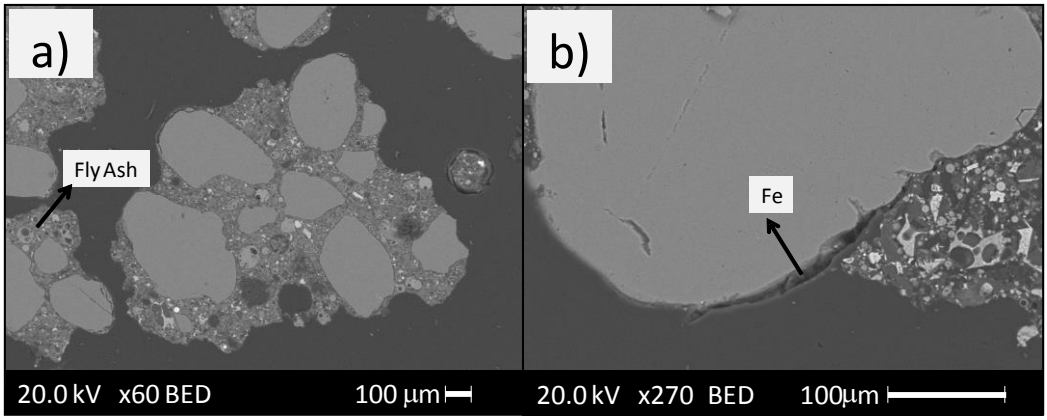

Figure 4.10. *SEM (backscattered electron-BSE) images of the polished bottom slice of the column experiment MORTAR_1: a) Cement paste, quartz aggregates and some fly ash particles and b) presence of iron-rich precipitates over the grains.*

4.4.2 Reactive transport modeling

4.4.2.1 Fitting of the model parameters

The reactive transport simulations, together with the experimental variation of the output concentrations and output pH of the representative experiment MORTAR_1, are shown in Figure 4.11. Table 4.11 gives the values of the parameters used in the simulations. The rate constant values obtained for ettringite, monocarboaluminate, fly ash and Si-hydrogarnet were those that allow fit the output concentrations. Nonetheless, these values of rate constant should be compared with values obtained experimentally (e.g., performance of flow-through experiments).

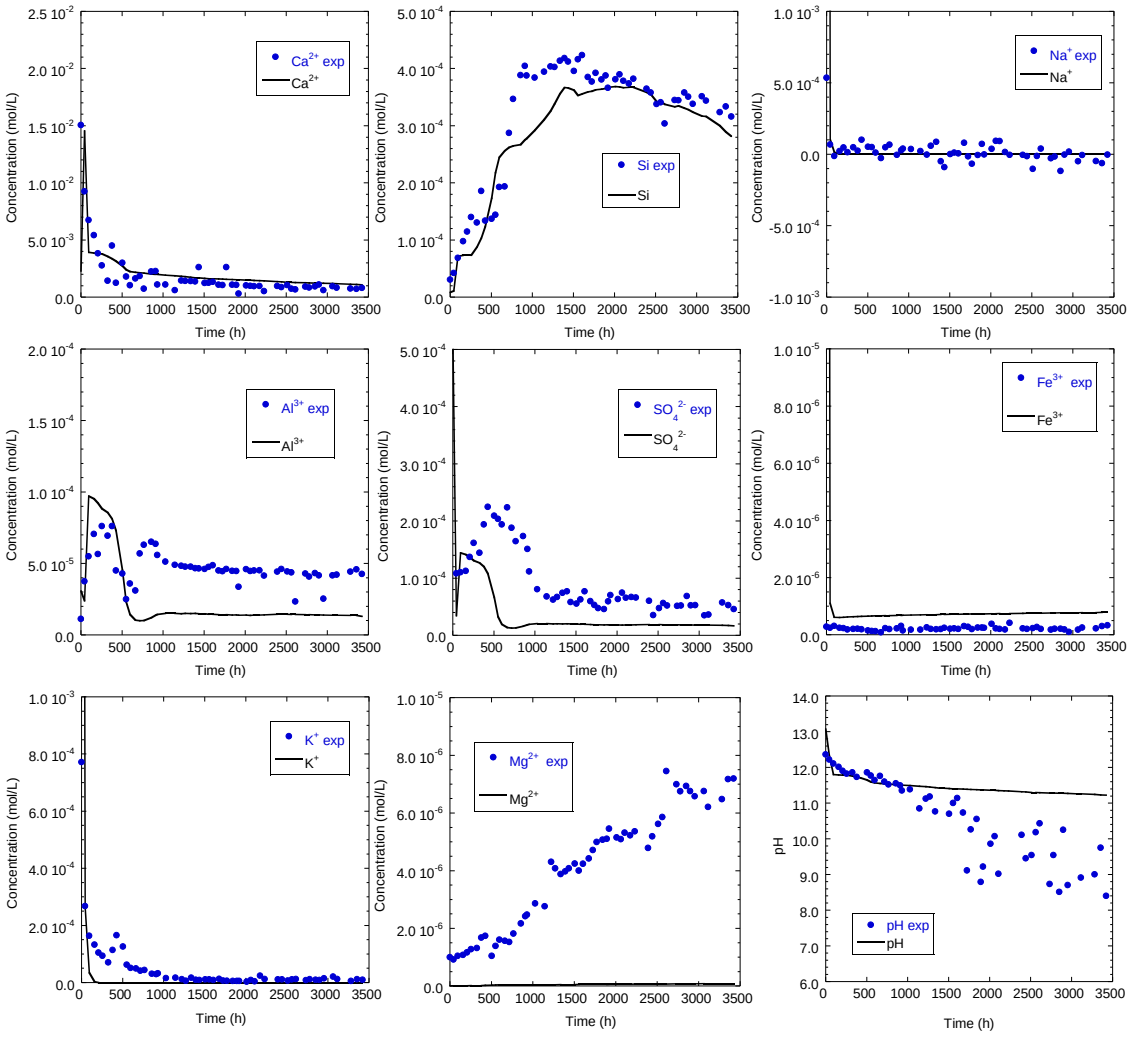

Figure 4.11. *Experimental and simulated variation of the output concentration and output pH with time in experiment MORTAR_1.*

Due to the complexity of the system, reasonable fitting was assumed when the model fitted the concentrations of major elements (e.g. Ca, Si, Na and K). Thus, the temporal variation of the Ca, Si and Na concentrations was reasonably fitted. The concentrations of Al and S were underestimated. Iron was slightly overestimated (although concentrations are very small and close to the detection limit). Precipitation of secondary phases, such as ferrihydrite ($Fe(OH)_3$), gibbsite ($Al(OH)_3$) and amorphous SiO_2, was included in the model. According to the predictions, ferrihydrite was in equilibrium near the inlet for the first three hours. In the rest of the column, the solution was undersaturated with respect to these phases. K concentration in the model results was understimated as the modeled depletion of K concentration occurs before (around 300 h) the experimental one. K was considered to be conservative in the model, but uptake by the C-S-H gel cannot be disregarded (Lothenbach et al., 2012). Fitting of Mg was not attempted because its concentration was also nearly that of the ICP-AES detection limit

($2.06 \cdot 10^{-6}$ mol L^{-1}). pH was adequately fitted up to ≈ 1300 h. Thereafter, the simulation overestimates the experimental output pH. As discussed previously, these lower pH values are more susceptible to be modified by carbonation after sampling.

Table. 4.11 *Experimental and model parameters.*

Experimental parameters		Experiments		
		Mortar_1	**Mortar_2**	**Mortar_3**
Experimental volumetric flux (mL min^{-1})		0.036	0.028	0.014
Flow (mL min^{-1})		0.02749	0.02137	0.01034
Fitted parameters				
Initial effective diffusion coefficient (De) (m^2s^{-1})		1.12E-13	5.39E-14	1.95E-14
Dispersivity, mobile water (m^2s^{-1})		0.16612		
Phases	Rate constants (log k, mol m^{-2} s^{-1})	Initial volumetric fraction		
Fly ash [(a)]	-12.00	0.04717	0.04692	
CSH-1667 [(b)]	-8.40	0.20766	0.20652	
CSH-165 [(b)]	-8.47	-	-	
CSH-160 [(b)]	-8.53	-	-	
CSH-155 [(b)]	-8.53	-	-	
CSH-150 [(b)]	-8.56	-	-	
CSH-145 [(b)]	-8.67	-	-	
CSH-140 [(b)]	-8.89	-	-	
CSH-135 [(b)]	-9.20	-	-	
CSH-130 [(b)]	-9.58	-	-	
CSH-125 [(b)]	-9.98	-	-	
CSH-120 [(b)]	-10.36	-	-	
CSH-115 [(b)]	-10.67	-	-	
CSH-110 [(b)]	-10.88	-	-	
CSH-105 [(b)]	-10.97	-	-	
CSH-100 [(b)]	-10.95	-	-	
CSH-095 [(b)]	-10.86	-	-	
CSH-090 [(b)]	-10.79	-	-	
CSH-085 [(b)]	-10.87	-	-	
CSH-083 [(b)]	-10.99	-	-	
Ettringite[(c)]	-8.80	0.02269	0.02257	
Hydrotalcite-OH [(c)]	-8.50	0.00745	0.00741	
Monocarboaluminate [(c)]	-13.50	0.05266	0.05237	
Si-hydrogarnet ($C_3(A,F)S_{0.84}H_{4.32}$) [(c)]	-12.80	0.03927	0.03905	
Portlandite [(d)]	-	0.04500	0.0500	
Calcite[(d)]	-	0.00065	0.00064	
Quartz[(d)]	-	0.45144	0.44897	

[(a)] fixed; [(b)] taken from Chapter 2; [(c)] fitted; [(d)]Table 4.9

The volumetric fraction and the specific surface area of the portlandite were used to model Ca concentration at early stages. Volumetric fractions of the other phases were recalculated from the hydration calculation results (GEMS) after adding portlandite in the system, keeping the porosity of the mortar grains at 12.5 %. Initial mortar surface area

was calculated from the measured BET specific surface area. The specific surface areas of the different phases, including the discretized C-S-H phase (C-S-H with Ca/Si < 1.67), were assumed to be the same as the initial specific surface area of the mortar. The surface area of portlandite was fitted to reproduce the high initial Ca concentration and the quartz surface area was calculated considering the geometric area of the grains as spheres of 0.5 mm of diameter. For portlandite the fitted area was 0.082 $m^2\ g^{-1}$ (8270 $m^2\ m^{-3}$) and for the quartz 5416 $m^2\ m^{-3}$ mortar.

The initial effective diffusion coefficient for the mortar was fitted. Values of $1.12 \cdot 10^{-13}$ $m^2\ s^{-1}$, $5.39 \cdot 10^{-14}$ $m^2\ s^{-1}$ and $1.95 \cdot 10^{-14}$ $m^2\ s^{-1}$ were obtained by fitting the model to the experimental data of experiments Mortar_1, Mortar_2 and Mortar_3, respectively. Differences are the fitting to the K (and Na) data. Slower drop in concentrations for experiment Mortar_3 gives smaller De.

4.4.2.2 Rates

The calculated dissolution and precipitation rates of the solid phases that compose the mortar during the Mortar_1 experiment are shown from Figures 4.12 to 4.16. Positive rates indicate precipitation and negative rates dissolution. The rate of C-S-H gel is expressed as the sum of all rates of the discrete C-S-H gel compositions

$$R_{C-S-H\ gel} = \sum_{Ca/Si=0.83}^{Ca/Si=1.667} R_{Ca/Si} \qquad \text{Eq. 4.17}$$

Also, considering the molar volume of each discrete C-S-H gel composition, the rate of C-S-H gel is expressed in volumetric terms, i,e., in $dm^3/L/y$, in order to account for the C-S-H volume variation as it dissolves incongruently.

Figure 4.12 shows rates at t = 0. It is worth mentioning that irreversible kinetics was imposed for the fly ash, which implies permanent far-from-equilibrium dissolution and release of Si, Ca, Al, Mg and Fe into solution. Thus, the consequent increase in solution concentration affects the saturation state of the rest of the mortar phases. Some rates are positive for precipitation (C-S-H gel and Si-hydrogarnet) or negative for dissolution (quartz and fly ash). In the mobile water region all the rates are zero by definition (zero surface areas).

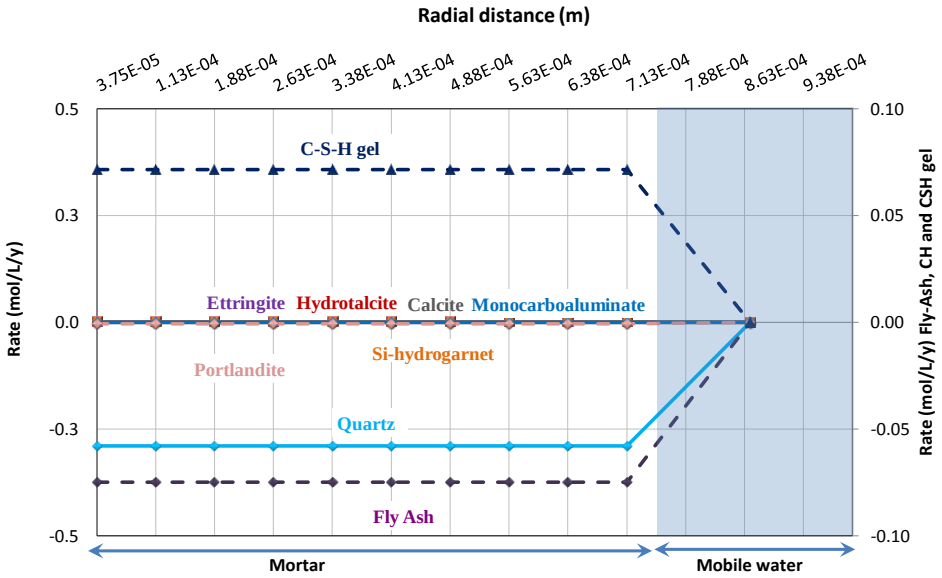

Figure 4.12. *Dissolution and precipitation rates of the solid phases at time 0. Dotted lines represent the rates of fly ash, CH and C-S-H gel that are referred to the right Ordinate. At the plot scale, monocarboaluminate, calcite, hydrotalcite, ettringite, Si-hydrogarnet and portlandite are not distinguished because their values are very close to 0.*

In early stages of the experiment ($t \leq 60$ h) (Fig. 4.13), two reactions occur close to the surface of the grains all over the column (from the inlet to the outlet): dissolution of portlandite and C-S-H gel. Dissolution of C-S-H is readily visible in the inlet (Fig. 4.14). A small precipitation rate for C-S-H gel is calculated at the surface of the grains in the middle of the column (Fig. 4.13 middle). However, when is calculated in volumetric terms C-S-H actually dissolves (Fig. 4.14). This difference in the calculated rates (mol/L/y vs. dm3/L/y) is given by the variable molar volume of C-S-H gel, which depends on the Ca/Si ratio (large molar volume for larger Ca/Si ratio).

The Ca/Si ratio of the C-S-H gel decreases from 1.667 to 1.623 at the inlet and to 1.650 in the middle (Fig. 4.15). Notice that at this time, portlandite has already been dissolved close to the surface of the grains of the inlet and middle parts of the column, causing the portlandite dissolution peak to move toward the interior of the grains. However, at the outlet, portlandite still largely dissolves and C-S-H neither precipitates nor dissolves, its Ca/Si ratio remaining constant along the grain (Fig. 4.15). Note that the observed precipitation in volumetric terms at the outlet is very small since variation in C-S-H volumetric fraction is negligible (Fig. 4.22). At the inlet, close to the surface of the grains, ettringite and calcite rates are also negative which indicate that these phases dissolve too (Fig. 4.13a). As a consequence, the Ca, Si, Al and sulfate concentrations in the mobile water increase, becoming oversaturated with respect to ettringite, and

promoting its precipitation in the middle and outlet parts of the column (Fig. 4.13b and c). Quartz and fly ash show a constant small dissolution rate.

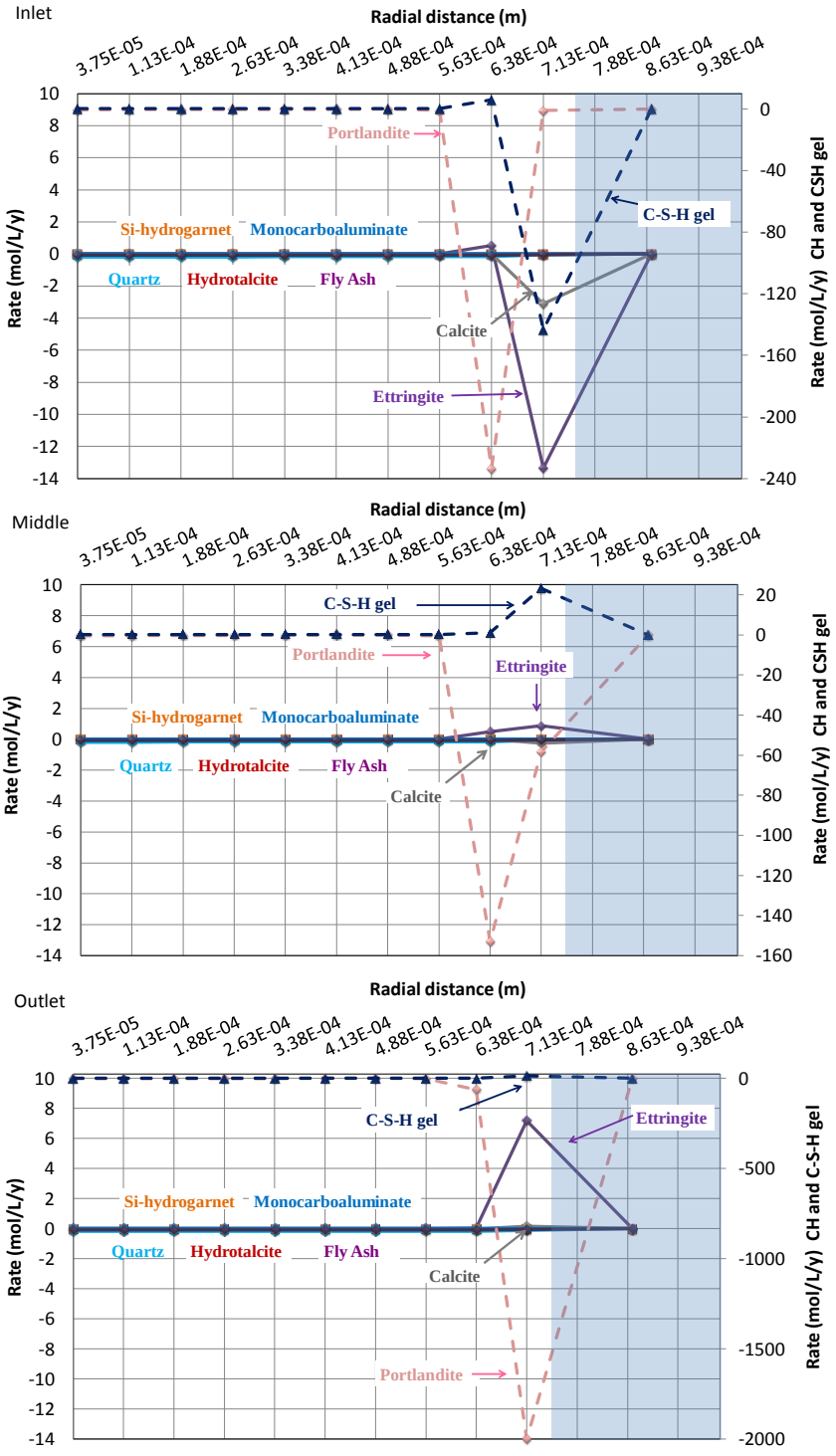

Figure 4.13. *Dissolution and precipitation rates of the solid phases after 60 h at three column zones: inlet, middle and outlet. Dotted lines represent the rates of CH and C-S-H gel that are referred to the right Ordinate.*

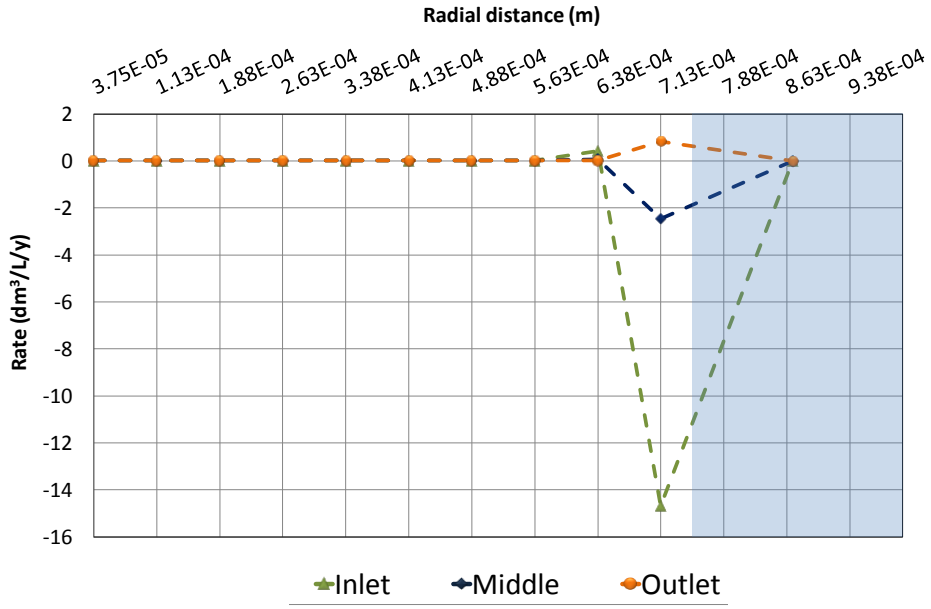

Figure 4.14. *Dissolution and precipitation rates of the C-S-H gel ($dm^3/L/y$) after 60 h in three column zones: inlet, middle and outlet.*

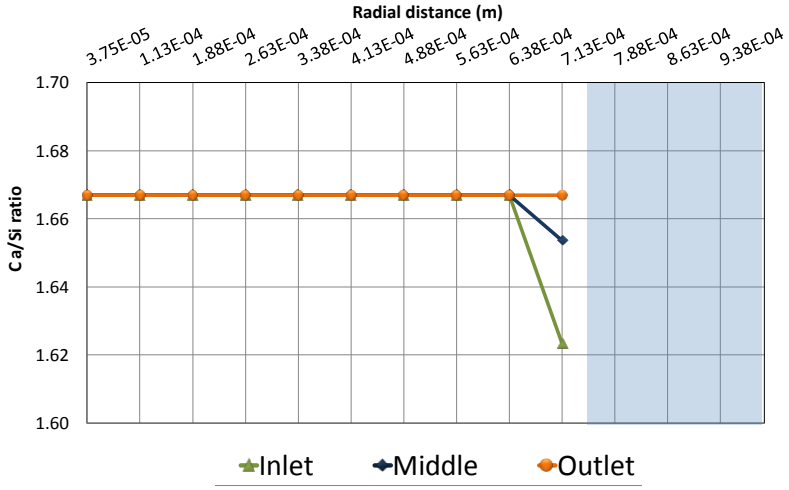

Figure 4.15. *Ca/Si ratio of the C-S-H gel along the column (inlet, middle and outlet) after 60 h (a).*

Over time ($60 < t \leq 3500$ h) the dissolution front of portlandite moves to the interior part of the grains followed by slight formation of a low Ca/Si ratio C-S-H gel along the column (Fig. 4.16). At the end of the experiment, at the inlet of the sample and at the surface of the grains, the C-S-H gel is consumed (Figs. 4.17 and Fig. 4.23). Consequently, diffusion of the released Ca and Si from the dissolved portlandite and C-S-H gel with high Ca/Si ratio goes in opposite directions (see section 4.4.2.3). The Ca/Si ratio of the gel starts to decrease at the surface of the grains in the inlet from 1.40 at 300 h to 1.00 after 100 h. It continues decreasing with time and advances to the interior or the

grain (Fig. 4.18). Ettringite dissolution takes place first at the inlet, releasing Ca, Al and S into solution, which moves downstream forward and promote its precipitation at the middle part and the outlet. After ca. 1000 h at the inlet and middle part of the column, ettringite is exhausted in the surface of the grains, but precipitates at the outlet, which, at the end of the experiment, starts to dissolve. The dissolution front of ettringite moves behind the dissolution front of portlandite. The formation of C-S-H gel with a low Ca/Si ratio continues to occur close to the surface of the grains. This front advances as does the dissolution front of the C-S-H gel with high Ca/Si ratio, yielding a remaining C-S-H with low Ca/Si ratio (Fig. 4.16).

Figure 4.17 depicts dissolution and precipitation rates of the C-S-H gel in $dm^3/L/y$ along the column to show that a net C-S-H dissolution occurs from 60 h to the experimental conclusion. However, after 600 h, low Ca/Si ratio gel slightly forms at the outlet (Fig. 4.18) from Si and Ca diffused from the mobile zone and from the interior of the grains, respectively (Fig. 4.20 outlet).

Precipitation rates of monocarboaluminate and Si-hydrogarnet are very slow. Calcite barely dissolves close to the interface at the late experimental stage. At the conclusion of the experiment (≈ 3500 h), dissolution of portlandite was still taking place in the interior part of the grains, along the length of the column. Close to the surface of the grains portalndite was totally consumed. C-S-H gel dissolves at the surface of the grains. Near the interface, ettringite dissolution is followed by a slight precipitation at the inner contiguous node due to the back-diffusion (Fig. 4.16). This is the trend that occurs along the column, with faster evolution close to the inlet.

The rates of the minor phases (Si-hydrogarnet, hydrotalcite and monocarboaluminate) are nearly zero at the surface of the grains where the major mortar phases are reacting.

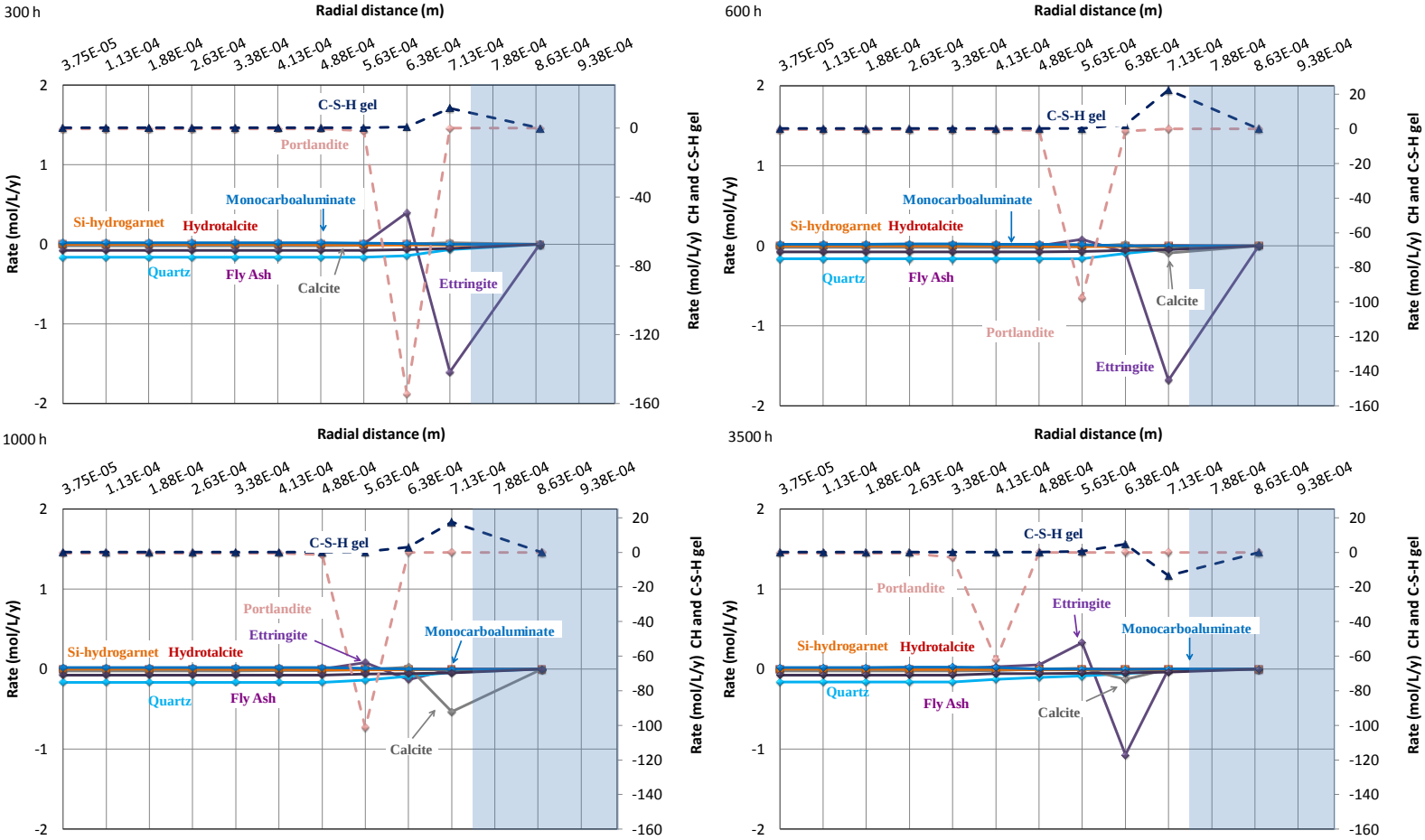

Figure 4.16. *Dissolution and precipitation rates of the solid phases at the outlet of the column (2.6 cm) at different reaction time (300, 600, 1000 and 3500 h). Dotted lines represent the rates of CH and C-S-H gel that are referred to the right Ordinate. At the plot scale, monocarboaluminate, Si-hydrogarnet and hydrotalcite are not visible because their values are very close to 0.*

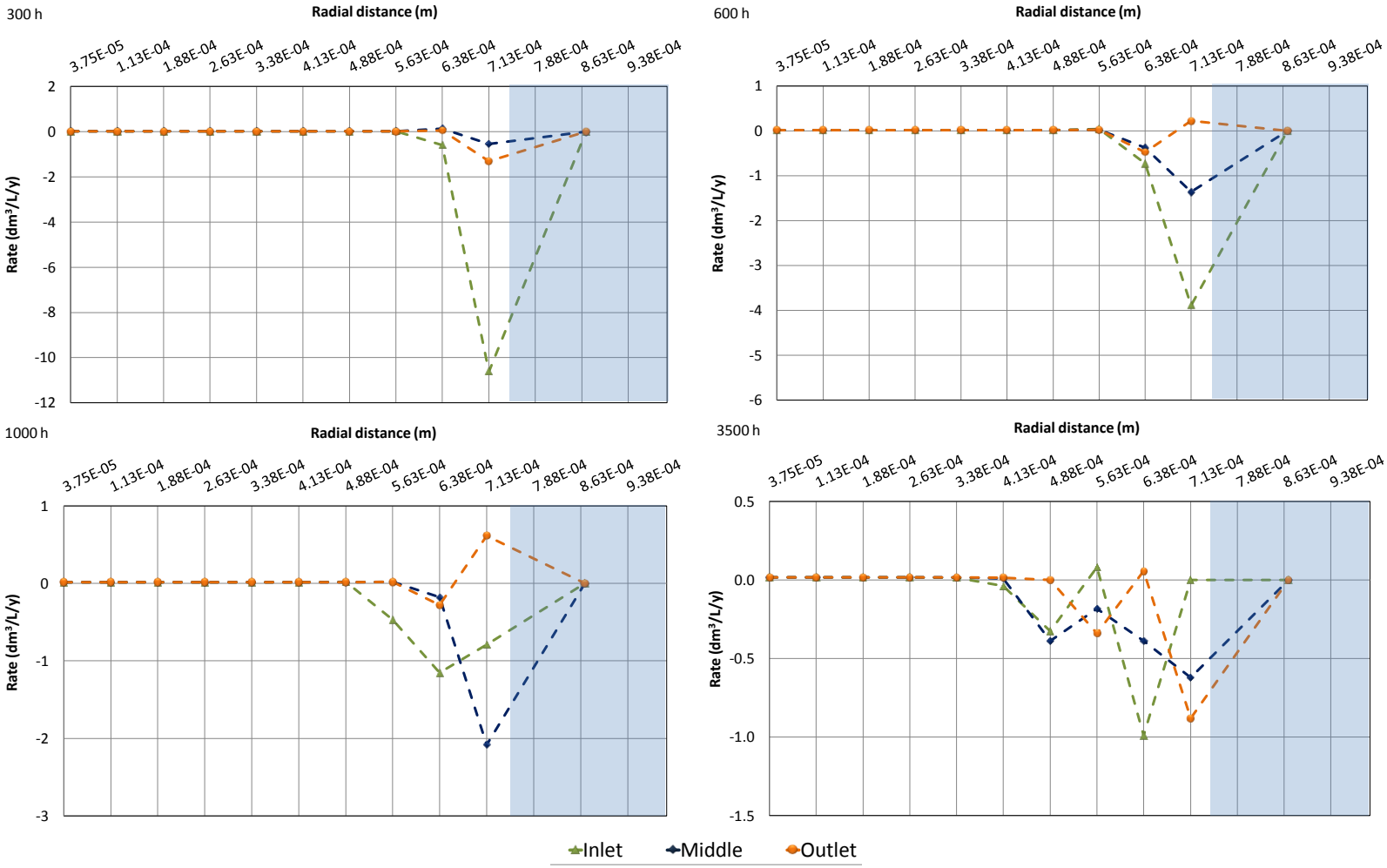

Figure 4.17. *Dissolution and precipitation rates expressed as ($dm^3/L/y$) of the C-S-H gel at different reaction time (300, 600, 1000 and 3500 h) at three column zones: inlet, middle and outlet.*

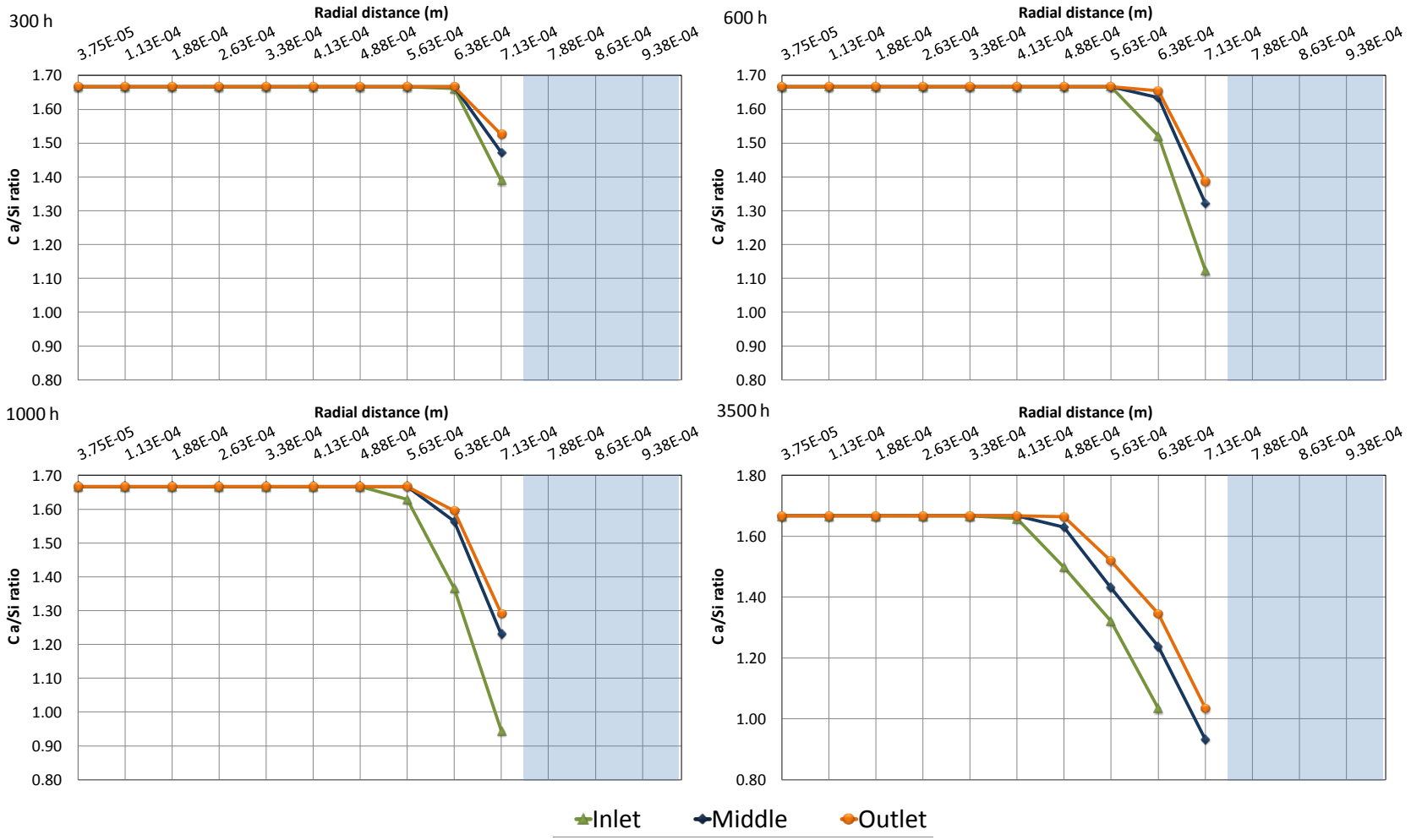

Figure 4.18. *Ca/Si ratio of the C-S-H gel along the column (inlet, middle and outlet) at different reaction times (300, 600, 1000 and 3500 h).*

4.4.2.3 Solute concentrations (mortar grains)

Figure 4.19a shows the solute concentration at time equal to 0. Regarding the solute concentrations at the early stage, it is observed that at the inlet of the experiment (e.g., t = 60 h), Ca concentration increases close to surface of the grains due to dissolution of C-S-H with high Ca/Si ratio, calcite and ettringite. Contiguously, Ca concentration rises up to portlandite solubility (2.0×10^{-2} M) as portlandite dissolves (Fig. 4.19b). Overall, at the middle and outlet, the behaviour of the Ca concentration is similar to that of the inlet (Figs. 4.19c and d). Si concentration increases at the surface of the grains, caused by the C-S-H gel dissolution at the inlet and middle part of the column (Figs. 4.19b and c). At the outlet, Si concentration is nearly zero because of the lack of C-S-H dissolution and Si release (Fig. 4.19d). At the inlet, S concentration increases due to ettringite dissolution. The released sulfur is transported to the oulet parts of the column yielding aqueous sulfur enrichment that at the middle and the outlet sufficiently supersaturates the solution and allows ettringite precipitation. Concentrations of K and Na diminish all along the column from the centre of the grains toward the surface of the grains due to diffusion (Figs. 4.19b, c and d).

The aforementioned processes persist until the conclusion of the experiment. The main difference is that exhaustion of portlandite occurs from the surface to the interior part of the grains, all along the column (Fig. 4.20). At the late stage of the experiment (t = 3500 h; Fig. 4.20bis), Ca concentration is 2.0×10^{-2} M, where portlandite still exists and drops to almost zero at the surface of the grains as it is consumed. K and Na run out before the end of the experiment by diffusion through the grain. At the inlet, Si concentration increases in the mobile zone mainly due to dissolution of the C-S-H gel. At the middle and outlet, because Si concentration is higher in the mobile zone that in the grains, back diffusion takes place toward the grains (Fig. 4.20). Likewise, with time (Fig. 4.20bis), the front of Si concentration moves toward the interior of the grains due to dissolution of the C-S-H gel. At the inlet and middle of the column, a peak of S concentration is observed at the interior part of the grain, attributable to ettringite dissolution. At the outlet, this peak approaches the grain surfaces. Precipitation of Si-hydrogarnet and monocarboaluminate and diffusion toward the mobile zone make Al decrease along the grains.

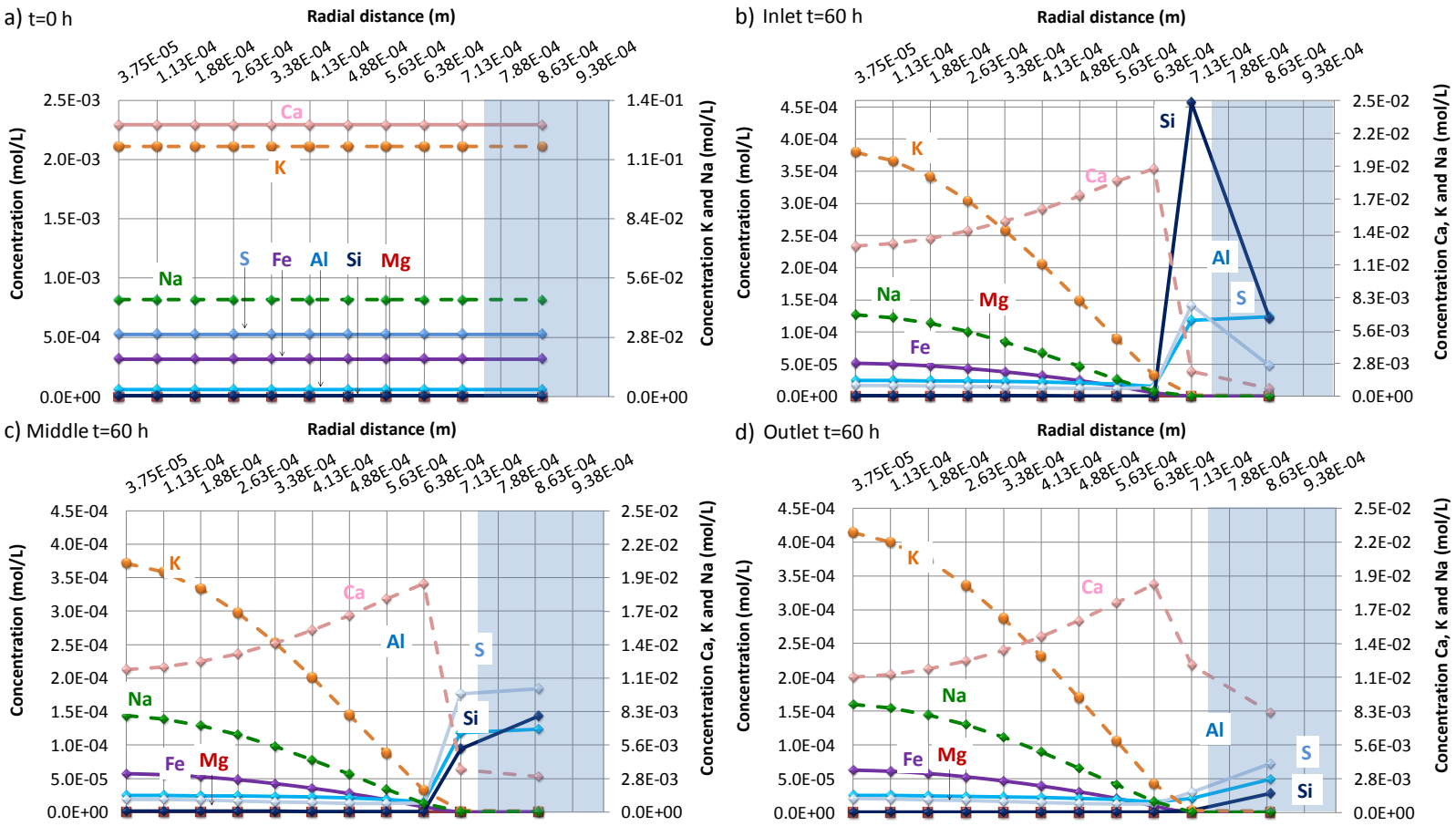

Figure 4.19. *Variation of total solute concentrations at time 0 h and and 60 h at three column zones: inlet, middle and outlet. Dotted lines represent concentration of Ca, K and Na that are referred to the right Ordinate.*

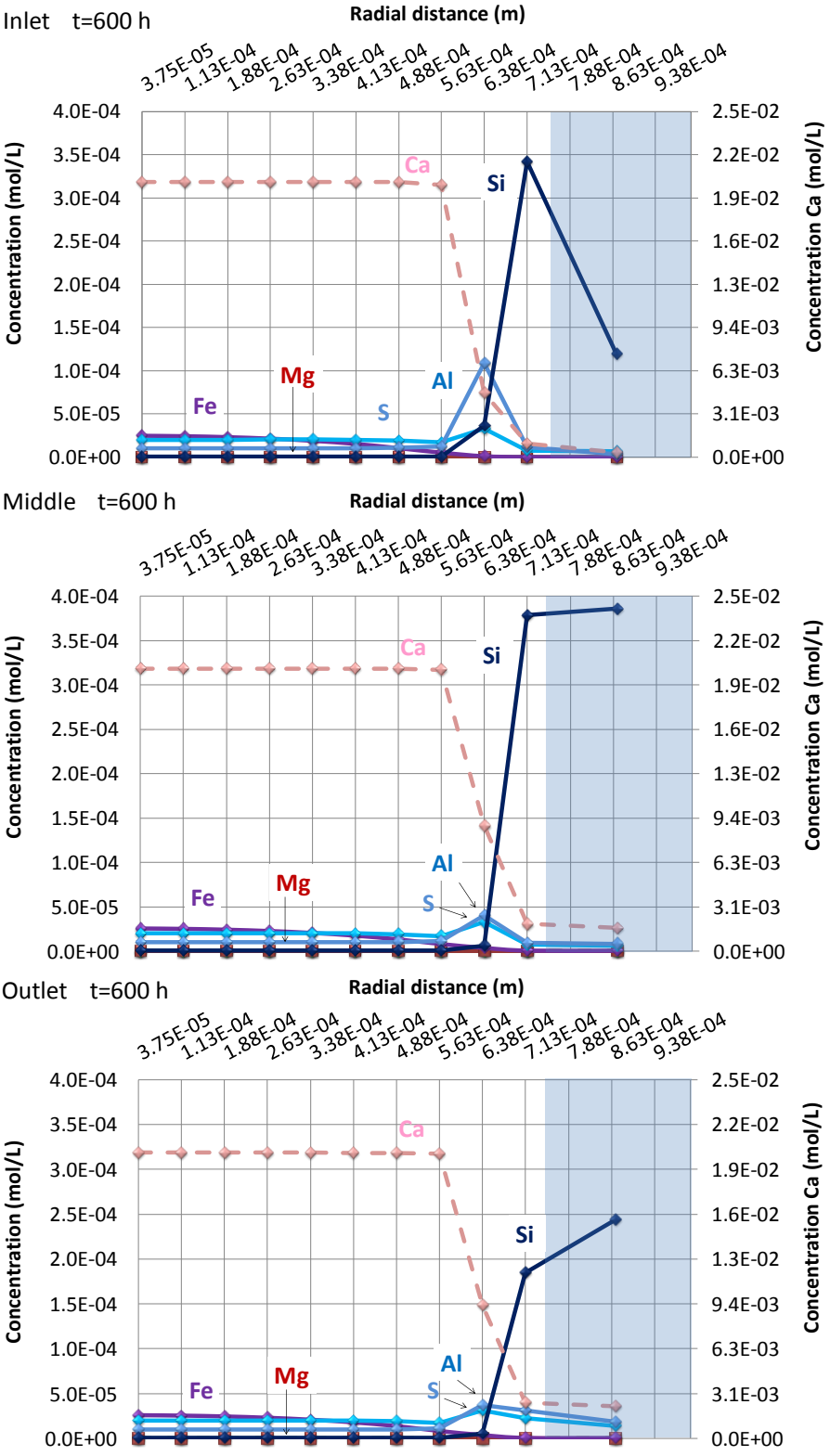

Figure 4.20. *Variation of the total solute concentrations after 600 at three column zones: inlet, middle and outlet. Dotted lines represent concentration of Ca that is referred to the right Ordinate. K and Na are not visible because their values are 0.*

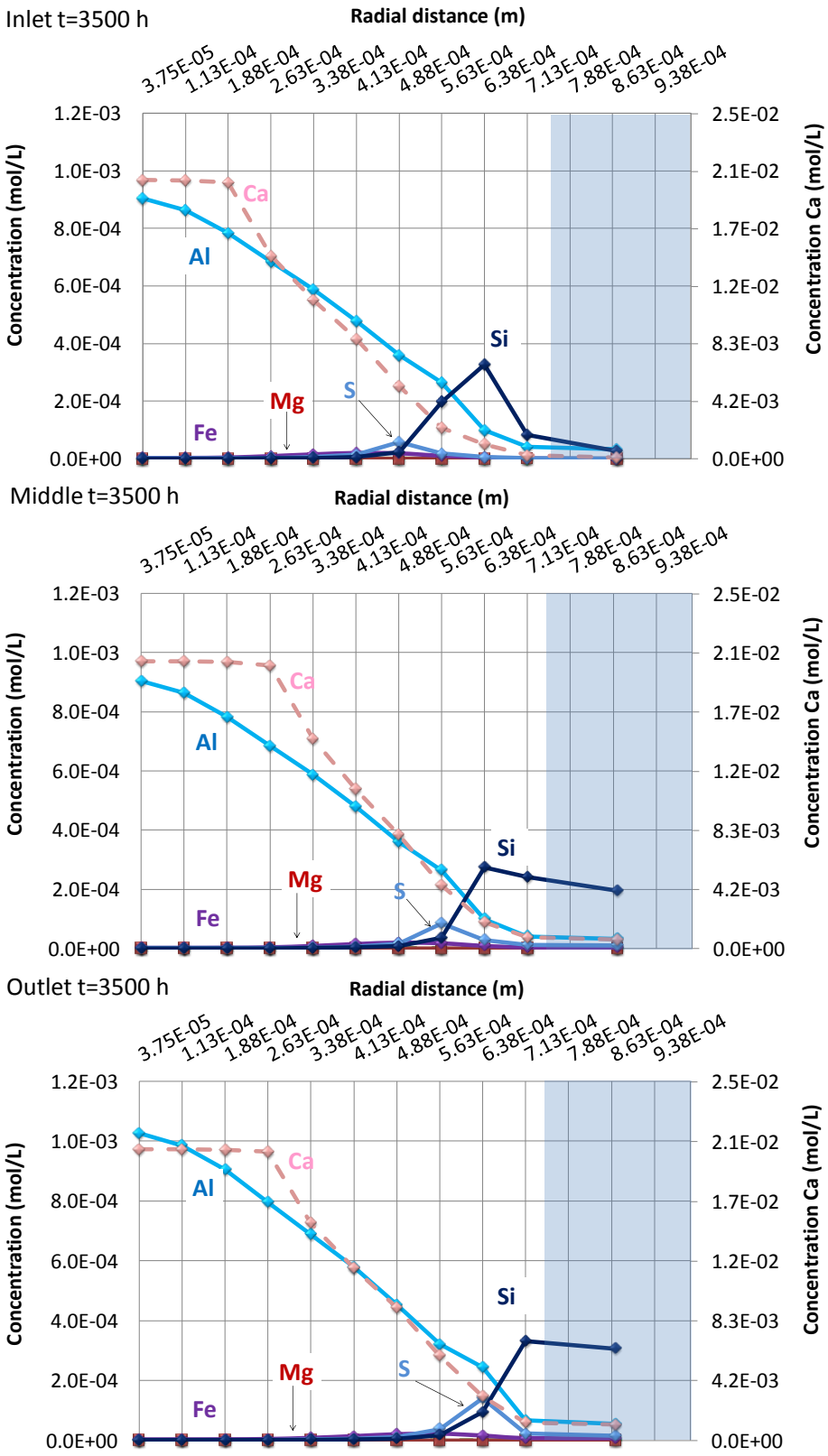

Figure 4.20 bis. *Variation of the total solute concentrations after 3500 h at three column zones: inlet, middle and outlet. Dotted lines represent concentration of Ca that is referred to the right Ordinate. K and Na are not visible because their values are 0.*

4.4.2.4 Solute concentrations (mobile zone)

Figure 4.21 shows the temporal variation of the aqueous solute composition along the column. Figure 4. 21a shows the initial aqueous solute composition along the column. At the early stage of the experiment (t = 60 h; Fig.4. 21b), Ca, K and Na concentrations increase along the column. The presence of Ca is mainly due to dissolution of portlandite. K and Na are leachates from the mortar porewater. Si concentration shows a maximum at the inlet zone due to C-S-H gel dissolution. After reaching a maximum value, the Si concentration tends to diminish due to slower dissolution of the C-S-H gel and back diffusion from the mobile zone to the mortar grains. S concentration increases at the inlet due to ettringite dissolution. In the rest of the column, S concentration gradually decreases as ettringite precipitates. Likewise, the Al concentration shows a maximum near the inlet as a consequence of dissolution of ettringite and slight dissolution of monocarboaluminate, and diminishes gradually as ettringite precipitates. Concentrations of Fe and Mg are close to the detection limit because the dissolution rates of fly ash, Si-hydrogarnet and hydrotalcite are very small. During the experiment, from the inlet to the outlet (Fig. 4. 21c, d, e and f), Ca concentration increases along the column but diminishes with time as portlandite is consumed. The Si concentration is highly dependent on the dissolution of the C-S-H gel with high Ca/Si ratio and the previously precipitated C-S-H with low Ca/Si ratio as well as back diffusion (concentration in the mobile zone larger than in the grains). The maximum Si concentration moves along the column as the C-S-H compositions with the higher Ca/Si ratios (e.g. Ca/Si from 1.40 to 1.67) dissolve. S and Al behave similarly depending on dissolution of ettringite. As happens with Si concentration, the maximum concentration of S and Al moves toward the outlet where ettringite still dissolves at the end of the experiment (t = 300h). With time (t = 600, 100 and 3500 h) the concentration of Al and S decreases as dissolution of ettringite is less. The difference between the Al and S concentrations with time is associated to the slight dissolution of monocarboaluminate and Si-hydrogarnet.

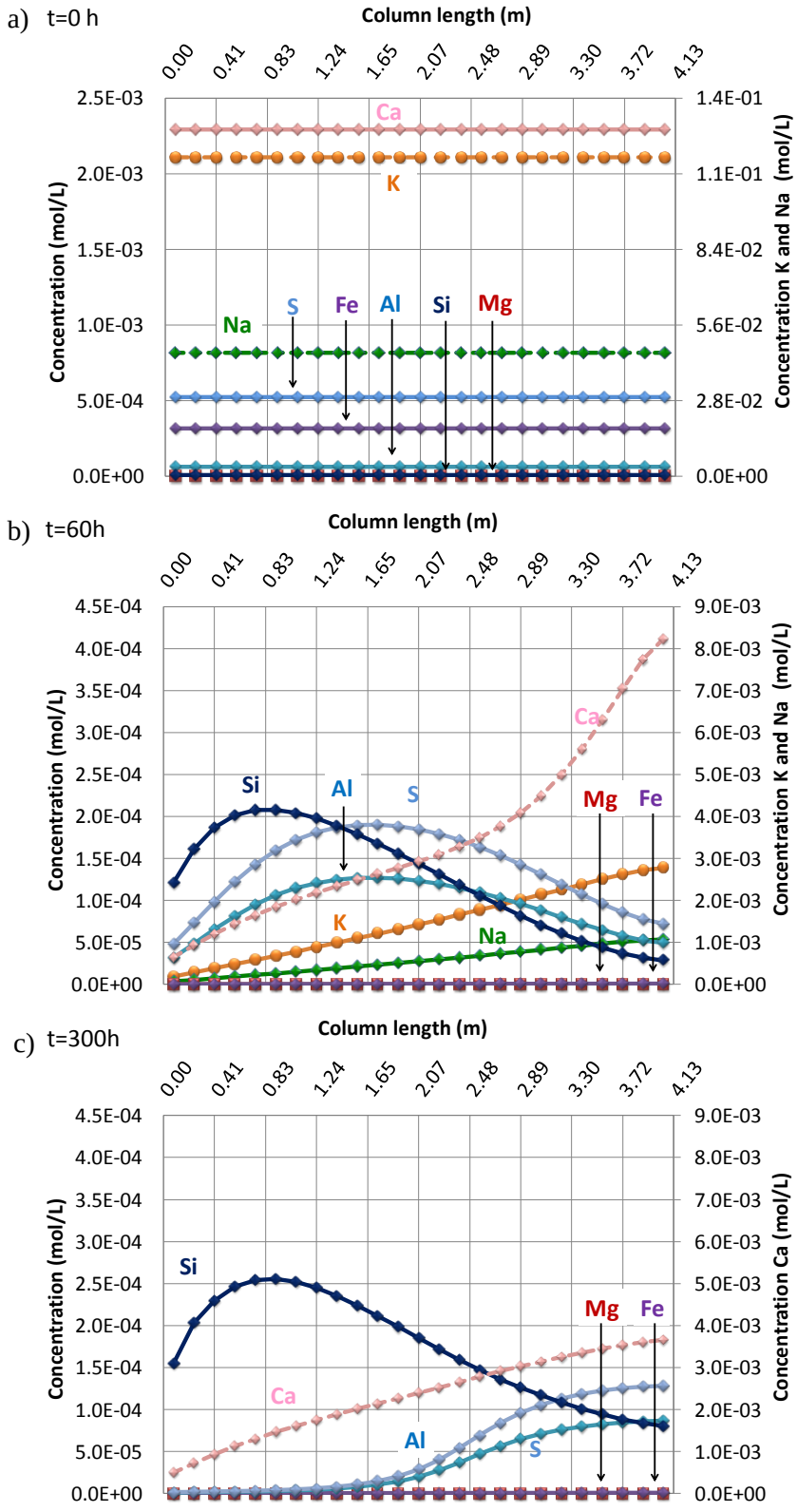

Figure 4.21. *Variation of solution composition along the column at four different times (0, 60 and 300 h). Dotted lines represent concentration of Ca, K and Na that are referred to the right Ordinate. K and Na are not visible because their values are 0.*

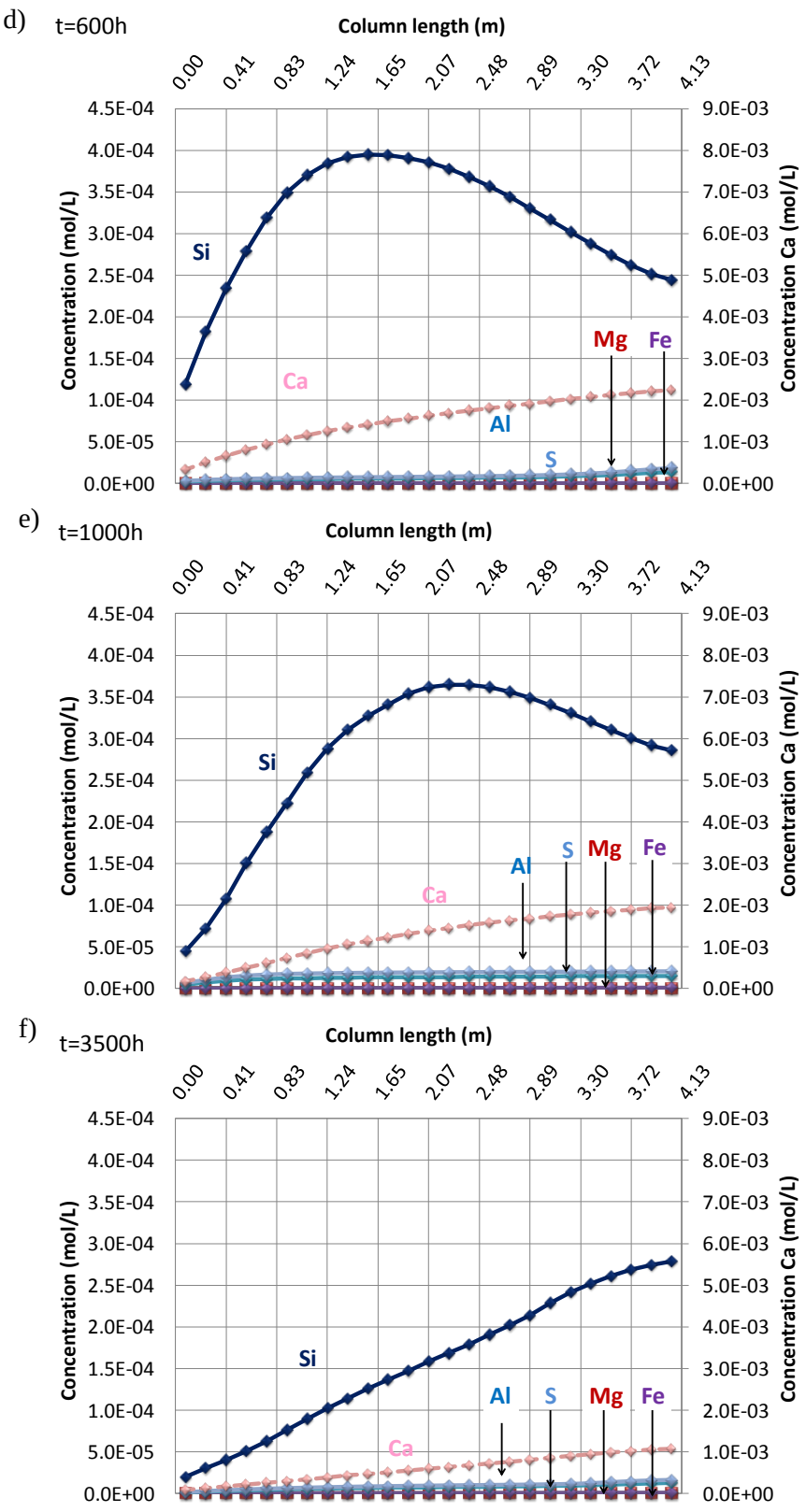

Figure 4.21 bis. *Variation of solution composition along the column at four different times (600, 1000 and 3500 h). Dotted lines represent concentration of Ca that is referred to the right Ordinate.*

4.4.2.5 Volumetric fractions of solids

The initial volumetric fractions of the phases are depicted in Figure 4.22a. After 60 h (Fig. 4.22b, c and d), the change in volumetric fraction of the mortar phases is observed along the column (at the inlet, middle and outlet of the column). At the inlet, the amount of portlandite highly decreased at the surface of the grains. The content of C-S-H gel also diminishes, as well as that of ettringite. At the middle and the outlet, the content of portlandite also decreases, but ettringite increases its content. The volumetric fraction of the C-S-H gel does not change as precipitation of C-S-H gel with low Ca/Si ratio balances the dissolution of the gel with high Ca/Si ratio. The content of the rest of the phases has not changed.

Fig.4.23 shows the variation of the calculated volumetric fractions of the mortar phases at the inlet and the outlet of the column after 300 and 3500 hours. After 300 h (Fig. 4.23a), the volumetric fraction of portlandite keeps on decreasing toward the interior of the grains. The C-S-H gel still decreases at the surface of the grains. Ettringite is exhausted at the surface of the grains, and it precipitates near the outlet (Fig. 4.23b). With time (from 300 to 3500 h), portlandite and C-S-H gel keep on dissolving up to exhaustion from the surface of the grains (the respective volumetric fractions are zero) (Fig. 4.23 c and d). The volumetric fraction of ettringite is nearly exhausted at the surface of the grains but increases next to the dissolution front (towards the interior of the grains) due to back diffusion of S. Volumetric fraction of monocarboaluminate, Si-hydrogarnet and hydrotalcite keeps constant due to the slow dissolution.

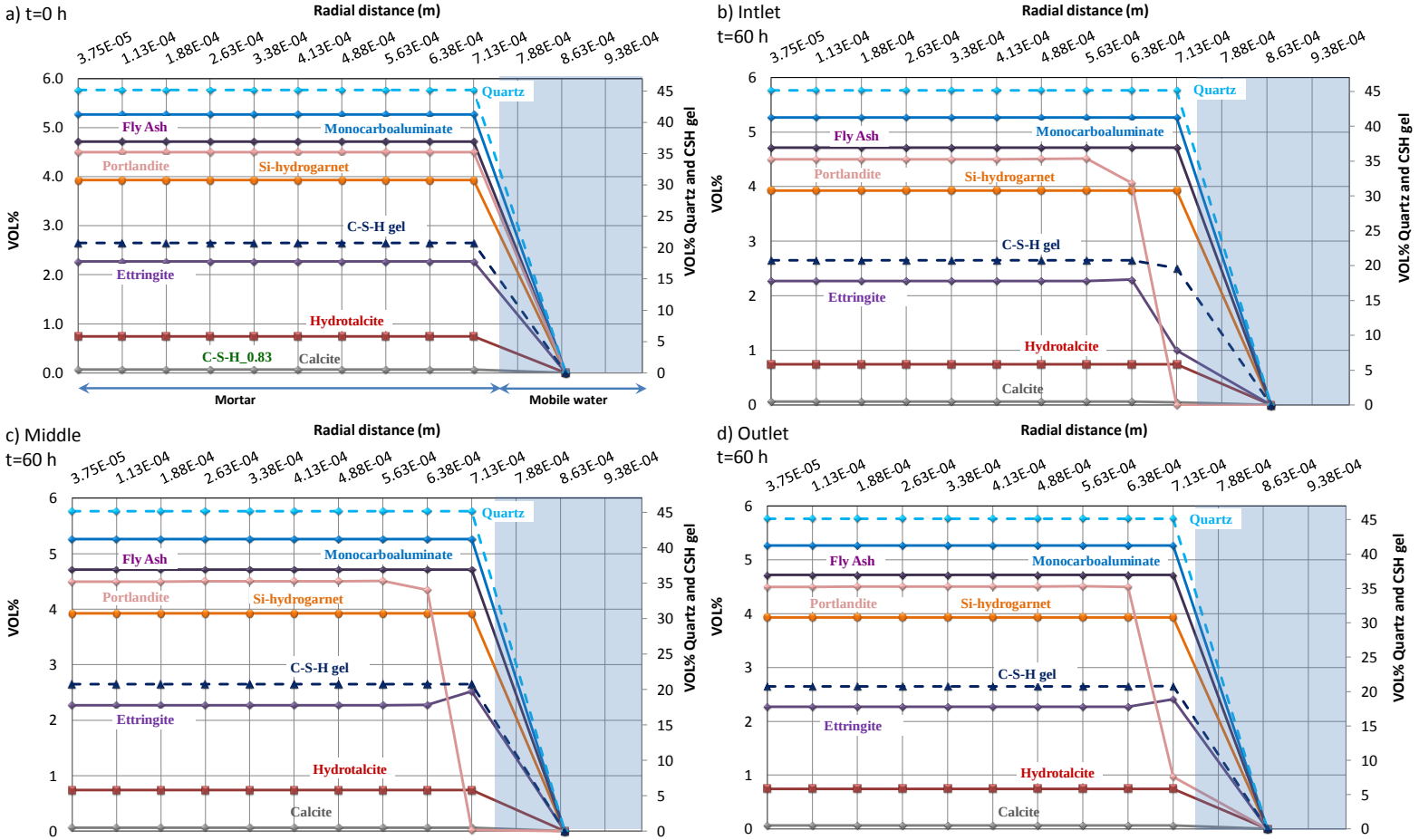

Figure 4.22. *Calculated volumetric fraction versus time at the outlet of the column at t = 0h (a) and t = 60h (b, c, d). Dotted lines represent concentrations of quartz and C-S-H gel that are referred to the right Ordinate.*

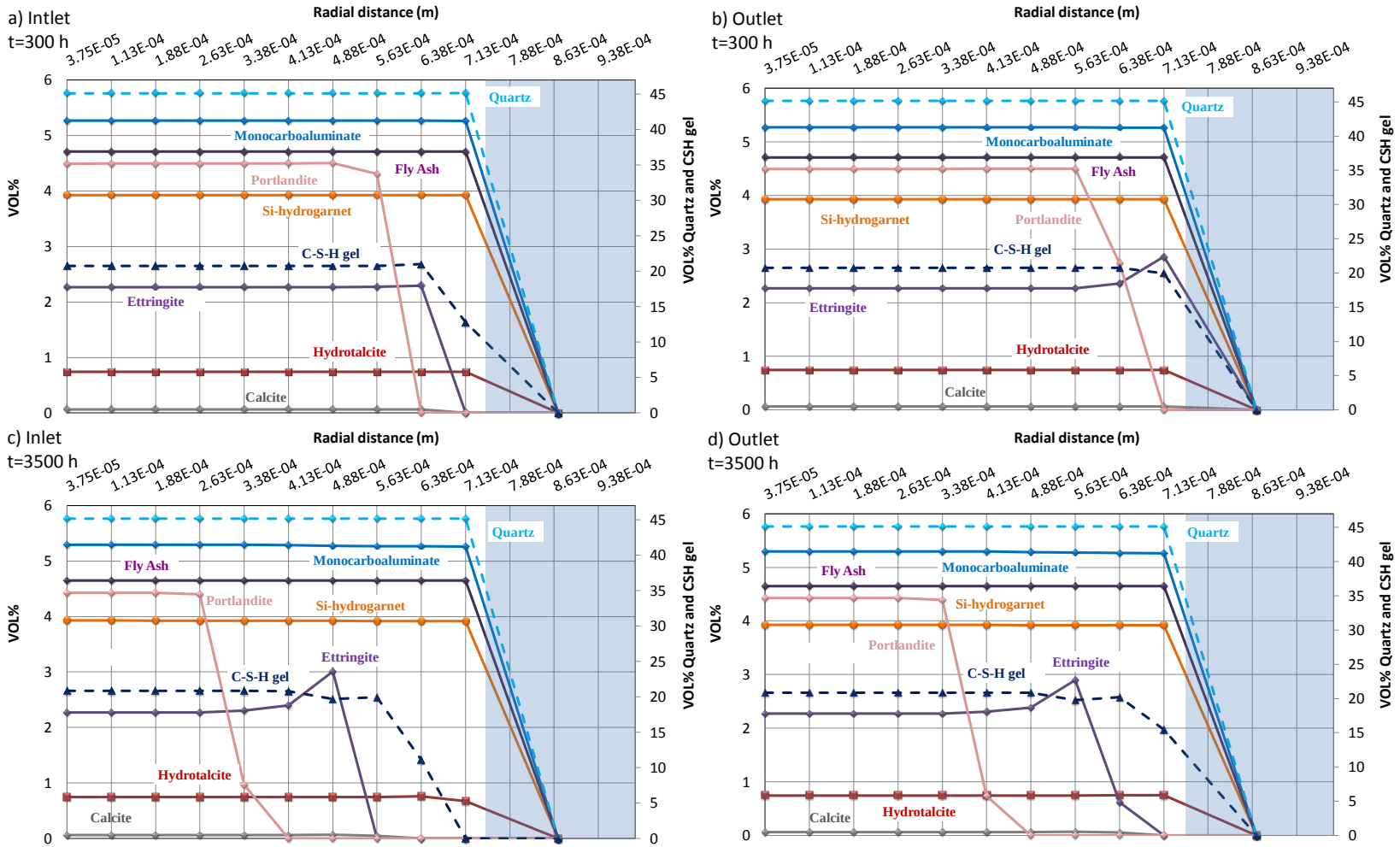

Figure 4.23. *Calculated volumetric fraction versus time at the inlet and outlet after 300 and 3500 h. Dotted lines represent concentrations of quartz and C-S-H gel that are referred to the right Ordinate.*

4.4.2.6 Porosity

The temporal variation of mortar porosity at three different positions along the column is shown in Figure 4.24.

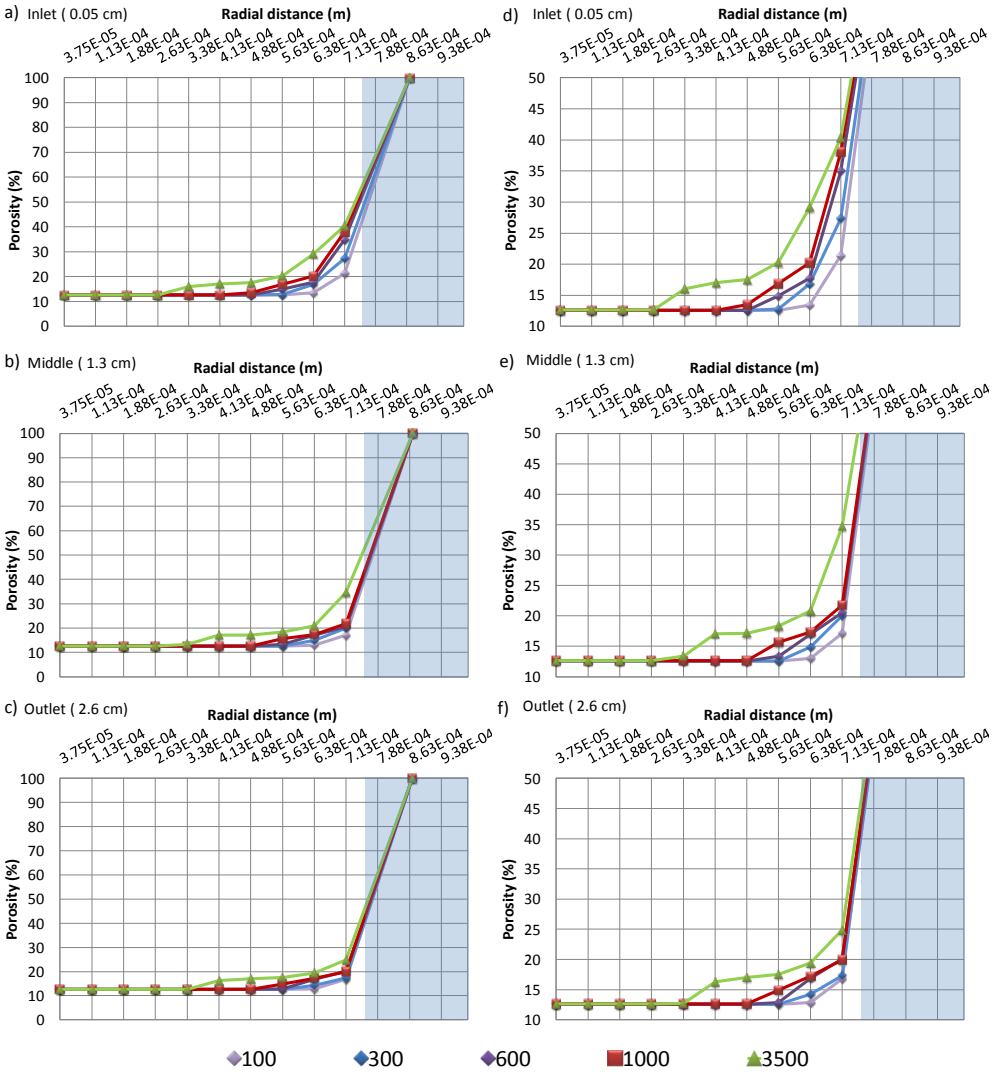

Figure 4.24. *Variation of mortar porosity with time (100, 300, 600, 1000 and 3500 h) at different lengths of the column (a, b and c). Zoom up of the region where the porosity changes (d, e and f).*

Overall, major dissolution of portlandite, C-S-H gel and ettringite, together with the minor dissolution of the monocarboaluminate and Si-hydrogarnet, contribute to the generation of porosity: an increase from 12.5 % to 40% up to the middle of the column and only up to 25 % from the middle part to the outlet. Figure 4.25 compares the temporal variation of porosity at the inlet, middle and outlet of the column after 100 h and 3500 h. It can be clearly seen that the creation of porosity is noticeably taking place near the surface of the grains.

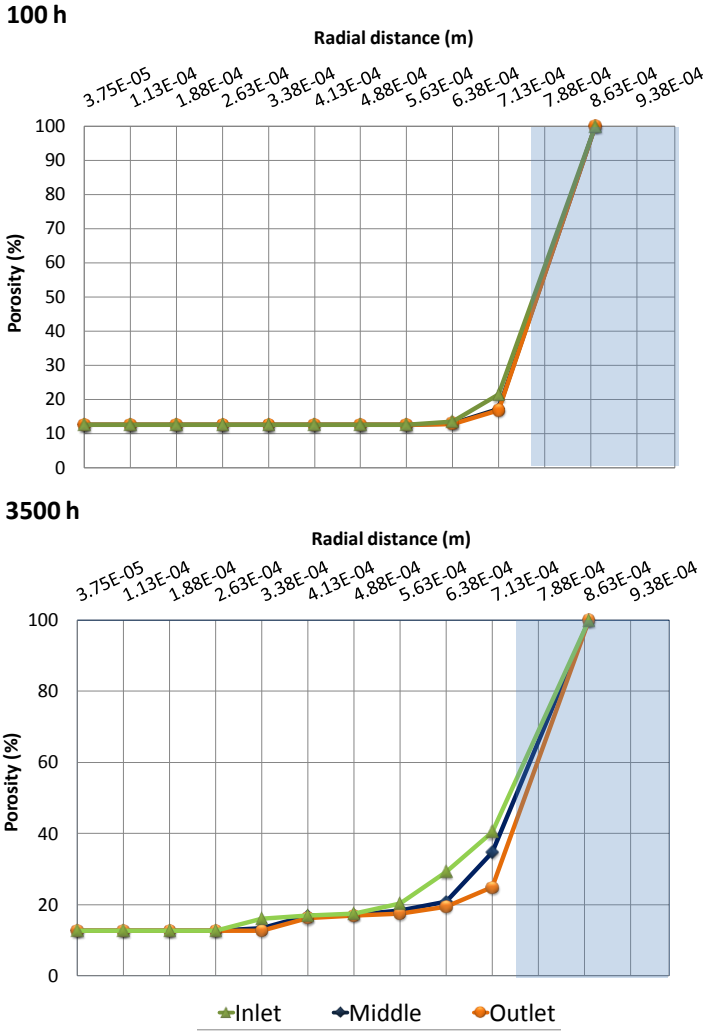

Figure 4.25. *Evolution of porosity of the mortar at different times of the experiment.*

4.4.2.7 pH

The temporal variation of pH at three different positions along the column is shown in Figure 4.25 (mortar grains) and Figure 4.26 (mobile zone).

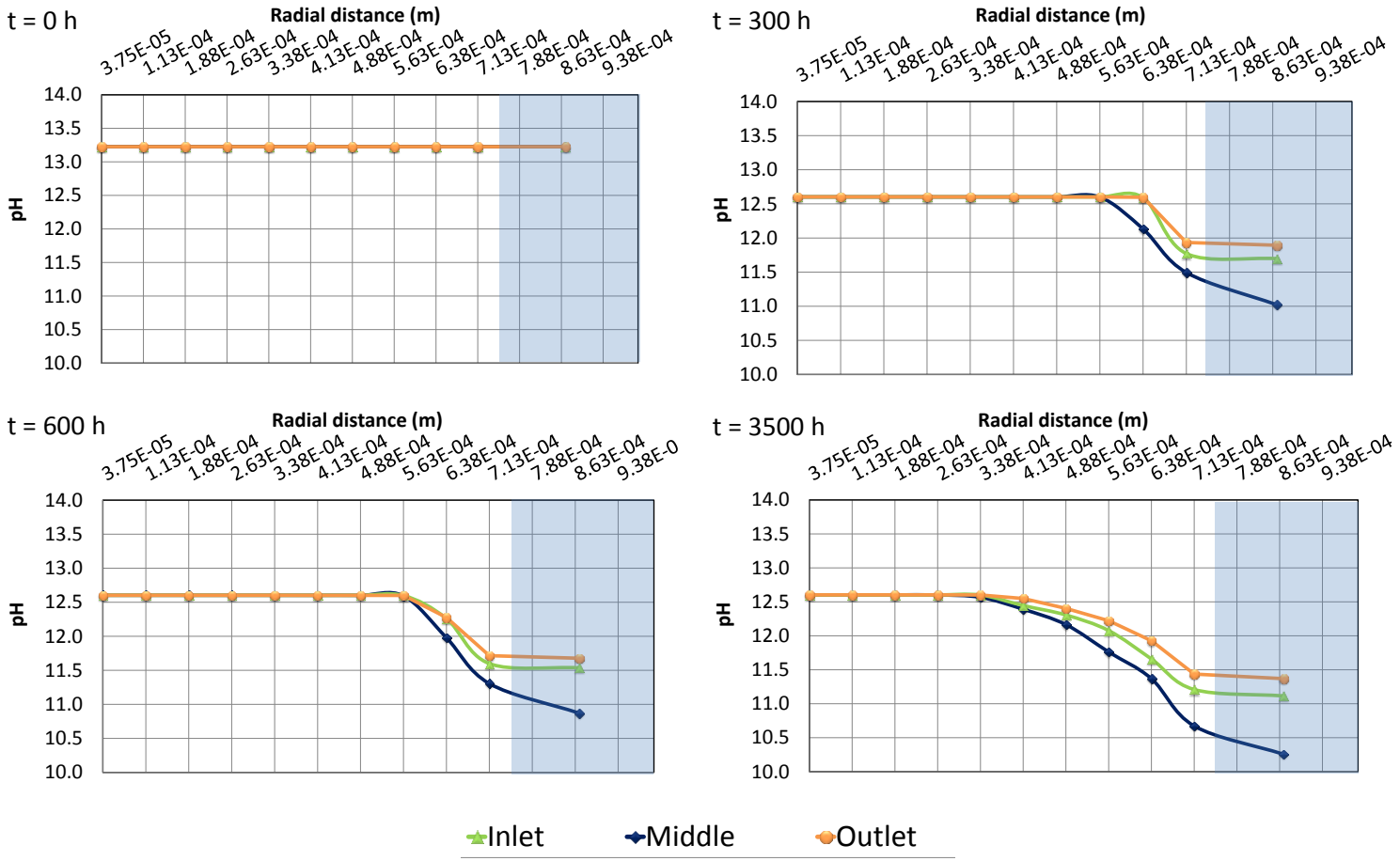

Figure 4.26. *Variation of pH with time (0, 300, 600 and 3500 h) at different length of the column.*

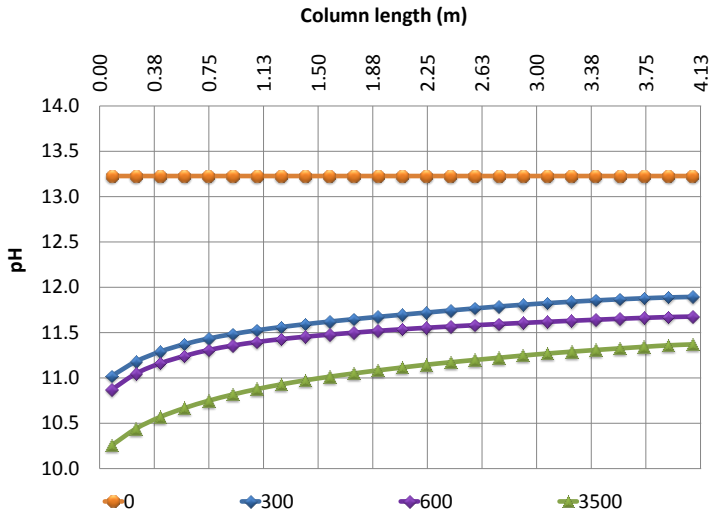

Figure 4.27. *Evolution of pH at different times of the experiment along the column.*

At the beginning of the experiment, pH decreases near the grain surface where the reactions start to take place. Toward the interior of the grains, pH decreases with the advance of the reactions (Fig. 4 .26). In the mobile zone, pH is lower than the initial value and increases upwards (from the bottom to the top of the column) by an accumulative and transport effect (Fig. 4 .27).

4.5. Conclusions

To check the applicability of the previously obtained C-S-H gel dissolution rate law, column experiments using columns filled with mortar grains of ≈ 2 mm size were performed. Under these conditions, dissolution of the mortar (64% I42.5R/SR cement and 36 % fly ash) released Ca, Si, Al, S and Fe from the main mortar components (C-S-H gel phase, portlandite, fly ash, ettringite, monocarboaluminate and Si-hydrogarnet).

A simplified two dimensional model with cylindrical symmetry was implemented in CrunchFlow to simulate the results of the experiments. The CrunchFlow reactive transport simulations reproduced the variation of the major components Ca, Si, Na and the output pH reasonably well. The behavior of the minor components (Al, S and Fe), as well as the diffusion of K, was difficult to match. To fully understand the processes involved in the mortar degradation was essential to integrate the dissolution rate law of the C-S-H gel obtained in this study (Chapter 2).

Experimental and modeling results showed that dissolution and decalcification of the C-S-H gel, dissolution of portlandite, ettringite, monocarboaluminate and Si-hydrogarnet were the main processes driving the mortar alteration. Diffusion of Na and K in the initial porewater was taken into account ignoring K-uptake by the C-S-H gel.

Simulations showed that during the time span of the experiments the reactions started taking place near the surface of the grains. With time, the reaction front moved toward the interior part of the grains. Initially, a preferential dissolution of portlandite, that released a large amount of Ca in solution, slowed the dissolution of the C-S-H gel. The C-S-H gel with a high Ca/Si ratio started to dissolve, while the rest of the gel with low Ca/Si ratios formed due to incongruent dissolution (decalcification of the C-S-H gel). The dissolution of fly ash was uniform along the radius of the grains as a consequence of the assumed irreversible dissolution kinetics. Ettringite dissolved mostly at the inlet of the column, releasing S in solution that promoted ettringite precipitation near the column outlet. Reactivity of monocarboaluminate and Si-hydrogarnet was minor. Quartz and hydrotalcite did not react in any significant amount.

Over time, portlandite kept on dissolving along the entire column, as well as the C-S-H gel which tends to form a C-S-H gel with low Ca/Si ratio of 1.4 indicating a progressive decalcification. Dissolution of fly ash, monocarboaluminate and Si-hydrogarnet took place along the column. At the final stage, the C-S-H gel kept on dissolving to form C-S-H gels with low Ca/Si ratio along the entire column. Continuous dissolution of ettringite, monocarboaluminate and Si-hydrogarnet diminished, resulting in lower concentration of sulfate and aluminum. Ettringite precipitation occurred close to the grain surfaces at the outlet.

Mortar porosity close to the surface of the grains increased along the column, ranging from about 40% at the inlet to 25% in the outlet.

In conclusion, the implementation of the C-S-H dissolution rate law in a reactive transport code, in addition to fitted rate constant values for ettringite, monocarboaluminate, fly ash and Si-hydrogarnet, allowed the interpretation of the column experiments (mortar grains) and confirmed the applicability of the C-S-H kinetic rate law. With the aim of improving the fitting of the model to the experimental data, future work should consider inclusion of Fe secondary phases and alkali uptake by C-S-H gel.

References

Adenot, F., and Buil, M. (1992). Modelling of the corrosion of the cement paste by deionized water. *Cement and Concrete Research*, 22(2), 489-496.

Bandstra, J. Z., Buss, H. L., Campen, R. K., Liermann, L. J., Moore, J., Hausrath, E. M., Navarre-Sitchler, A.K., Jang, J-H., and Brantley, S. L. (2008). Appendix: compilation of mineral dissolution rates. In: Brantley, S. L., Kubicki, J. D., White, A. F. (Eds.), Kinetics of water-rock interaction. Springer, New York, pp.737-823.

Berner, U. R. (1992). Evolution of pore water chemistry during degradation of cement in a radioactive waste repository environment. *Waste Management*, 12(2), 201-219.

Bullard, J. W., Enjolras, E., George, W. L., Satterfield, S. G., and Terrill, J. E. (2010). A parallel reaction-transport model applied to cement hydration and microstructure development. *Modelling and Simulation in Materials Science and Engineering*, 18(2), 025007.

Damidot, D., Lothenbach, B., Herfort, D., and Glasser, F. P. (2011). Thermodynamics and cement science. *Cement and Concrete Research*, 41(7), 679-695.

De Weerdt, K., Haha, M. B., Le Saout, G., Kjellsen, K. O., Justnes, H., and Lothenbach, B. (2011). Hydration mechanisms of ternary Portland cements containing limestone powder and fly ash. *Cement and Concrete Research*, 41(3), 279-291.

Dilnesa, B.Z., Lothenbach, B., Renaudin, G., Wichser, A., Kulik, D. (2014). Synthesis and characterization of hydrogarnet $Ca_3(Al_xFe_{1-x})_2(SiO_4)_y(OH)_{4(3-y)}$. *Cement and Concrete Research*, 59, 96-211.

Dilnesa, B. Z., Lothenbach, B., Renaudin, G., Wichser, A., and Wieland, E. (2012). Stability of Monosulfate in the Presence of Iron. *Journal of the American Ceramic Society*, 95(10), 3305-3316.

Dilnesa, B. Z., Lothenbach, B., Le Saout, G., Renaudin, G., Mesbah, A., Filinchuk, Y., Wichser A. and Wieland, E. (2011). Iron in carbonate containing AFm phases. *Cement and Concrete Research*, 41(3), 311-323.

Feldman, R. F., Carette, G. G., Malhotra, V. M. (1990). Studies on mechanics of development of physical and mechanical properties of high-volume fly ash-cement pastes. *Cement and Concrete Composites*, 12(4), 245-251.

Galíndez, J. M., and Molinero, J. (2010). Assessment of the long-term stability of cementitious barriers of radioactive waste repositories by using digital-image-based microstructure generation and reactive transport modelling. *Cement and Concrete Research*, 40(8), 1278-1289.

Gérard B. Le Bellego C. (2002). Simplified modeling of Ca leaching of concrete in various environments. *Material and Structure*, 35(10), 632-640.

Haga, K., Sutou, S., Hironaga, M., Tanaka, S., and Nagasaki, S. (2005). Effects of porosity on leaching of Ca from hardened ordinary Portland cement paste. *Cement and Concrete Research*, 35(9), 1764-1775.

Hummel, W., Berner, U., Curti, E., Pearson, F. J., Thoenen, T. (2002). Nagra/PSI chemical thermodynamic data base 01/01. *Radiochimica Acta*, 90(9-11/2002), 805-813.

Kamali, S., Moranville, M., and Leclercq, S. (2008). Material and environmental parameter effects on the leaching of cement pastes: experiments and modelling. *Cement and Concrete Research*, 38(4), 575-585.

Kulik, D. A., Wagner, T., Dmytrieva, S. V., Kosakowski, G., Hingerl, F. F., Chudnenko, K. V., and Berner, U. R. (2013). GEM-Selektor geochemical modeling package: revised algorithm and GEMS3K numerical kernel for coupled simulation codes. *Computational Geosciences*, *17*(1), 1-24.

Kulik, D. A., Kersten, M. (2001). Aqueous solubility diagrams for cementitious waste stabilization systems: II, end-member stoichiometries of ideal calcium silicate hydrates solid solutions. *Journal of the American Ceramic Society*, *84*(12), 3017-3026.

Lothenbach, B., Le Saout, G., Ben Haha, M., Figi, R., and Wieland, E. (2012). Hydration of a low-alkali CEM III/B–SiO_2 cement (LAC). *Cement and Concrete Research*, 42, 410-423.

Lothenbach, B., Bary, B., Le Bescop, P., Schmidt, T., and Leterrier, N. (2010). Sulfate ingress in Portland cement. *Cement and Concrete Research*, 40(8), 1211-1225.

Lothenbach, B., Le Saout, G., Gallucci, E., and Scrivener, K. (2008a). Influence of limestone on the hydration of Portland cements. *Cement and Concrete Research*, 38(6), 848-860.

Lothenbach, B., Matschei, T., Möschner, G. and Glasser, F. (2008b). Thermodynamic modelling of the effect of temperature on the hydration and porosity of Portland cement. *Cement and Concrete Research*, 38(1), 1-18.

Lothenbach, B., and Winnefeld, F. (2006). Thermodynamic modelling of the hydration of Portland cement. *Cement and Concrete Research*, 36(2), 209-226.

Mainguy, M., Tognazzi, C., Torrenti, J. M., and Adenot, F. (2000). Modelling of leaching in pure cement paste and mortar. *Cement and Concrete Research*, 30(1), 83-90.

Maltais, Y., Samson, E., and Marchand, J. (2004). Predicting the durability of Portland cement systems in aggressive environments—laboratory validation. *Cement and Concrete Research*, 34(9), 1579-1589.

Matschei, T., Lothenbach, B., and Glasser, F. P. (2007). Thermodynamic properties of Portland cement hydrates in the system $CaO–Al_2O_3–SiO_2–CaSO_4–CaCO_3–H_2O$. *Cement and Concrete Research*, 37(10), 1379-1410.

Moranville, M., Kamali, S., and Guillon, E. (2004). Physicochemical equilibria of cement-based materials in aggressive environments—experiment and modeling. *Cement and Concrete Research*, 34(9), 1569-1578.

Palandri, J. L., and Kharaka, Y. K. (2004). A compilation of rate parameters of water-mineral interaction kinetics for application to geochemical modeling (No. OPEN-FILE-2004-1068). GEOLOGICAL SURVEY MENLO PARK CA.

Reardon, E. J. (1992). Problems and approaches to the prediction of the chemical composition in cement/water systems. *Waste Management*, 12(2), 221-239.

Revertegat, E., Richet, C., and Gegout, P. (1992). Effect of pH on the durability of cement pastes. *Cement and Concrete Research*, 22(2), 259-272.

Samson, E., and Marchand, J. (2007). Modeling the transport of ions in unsaturated cement-based materials. *Computers and Structures*, 85(23), 1740-1756.

Schmidt, T., Lothenbach, B., Romer, M., Scrivener, K., Rentsch, D., and Figi, R. (2008). A thermodynamic and experimental study of the conditions of thaumasite formation. *Cement and Concrete Research*, 38(3), 337-349.

Soler, J. M. (2013). Reactive transport modeling of concrete-clay interaction during 15 years at the Tournemire Underground Rock Laboratory. *European Journal of Mineralogy*, 25(4), 639-654.

Soler, J. M. (2012). High-pH plume from low-alkali-cement fracture grouting: Reactive transport modeling and comparison with pH monitoring at ONKALO (Finland). *Applied Geochemistry*, 27(10), 2096-2106.

Soler, J. M., Vuorio, M., Hautojärvi, A. (2011). Reactive transport modeling of the interaction between water and a cementitious grout in a fractured rock. Application to ONKALO (Finland). *Applied Geochemistry*, 26(7), 1115-1129.

Soler, J.M, Mäder, U. K. (2010). Cement-rock interaction: Infiltration of a high-pH solution into a fractured granite core. *Geologica Acta*, 8(3), 221-233.

Steefel, C.I., (2009). CrunchFlow software for modeling multicomponent reactive flow and transport. User's manual, Earth Sciences Division. Lawrence Berkeley, National Laboratory, Berkeley, CA.

Thoenen, T., Kulik, D. (2003). Nagra/PSI Chemical Thermodynamic Data Base 01/01 for the GEM-Selektor (V. 2-PSI) Geochemical Modeling Code: Release 28-02-03. PSI Technical Report TM-44-03-04 about the GEMS version of Nagra/PSI chemical thermodynamic database 01/01.

Trotignon, L., Devallois, V., Peycelon, H., Tiffreau, C., Bourbon, X. (2007). Predicting the long term durability of concrete engineered barriers in a geological repository for radioactive waste. *Physics and Chemistry of the Earth*, Parts A/B/C, 32, 259-274.

Wagner, T., Kulik, D. A., Hingerl, F. F., Dmytrieva, S. V. (2012). GEM-Selektor geochemical modeling package: TSolMod library and data interface for multicomponent phase models. *The Canadian Mineralogist*, 50, 1173-1195.

Wolery, T. J., Jackson, K. J., Bourcier, W. L., Bruton, C. J., Viani, B. E., Knauss, K. G., Delany, J. M. (1990). Current status of the EQ3/6 software package for geochemical modeling. Chemical modeling of aqueous systems II, 416, 104-116.

Zajac, M., Rossberg, A., Le Saout, G., and Lothenbach, B. (2014). Influence of limestone and anhydrite on the hydration of Portland cements. *Cement and Concrete Composites*, 46, 99-108.

Zuloaga, P., Ordonez, M., Saaltink, M. W., and Castellote, M. (2009). Capillarity in Concrete Disposal Vaults and Its Influence in the Behavior of Isolation Barriers at El Cabril Low and Intermediate Level Radioactive Waste Disposal Facility in Spain-9015.

UNE 80-210-94 Methods of testing cement. Chemical analysis. Determination of the chemical composition of Portland clinker and cement by X-ray fluorescence. AENOR 1994.

UNE 80304 Cements calculations of potencial composition of portland clinker. AENOR 2006.

Chapter 5

Evaporation experiments in the non saturated matrix

This chapter deals with the laboratory evaporation experiments with mortar cylindrical samples which were made to investigate the geochemical processes that occur in the inner part of the El Cabril cell walls as a consequence of water flow driven by evaporation. It includes the full characterization of the unreacted and reacted mortar samples, as well as the coupled transient thermohydraulic and reactive transport model to interpret the geochemical variation in the evaporation experiments.

5.1. Introduction

After 10 years of operation in El Cabril, small quantities of water started to appear in the control tanks of some of the concrete vaults. Capillary rise was identified as the origin of this phenomenon, together with evaporation and condensation caused by temperature differences between the concrete blocks and the surfaces of the vaults walls. A set of experiments and

numerical modeling were carried out to study these processes in the concrete and the impact on the potential migration of radionuclides (Saaltink et al., 2005; Ayora et al., 2006; Zuloaga et al., 2009).

The conceptual flow model can be summarized by defining two seasonal cycles (Saaltink et al., 2005): in the summer cycle the outer wall of the vaults is heated. There is a delay and attenuation in the heating of the concrete containers inside the vault. There is a gap of 0.02 m between containers and the inner wall surface. This air gap provokes a gradient in temperature and allows a flux of water vapor from the wall surface to the containers surface. The balance of mass and energy in the system shows an evaporation at the wall pores, which provokes significant capillary suction and a capillary rise from the water table. The water vapor flows to the containers, condensing at the pores and increasing their saturation. When 100% humidity is reached at the surface the condensed water drips down the containers' surface. In wintertime, the process is inversed. Walls are colder and there is evaporation in the containers, with diffusion of water vapor to the surface of the walls, increasing the saturation state, decreasing the capillary suction, and thus permitting liquid flow from the pores to the water table. Once 100% saturation is reached, some liquid is condensed at the surface and collected in the control tank. This conceptual model was tested by Saaltink et al. (2005) with a numerical model using CodeBright (Olivella et al., 1996), which allows the simulation of water (liquid and vapor) and heat transport, in unsaturated media. The model showed that the seasonal behavior of the system has a good correlation with the amount of water collected. It also showed that the calculated temperature differences (5ºC) between inside and outside provoke evaporation and condensation inside the cells.

To improve the preliminary models, a reactive transport model was developed by Ayora et al. (2007), based on the water flow model previously described, using the reactive transport code Retraso-CodeBright (Saaltink et al., 2004). A specific development was made for C-S-H dissolution kinetics by representing C-S-H as a solid solution (Lichtner and Carey; 2006), though the kinetic rate laws for C-S-H were not known. The Retraso-CodeBright calculations predicted a degraded thickness of 2 mm in concrete after 80 years.

Considering the existing knowledge of the processes affecting the El Cabril concrete walls, the main goal of this study is to improve the current understanding of the effects that these physicochemical processes (capillary flow of water, conduction of heat, evaporation and condensation of vapor on the concrete surface, diffusion of solutes in the liquid of the pores, advective transport of solutes in the flowing water, mechanical dispersion of solutes associated with advective transport, chemical reactions between dissolved aqueous species, and dissolution and precipitation reactions of solid phases) exert on the El Cabril concrete.

To achieve this goal, a series of evaporation experiments were performed to reproduce this phenomenon at the laboratory scale as well as a thorough *ex-situ* examination of the mortar before and after the experiments. A second objective was to perform numerical simulations to evaluate the influence of water evaporation on the reacting mortar in a non-saturated matrix, using the CodeBright code, and to identify the geochemical processes governing the mortar reactivity. Retraso-CodeBright was used for this process. An improvement on the modeling presented compared to the previous ones is that the C-S-H dissolution kinetic approach previously used is the one obtained in this study (Chapter 2). Measurement of the chemical composition of the porewater after the experiment was not possible. Hence, the numerical simulations were the only possible approach to understand porewater chemistry.

5.2. Experimental methodology

The scheme depicted in Figure 5.1 summarizes the experimental and modeling tasks performed in this study.

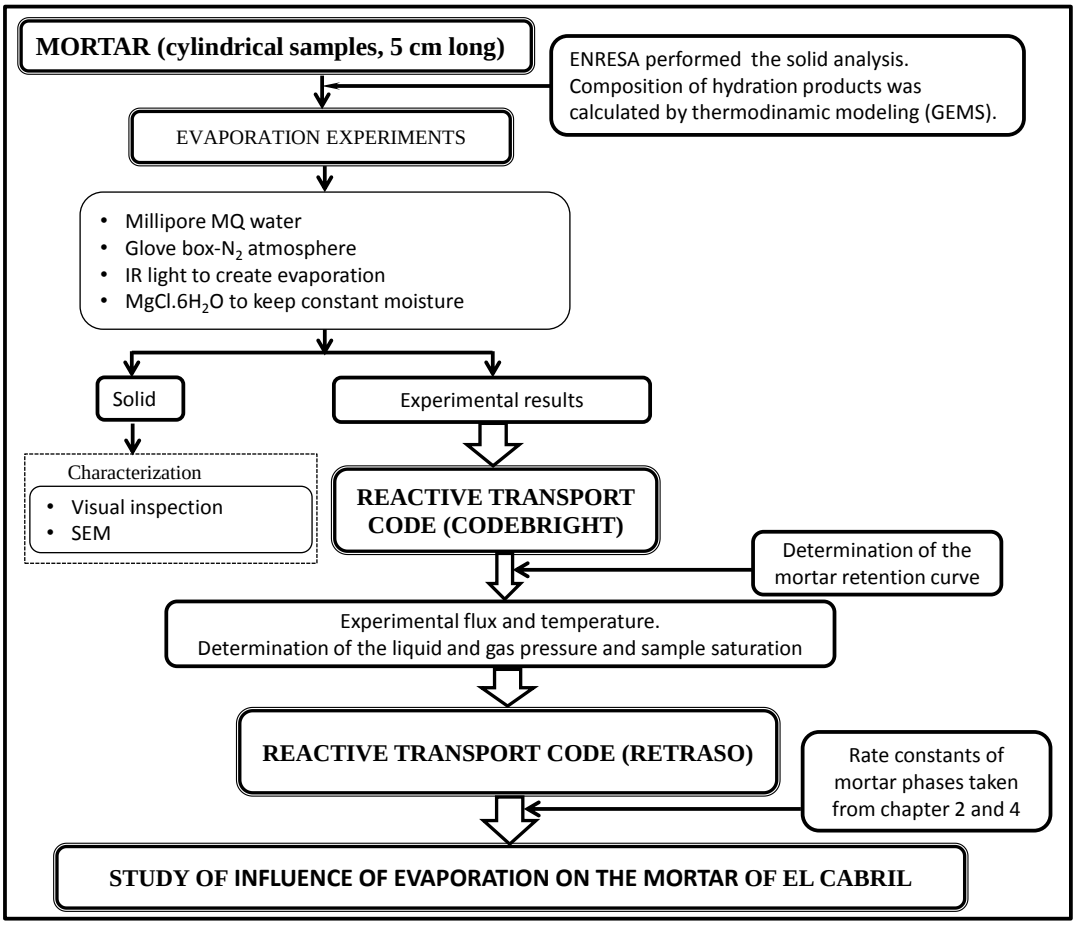

Figure 5.1. *Scheme of the tasks carried out to study the degradation of mortar in the evaporation experiments.*

5.2.1 Sample characterization

ENRESA provided mortar samples (10 cm in length and 11 cm in diameter) as representative samples of the mortar used in El Cabril walls. The composition of the hydrate assemblage formed during the hydration of the OPC + fly ash mixtures was calculated based on the cement and fly ash composition (Table 4.2) using the GEM-Selektor (GEMS) software package (Lothenbach and Winnefeld, 2006; Lothenbach et al., 2008a; De Weerdt et al.; 2011; Wagner et al., 2012; Kulik et al., 2013). Table 4.4 in Chapter 4 lists the calculated phases in the mortar.

5.2.2 Experimental sample preparation

For the evaporation experiments, two of the provided samples were saw-cut to be 5 cm long. In the experiments, evaporation was allowed to take place exclusively at the top surface. To this end the cylinder walls were thoroughly coated with latex paint. Once the paint was dried, the samples were weighted, and thereafter, fully immersed in 500 cm^3 of Millipore MQ water in order to be totally saturated. Variation in weight of the samples was timed during this saturation stage. The two specimens were considered to be fully saturated when the weight ceased increasing with time (≈ 15 days). This stage was carried out inside a glove box under N_2 controlled atmosphere to avoid sample carbonation. Once the weight remained constant, the specimens were considered to be saturated with volumes of water of 64.7 cm^3 and 62.4 cm^3 (g), respectively. These resulting effective volumes were smaller than 77.8 cm^3, which is the pore volume of the samples considering their total volume (522.4 cm^3) and reported porosity (14. 9 %). Possible reasons for this discrepancy were (i) that total displacement of pore air was not possible or (ii) that samples were already partially saturated before immersion in Millipore water.

5.2.3 Sample solid analyses

The unreacted surfaces of the bottom (inlet) and top (outlet) of the samples were visually inspected and SEM-EDS examined. The inspection was carried out using a Leica M125 stereomicroscope with a 12.5:1 zoom, and SEM (Scanning Electron Microscopy) examination was performed using a JEOL JSM-840 microscope and a field-emission scanning microscope Hitachi H-4100FE. Figure 5.2 shows the top and bottom surfaces. It was observed that quartz grains were surrounded by the cement paste, and that the content of quartz grains appeared to be higher at the bottom. It is likely that grains dropped down by gravity during the mortar curing.

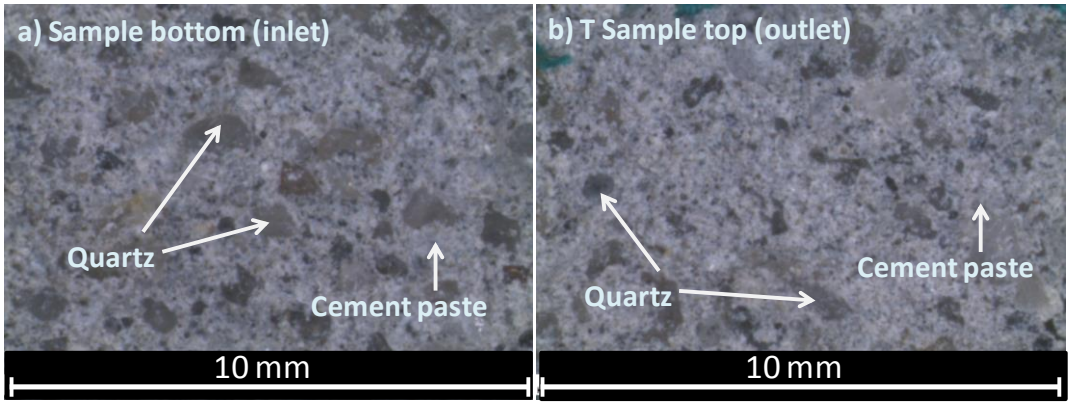

Figure 5.2. *Photographs of the surfaces of the unreacted samples: (a) bottom surface (inlet) and (b) top surface (outlet). The content of quartz grains is higher at the bottom.*

After the experiments, the samples were cut with diamond disc in seven portions, whose surfaces, perpendicular to the flow, were likewise examined. The seven portions of each sample were impregnated in epoxy resin, and their surfaces polished and carbon coated.

5.2.4 Mortar retention curve

Retention curves represent the capillary suction (Pc in MPa) as a function of the state of saturation at a given temperature. The retention curve of the mortar was obtained by calculating the capillary suction from measurements of vapor pressure at dew-point temperature using a WP4-T potentiometer (range between 0 to 300 MPa with a resolution of 0.1 MPa). From the measured equilibrium vapor pressure, suction was calculated using the Kelvin equation:

$$\psi = \frac{\rho_{wRT}}{M_w} \ln\left(\frac{p}{p_o}\right) \qquad \text{Eq. 5.1}$$

where ψ is total suction, R is gas constant (8.314 J/mol), T is temperature (K), M_w is molar mass of water (18 g/mol), ρ_w is water density, p is vapor pressure and p_o is saturated vapor pressure ($p/p0$ is relative humidity). Capillary pressure (ψ in MPa) was expressed as a function of volumetric content of water (θ_l) or effective saturation (S_e, Van Genuchten model (1978), see Figure 5.3).

Four mortar samples were used to determine the retention curve: two dry samples and two saturated samples. The dry samples were used to determine the retention curve from dry state to saturated state. Inversely, the saturated samples were used to obtain the retention curve from a saturated state to dry state. Owing to the complex nature of the liquid-phase configuration in an unsaturated porous medium such as mortar, the relationship between water pressure and water content is not unique and presents hysteresis effects, which can be attributed to four main

reasons (Maqsoud et al., 2004): i) geometric nonuniformity of individual pores, resulting from the so-called "Ink Bottle" effect, ii) different spatial connectivity of pores during drying or wetting process, iii) variation in liquid-solid contact angle, and iv) air entrapment.

Two initially weighted samples (fragments of ≈ 1-2 cm of size) were dried in oven at 40 ºC. The loss of weight was timed, and total dryness was achieved when the weight remained constant. To obtain saturated samples, two mortar samples were immersed in a $Ca(OH)_2$-saturated solution (to avoid dissolution of portlandite of the mortar) inside the glove box under N_2 controlled atmosphere until constant weight was reached. The $Ca(OH)_2$-saturated solution was prepared with Millipore MQ water previously bubbled with N_2 to prevent CO_2 absorption. The solution pH was measured to be 12.23 ± 0.05. Thereafter, the solution was filtered with a 0.45 μm filter.

To obtain the retention curve from dry state to saturated state, a drop of the filtered saturated $Ca(OH)_2$ solution was poured onto the dry fragments and they were maintained under high relative humidity inside a box. After 24 h, when the drop of $Ca(OH)_2$-saturated solution was absorbed by the mortar, the capillary pressure or suction was measured. Wet samples were isolatedly stored inside a box surrounded by Na(OH) pellets to keep the humidity level very low. After 24 h, the capillary pressure of the mortar sample was measured. This process was successively repeated until the retention curves were appropriately determined.

The retention curves obtained are shown in Figure 5.3. The fit parameters for these curves are listed in Table 5.5. The parameters of the retention curve used in the CodeBright model were the average of the retention curve fits to the experimental data obtained starting from the dry and saturated samples.

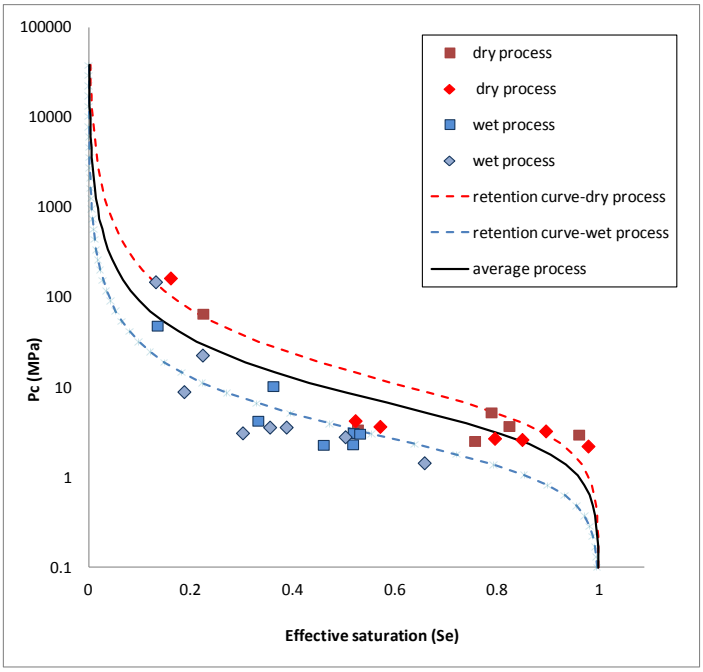

Figure 5.3. *Retention curve that fits the measured data of the El Cabril mortar.*

5.2.5 Experimental setup

Two evaporation experiments (namely A and B) were carried out in a glove box under CO_2-free N_2 controlled atmosphere to avoid sample carbonation. In each experiment, the paint-coated sample was partially immersed in Millipore MQ water (Fig. 5.4 a). The top surface was heated with an infrared lamp Philips Infrared PAR 38 IR 175 W to force porewater evaporation. The consequent decrease in water pressure induced a water flux from the inlet upwards by capillary ascension.

The IR lamp was placed 60 cm above the top surface (Fig. 5.4 a). Temperature at the top surface was continuously measured by two thermal probes to be 62.6 ± 2 ºC (experiment A) and 65.5 ± 2 ºC (experiment B). The bulk temperature inside the glove box was also controlled and was 40 ± 2 ºC (experiment A) and 44 ± 2 ºC (experiment B). A measured constant relative humidity of 34 % was guaranteed in the glove box during the experiment by placing an open container filled with a solution equilibrated with $MgCl_2 \cdot 6H_2O$. The CO_2 content in the glove box was indirectly controlled by measuring the O_2 concentration, which never exceeded 2 % (corresponding to 38 ppm of CO_2).

The sample was placed into a polymethyl methacrylate (PMMA) cylindrical container. The 1 mm gap between the top of the container wall and the sample walls was covered with a PMMA piece and sealed with silicon glue to prevent any water flux and evaporation from the water reservoir (Fig. 5.4). The sample was completely immersed in water in experiment A and half-immersed in experiment B (up to 2.5 cm in height). A tube connected the PMMA container

with a 5 L plastic jar placed in an adjacent CO_2-free glove box (Fig. 5.4 b) to ensure the water level to be constant.

CO_2-free Millipore MQ water in the 5 L jar was constantly supplied to the PMMA container. Millipore MQ water evaporation from the 5 L jar bottle was observed to be negligible. An open container with 1 L of 12 M NaOH solution was placed inside this glove box to help minimize a CO_2 contamination. The loss of Millipore MQ water with time, due to evaporation on the top surface of the mortar sample, was controlled by continuously weighting the 5 L bottle during the experiment (weight uncertainty was ± 0.01 g). Before evaporation started in the experiments, the initial Millipore MQ water weight in the 5 L jar decreased by 6.0 g (experiment A) and 10.4 g (experiment B) during approximately four days, and remained constant afterwards. This fact indicated that the remaining pore air was totally displaced from the samples, which were now considered to be fully saturated.

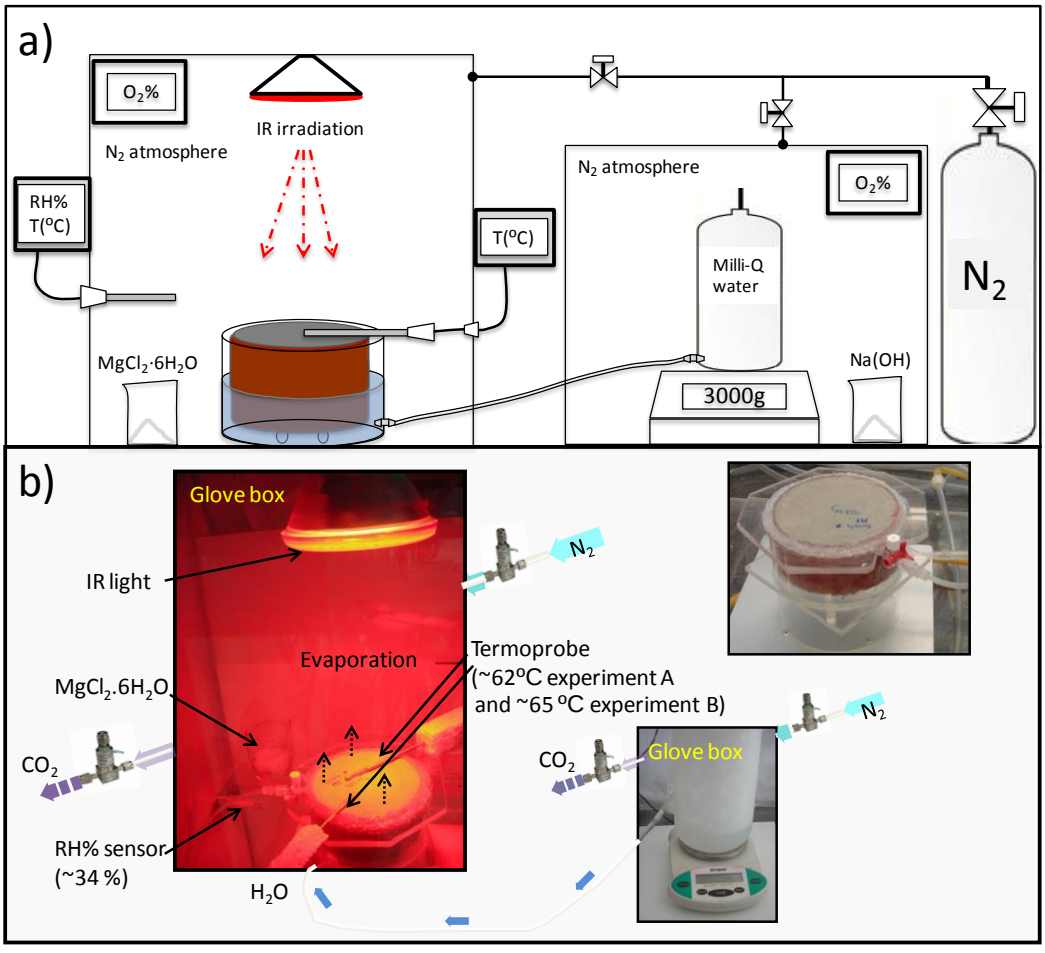

Figure 5.4. *Setup of the evaporation experiments: a) scheme that shows the heated sample in the glove box and the Millipore MQ water supply inside an adjacent glove box; b) photographs showing the experimental components (IR lamp, sample, valves, thermoprobe, moisture sensor, water container, 5L jar and scale). Room temperature was 23 ± 2 ºC.*

Experiment A lasted 96 days (92 days irradiated). After that time the sealed contact between the sample and the PMMA cylinder was damaged. Experiment B was stopped after 236 days (230 days irradiated) a period considered to be sufficient for a proper evaluation of the processes.

Once the experiments were finished, the samples were retrieved, dried with isopropanol and stored in a desiccator. Thereafter, they were cut into two halves using the Brazilian test method (ASTM D3967 – 08) to guarantee a clean surface along the flux direction (Fig. 5.5a). One of the halves of each sample was sliced perpendicular to the flux direction into seven sub-samples by diamond-cutting. The seven portions were ordered from bottom upwards, according to the flux direction (slices 1 to 6 were fully immersed in Millipore MQ water and slice 7 was heated in experiment A; slices 1 to 3 were fully immersed in Millipore MQ water and slice 7 was heated in the experiment B; Figure 5.5). The surfaces parallel to the flux direction of the seven sub-samples were examined optically and by EDS-SEM.

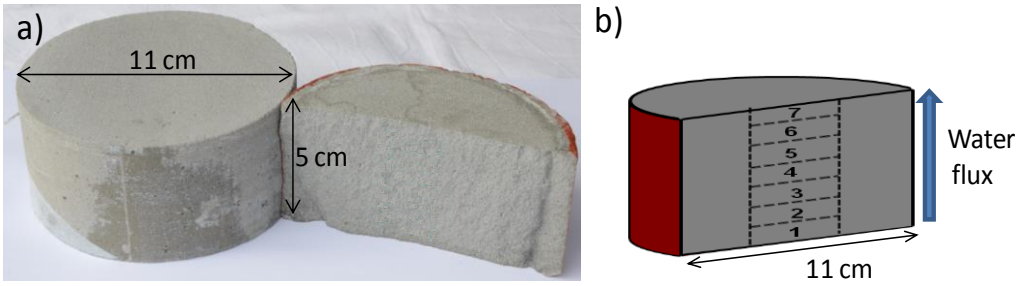

Figure 5.5. *Retrieved sample: a) photograph of the surface parallel to the flux direction and b) scheme of the seven sub-samples before diamond disc-cutting.*

5.3. Model description

5.3.1 Conceptual model

The processes occurring in the evaporation experiments are depicted in Figure 5.6.

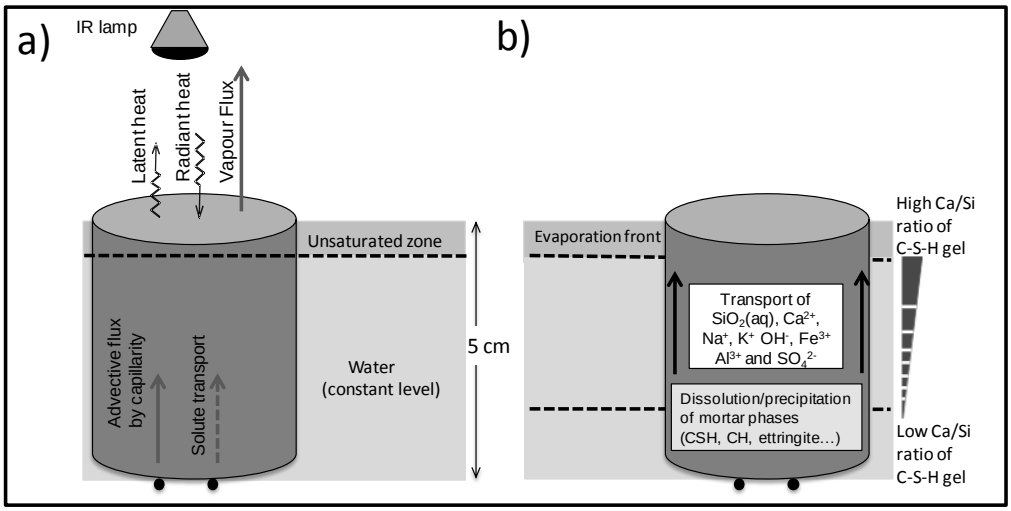

Figure 5.6. *Conceptual model for the physicochemical processes considered to occur: a) physical processes and b) chemical processes.*

The mortar samples were initially saturated. Water evaporation at the top surface induced porewater ascension by capillarity. Entering Millipore MQ water interacted with the mortar components (C-S-H gel, portlandite, ettringite, monocarboaluminate, hydrotalcite, fly ash, Si-hydrogarnet, calcite and quartz). Dissolution of primary phases and precipitation of secondary phases were considered to be responsible for the change in the initial porewater composition with time. A working hypothesis was that as renewed porewater approached the top heated surface, evaporation could cause an increase in solute concentration to yield a supersaturated solution. Hence, precipitation of secondary phases could plausibly take place in the upper region (outlet), resulting in a decline in porosity and permeability.

5.3.2 Thermohydraulic modeling

The multiphase flow and heat transport code CodeBright (Oilvella et al., 1996) was used to simulate the water flux and temperature in the evaporation experiments. The model considers three phases: solid phase (mortar), liquid phase (liquid water) and gas phase (mixture of water vapor and dry air). Likewise, three components are considered: water, dry air and temperature. For each component a mass balance equation is formulated and resolved. CodeBright solves the energy mass balance in terms of temperature (heat transport equation) and the mass balance for water and dry air in terms of pressure (liquid and gas pressure, respectively). Change in phase

mass is related to the response to external inputs and outputs and to fluxes within the domain (mass redistribution). Phase storage is basically controlled by phase saturation; liquid saturation (S_l) is related to pressure by means of the retention curve (Table 5.1). Gas saturation (S_g) is defined as *1*-S_l.

The total mass balance of water is expressed as:

$$\frac{\partial}{\partial t}\left(\omega_l^w \rho_l S_l \phi + \omega_g^w \rho_g S_g \phi\right) + \nabla\left(j_l^w + j_g^w\right) = f^w \qquad \text{Eq. 5.2}$$

where subscripts l and g refer to liquid and gas, respectively. Superscript w refers to water, ω is the mass fraction (kg kg^{-1}) of a component in the liquid phase or gas, j (kg m^{-2} s^{-1}) is the total flux (advective, dispersive and diffusive), ρ is the density (kg m^{-3}) of a phase, S_l is the hydraulic saturation (m^3 m^{-3}), ϕ is the porosity (m^3 m^{-3}), and f^w is the term that considers an external source (kg m^{-3} s^{-1}). A similar mass balance is solved for air.

The heat transport equation expresses energy conservation. Heat is transported mainly by conduction (Fourier's law) and by advection-dispersion. Specific enthalpies of each phase are obtained assuming constant heat capacities for solids, water and air and adding the latent heat of water vapor. Since thermal conductivity of liquid and solids is much larger than that of gases, the overall thermal conductivity varies with porosity and liquid saturation.

With the internal energy defined as the product of heat capacity and temperature, the equation for internal energy balance in the porous medium is defined taking into account the internal energy in each phase (E_l, E_g and E_S in J kg^{-1}):

$$\frac{\partial}{\partial t}\left(E_s \rho_s (1-\phi) + E_l \rho_l S_l \phi + E_g \rho_g S_g \phi\right) + \nabla\left(i_c + j_{Es} + j_{El} + j_{Eg}\right) = f^Q \qquad \text{Eq. 5.3}$$

$$E_l = E_l^w \omega_l^w + E_l^a \omega_l^a \qquad \text{Eq. 5.4}$$

$$E_l^w = 4184\,T \quad ; \; E_l^a = 1000\,T$$

$$E_g = E_g^w \omega_g^w + E_g^a \omega_g^a \qquad \text{Eq. 5.5}$$

$$E_g^w = 2.5 \times 10^6 + 1900\,T \quad ; E_g^a = 1000\,T$$

where i_c is the energy flux (J m^{-2} s^{-1}) due to conduction through the porous medium (Fourier's law), j_{Es}, j_{El} and j_{Eg} (J m^{-2} s^{-1}) are advective fluxes of energy caused by mass motions, f^Q is an energy supply (J m^{-2} s^{-1}) externally (radiation) or internally (chemical reaction), ρ is the density (kg m^{-3}) of a phase, S_l is the hydraulic saturation (m^3 m^{-3}) and ϕ is the porosity (m^3 m^{-3}). E_l^w, E_l^a and E_g^a have a linear dependence with the temperature, given by the heat capacity.

A set of constitutive laws and equilibrium relationships are required to express the dependent variables (S_e, ρ, i_c, q_α, etc; see Table 5.1) of the mass balance equations as a function of the state variables (P_l, P_g and T). Such constitutive laws are, for example, Fourier's law relating conductive heat flux to temperature gradient, Darcy's law defining the advective phase fluxes as a function of pressure gradients, Van Genuchten law to express the retention curve relating capillarity pressure with saturation, and Fick's law to express the diffusive fluxes. Phase changes (e.g., water evaporation/condensation or air dissolution/degassing) are calculated according to equilibrium between phases. Henry's Law expresses the solubility of air dissolved in water. The Psychrometrics law expresses the equilibrium between liquid water and vapor. The main laws controlling these balances are listed in Table 5.1 and briefly explained below.

Table 5.1. *Summary of constitutive laws and equilibrium relationships.*

Constitutive Laws	
Advective fluxes (q_α; where α = l for liquid and α = g for gas) (*Darcy's Law*)[(1)] $q_\alpha = -\frac{k_{int} \cdot k_{r\alpha}}{\mu_\alpha} \cdot (\nabla P_\alpha - \rho_\alpha g)$ $\mu_\alpha = A_\alpha^{\left(\frac{B_\alpha}{273.15+T}\right)}$ $k_{rl} = \sqrt{S_e}\left(1 - \left(1 - S_e^{\frac{1}{m}}\right)^m\right)^2$ $k_{int} = k_{int,0}\frac{\phi^3}{(1-\phi)^2}\frac{(1-\phi_0)^2}{\phi_0^3}$ (Kozeny's model)	$k_{int,0} = 4.2 \cdot 10^{-18}$ m^2 $\phi_0 = 14.9\%$ $A_l = 1.48 \cdot 10^{-12}$ MPa s $B_l = 119.4$ ºC $A_g = 2.1 \cdot 10^{-12}$ MPa s $B_g = 1808.5$ ºC
Diffusive fluxes of air and vapor (q_α^β ; where α = l for liquid and α = g for gas and β = v for vapor and β = a for air)(*Fick's Law*)[(2)] $q_\alpha^\beta = -(\tau\phi\rho_\alpha S_\alpha D_\alpha^\beta \mathbf{I})\nabla\omega_\alpha^\beta$ $D_\alpha^{vapor} = D_v\left(\frac{(273.15+T)^n}{P_g}\right)$ $D_\alpha^{air} = \tau D_a^{\left(\frac{-Q}{R(273.15+T)}\right)}$	$D_v = 5.9 \cdot 10^{-6}$ m^2 s^{-1} K^{-n} Pa n = 2.3 $D_a = 1.1 \cdot 10^{-4}$ m^2 s^{-1} Q = 24530
Heat conductive Flux (i_c) (*Fourier's Law*)[(3)] $i_c = -\lambda\nabla T$ $\lambda = \lambda_{sat}^{S_l}\lambda_{dry}^{(1-S_l)}$ $\lambda_{sat} = \lambda_{solid}^{(1-\phi)}\lambda_{liq}^{\phi}$ $\lambda_{dry} = \lambda_{solid}^{(1-\phi)}\lambda_{gas}^{\phi}$	$\lambda_{solid} = 1.56$ WmK^{-1} $\lambda_{liq} = 0.6$ WmK^{-1} $\lambda_{gas} = 0.024$ WmK^{-1}
Retention curve (S_l) (*Van Genuchten*)[(4)] $S_e = \frac{S_l - S_{rl}}{S_{ls} - S_{rl}} = \left(1 + \left(\frac{P_g - P_l}{P}\right)^{\frac{1}{1-m}}\right)^{-m}$ $P = P_0\frac{\sigma}{\sigma_0}$	$\sigma_0 = 0.072$ N m^{-1} at 20ºC
Equilibrium relationships	
Henry's Law [(5)] $\omega_l^{air} = \frac{P_{air}}{H}\frac{M_w}{M_{air}}$	Mass fraction of dissolved air (ω_l^{air})
Psychometric's Law[(6)] $\rho_g^{vapor} = \rho_g\omega_g^{vapor} = \rho_{g,sat}^{vapor} \cdot e^{\left(\frac{M_w g \phi_c}{RT}\right)}$	Mass vapor fraction (ω_g^{vapor})

[(1)] flow rate, q_α (m s^{-1}); viscosity of the phase, μ_α (Pa s); relative permeability of the phase, $k_{r\alpha}$ (m^2); intrinsic permeability, k_{int} (m^2); density of the phase, ρ_α (kg m^{-3}); gravity vector, g (9.8 m s^{-2}); effective saturation, Se; porosity, ϕ; reference porosity, ϕ_0; intrinsic permeability at ϕ_0.

[(2)] q_α^β (m s^{-1}); diffusion coefficient of species β in phase α, D_m^β (m^2 s^{-1}); density , ρ_α (Kg m^{-3}); porosity, ϕ; tortuosity, τ; degree of saturation, S_α; mass fraction of species β in phase α, ω_α^β; identity matrix, I.

[(3)] heat conductive flux, i_c (J s^{-1}); thermal conductivity, λ.

[(4)] saturation degree, S_l; effective saturation, Se; residual saturation, S_{rl} ; maximum saturation, S_{ls}; input pressure of gas and liquid respectively, P_g and P_l (Pa); measured pressure at 20 ºC, P_0 (Pa); surface tension at temperature in which P_0 was measured, σ_0 (N m^{-1}); water surface tension at 20 ºC, σ_0 (N m^{-1}); shape function for retention curve, m.

[(5)]dry air pressure, P_{air} (Pa); molecular weight of water, M_w.(g mol^{-1}); molecular weight of dry air, M_{air} (g mol^{-1}), Henry's constant, H (10000 MPa).

[(6)] density of water in gas, ρ_g^{vapor} (kg m^{-3}); density of water in saturated gas, $\rho_{g\,sat}^{vapor}$ (kg m^{-3}); capillary potential, ϕ_χ.

Also boundary conditions are needed to take into account the exchange of vapor and heat between the sample and the environment. The boundary conditions and parameters used in the model are summarized in Table 5.2. The second term on the right-hand-side of the liquid and vapor fluxes represents the advective mass flow due to pressure difference between the sample and the environment. This term is considered when the gas or liquid pressure (P_g^0 or P_l^0) is prescribed. γ_g and γ_l are the leakage coefficients for advective flux and allow imposing the Cauchy-type boundary condition (Delahaye et al., 2002). In practical terms they fix the pressure at the boundary to a prescribed value (Chaparro et al., 2013). The last term represents a diffusive-type mass flow due to the differences of density between the boundary and the medium that take place when the mass fractions ($(w_l^w)^0$, $(w_l^a)^0$, $(w_g^w)^0$ or $(w_g^a)^0$) are prescribed at the boundary. β_g and β_l are the leakage coefficients for diffusive-type flux.

Table 5.2. *Boundary conditions considered in the CodeBright model.*

Boundary Conditions	Parameters required	Units
Liquid Flux		
$j_l^w = (\omega_l^w)^0 j_l^0 + (\omega_l^w)^0\,\gamma_l(P_l^0 - P_l) + \beta_l\left((\rho_l\omega_l^w)^0 - (\rho_l\omega_l^w)\right)$	j_l^0	kg m^{-2} s^{-1}
$j_l^a = (\omega_l^a)^0 j_l^0 + (\omega_l^a)^0\,\gamma_l(P_l^0 - P_l) + \beta_l\left((\rho_l\omega_l^a)^0 - (\rho_l\omega_l^a)\right)$	$(\omega_l{}^w)^0$, $(\omega_l{}^a)^0$ (1)	kg kg^{-1}
	$P_l{}^0$ (2)	MPa
	ρ_l (3)	kg m^{-3}
	β_l(4)	kg s^{-1} MPa^{-1} m^{-2}
	γ_l(5)	kg s^{-1} MPa^{-1} m^{-2}
Vapor Flux		
$j_g^w = \left(\omega_g^w\right)^0 j_g^0 + \left(\omega_g^w\right)^0\,\gamma_g\left(P_g^0 - P_g\right) + \beta_g\left(\left(\rho_g\omega_g^w\right)^0 - \left(\rho_g\omega_g^w\right)\right)$	$(\omega_g{}^w)^0$,$(\omega_g{}^a)^0$ (1)	kg kg^{-1}
	$P_g{}^0$ (2)	MPa
	ρ_g (3)	kg m^{-3}
Gas flux	β_g (4)	kg s^{-1} MPa^{-1} m^{-2}
$j_g^a = \left(\omega_g^a\right)^0 j_g^0 + \left(\omega_g^a\right)^0\,\gamma_g\left(P_g^0 - P_g\right) + \beta_g\left(\left(\rho_g\omega_g^a\right)^0 - \left(\rho_g\omega_g^a\right)\right)$	γ_g (5)	kg s^{-1} MPa^{-1} m^{-2}
Energy flux		
$j_e = j_e^0 + \gamma_e(T^0 - T) + E_g^w\left(j_g^w\right) + E_l^w(j_l^w)$	j_e^0 (6)	J s^{-1}m^{-2}
	γ_e (7)	J s^{-1}C^{-1} m^{-2}
	T^0 (8)	ºC

(1) $(\omega_g{}^w)^0$ and $(\omega_g{}^a)^0$ are mass fraction of water in gas and air in gas, respectively; values calculated by means of measured relative humidity during the experiments; $(\omega_l{}^w)$, $(\omega_l{}^a)$ are mass fraction of water in liquid and air in liquid, respectively;
(2) $P_g{}^0$ and $P_l{}^0$ are the prescribed gas and liquid pressure;
(3) ρ_l and ρ_g are the prescribed liquid and gas density (ρ_g = 1.12 kg m^{-3});
(4) β_l and β_g are leakage coefficients between the bottom of the sample and the bottom boundary or between the top of the sample and atmosphere for non-advective flux;
(5) γ_l and γ_g are the leakage coefficients for liquid and vapor advective flux;
(6) j_e^0 is inflow of radiant heat from lamp;
(7) γ_e is leakage (surface transfer) coefficient for energy flux;
(8) T^0 is the external temperature.

5.3.2.1. Thermohydraulic parametrization

To model the 5 cm long sample a 1D mesh was generated and divided into 51 nodes and 50 elements in the flux direction (z axis). Nodes 1 and 51 correspond to the bottom (inlet) and the top (outlet) of the sample.

The boundary conditions considered are shown schematically in Figure 5.7 and explained below. The boundary condition for energy flux at the top of the sample was fixed considering both the heat flux of the IR lamp (j_e^0 = 400 J m^{-2} s^{-1}) and the averaged measured temperature (T^0) in the glove box (40 ºC and 44 ºC for the experiment A and B, respectively). The boundary condition for temperature at the bottom of the sample was fixed to 49 ºC and 52 ºC for experiments A and B, respectively. These values allowed fitting of the model to the measured temperatures at the top by adjusting the γ_e parameters. Regarding the boundary conditions for liquid flux, at the bottom of the sample pressure was calculated to be 0.101815 MPa and 0.101570 MPa for experiments A and B, respectively, by adding the corresponding water pressure to the atmospheric pressure and fixing a large γ_l value. Regarding the boundary conditions for vapor flux, at the top the mass fraction of water in gas was calculated from the relative humidity inside the glove box (34 %) and T^0 (40 ºC and 44 ºC for experiments A and B, respectively). γ_g and β_g coefficients were fitted to reproduce the atmospheric pressure at the top of the sample (negligible advection of gas) and the flux of vapor, respectively. Tortuosity of vapor and air were kept at default values of 1.

All the parameters considered in the model are listed in Table 5.3 and Table 5.4. The fitted parameters from the measured retention curve are shown in Table 5.5. The high pressure (P_0) indicates a very retentive material due to its small pores. Although porosity measured at the Eduardo Torroja Institute (CSIC) by mercury intrusion porosimetry at 28 days of hydration was 0.149, a hydration calculation estimated porosity to be 0.125 (see Chapter 4; Section 4.2.2). The latter value was used in the Retraso-CodeBright simulations.

Table 5.3. *Mortar parameters and constitutive laws considered in the model.*

Mortar parameters and Constitutive Laws		Units
Porosity (ϕ)	0.125 [(e)]	-
Tortuosity (τ_a) diffusion air	1.0 [(d)]	-
Tortuosity (τ_v) diffusion vapor	1.0 [(d)]	
Retention Curve (Van Genuchten)		
Po	3.85 [(e)]	Mpa
m	0.42 [(e)]	-
S_{lr}	0	-
S_{ls}	1	-
Density of the solid (ρ_{sol})	2360 [(b)]	kg m^{-3}
Specific heat of the solid	789 [(b)]	J kg^{-1} K^{-1}

[(b)] from Saaltink et al. (2005)
[(e)] hydration calculation
[(c)] CodeBright value
[(d)] Default CodeBright value

Table 5.4. *Boundary conditions considered in the model.*

Boundary Conditions		Top (outlet)	Bottom (inlet)	Units
Liquid Flux	j_{liq}	0.0	0	kg $s^{-1}m^{-2}$
	$P_{l\ (experiment\ A)}$	-	0.101815	MPa
	$P_{l(experiment\ B)}$	-	0.101570	MPa
	γ_l		1.0	kg s^{-1} MPa^{-1} m^{-2}
Vapor Flux	$(\omega_g^w)^0_{(experiment\ A)}$	$1.54\cdot10^{-2}$	-	kg kg^{-1}
	$(\omega_g^w)^0_{(experiment\ B)}$	$1.88\cdot10^{-2}$		kg kg^{-1}
	P_g^0	0.101325	-	MPa
	β_g	$6.2\cdot10^{-6}$ [(c)]	-	m^3 $s^{-1}m^{-2}$
	γ_g	$2.0\cdot10^{-3}$ [(c)]	-	kg s^{-1} Pa^{-1} m^{-2}
Energy flux	j_e^0	$4\cdot10^2$	0	J $s^{-1}m^{-2}$
	γ_e	0.01 [(c)]	1500 [(c)]	J $s^{-1}C^{-1}$ m^{-2}
	$T^0_{(experiment\ A)}$	40	49	ºC
	$T^0_{(experiment\ B)}$	44	52	ºC

[(c)] CodeBright fit
(-) not needed

Table 5.5. *Parameters fitted for the retention curve.*

Parameters	Wet process	Dry process	Average curve
P (MPa)	1.7	6	3.85
λ	0.44	0.39	0.42
S_{rl}	0	0	0
S_{ls}	1	1	1

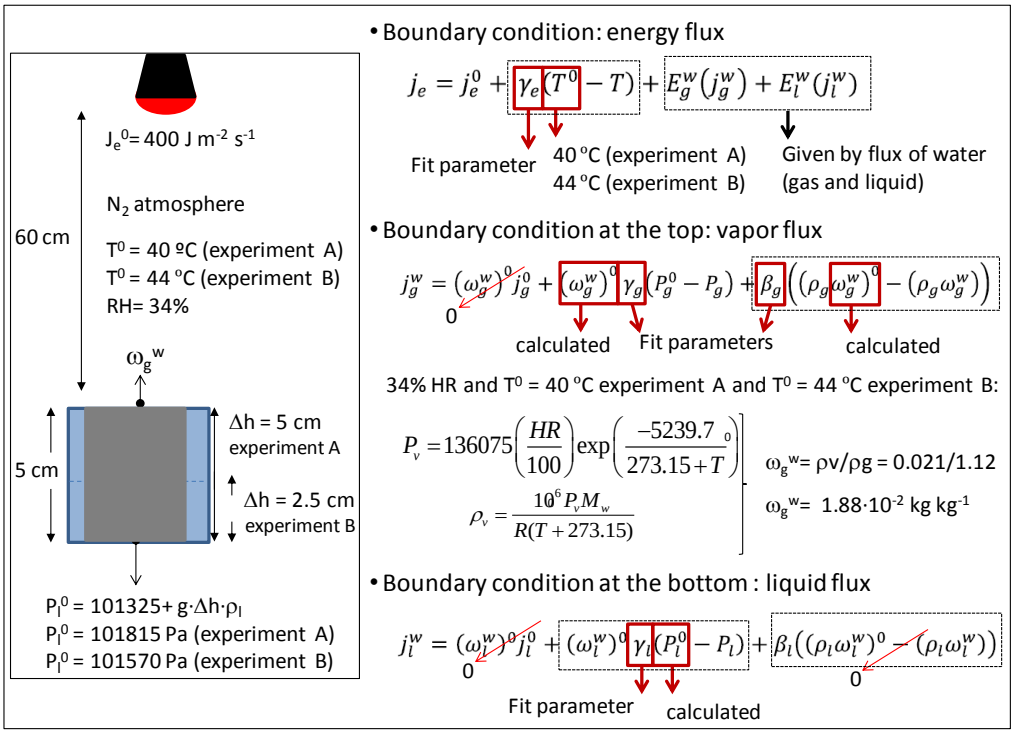

Figure 5.7. *Scheme of the boundary conditions considered in the model.*

5.3.3 Reactive transport

The multicomponent reactive transport code Retraso (Saaltink et al., 2004) which is coupled to the CodeBright code (Olivella et al., 1996), was used to simulate the variation of solution composition along the samples during the evaporation experiments.

Regarding solute concentrations in the liquid, Retraso solves numerically the equation of mass conservation of the solute for every component or primary species (Saaltink et al., 2004):

$$\frac{\partial(\theta u_j)}{\partial t} = \nabla(D\nabla u_j) - \nabla(q u_j) - \Sigma \upsilon_{jm} R_m \quad (j= 1,2,\ldots,Nc) \qquad \text{Eq. 5.6}$$

where u_j is the total concentration in solution of primary species j, θ is the volumetric content of water, t is the time, D is the effective diffusion coefficient plus the mechanic dispersion coefficient, q is the Darcy flux, R_m is the dissolution (-) or precipitation (+) rate of the mineral and υ_{jm} is the stoichiometric coefficient of j in mineral m.

The total number of species (N_{tot}) involved in the various reactions, such as dissolution and precipitation, is divided into primary species (N_c) and secondary species (N_x). The number of primary species is equivalent to the number of independent chemical components in the system, which is equal to the total number of species in solution (N_{tot}) minus the number of reactions in equilibrium that relates them. These reactions in equilibrium can be written as

$$A_i = \sum_{j=1}^{N_c} \nu_{ij} A_j \quad \text{(i= 1,2,…,Nx)} \qquad \text{Eq. 5.7}$$

where A_j and A_i are the chemical formulas of the primary and secondary species, respectively, and υ_{ij} is the number of the moles of the primary species j in one mole of secondary species i. Chemical equilibrium provides an algebraic relationship between the concentrations of primary and secondary species by the law of mass action. Then, for every reaction, the concentration of secondary species is expressed as:

$$x_i = K_i^{-1} \gamma_i^{-1} \prod_{j=1}^{N_c} (\gamma_j c_j)^{\nu_{ij}} \quad \text{(i= 1,2,…,Nx)} \qquad \text{Eq. 5.8}$$

where K_i is the equilibrium constant of the reaction, c_j is the molal concentration of primary species j, and γ_i and γ_j are the activity coefficients of the secondary and primary species, respectively. The activity coefficients are calculated by the extended Debye-Hückel model. The Pitzer model cannot be used due to the lack of data for silicates. Also, the total concentration of the component j in solution (u_j) is defined as

$$u_j = c_j + \sum_{i=1}^{N_x} \nu_{ij} x_i \qquad \text{Eq. 5.9}$$

The reactions between the aqueous and gaseous phases are fast enough and chemical equilibrium is assumed between these two phases. The gases close to atmospheric pressure are considered to behave similarly to ideal gases and their concentrations can be calculated from the partial pressure divided by temperature and by the gas constant.

Regarding multiphase reactive transport, an equation of conservation of mass is written for each component:

$$\frac{\partial}{\partial t}\left(\phi S_L u_a + (1-\phi) c_m + \phi (1-S_L) c_g\right) = L_L(u_a) + L_G(c_g) + R(c_i) \qquad \text{Eq. 5.10}$$

where u_a, c_m and c_g vectors are the concentrations of chemical species in the water, minerals and in the gaseous phase, respectively. R is a term which takes into account the mass of component that comes from chemical reactions between the phases. L_L and L_G are the operators for advection and dispersion/diffusion, respectively. These operators can be expressed as

$$L_L(u_a) = -\nabla q_L u_a + \nabla\phi S_L(D_{dis,a} + D_{dif,a})\nabla u_a \quad \text{Eq. 5.11}$$

$$L_G(c_g) = -\nabla q_G c_g + \nabla\phi(1 - S_L)(D_{dis,g} + D_{dif,g})\nabla c_g \quad \text{Eq. 5.12}$$

In Eq. (5.11), the dispersive term is usually very significant, while in Eq. (5.12), the diffusive term is the most important.

Some geochemical processes, such as dissolution and precipitation of many minerals, are known to progress so slowly with respect to fluid flow that they may never reach equilibrium. This is expressed through kinetic rate laws that are expressed as

$$R_m = sgn\left(log\left[\frac{Q_m}{K_m}\right]\right) A_m \sum k_m a_{H^+}^n f(\Delta G) \quad \text{Eq. 5.13}$$

where the term $sgn\left(log\left[\frac{Q_m}{K_m}\right]\right)$ defines the sign of the reaction (negative for dissolution and positive for precipitation), Q_m is the product of ionic activities, K_m is the equilibrium constant corresponding to the dissolution reaction of a mineral m, A_m is the surface of the mineral by volume of porous media, k_m is the reaction rate constant, $a_{H^+}^n$ is the pH dependence of the dissolution/precipitation reactions and $f(\Delta G)$ is a function that describes the dependence of the reaction rate with respect on the saturation state of the solution and is in the form

$$f_m(\Delta G) = (1 - (\Omega)^{m_2})^{m_1} \quad \text{Eq. 5.14}$$

in which ΔG is the Gibbs energy of the reaction (J mol^{-1}), Ω is the ionic activity product (IAP) of the solution with respect to the mineral divided by K_{eq} (equilibrium constant for that mineral reaction), and m_1 and m_2 are empirical exponents.

The rate constant at temperature T (K) is calculated from

$$k_{m,T} = k_{m,25} exp\left(\frac{Ea}{R}\left(\frac{1}{T_{25}} - \frac{1}{T}\right)\right) \quad \text{Eq. 5.15}$$

where $k_{m,25}$ is the rate constant at 25 °C, E_a is the apparent activation energy of the overall reaction (J mol^{-1}), T is temperature in Kelvin and R is the gas constant (J mol^{-1} K^{-1}).

The porosity is updated through the calculation and is calculated as

$$\phi = 1 - \sum_{m} \phi_m \qquad \text{Eq. 5.16}$$

where ϕ_m is the volumetric fraction of a solid phase.

The change in porosity ($\Delta\phi$) is calculated from the change in the concentrations of the minerals (Δc_m) through

$$\Delta\phi = -\sum_{i} V_{m,i}\,\Delta c_{m,i} \qquad \text{Eq. 5.17}$$

where V_m is the molar volume of a mineral. The intrinsic permeability may depend on the porosity through the Kozeny model (see Table 5.1).

5.3.3.1 Reactive transport parametrization

Mortar composition was considered to be homogeneous along the sample. The composition of the formed hydrate assemblage during the hydration of the OPC + fly ash mixture was calculated using the GEM-Selektor (GEMS) software package (Lothenbach and Winnefeld, 2006; Lothenbach et al., 2008a; De Weerdt et al.; 2011; Wagner et al., 2012; Kulik et al., 2013), as described in Chapter 4. The initial volumetric fractions (ϕ_{mi}) of the mortar phases are the same as those given in Chapter 4.

The spatial 1D domain was that used in the CodeBright model (51 nodes and 50 elements of equal length). The 10 primary aqueous species considered were Ca^{2+}, SiO_2(aq), K^+, Na^+, SO_4^{2-}, Al^{3+}, Fe^{3+}, Mg^{2+}, CO_3^{2-} and OH^-. 25 secondary species and 27 minerals were considered to describe the system.

All the equilibrium constants at the eight temperatures (0 ºC, 25 ºC, 60 ºC, 100 ºC, 150 ºC, 200 ºC, 250 ºC and 300 ºC) for aqueous species and solid phases are listed in Table 5.6 and Table 5.7. Except for C-S-H, they were taken from the cemdata07 database (Matschei et al., 2007; Lothenbach et al., 2008b), which is based on the Nagra/PSI thermodynamic database (Hummel et al., 2002) for the solutes. Constants for the C-S-H were calculated from the solid solution model by Kulik and Kersten (2001) and for quartz and calcite that were taken from the database included in Retraso, which is based on the EQ3/6 database (Wolery et al., 1990). The log K_{eq} values and the molar volume for Si-hydrogarnet ($C_3(A,F)S_{0.84}H_{4.32}$) were calculated assuming an ideal solid solution between $C_3AS_{0.84}H_{4.32}$ and $C_3FS_{0.84}H_{4.32}$ as reported by Dilnesa

et al. (2014). Activity coefficients were calculated using the extended Debye-Hückel formulation (b-dot model). The activity of water was taken to be unity.

The composition of the C-S-H gel was discretized between C-S-H-1.667 and C-S-H-0.83 (1.667 and 0.83 are Ca/Si atomic ratios). The equilibrium constants of the C-S-H gel end members as a function of temperature were calculated as (Kulik and Kersten, 2001)

$$logK = -15.283 + \frac{9505.97}{T} + 2.19963 \cdot lnT \qquad \text{for C-S-H\_1.667} \qquad \text{Eq. 5.18}$$

$$logK = -6.818 + \frac{3429.95}{T} + 1.1345 \cdot lnT \qquad \text{for C-S-H\_0.83} \qquad \text{Eq. 5.19}$$

K_{eq} values for the intermediate C-S-H gel compositions with temperature were calculated from the equilibrium constants of the end members according to:

$$K_{(Ca/Si)}(T(°C)) = (K_{C-S-H\_1667}(T(°C)) \cdot x_1)^{x_1} \cdot (K_{C-S-H\_083}(T(°C)) \cdot (1 - x_1))^{(1-x_1)} \qquad \text{Eq. 5.20}$$

$$\left(Ca/Si\right)_{C-S-H} = (1.667 \cdot x_1) + (0.83 \cdot (1 - x_1)) \qquad \text{Eq. 5.21}$$

where $K_{(Ca/Si)}$ is the equilibrium constant for C-S-H gel with a composition between that of the end members, x_1 is the mol fraction of the C-S-H_1667 end member and $(1-X_1)$ is the mole fraction of the C-S-H_083 end member.

Regarding kinetics, the portlandite rate constant value at 25 ºC was $10^{-5.4}$ mol m^{-2} s^{-1} as reported in Bullard et al. (2010). The rate constants for quartz and calcite were obtained from Bandstra et al. (2008) and Palandri and Kharaka (2004), respectively. The rate parameters are shown in Table 5.8. The C-S-H gel solid solution was discretized into 15 different stoichiometries, in which the Ca/Si ratios ranged from 0.83 to 1.667 and are listed in Table 5.8. The dissolution rate constants of the discretized C-S-H gel were obtained in Chapter 2. The rate constants of the other phases present in the mortar (ettringite, monocarboaluminate, Si-hydrogarnet, hydrotalcite and fly ash) were obtained from Chapter 4. Precipitation of secondary phases such as gibbsite, gypsum, anhydrite and arcanite was modeled in equilibrium. Given that monosulfate forms from ettringite and monocarboaluminate above 50 °C (Lothenbach et al., 2008b), a second model was performed considering this phase. Irreversible kinetics was assumed (no dependence on solution saturation state) for the fly ash. Values of activation energies for quartz and calcite were taken from Bandstra et al. (2008) and Palandri and Kharaka (2004), respectively. For the rest of the mortar phases the apparent activation energy values

were set at 15 kcal/mol, which is a typical value for mineral dissolution/precipitation (Lasaga, 1998). The parameters that relate the rate constant with pH variation are also given in Table 5.8.

The initial effective diffusion coefficient (D_e) was considered to be $1.12 \cdot 10^{-13}$ m^2 s^{-1}, which was obtained by fitting the CrunchFlow model to the experimental data from the mortar column experiments described in Chapter 4. The code then assumes a linear dependence of D_e with ϕ. Dispersivity was set to a large value of 0.02 m to avoid very high concentrations at the top of the sample.

The specific surface area of the mortar was measured by the BET method, with samples previously degassed at 50 ºC for 10 h. The measured BET surface area was of 2.88 m^2 g^{-1}. The total surface area of the mortar phases was assumed to be proportional to 2.88 m^2 g^{-1} according to the volumetric fraction of each phase (see Table 5.8). The quartz surface area was calculated considering the geometric area of the grains as spheres of 0.5 mm of diameter being 5416 m^2 m^{-3} mortar. For portlandite the area was considered to be the fitted one from Chapter 4 (0.082 m^2 g^{-1} or 8270 m^2 m^{-3}).

Table 5.6. *Equilibrium constants (log K_{eq}) and stoichiometric coefficients for equilibria in solution.*

Reaction			log K_{eq}							
			0°C	25 °C	60°C	100°C	150°C	200°C	250°C	300°C
$Al(OH)_{3\,(aq)} + 3\,H^+$	⇅	$Al^{3+} + 3\,H_2O$	18.98	16.44	13.65	11.25	9.06	7.49	6.33	5.48
$Al(OH)^{2+} + 1\,H^+$	⇅	$Al^{3+} + 1\,H_2O$	5.73	4.96	4.00	3.09	2.10	1.24	0.49	-0.17
$CO_{2(aq)} + 1\,H_2O$	⇅	$HCO_3^- + H^+$	-6.58	-6.34	-6.27	-6.39	-6.86	-7.42	-8.06	-8.74
$CO3^{2-} + 1\,H^+$	⇅	HCO_3^-	10.62	10.33	10.14	10.12	10.30	10.60	10.98	11.40
$CaSO_{4\,(aq)}$	⇅	$Ca^{2+} + SO_4^{2-}$	-2.27	-2.30	-2.44	-2.69	-3.07	-3.51	-3.96	-4.41
$CaHCO_3^+$	⇅	$Ca^{2+} + HCO_3^-$	-1.15	-1.11	-1.22	-1.51	-2.02	-2.62	-3.26	-3.92
$CaCO_{3\,(aq)} + 1\,H^+$	⇅	$Ca^{2+} + HCO_3^-$	7.62	7.10	6.55	6.08	5.66	5.36	5.16	5.01
$CaOH^+ + 1\,H^+$	⇅	$Ca^{2+} + 1\,H_2O$	14.03	12.85	11.37	10.11	8.89	7.96	7.22	6.63
$MgOH^+ + 1\,H^+$	⇅	$Mg^{2+} + 1\,H_2O$	12.41	11.44	10.28	9.17	8.03	7.07	6.26	5.56
$Fe(OH)_{3(aq)} + 3\,H^+$	⇅	$3\,H_2O + Fe^{3+}$	14.89	12.56	10.10	8.09	6.40	5.32	4.65	4.26
$Fe(OH)_2^+ + 2\,H^+$	⇅	$2H_2O + Fe^{3+}$	7.00	5.67	4.25	3.08	2.08	1.42	0.99	0.73
$Fe(OH)^{2+} + 1\,H^+$	⇅	$H_2O + Fe^{3+}$	2.19	2.19	2.19	2.19	2.19	2.19	2.19	2.19
$FeCO_3^+ + 1\,H+$	⇅	$Fe^{3+} + HCO_3-$	-0.26	0.61	1.42	1.90	2.01	1.72	1.07	0.03
$SiO_2(OH)_2^{2-} + 2\,H^+$	⇅	$Si(OH)_4$	24.34	23.14	21.76	20.50	19.26	18.28	17.49	16.84
$SiO(OH)_3^- + 1\,H^+$	⇅	$Si(OH)_4$	10.32	9.81	9.34	9.04	8.90	8.92	9.05	9.25
KSO_4^-	⇅	$K^+ + SO_4^{2-}$	-0.84	-0.85	-0.97	-1.22	-1.62	-2.07	-2.55	-3.04
$MgCO_{3(aq)} + 1\,H^+$	⇅	$Mg^{2+} + HCO_3^-$	7.74	7.35	6.93	6.58	6.29	6.09	5.97	5.89
$MgHCO_3^+$	⇅	$Mg^{2+} + HCO_3^-$	-1.10	-1.07	-1.20	-1.52	-2.06	-2.69	-3.36	-4.06
$MgSO_{4(aq)}$	⇅	$Mg^{2+} + SO_4^{2-}$	-2.14	-2.41	-2.84	-2.35	-4.07	-4.96	-4.25	-4.74
$NaCO_3^- + 1\,H^+$	⇅	$Na^+ + HCO_3^-$	8.94	9.06	9.23	9.42	9.64	9.86	10.06	10.25
$NaHCO_{3(aq)}$	⇅	$Na^+ + HCO_3^-$	-0.37	-0.15	0.11	0.41	0.79	1.21	-1.17	-1.61
$NaSO_4^-$	⇅	$Na^+ + SO_4^{2-}$	-0.69	-0.70	-0.82	-1.06	-1.44	-1.87	-2.32	-2.77
$Fe(OH)_4^- + 4\,H^+$	⇅	$4H_2O + Fe^{3+}$	24.51	21.60	18.42	15.72	13.29	11.58	10.35	9.48
$Al(OH)_4^- + 4\,H^+$	⇅	$Al^{3+} + 4\,H_2O$	25.73	22.88	19.64	16.74	13.93	11.76	10.04	8.66
$NaOH_{(aq)} + 1\,H^+$	⇅	$Na^+ + 1\,H_2O$	15.11	14.18	13.19	12.36	11.64	11.16	10.84	10.62
$KOH_{(aq)} + 1\,H^+$	⇅	$K^+ + 1\,H_2O$	15.52	14.46	13.34	12.42	11.64	11.13	10.81	10.62
$OH^- + 1\,H^+$	⇅	H_2O	14.94	14.00	13.04	12.29	11.71	11.40	11.25	11.23

Table 5.7. *Equilibrium constants (log K_{eq}) and stoichiometric coefficients for mineral reactions.*

		log K_{eq}							
	Reaction	0°C	25 °C	60°C	100°C	150°C	200°C	250°C	300°C
CSH-1667 + 3.34 H^+	⇆ 1.67 Ca^{2+} + 4.34 H_2O+ 1 $Si(OH)_4$	31.86	29.13	26.03	23.22	20.48	18.36	16.66	15.27
CSH-165 + 3.3 H^+	⇆ 1.65 Ca^{2+}+ 4.3 H_2O + 1 $Si(OH)_4$	31.41	28.72	25.66	22.89	20.19	18.09	16.41	15.05
CSH-160 + 3.2 H^+	⇆ 1.6 Ca^{2+}+ 4.19 H_2O + 1 $Si(OH)_4$	30.16	27.57	24.63	21.97	19.38	17.36	15.75	14.44
CSH-155 + 3.1 H^+	⇆ 1.55 Ca^{2+}+ 4.08 H_2O + 1 $Si(OH)_4$	28.92	26.44	23.62	21.07	18.58	16.65	15.11	13.85
CSH-150 + 3 H^+	⇆ 1.5 Ca^{2+}+ 3.97 H_2O + 1 $Si(OH)_4$	27.70	25.33	22.63	20.18	17.81	15.96	14.48	13.28
CSH-145 + 2.9 H^+	⇆ 1.45 Ca^{2+}+ 3.86 H_2O + 1 $Si(OH)_4$	26.49	24.22	21.64	19.31	17.04	15.27	13.86	12.72
CSH-14 + 2.8 H^+	⇆ 1.4 Ca^{2+}+ 3.75 H_2O + 1 $Si(OH)_4$	25.28	23.12	20.66	18.44	16.28	14.60	13.25	12.16
CSH-135 + 2.7 H^+	⇆ 1.35 Ca^{2+} + 3.64 H_2O + 1 $Si(OH)_4$	24.09	22.03	19.69	17.58	15.52	16.93	12.65	11.61
CSH-130 +2.6 H^+	⇆ 1.3 Ca^{2+} + 3.53 H_2O + 1 $Si(OH)_4$	22.90	20.95	18.73	16.73	14.78	13.26	12.05	11.07
CSH-125 + 2.5 H^+	⇆ 1.25 Ca^{2+} + 3.31 H_2O + 1 $Si(OH)_4$	21.72	19.87	17.77	15.88	14.04	12.61	11.47	10.54
CSH-12 + 2.4 H^+	⇆ 1.2 Ca^{2+} + 3.42 H_2O + 1 $Si(OH)_4$	20.54	18.80	16.82	15.04	13.30	11.96	10.88	10.01
CSH-115 + 2.3 H^+	⇆ 1.15 Ca^{2+} + 3.19 H_2O + 1 $Si(OH)_4$	19.37	17.74	15.88	14.20	12.58	11.31	10.30	9.49
CSH-110 +2.2 H^+	⇆ 1.1 Ca^{2+} + 3.08 H_2O + 1 $Si(OH)_4$	18.20	16.68	14.94	13.38	11.86	10.67	9.73	8.97
CSH-105 +2.1 H^+	⇆ 1.05 Ca^{2+}+ 2.97 H_2O + 1 $Si(OH)_4$	17.05	15.63	14.01	12.56	11.14	10.04	9.17	8.46
CSH-10 +2 H^+	⇆ 1 Ca^{2+} + 2.86 H_2O + 1 $Si(OH)_4$	15.90	14.58	13.09	11.74	10.44	9.42	8.61	7.96
CSH-095 + 1.9 H^+	⇆ 0.95 Ca^{2+} 2.75 H_2O + 1 $Si(OH)_4$	14.76	13.55	12.18	10.94	9.74	8.81	8.07	7.47
CSH-090 +1.8 H^+	⇆ 0.9 Ca^{2+} + 2.64 H_2O + 1 $Si(OH)_4$	13.63	12.53	11.28	10.15	9.06	8.21	7.54	6.99
CSH-085 + 1.7 H^+	⇆ 0.85 Ca^{2+} + 2.53 H_2O + 1 $Si(OH)_4$	12.53	11.53	10.40	9.38	8.39	7.63	7.03	6.54
CSH-083 + 1.66 H^+	⇆ 0.83 Ca^{2+} + 2.49 H_2O + 1 $Si(OH)_4$	12.10	11.15	10.07	9.09	8.15	7.42	6.84	6.37
$Ca(OH)_2$ + 2 H^+	⇆ Ca^{2+} + 2H_2O	24.90	22.81	20.42	18.26	16.16	14.53	13.22	12.16
Quartz+ 2 H_2O	⇆ $Si(OH)_4$	-4.63	-4.00	-3.47	-3.08	-2.72	-2.44	-2.21	-2.02
Calcite +H^+	⇆ Ca^{2+} + HCO_3^-	2.23	1.85	1.33	0.77	0.10	-0.58	-1.33	-2.22
Ettringite	⇆ 6 Ca^{2+}+ 2 $Al(OH)_4^-$ + 3 SO_4^{2-} + 4 OH^- + 30 H_2O	-48.37	-44.84	-41.64	-39.69	-38.90	-39.29	-40.42	-42.02
Hydrotalcite	⇆ 4 Mg^{2+} + 2 $Al(OH)_4^-$ + 6 OH^- + 5 H_2O	-57.86	-56.02	-54.53	-53.87	-54.05	-54.93	-56.23	-57.80
monocarboaluminate	⇆ 4 Ca^{2+} + 2 $Al(OH)_4^-$ +1 CO_3^{2-} + 4 OH^- +3 H_2O	-32.65	-31.47	-30.78	-30.95	-32.04	-33.73	-35.77	-37.99
Si -hydrogarnet	⇆ 3 Ca^{2+} + 1 $Fe(OH)_4^-$ +1 $Al(OH)_4^-$ +0.84 $Si(OH)_4$ + 4 OH^- + 2.32 H_2O	-29.59	-29.60	-30.22	-31.50	-33.60	-35.99	-38.52	-41.10
Gibbsite+ 3 H^+	⇆ 1 Al^{3+} + 3 H_2O	9.38	7.75	5.83	3.99	2.08	0.44	-1.06	-2.47
Gypsum	⇆ 1 Ca^{2+}+ 1 SO_4^{2-} + 2 H_2O	-4.53	-4.48	-4.60	-4.90	-5.42	-6.12	-7.03	-8.30
arcanite	⇆ 1 SO_4^{2-} + 2 K^+	-2.27	-1.80	-1.46	-1.36	-1.50	-1.89	-2.53	-3.52

Table 5.8. *Rate constant (log k) at 25 ºC, surface are (m^2 mineral m^{-3} mortar) apparent activation energy (E_a),pH-rate parameters($a_H{}^n$)and ΔG-term parameters (m_1 and m_2).*

Mineral	log k	Surface area	Ea	$a_{H^+}^{n_{H^+}}$	m_1	m_2
	mol m^{-2} s^{-1}	m^2 mineral m^{-3} mortar	kcal mol^{-1}			
	-0.3	5073	3.44	1	1.0	1.0
Calcite	-5.81		5.62	0	1.0	1.0
	-11.4	5416	18	0.3	1.0	1.0
Quartz	-14.9		18	-0.4	1.0	1.0
Portlandite	-5.14	8270	15		1.0	1.0
Fly ash	-12.00	298869	15	0	1.0	1.0
Ettringite	-8.80	116007	15	0	1.0	1.0
Monocarboaluminate	-13.50	327587	15	0	1.0	1.0
Hydrotalcite	-8.50	43236	15	0	1.0	1.0
Si-hydrogarnet	-12.80	332133	15	0	1.0	1.0
CSH-083	-10.99	1649468	15	0	1.0	1.0
CSH-085	-10.87	1649468	15	0	1.0	1.0
CSH-090	-10.79	1649468	15	0	1.0	1.0
CSH-095	-10.86	1649468	15	0	1.0	1.0
CSH-100	-10.95	1649468	15	0	1.0	1.0
CSH-105	-10.97	1649468	15	0	1.0	1.0
CSH-110	-10.88	1649468	15	0	1.0	1.0
CSH-115	-10.67	1649468	15	0	1.0	1.0
CSH-120	-10.36	1649468	15	0	1.0	1.0
CSH-125	-9.98	1649468	15	0	1.0	1.0
CSH-130	-9.58	1649468	15	0	1.0	1.0
CSH-135	-9.20	1649468	15	0	1.0	1.0
CSH-140	-8.89	1649468	15	0	1.0	1.0
CSH-145	-8.67	1649468	15	0	1.0	1.0
CSH-150	-8.56	1649468	15	0	1.0	1.0
CSH-155	-8.56	1649468	15	0	1.0	1.0
CSH-160	-8.53	1649468	15	0	1.0	1.0
CSH-165	-8.47	1649468	15	0	1.0	1.0
CSH-1667	-8.40	1649468	15	0	1.0	1.0

5.4. Results and discussion

5.4.1 The evaporation process

Loss of water over time showed similar trends in experiments A and B (respective durations of 92 and 230 days considering only the irradiation period; Fig. 5.8). At the start of the experiments, before the top of the sample was irradiated, 6.0 and 10.2 g of water were taken up by mortar in experiments A and B, respectively (blue solid symbols in Fig. 5.8). Once irradiation started, water loss with time became linear (red solid symbols in Fig. 5.8). The total amounts of evaporated water were 87 cm^3 and 223 cm^3, respectively. Taking into account that the respective experiments lasted 92 and 230 days and the volume of pores in the sample was 77.8 cm^3, the flow rates were 0.94 cm^3 d^{-1} and 0.97 cm^3 d^{-1}, respectively, which yielded residence times of 82.7 days and 80.2 days, respectively. Therefore, porewater was renewed 1.1 times and 2.8 times in experiments A and B, respectively.

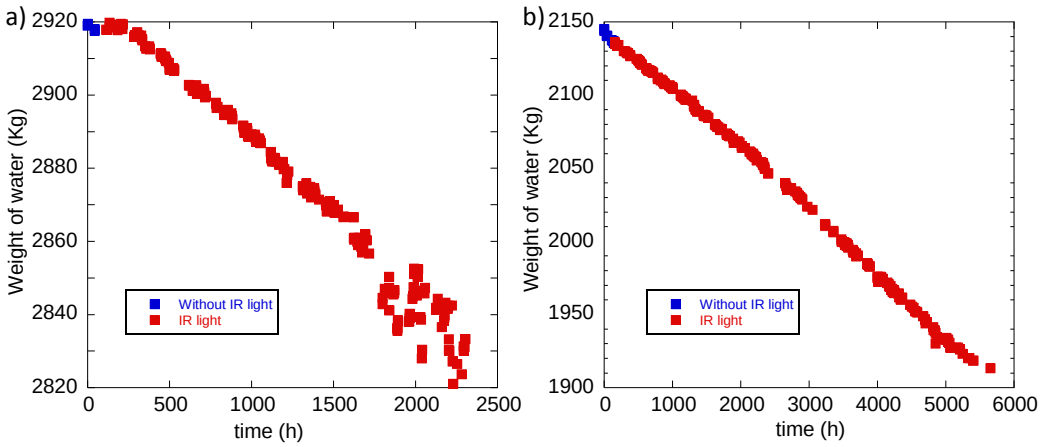

Figure 5.8. *Water loss with time in the evaporation experiments: A (a) and B (b). Blue symbols show water taken up by mortar before IR light irradiation, and red symbols show water loss during IR light irradiation.*

Figure 5.9 shows that temperature at the top surface was fairly constant during all the experiment (62.6 ± 1.6 ºC for the experiment A and 65.5 ± 2.0 ºC for the experiment B) after 96h (4 days) in experiment A and 190 h (8 days) in experiment B. The first 110 h in experiment A and 140 h in experiment B correspond with the time that the IR light was not irradiating the top of the samples. Inside the glove box, the bulk temperature reached a constant value of 40 ± 2 ºC after 96 h (4 days) in experiment A and 44 ± 2 ºC after 96 h (8 days) in experiment B (Fig. 5.10). The relative humidity (RH) was set at approximately 34 % (Fig. 5.11), which was

approximately maintained for 1500 h in experiment A and 3000 h in experiment B. Oscillations occurred when some N_2 entered the glove box while purging (Fig. 5.11a). Oscillations were mostly avoided in experiment B after improving the glove box sealing. After this period of time, RH dropped below 34 % after $MgCl_2 \cdot 6H_2O$ salt converted to anhydrous $MgCl_2$ while heated (Zondag et al., 2010). Nonetheless, the unexpected changes in relative humidity did not affect the water flux, which was constant during the experiments. To corroborate that the anhydrous $MgCl_2$ salt caused the relative humidity drop, hydrated salt ($MgCl_2 \cdot 6H_2O$) was used for the last five days in experiment B, and relative humidity went back to the expected value of 34 % (Fig. 5.11b).

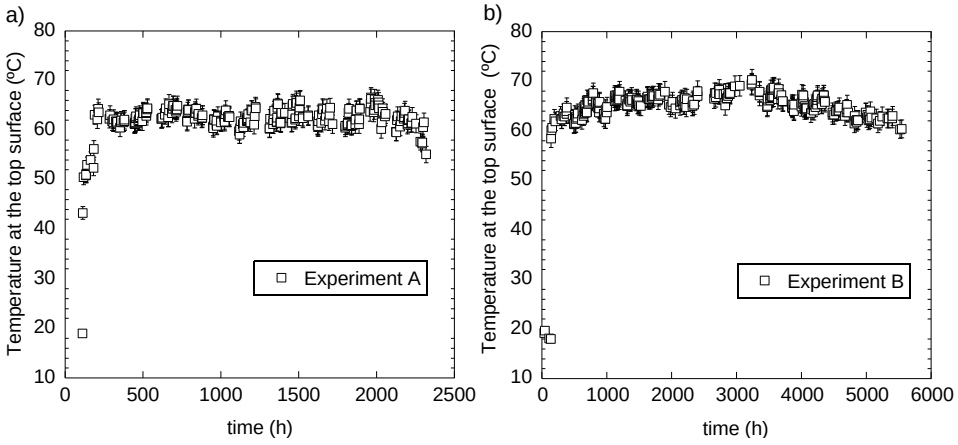

Figure 5.9. *Temporal variation of temperature at the top surface with time: (a) experiment A and (b) experiment B.*

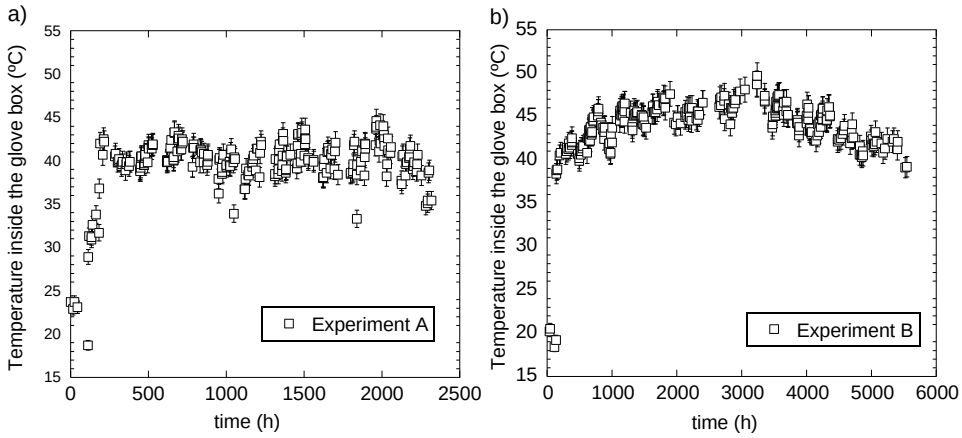

Figure 5.10. *Temporal variation of bulk temperature inside the glove box: (a) experiment A and (b) experiment B.*

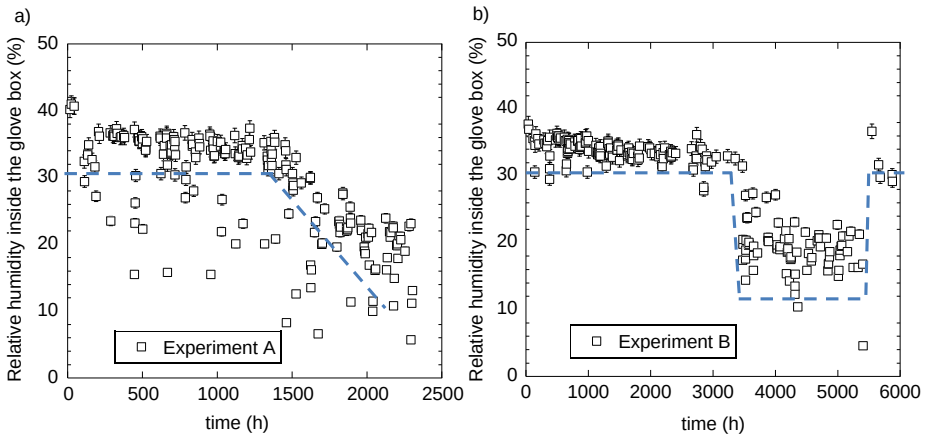

Figure 5.11. *Temporal variation of relative humidity with time inside the glove box: (a) experiment A; (b) experiment B. Dashed line only illustrates tendency.*

5.4.2 Mineralogical changes

As explained in Section 5.2.3, the visual inspection of the top and bottom surfaces of the samples before the experiment showed negligible differences in the appearance of the mortar. After the end of the experiments (Fig. 5.12), the quartz grains in the mortar appeared to be more visible at the bottom (0.5 cm) than in the middle (2.5 cm) and top (5 cm). However, morphological differences in the shapes of quartz grains were not observed between the unreacted and reacted specimens.

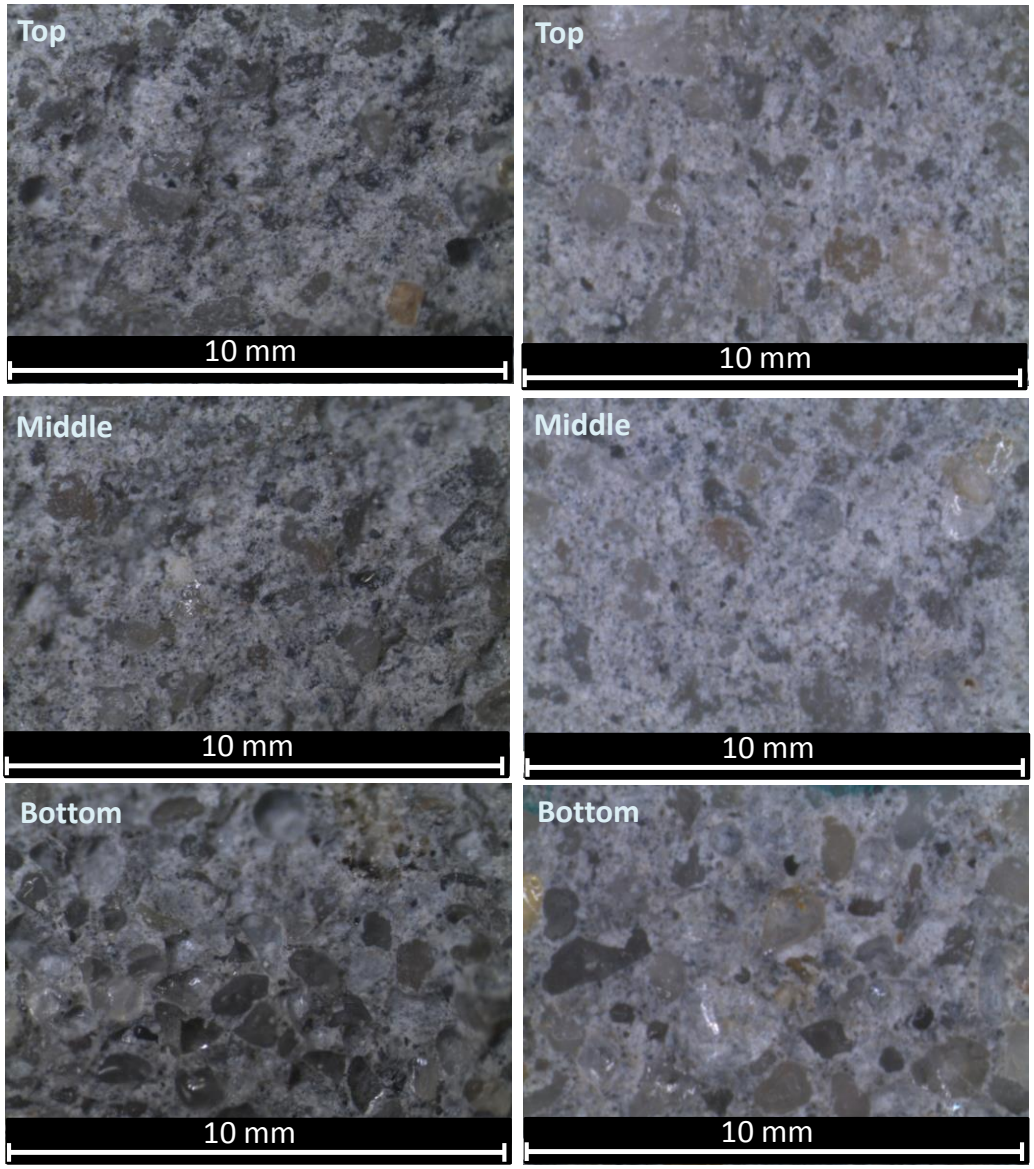

Figure 5.12. *Photographs of the mortar surfaces of reacted experiment A (left) and experiment B (right): bottom (0.5 cm), middle (2.5cm) and top (5cm). At the scale of observation, quartz grains are less clear in the top and middle surfaces in comparison with those at the bottom surface of the sample.*

The bottom and top surfaces of the samples were examined by SEM (Fig. 5.13). The images taken from polished mortar slices showed a uniform cement matrix with the presence of quartz grains, fly ash particles (small spheres) and C_3S particles. No differences in this configuration were observed between the bottom and top regions of the samples after reaction.

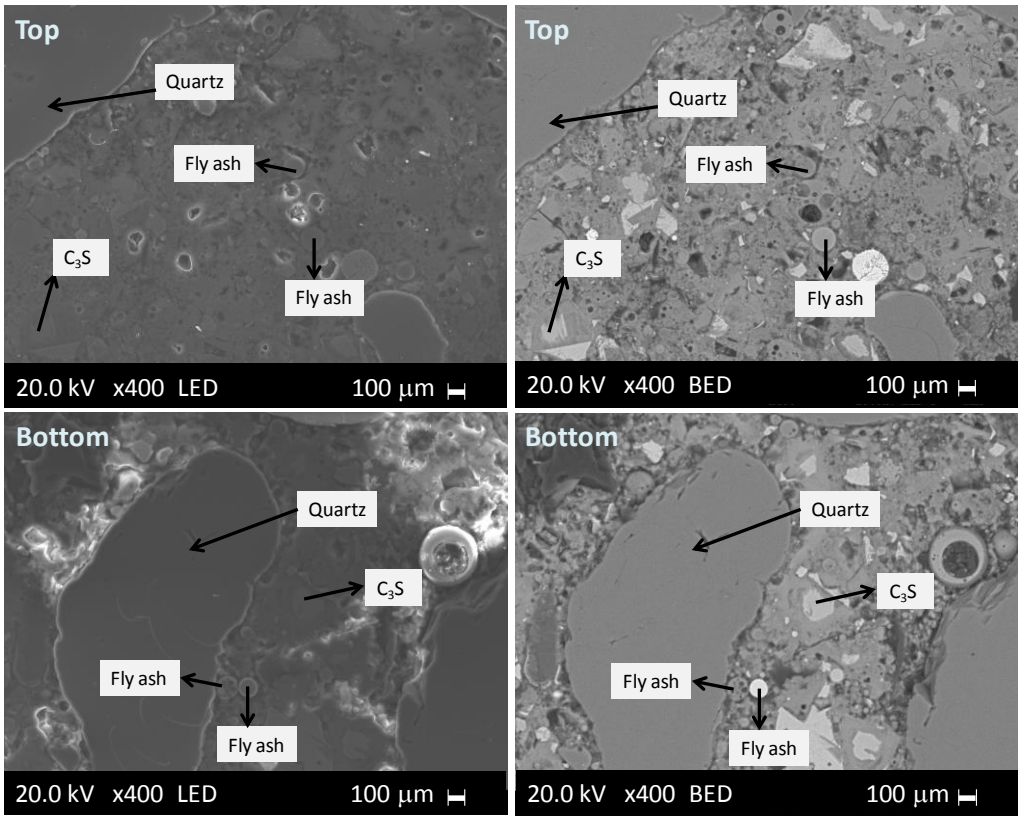

Figure 5.13. *SEM images (secondary electrons (left) and backscattered electrons (right)) of polished mortar slices of the bottom and top of the mortar sample.*

5.4.3 Water flux simulation

The coefficients of vapor exchange between the sample and the atmosphere (β_g and γ_g) and heat exchange between the sample and the atmosphere (γ_e) were fitted parameters in each experiment. γ_g and the tortuosities allow the fixing of the gas pressure to the atmospheric value. Values of γ_g lower than $5 \cdot 10^{-3}$ kg s^{-1} Pa^{-1} m^{-2} give a lower gas pressure in the last node of the sample, producing a high gas pressure difference between the sample and the environment. The small value of γ_g results in advection of gas not significant. β_g of $6.2 \cdot 10^{-6}$ $m^3 m^{-2} s^{-1}$ allows fitting to the vapor flux of water (j_g^w). Although the value is small, j_g^w is largely sensitive to this coefficient (see Table 5.2). In the end, vapor diffusion is the main water flux mechanism. A γ_e of 0.01 J s^{-1} C^{-1} m^{-2} at the top was small enough to fit the experimental values of temperature at the top of the sample. γ_e equal to 1500 J s^{-1} C^{-1} m^{-2} was used at the bottom. This value is large enough to fix the temperature in the first node to the lowest temperature. A value of γ_l of 1 kg s^{-1} MPa^{-1} m^{-2} allows keeping the pressure of 0.101815 MPa (P_l) during the experiment A and 0.101570 MPa (P_l) during the experiment B at the bottom of the sample.

Figure 5.14 shows the model fitting of the experimental water loss (kg of water per surface) in both experiments. Water loss at the beginning of the experiment was not considered in the fitting because evaporation was not yet taking place.

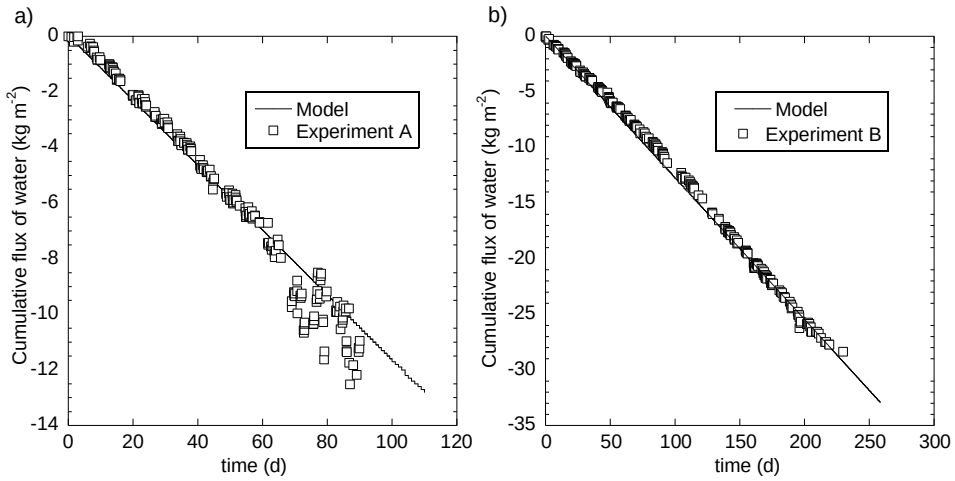

Figure 5.14. *Empty symbols and solid lines represent experimental and modeling results of the cumulative water flux with time; a) experiment A and b) experiment B.*

Figure 5.15 depicts the calculated variation of the liquid (Figs. 5.15 a and c) and gas pressure (MPa) (Figs. 5.15 b and d) in both experiments (A and B). At the bottom of the sample (0.0 cm) the liquid pressure was fixed to be 0.101815 MPa (experiment A) and 0.101570 MPa (experiment B) (boundary condition, see Fig. 5.7) and at the top atmospheric gas pressure was fixed for both experiments (0.101320 MPa).

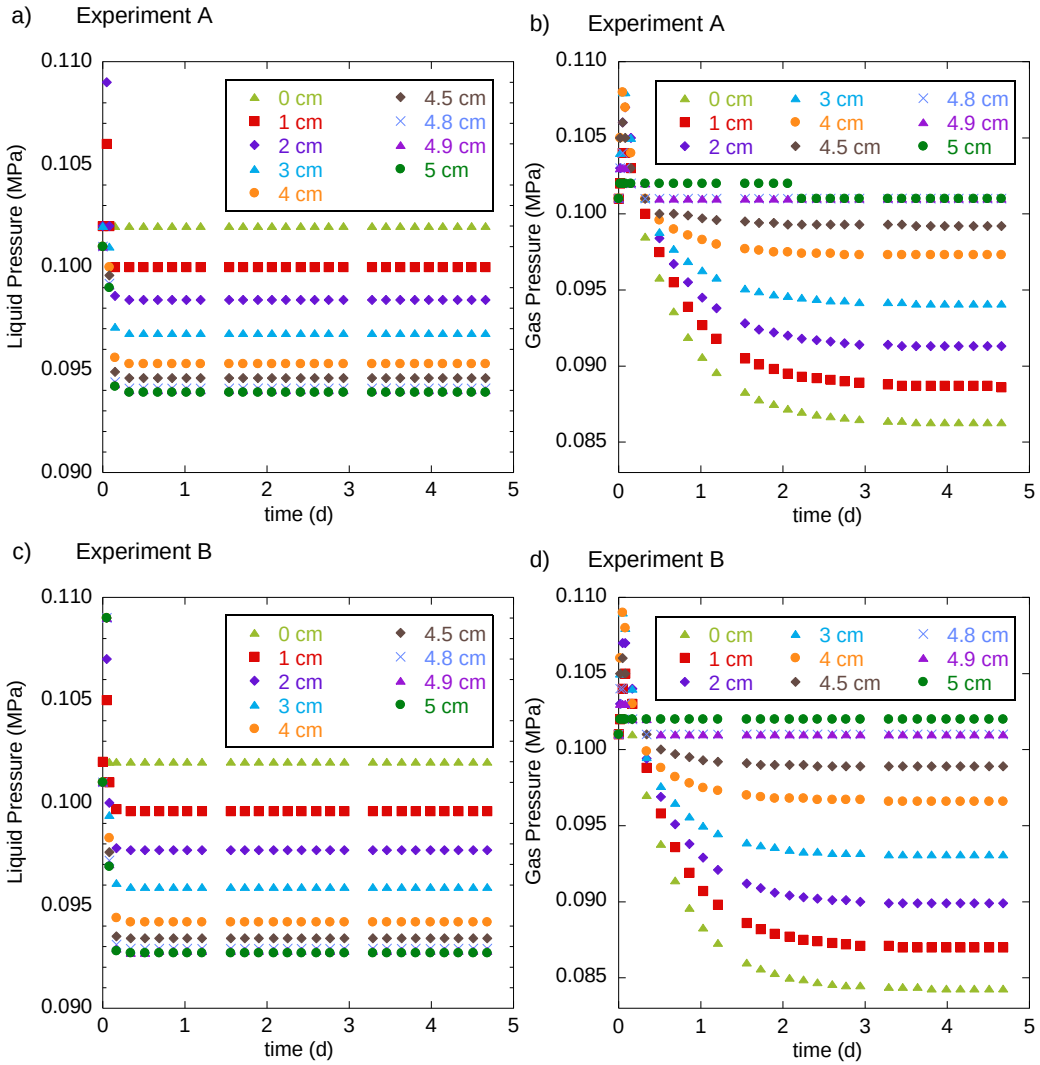

Figure 5.15. *Symbols represent the numerical variation of (a and c) liquid pressure and (b and d) gas pressure over time for both experiments A and B.*

Figure 5.16 shows the calculated and experimental temperature at the top surface. The temperature was fitted to the experimental values by fixing the γ_e value considering the energy flux of the lamp (400 J s^{-1} m^{-2}) (Table 5.2). Experimental data show some scattering around the average values of 62.6 ºC and 65.5 ºC in experiments A and B, respectively. In experiment B the experimental and calculated temperatures are slightly higher than those in experiment A. An explanation for this fact is that the glove box was insufficiently insulated during experiment A compared to experiment B, in which the glove box was wrapped in aluminum foil and coated with polyurethane expanding foam. Figure 5.17 shows the calculated variation of temperature along the sample, where temperature increases from bottom upwards as expected.

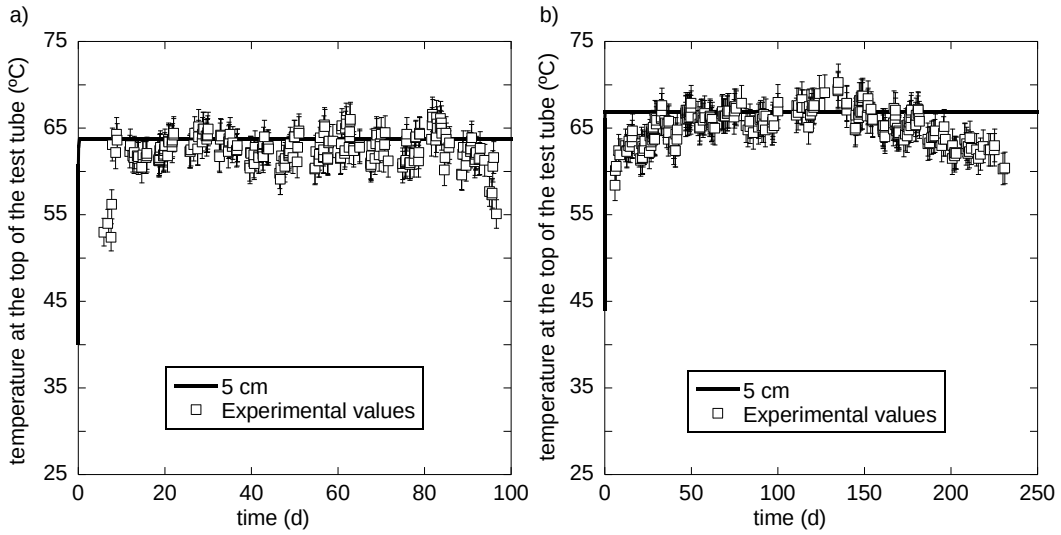

Figure 5.16. *Variation of the experimental (open symbols) and numerical (solid line) temperature at the top of the sample: a) experiment A and b) experiment B. The numerical temperature corresponds to that obtained at node 50 (4.9 cm).*

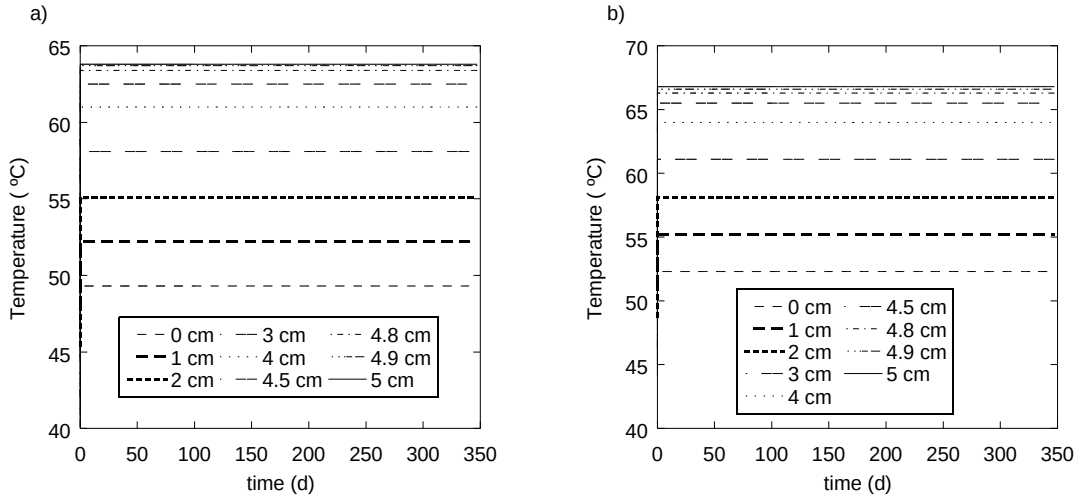

Figure 5.17. *Calculated variation of temperature along the sample: a) experiment A and b) experiment B.*

Finally, simulations showed that the calculated water saturation of the sample for both experiments was close to 1, indicating complete saturation all along the samples during the experiments and evaporation exclusively at the top surface of the samples.

5.4.4 Reactive transport simulations (Retraso-CodeBright Modeling)

The reactive transport simulations were conducted to obtain an overall interpretation of the processes that took place in the mortar samples during evaporation. Only the fitted parameters for experiment B were used in the Retraso-CodeBright simulations. In fact, only slight differences were obtained in the fitted parameters for experiment A and B, and the same flux of water was observed. The evaporation experiment B lasted 230 days and the simulation time spans up to 1416 days (4 years).

Figure 5.18 compares the model fitting of the experimental water loss (kg of water per surface) in experiment B calculated by CodeBright, which considers mass and heat flow (Fig. 5.14), with that calculated by Retraso-CodeBright, which couples the chemical reactions with the flux calculation and updates flow properties affected by reactive transport (based on changes in the minerals by dissolution and precipitation) such as porosity and relative permeability.

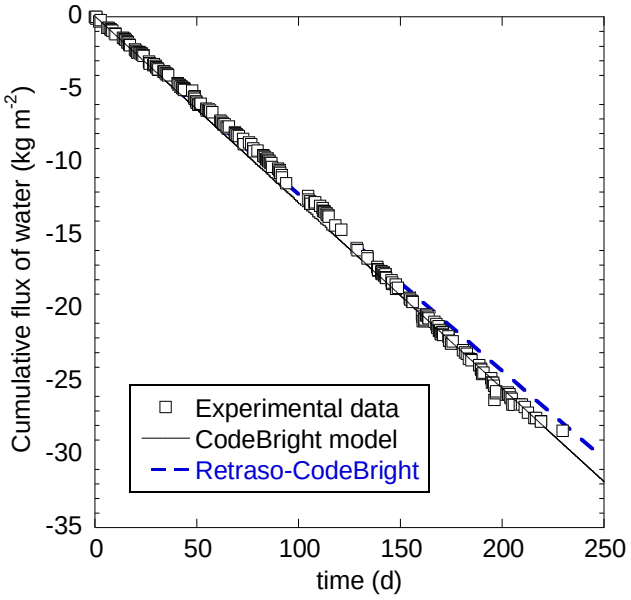

Figure 5.18. *Empty symbols represent experimental data of the cumulative water flux with time. Solid and dashed lines represent modeling results of the cumulative water flux with time using CodeBright and Retraso-CodeBright, respectively.*

As in the case of flux calculation, modeling results from the coupled Retraso-CodeBright match the experimental water loss (kg of water per surface; Fig. 5.18). The conclusion is drawn that the magnitude of the chemical reactions barely affects the flux.

5.4.4.1 Dissolution and precipitation of the mortar components

Figures 5.19, 5.20, 5.22, 5.23, 5.24 and 5.25 show the calculated evolution of the mortar phases (m^3 of mineral m^{-3} of mortar) along the length of the sample during the experimental time (230 days) and longer (4 years). A decrease or increase in the volumetric fraction value indicates dissolution or precipitation, respectively.

With regard to the two major mortar components (portlandite and C-S-H gel), simulations show that, overall, portlandite dissolves along the sample (Figs. 5.19a and b), yielding a decrease in volumetric fraction (initially, 0.045 m^3 mineral/m^3 mortar) with time. Fast dissolution takes place at the very bottom as inflow MilliQ water is highly undersaturated with respect to it, and portlandite is exhausted after 100 days. Along the sample, as porewater becomes less undersaturated with respect to portlandite, it is more slowly consumed with time, allowing C-S-H gel formation. The increase in temperature with height causes an increase in portlandite dissolution by having a faster rate. At the very top (5 cm), during the first 50 days, portlandite precipitates from the dissolution and exhaustion of calcite and ettringite (Fig. 5.23), and with time Ca accumulation makes portlandite precipitate between 300 and 500 d. Thereafter portlandite dissolves since Ca is used by the precipitation of ettringite, Si-hydrogarnet and hydrotalcite.

Simulations show that C-S-H gel with a Ca/Si ratio of 1.667 always precipitates from Si released by dissolution of quartz and fly ash and Ca released from portlandite and calcite and ettringite (at the very top) (Figs. 5.19c and d and Figs. 20a and b). After 3 years, C-S-H gel slightly dissolves only at the very bottom with a Ca/Si between 1.60 and 1.667 (Fig. 5.19d and Figs. 20a and b), where dissolution of ettringite diminishes and undersaturates the solution with respect to C-S-H gel (Fig. 5.19c). Along the sample, as portlandite is being exhausted, the Ca/Si ratio becomes lower than 1.667 at 4.5 cm after 1.5 years (Figs. 5.20a and b).

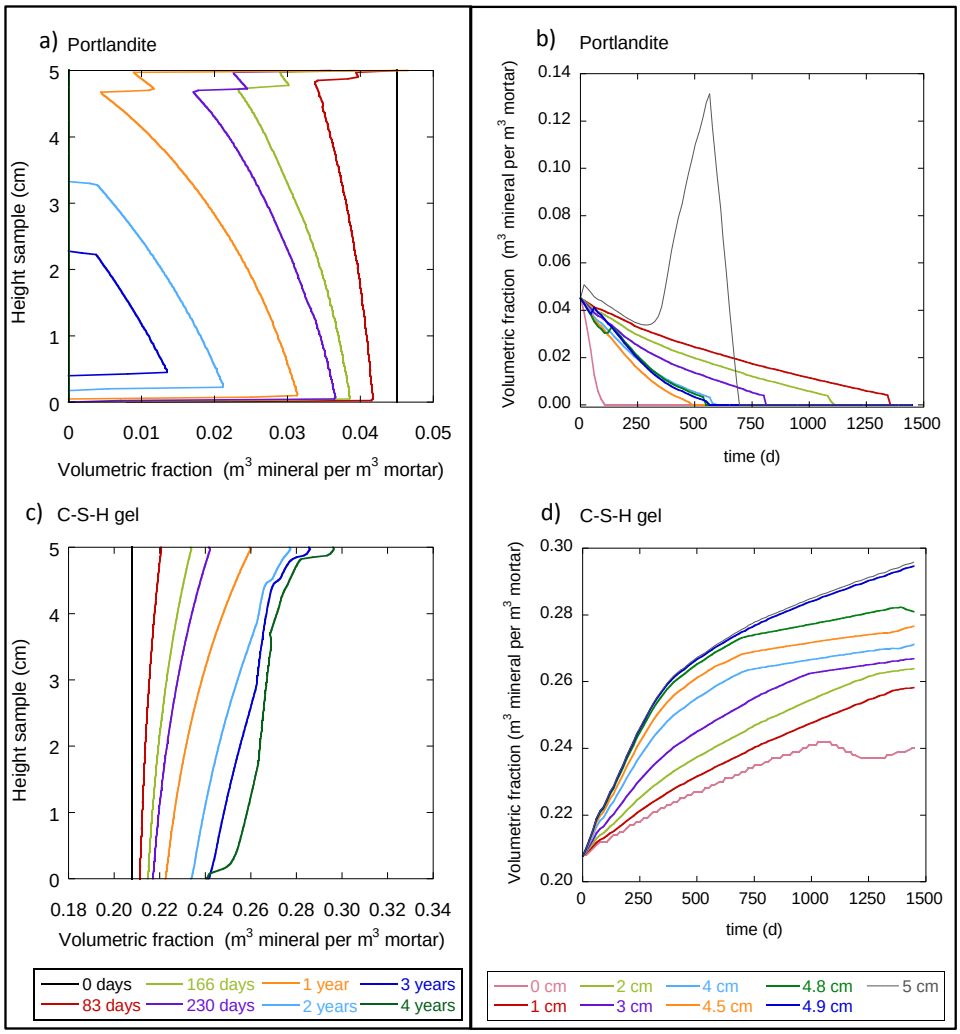

Figure 5.19. *Variation of volumetric fraction of portlandite (top row) and C-S-H gel (bottom row) along the length of the sample (a and c) and over time (b and d).*

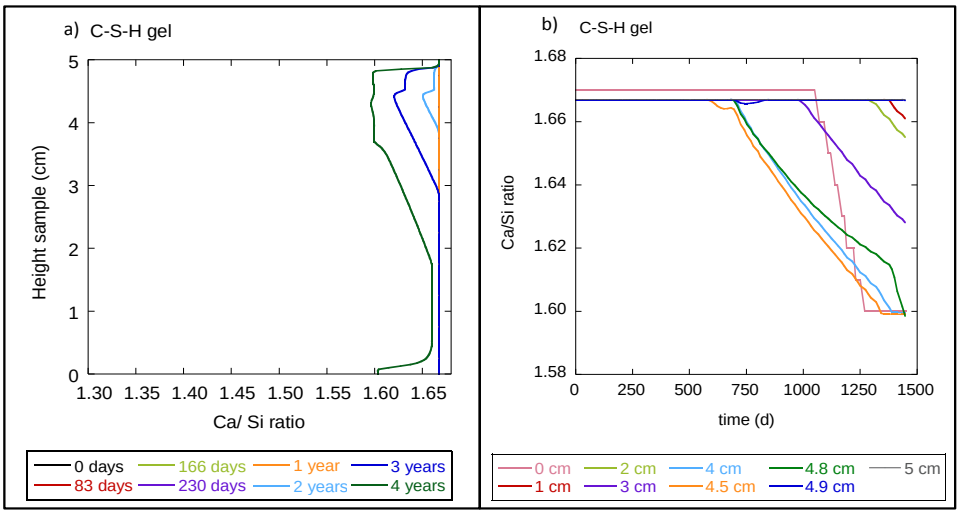

Figure 5.20. *Variation of the Ca/Si ratio along the length of the sample (a) and over time (b).*

The temporal variation of pH reflects the progress of the reactions throughout the sample (Figs. 5.21a and b). Along the sample, initial porewater is being renewed by Milli-Q water (pH = 7), resulting in a sharp pH drop (from 13.2 to around 12.5) and a displacement of Na^+ and K^+. Conversely, at the top region, the solution pH sharply increases due to an accumulative effect (Figs. 5.21a and b). After ca. 300 days the solution pH remains constant as calcite, portlandite and ettringite (only at the first node) dissolve. During this time span, pH decreases are related to portlandite exhaustion.

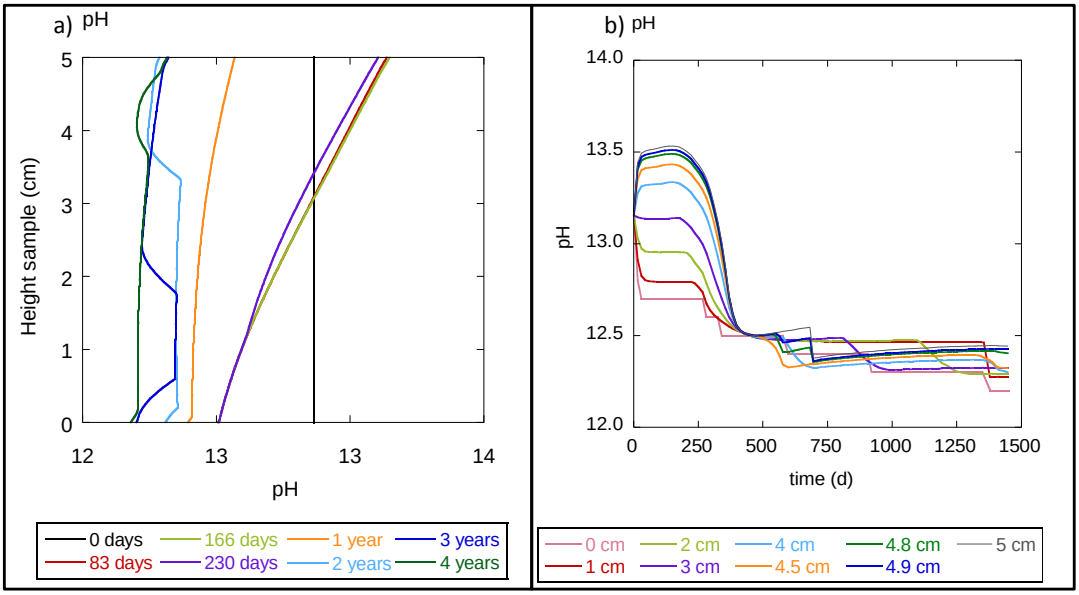

Figure 5.21. *pH variation along the length of the sample (a) and over time (b).*

Quartz dissolution is catalyzed by the high pH of the solution along the sample (from 12.5 to 13.5; Figs. 5.22a and b). Two different stages are observed according to pH variation. In the first one (before 350 days) dissolution of quartz is larger than in the second stage (after 350 days) as pH decreases while portlandite is being exhausted (Figs. 5.22a and b). Quartz dissolution also increases by the increase in temperature with height. The fly ash also dissolves throughout the sample (Figs. 5.22c and d). After 3 years, it is consumed at the very top, and after 4 years it is totally exhausted at 3.3 cm.

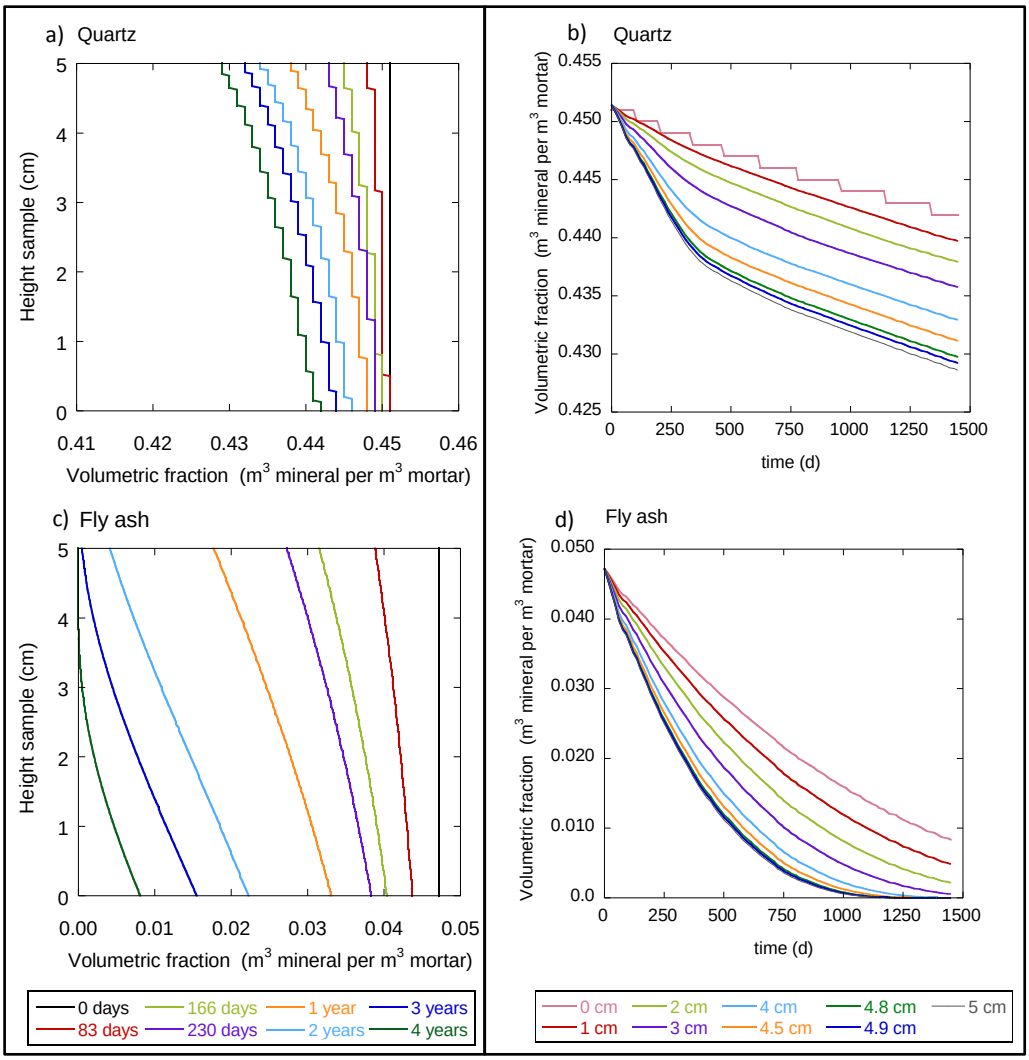

Figure 5.22. *Variation of volumetric fraction of quartz (top row) and fly ash (bottom row) along the length of the sample (a and c) and over time (b and d).*

Calcite dissolves along the sample as precipitation of C-S-H, Si-hydrogarnet, hydrotalcite and monocarboaluminate occurs, undersaturating the porewater solution. Initially, at the very bottom, calcite precipitates when portlandite dissolves, and the former starts to dissolve only when portlandite is exhausted (Figs. 5.23a and b). Calcite is totally consumed after 250 days.

Ettringite precipitates at the very bottom when portlandite dissolves and when portlandite is exhausted it dissolves (after 90 days). After 250 days, dissolution of ettringite lessens as the volumetric fraction of monocarboaluminate remains constant. Up to 4.5 cm, ettringite precipitates as porewater is enriched by Ca and SO_4^{2-} accumulation. At the very top, ettringite is rapidly exhausted after 156 days owing to an increase in dissolution rate with temperature and with porewater undersaturation caused by precipitation of the Ca-bearing phases (C-S-H, Si-hydrogarnet, hydrotalcite and monocarboaluminate) that consumes Ca, Al and CO_3 (Figs. 5.23c and d).

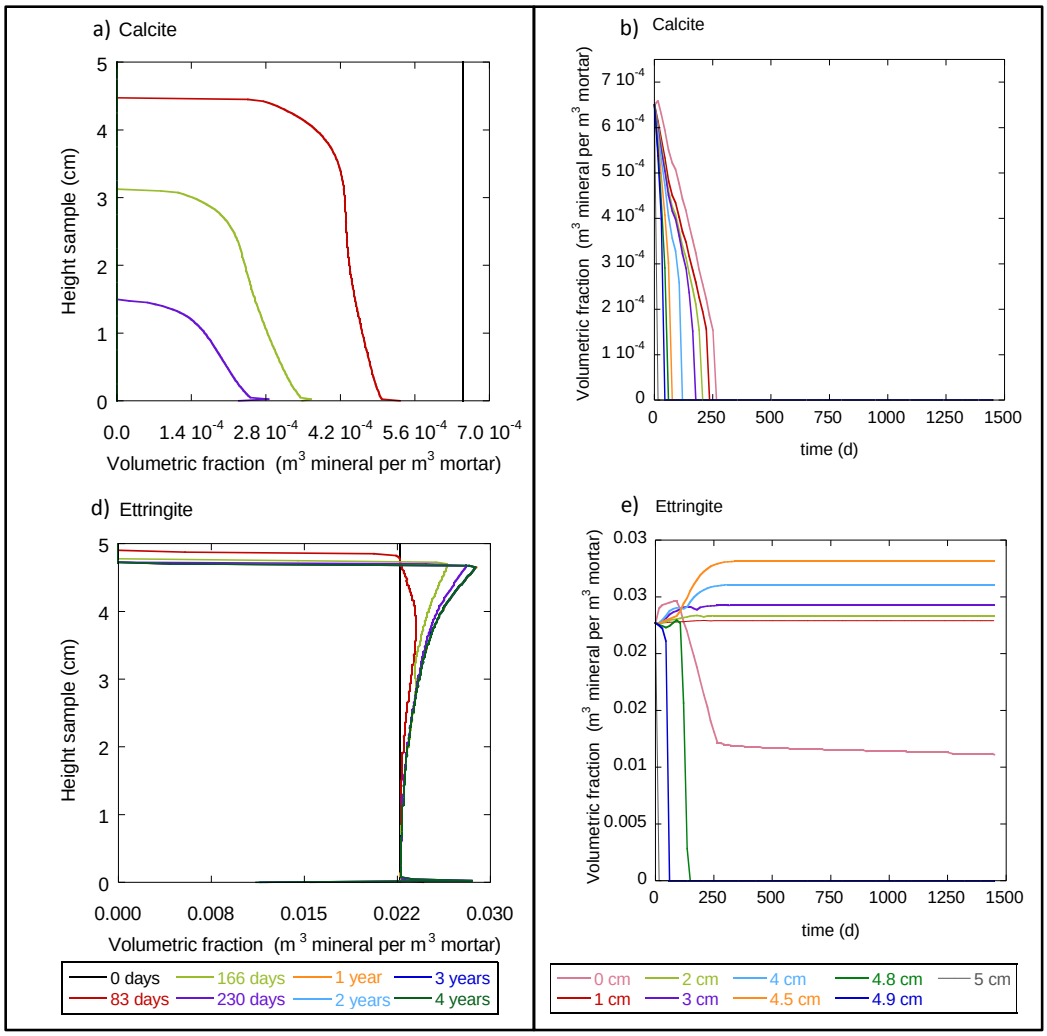

Figure 5.23. *Variation of volumetric fraction of calcite (top row) and ettringite (bottom row) along the length of the sample (a and c) and over time (b and d).*

Regarding the minor mortar components (hydrotalcite, Si-hydroganet and monocarboaluminate), the simulation shows that changes in their volumetric fractions are very small (Fig. 5.24).

Hydrotalcite precipitates all over the sample, and its precipitation increases with height (Figs. 5.24a and b). Hydrotalcite precipitation occurs at expense of fly ash and ettringite dissolution, which releases Mg and Al into solution. Si-hydrogarnet precipitates all along the sample due to dissolution of portlandite, quartz, ettringite and fly ash that respectively releases Ca, Si and Al (Figs. 5.24c and d). Monocarboaluminate precipitates only during the first 250 days as calcite dissolves, releasing Ca and CO_3^{2-}. Thereafter, as calcite is exhausted, volumetric fraction of monocarboaluminate keeps constant. At the very top, monocarboaluminate precipitation is larger due to Ca and CO_3^{2-} accumulation (Figs. 5.24e and f). Note that such

amounts of precipitated mineral would be very difficult to be observed by optical and SEM inspections.

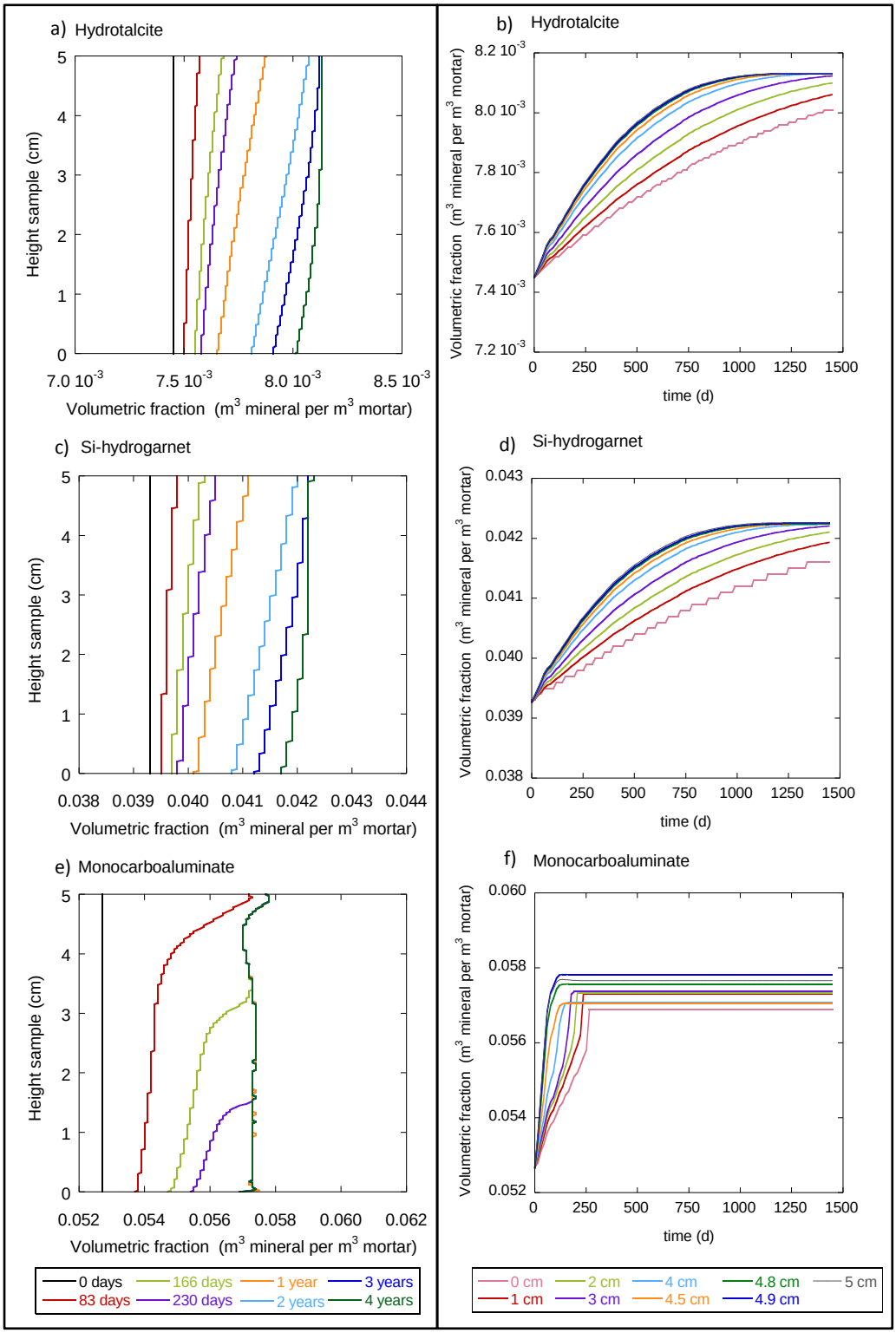

Figure 5.24. *Variation of volumetric fraction of hydrotalcite, Si-hydrogarnet and monocarboaluminate along the length of the sample (a, c and e) and over time (b, d and f).*

Simulation shows that gibbsite ($Al(OH)_3$) starts to form from 3cm to the top only after 615 days from Al released by dissolution of ettringite and fly ash (Figs. 5.25a and b). Accordingly, gibbsite precipitation should not be expected over the course of the experiment. Anhydrite, arcanite and gypsum did not precipitate. When monosulfate is considered in the model, its precipitation occurs from 1 cm to the top after 300 h, barely affecting the dissolution and precipitation of C-S-H and portlandite, but affecting ettringite, which now tends to dissolve. However, from the experimental results of the evaporation experiments it is hard to detect the formation of monosulfate or any other secondary phase. Therefore, taking into account that only the water flux can be fitted with the model, the possible secondary phases to consider can be diverse. This type of experiments cannot be used to study the mineralogical evolution of the mortar.

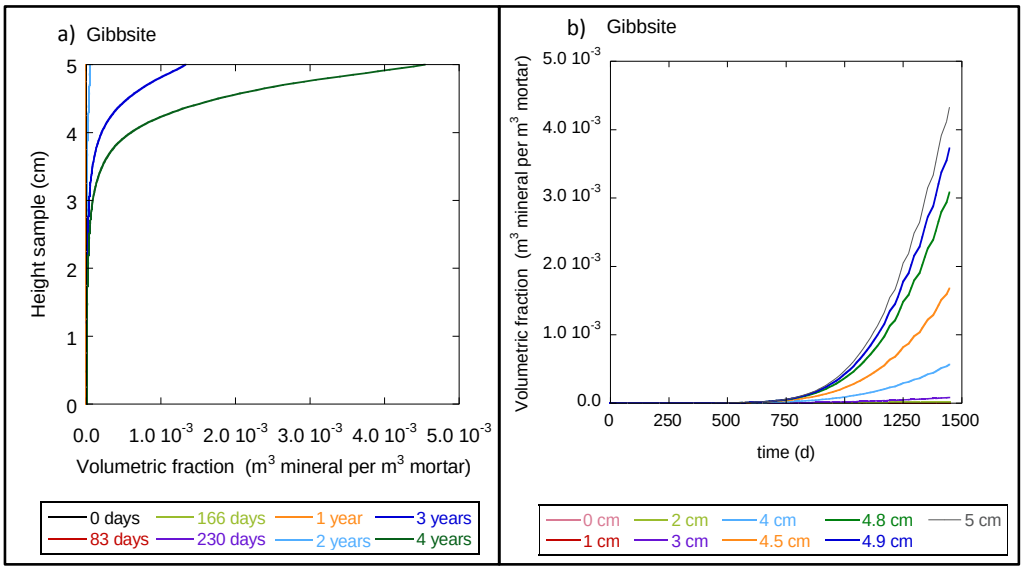

Figure 5.25. *Variation of volumetric fraction of gibbsite, along the length of the sample (a) and over time (b).*

5.4.4.2 Total aqueous concentrations

K and Na behave as conservative elements (Figs. 5.26a, b, c, and d) in the simulations. Entering Milli-Q water displace these elements from the bottom upwards. A maximum of concentration after 100 days is reached at the top by the accumulative and evaporation effects.

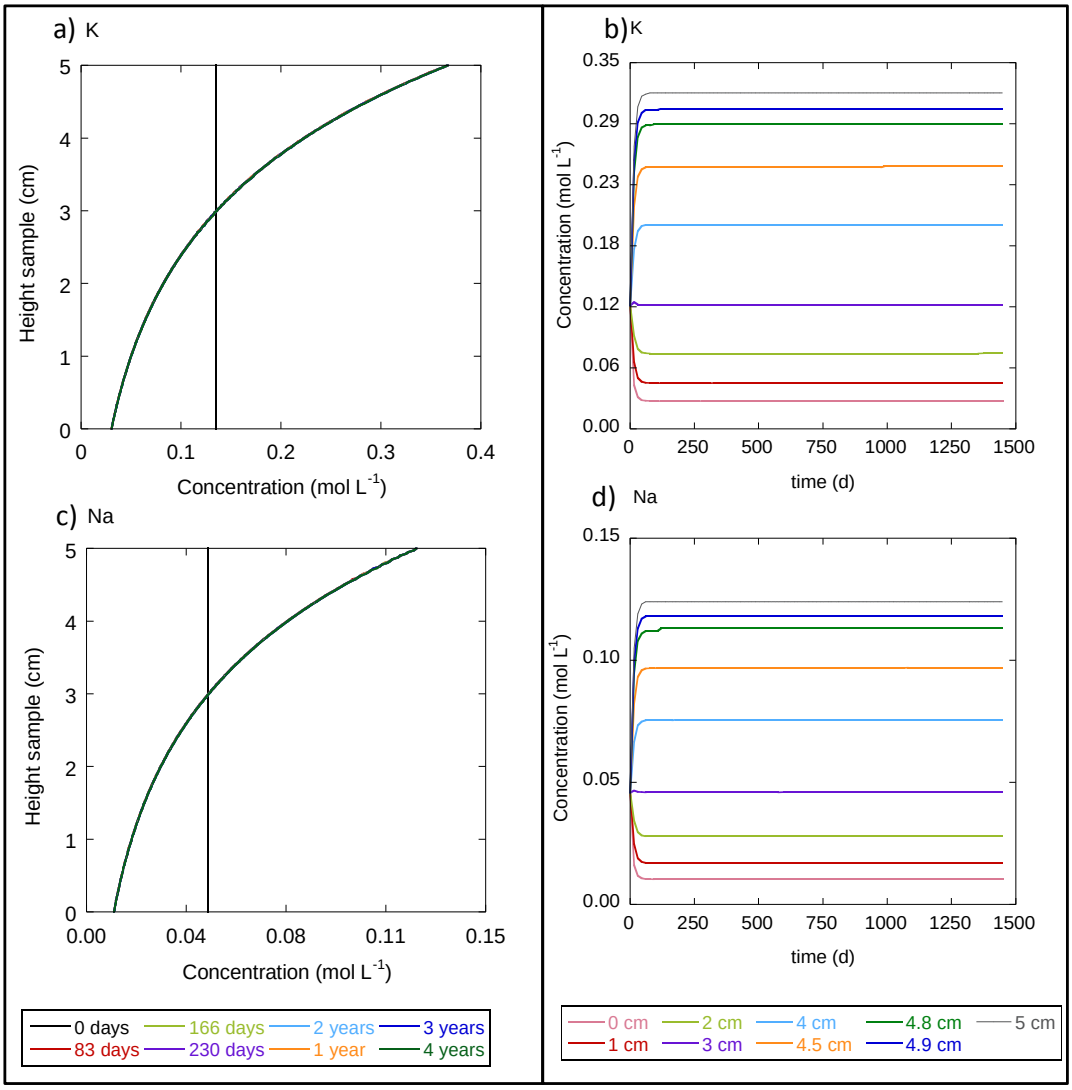

Figure 5.26. *Variation in K concentration (top row) and Na concentration (bottom row) along the length of the sample (a and c) and over time (b and d).*

Variation in aqueous concentration of the elements is shown from Figure 5.27 to Figure 30. During the first year, concentration of Ca and Al is nearly zero due to the uptake of Ca (Figs. 5.27a and b) and Al (Figs. 5.28a and b) by precipitation of C-S-H gel, ettringite, monocarboaluminate and Si-hydrogarnet, which partially consumes Si (Figs. 5.27c and d), S (Figs. 5.28c and d), Fe (Figs. 5.29a and b), CO_3 (Figs. 5.29c and d) and Mg (Figs. 5.30a and b).

After one year, Ca and Al concentrations increase along the sample as (1) monocarboaluminate and hydrotalcite cannot precipitate by the respective lack of CO_3 and Mg, and (2) Si-hydrogarnet and C-S-H gel cannot precipitate by the lack of Si (Figs. 5.27a and b and Figs. 5.28a and b). Si concentration decreases all along the sample as quartz and fly ash dissolution is smaller because pH decreases and C-S-H gel and Si-hydrogarnet continues precipitating (Figs. 5.27c and d). S concentration is nearly zero because it has been used to previously precipitate ettringite (Figs. 5.28c and d). The Fe concentration drop to nearly zero is

caused by the continuous Si-hydrogarnet precipitation (Figs. 5.29a and b). CO_3^{2-} drops to zero as all carbonate is consumed by monocarboaluminate precipitation and calcite exhaustion (Figs. 5.29c and d). Mg concentration decreases as a result of continuous precipitation of hydrotalcite and slower dissolution of fly ash (Figs. 5.30a and b). The effects of evaporation and accumulation on the concentrations are observed at the very top, where the concentration increase is much higher than in the rest of the sample (Figs. 5.28a, b and c).

High concentration of Al is obtained in the top of the sample. Inclusion of other phases in the model (e.g. bohemite, diaspore) could perhaps improve the results.

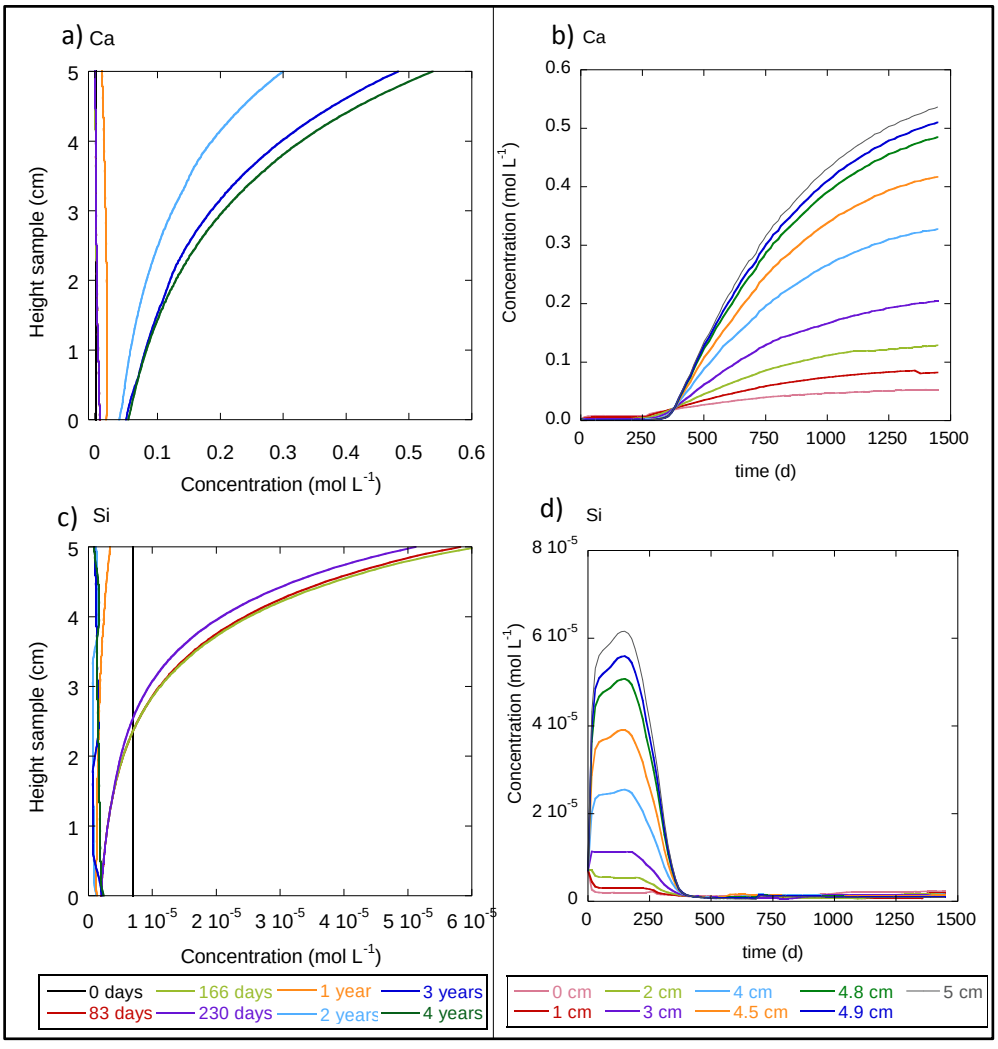

Figure 5.27. *Variation in Ca concentration (top row) and Si concentration (bottom row) along the length of the sample (a and c) and over time (b and d).*

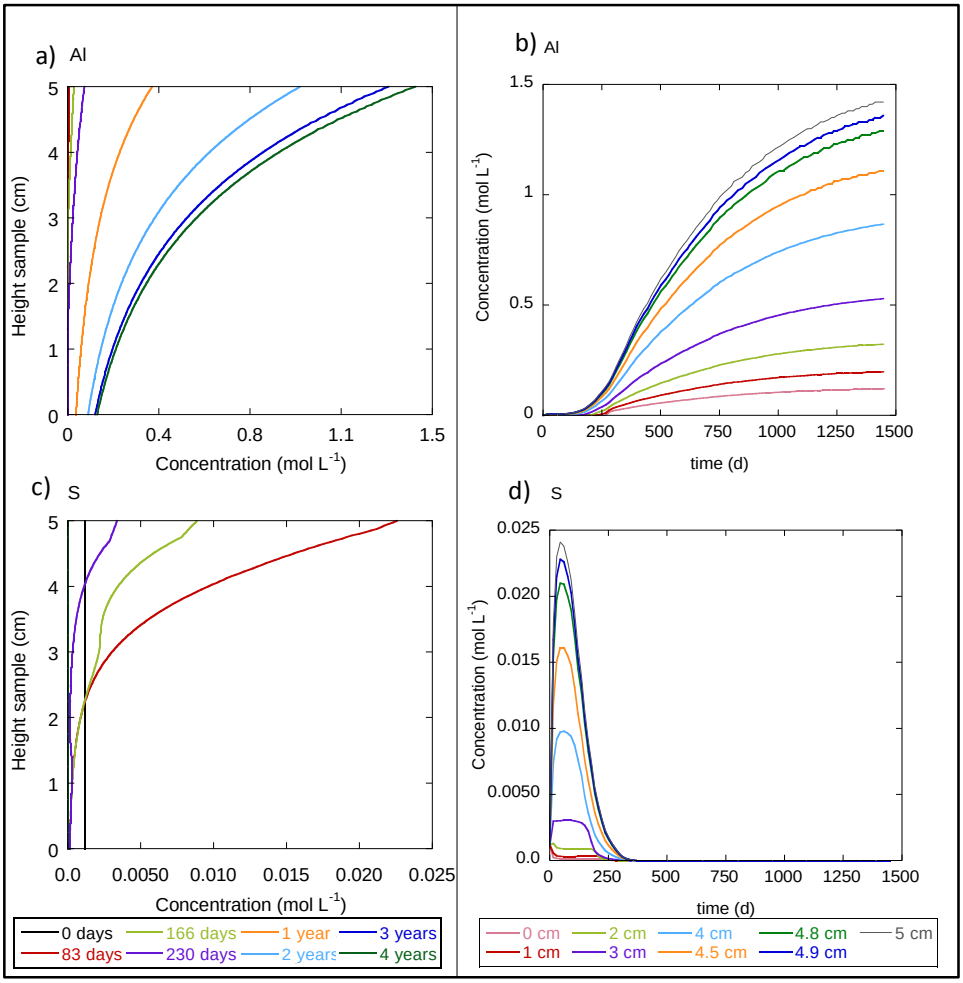

Figure 5.28. *Variation in Al concentration (top row) and S concentration (bottom row) along the length of the sample (a and c) and over time (b and d).*

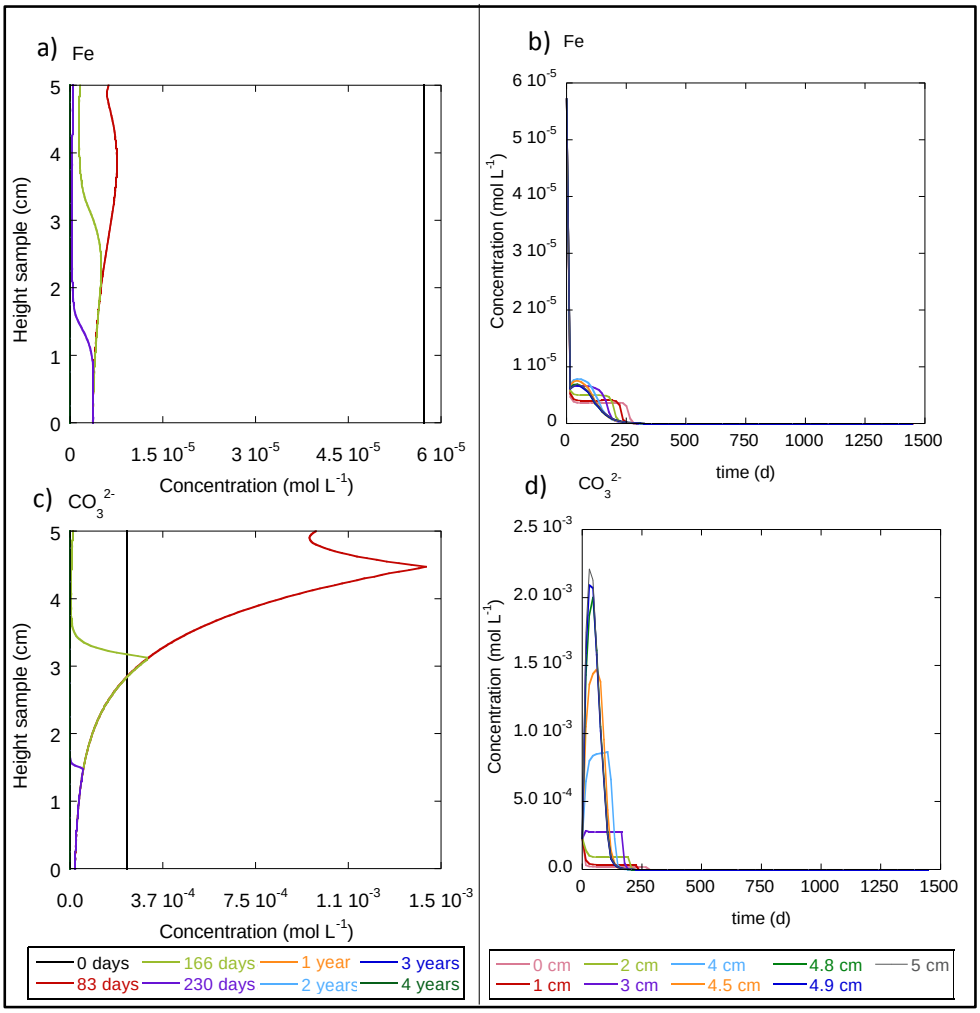

Figure 5.29. *Variation in Fe concentration (top row) and CO_3^{2-} concentration (bottom row) along the length of the sample (a and c) and over time (b and d).*

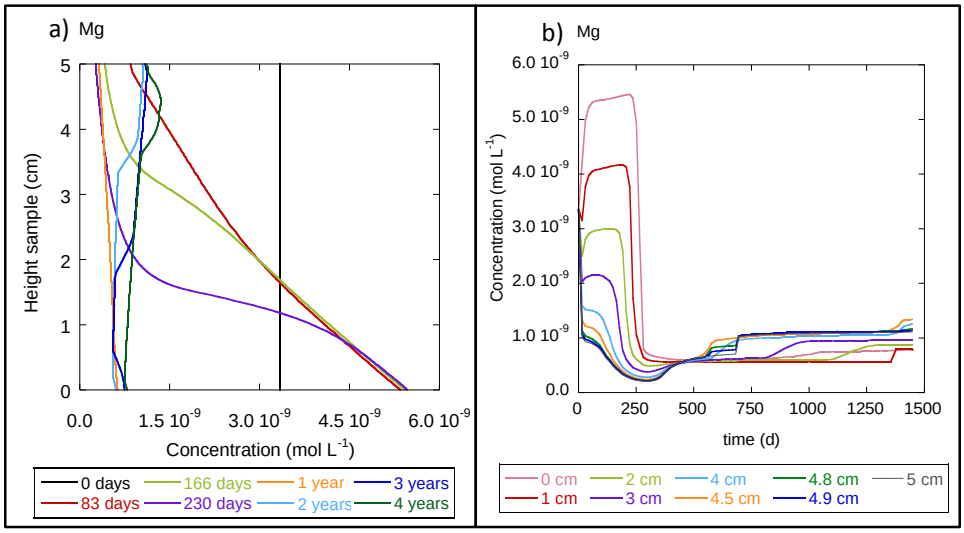

Figure 5.30. *Variation in Mg concentration along the length of the sample (a) and over time (b).*

Variation in porosity along the sample and time is shown in Figures 5.31 a and b. At the very bottom, porosity increases with time from 12.5% to 18% caused by dissolution of portlandite, quartz, calcite and ettringite. During the simulation, porosity increases up to 18 % along the sample up to 4.8 cm. In the upper region, porosity reaches a value between 16 % and 18 % due to exhaustion of ettringite, calcite and portlandite. Only at 5 cm, at ≈ 500 days, porosity temporarily decreases to ≈ 5 % due to the large precipitation of portlandite along with precipitation of C-S-H gel, ettringite, Si-hydrogarnet, monocarboaluminate and hydrotalcite.

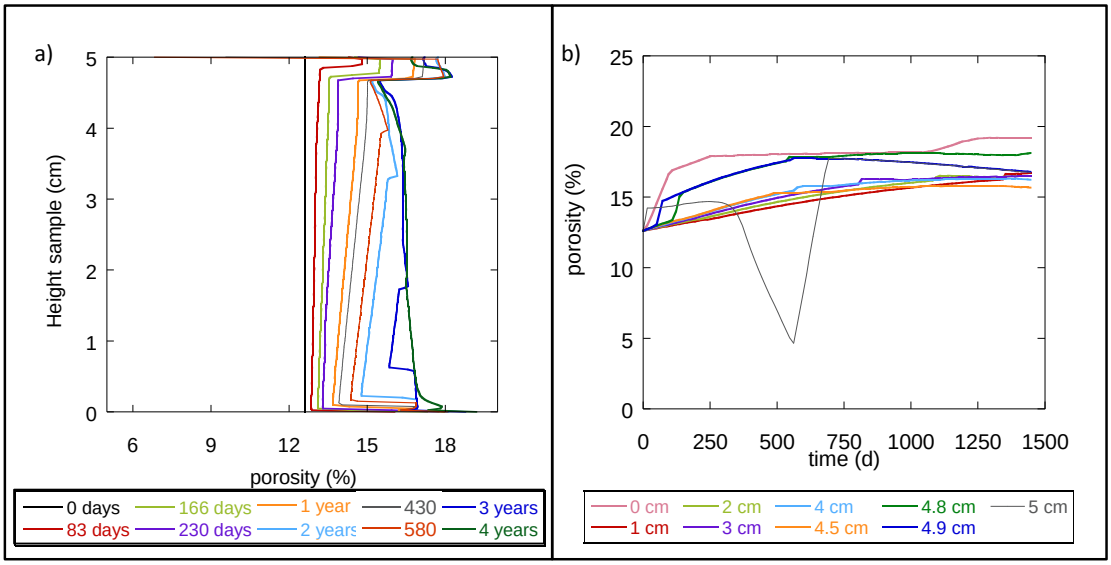

Figure 5.31. *Variation in porosity along the length of the sample (a) and over time (b).*

5.5. Conclusions

Evaporation experiments at the laboratory scale were designed to reproduce the physicochemical processes in the inner part of the El cabril vault walls. Two samples of mortar with insulated lateral surfaces were irradiated with IR light at the top surface (outlet) to induce evaporation. Evaporation at the top causes water ascension from the bottom (inlet) upwards. To avoid carbonation the experiments were carried out under N_2 controlled atmosphere and N_2-bubbled Millipore MQ water. The top surface and bulk temperatures, as well as bulk relative humidity, were kept approximately constant.

Loss of water with time due to evaporation was linear at an approximate flow rate of 0.9 $cm^3\ d^{-1}$. One and three pore volumes were exchanged in experiments A and B, respectively. Inspection of the unreacted and reacted mortar was performed at the millimeter scale using a visual lens and at the micrometer scale using SEM. At the millimeter scale, possible

mineralogical alterations and changes in grain boundaries originated by dissolution or precipitation reactions could not be observed. Only in the lower 4 mm (inlet), quartz grains appeared to be more visible. At the micrometer scale, characteristic features of mineral dissolution and precipitation and changes in grain morphologies could not be distinguished. No mineralogical changes were observed in the very top region (outlet) of the samples, where evaporation was taking place.

Using the CodeBright code and assuming constant porosity, the simulated water loss matched the experimental water loss by fitting γ_e, β_g and γ_g and using the experimentally obtained parameters associated with the retention curve (P_0 and m). The calculations predicted a completely saturated sample throughout the experiment, and accordingly, evaporation only took place at the top surface.

1-D reactive transport simulations were performed with the coupled Retraso-CodeBright code, which couples the chemical reactions with the flux calculation. The initial composition of the samples was calculated using GEMS (Lothenbach et al. 2008a). The BET specific surface area of the mortar was used to calculate the reactive surface areas of the mortar phases. The C-S-H gel dissolution kinetic rate law as well as rate parameters for the mortar phases, were included in the calculations. The Retraso-CodeBright simulated water loss, taking into account porosity and permeability changes, also matched the experimental water loss.

The simulations show small variation in the content of the mortar phases over the course of the experiment (≈ 2.8 pore volumes):

1. During the simulation, dissolution of major phases (portlandite, calcite, ettringite, fly ash and quartz) and precipitation of C-S-H gel with a Ca/Si ratio of 1.667, Si-hydrogarnet, hydrotalcite and monocarboaluminate occurs near the inlet.
2. Along the sample, C-S-H gel (Ca/Si = 1.667), hydrotalcite, Si-hydrogarnet and monocarboaluminate precipitate all over the experiment. Precipitation of C-S-H gel with a Ca/Si ratio that varies from 1.60 to 1.667 occurs after three years and is associated to portlandite dissolution and exhaustion. Dissolution of portlandite, calcite, fly ash and quartz takes place and precipitated ettringite remains constant from the inlet to 4.5 cm. Approaching the top (up to 4.8 cm), dissolution of portlandite, calcite, ettringite, fly ash and quartz increases due to the temperature increase. Gibbsite precipitation occurs from 3 cm to the top only after 615 days.
3. At the very top (4.9 to 5 cm), where temperature is higher (67 °C) than in the rest of the sample (53-60 °C), fast dissolution and exhaustion of calcite and ettringite originates solution supersaturation with respect to portlandite yielding portlandite

precipitation. Thereafter, Ca accumulation still promotes portlandite precipitation (between 350 and 500 days). Finally, portlandite dissolves as the amount of aqueous Ca is insufficient to supersaturate the solution and is consumed by precipitation of C-S-H gel, Si-hydrogarnet and hydrotalcite.

4. pH variation is mainly bound to portlandite dissolution. In the first 300 days, the dilution effect is caused by the inflow water, making the porewater pH reduce from 13.15 to 12.7 at the bottom. The pH increase along the sample reaches a value of 13.5 at the top by an accumulative effect. After 300 days, portlandite dissolves, and pH decreases down to 12.5 to remain fairly constant.

During the experimental run, the small changes in the volumetric fraction of the mortar phases yield small variation in porosity. The largest increase in porosity (from 12.5 % to 18 %) is predicted to occur at the very bottom of the sample mainly due to dissolution of portlandite, quartz, calcite and ettringite. Along the sample, porosity increases with time up to around 18 % after 4 years. Near the sample top, porosity increases quickly from 15 % to 18 % due to exhaustion of ettringite, calcite and portlandite. At the very top porosity temporarily decreases to 5 % at ≈ 500 days due to large precipitation of portlandite. The little porosity variation at 230 days accounts for the negligible changes in mortar composition and texture observed by optical and SEM inspections.

References

ASTM D3967 – 08. Standard Test Method for Splitting Tensile Strength of Intact Rock Core Specimens.

Ayora C., Soler J.M., Saaltink M.W. y Carrera J. (2006) Modelo de transporte reactivo sobre la lixiviación del hormigón por agua subterránea en la celda 16 de El Cabril. *Informe CTJA-CSIC para ENRESA*, 38 pp.

Bandstra, J. Z., Buss, H. L., Campen, R. K., Liermann, L. J., Moore, J., Hausrath, E. M., Navarre-Sitchler, A.K., Jang, J.-., Brantley, S. L. (2008). Appendix: compilation of mineral dissolution rates. In: Brantley, S. L., Kubicki, J. D., White, A. F. (Eds.), Kinetics of water-rock interaction. Springer, New York, pp.737-823.

Bullard, J. W., Enjolras, E., George, W. L., Satterfield, S. G., and Terrill, J. E. (2010). A parallel reaction-transport model applied to cement hydration and microstructure development. *Modelling and Simulation in Materials Science and Engineering*, 18(2), 025007.

Chaparro, M. C., Saaltink, M. W., and Villar, M. (2013). Modelling of multiphase flow in evaporation tests in concrete columns. In EGU *General Assembly Conference Abstracts* (Vol. 15, p. 5781).

Delahaye, C. H., and Alonso, E. E. (2002). Soil heterogeneity and preferential paths for gas migration. *Engineering geology*, 64(2), 251-271.

De Weerdt, K., Haha, M. B., Le Saout, G., Kjellsen, K. O., Justnes, H., and Lothenbach, B. (2011). Hydration mechanisms of ternary Portland cements containing limestone powder and fly ash. *Cement and Concrete Research*, 41(3), 279-291.

Dilnesa, B.Z., Lothenbach, B., Renaudin, G., Wichser, A., Kulik, D. (2014). Synthesis and characterization of hydrogarnet $Ca_3(Al_xFe_{1-x})_2(SiO_4)_y(OH)_{4(3-y)}$. *Cement and Concrete Research*, 59, 96-211.

Dilnesa, B. Z., Lothenbach, B., Renaudin, G., Wichser, A., and Wieland, E. (2012). Stability of Monosulfate in the Presence of Iron. *Journal of the American Ceramic Society*, 95(10), 3305-3316.

Dilnesa, B. Z., Lothenbach, B., Le Saout, G., Renaudin, G., Mesbah, A., Filinchuk, Y., Wichser A. and Wieland, E. (2011). Iron in carbonate containing AFm phases. *Cement and Concrete Research*, 41(3), 311-323.

Hummel, W., Berner, U., Curti, E., Pearson, F. J., Thoenen, T. (2002). Nagra/PSI chemical thermodynamic data base 01/01. *Radiochimica Acta*, 90(9-11/2002), 805-813.

Kulik, D. A., Wagner, T., Dmytrieva, S. V., Kosakowski, G., Hingerl, F. F., Chudnenko, K. V., and Berner, U. R. (2013). GEM-Selektor geochemical modeling package: revised algorithm and GEMS3K numerical kernel for coupled simulation codes. *Computational Geosciences*, 17(1), 1-24.

Kulik, D. A., Kersten, M. (2001). Aqueous solubility diagrams for cementitious waste stabilization systems: II, end-member stoichiometries of ideal calcium silicate hydrates solid solutions. *Journal of the American Ceramic Society*, 84(12), 3017-3026.

Lichtner, P. C., and Carey, J. W. (2006). Incorporating solid solutions in reactive transport equations using a kinetic discrete-composition approach. *Geochimica et cosmochimica acta*, 70(6), 1356-1378.

Lothenbach B., Le Saout G., Gallucci E., Scrivener K. (2008a). Influence of limestone on the hydration of Portland cements. *Cement and Concrete Research*, 38(6), 848-860.

Lothenbach, B., Matschei, T., Möschner, G., Glasser, F. (2008b). Thermodynamic modelling of the effect of temperature on the hydration and porosity of Portland cement. *Cement and Concrete Research*, 38(1), 1-18.

Lothenbach B., Winnefeld F. (2006). Thermodynamic modelling of the hydration of Portland cement. *Cement and Concrete Research*, 36(2), 209-226.

Maqsoud A., Bussière B., Mbonimpa M. and Aubertin M. (2004). Hysteresis effects on the water retention curve: a comparison between laboratory results and predictive models. 57TH Canadian geotechnical conference.

Martys N.S., Ferraris C.F. (1997). Capillary transport in mortars and concrete. *Cement and Concrete Research*, 27(5), 747–760.

Matschei, T., Lothenbach, B., and Glasser, F. P. (2007). Thermodynamic properties of Portland cement hydrates in the system CaO–Al2O3–SiO2–CaSO4–CaCO3–H2O. *Cement and Concrete Research*, 37(10), 1379-1410.

Olivella, S., Gens, A., Carrera, J., and Alonso, E. E. (1996). Numerical formulation for a simulator (CODE_BRIGHT) for the coupled analysis of saline media. *Engineering computations*, 13(7), 87-112.

Palandri, J. L., and Kharaka, Y. K. (2004). A compilation of rate parameters of water-mineral interaction kinetics for application to geochemical modeling (No. OPEN-FILE-2004-1068). GEOLOGICAL SURVEY MENLO PARK CA.

Saaltink M. W., Sánchez-Vila X., Carrera J. (2005) Estudio Cualitativo sobre la Posibilidad que el Agua Recogida en la Celda 16 Proceda de un Proceso de Condensación, Octubre 2005. Informe UPC, Dep. de Ingeniería del Terreno, Cartográfica y Geofísica.

Saaltink, M. W., Batlle, F., Ayora, C., Carrera, J., and Olivella, S. (2004). RETRASO, a code for modeling reactive transport in saturated and unsaturated porous media. *Geologica Acta*, 2(3), 235.

Schmidt, T., Lothenbach, B., Romer, M., Scrivener, K., Rentsch, D., and Figi, R. (2008). A thermodynamic and experimental study of the conditions of thaumasite formation. *Cement and Concrete Research*, 38(3), 337-349.

Thoenen, T., Kulik, D. (2003). Nagra/PSI Chemical Thermodynamic Data Base 01/01 for the GEM-Selektor (V. 2-PSI) Geochemical Modeling Code: Release 28-02-03. PSI Technical Report TM-44-03-04 about the GEMS version of Nagra/PSI chemical thermodynamic database 01/01.

Van Genuchten, R. (1978). Calculating the unsaturated hydraulic conductivity with a new closed-form analytical model. Research report 78-WR-08, Water Resource Program, Princeton, NJ, Department of Civil Engineering, Princeton University, 63 pp.

Wagner, T., Kulik, D. A., Hingerl, F. F., Dmytrieva, S. V. (2012). GEM-Selektor geochemical modeling package: TSolMod library and data interface for multicomponent phase models. *The Canadian Mineralogist*, 50(5), 1173-1195.

Wolery, T. J., Jackson, K. J., Bourcier, W. L., Bruton, C. J., Viani, B. E., Knauss, K. G., Delany, J. M. (1990). Current status of the EQ3/6 software package for geochemical modeling. Chemical modeling of aqueous systems II, 416, 104-116.

Zondag H.A., Van Essen V.M., Bleijendaal L.P.J., Kikkert B.W.J. and Bakker M. Application of $MgCl_2.6H_2O$ for thermochemical seasonal solar heat storage. Abstract IRES 2010. November 22-24, 2010, Berlin, Germany.

Zuloaga, P., Ordonez, M., Saaltink, M. W., and Castellote, M. (2009). Capillarity in Concrete Disposal Vaults and Its Influence in the Behavior of Isolation Barriers at El Cabril Low and Intermediate Level Radioactive Waste Disposal Facility in Spain-9015.

CHAPTER 6

General conclusions

The first part of the thesis is concerned with obtaining the dissolution kinetics applicable to the long-term dissolution behavior of C-S-H gel, which constitutes at least 60 % of hydrated cement paste, and studies the changes in the nanostructure to fully understand the process of cement degradation.

The kinetics of the C-S-H gel dissolution has been studied at room temperature using flow-through experiments with variation of the flow rate and the C-S-H gel mass. pH, Ca and Si concentrations where monitored and showed three distinct stages during the experiments. In the first stage, Ca concentration was much larger than Si, indicating preferential dissolution of portlandite and slow close-to-equilibrium dissolution of C-S-H. The initial Ca/Si ratio in solution was much larger than in the solid and the pH was around 12. In the second stage, as the portlandite content diminished, a gradual decrease in Ca and increase in Si was observed, indicating an increase in C-S-H gel dissolution. The aqueous Ca/Si ratio decreased to values below 10 and the ratio also decreased in the solid. pH decreased to values about 11.5 - 11. In the last stage, concentrations of Ca and Si and pH (≈11) reached steady state. At this stage the Ca/Si ratio in the solid and in the aqueous phase tended to a constant value of about 0.9 suggesting that (i) the C-S-H gel was the main dissolving phase and (ii) the dissolution reaction evolved to the congruent dissolution of a phase with tobermorite stoichiometry (Ca/Si = 0.83), which is consistent with the C-S-H solubility model used in the current study.

In the experiments where steady state and congruent dissolution were achieved it was feasible to obtain a rate law of the tobermorite-like C-S-H gel phase accounting for the effect of solution saturation state on the dissolution rate (i.e., a rate-ΔG dependency) and is expressed as

$$Rate_{C-S-H\_0.83}(mol \quad m^{-2}s^{-1}) = -2.6 \pm 0.7 \text{ x}10^{-11} \cdot (1-\Omega)$$

where Ω is the saturation degree (ionic activity product divided by equilibrium constant). The form of this expression indicates that the simplest TST-derived rate law suitably accounts for the C-S-H_0.83 dissolution kinetics. In accordance to these results, the experimental variation of the output concentrations with time were modeled with the CrunchFlow reactive transport code, assuming a dissolution rate law of the form $R = -A \cdot k \cdot (1-\Omega)$, where R is rate (mol m^{-3} s^{-1}), A is surface area (m^2 m^{-3}), and k is the rate constant (mol m^{-2} s^{-1}). The obtained values of the rate constants change with Ca/Si ratio from about 10^{-8} mol m^{-2} s^{-1} at Ca/Si ratio = 1.67 to 10^{-11} mol m^{-2} s^{-1} at Ca/Si ratio = 0.83, when normalizing to BET specific surface area. No pH effect is included in the rate law. Therefore, it is only applicable to the pH conditions of the study (pH 11 – 12.5), which is relevant in cement media. It is possible that the variability in the rate constants reflects (at least partially) an actual dependency on pH.

The implementation of the proposed rate law for C-S-H gel dissolution in reactive transport codes could result in a substantial gain of reliability of the predictions of cement/concrete durability when advective flow through cementitious materials is expected (reaction control of the dissolution).

As in the present study, no solutes other than H^+, OH^-, Ca and Si intervened in the reaction, a possible avenue for the future research could be to study the effect of other cations on the C-S-H dissolution kinetics, as well as at different T and pH.

Related with change in composition of the C-S-H gel, variation in the C-S-H gel nanostructure through dissolution was investigated using SEM-EDX, EPMA, ^{29}Si MAS-NMR and SANS techniques.

Although an apparent change in morphology was not observed after dissolution, the specific surface area increased from about 12 to 14-142 m^2 g^{-1}. SEM-EDX and EPMA multipoint analyses showed that the solid Ca/Si ratio of the initial C-S-H particles was approximately 1.7 ± 0.1. Ca/Si of 2.2 ± 0.2 corresponded to C-S-H gel particles with precipitated portlandite. Ca/Si ratios larger than 6 evidenced the presence of portlandite. The solid Ca/Si ratio of the C-S-H particles decreased to values about 0.9 ± 0.1 as dissolution progressed. The obtained Ca/Si ratios from the multipoint analyses indicate some compositional variability over the analyzed particles, suggesting the existence of compositional domains with variable Ca/Si ratios.

^{29}Si MAS-NMR spectra showed that the reacted C-S-H structure evolved to longer chain length with the formation of cross-linked chains. Also, Si-rich domains were identified in samples reacted under a slow flow regime. These domains are probably associated to the formation of leached diffusion layers over the course of the incongruent dissolution.

SANS data for the unreacted C-S-H gel indicated that the resulting contrast curve was consistent with a C-S-H gel phase with composition $C_{1.7}SH_{1.8}$ and density of 2.604 g cm^{-3} as suggested by Allen et al. (2007). This is in agreement with the calculated relative scattering contrast and the applied matchpoint measurement. The SANS total internal surface (S_T) increased as the Ca/Si ratio decreased (for ≈ 31 days) and thereafter decreased when the Ca/Si ratio was ≈ 1. These observations agree with the measurements reported by Thomas et al. (2004) and suggest that the accessibility of HD C-S-H gel increases with dissolution, contributing to the S_T enhancement. The variation of surface area with time, i.e., when the Ca/Si ratio decreases to reach a tobermorite stoichiometric ratio, is similar to the measured specific surface area (BET) and comparable to the derived SANS surface area (SSA). This observed behavior suggests that, as C-S-H dissolves, the morphology of the LD C-S-H compound is being transformed and enhances the specific surface area. Therefore, the use of the BET surface area to normalize the C-S-H dissolution rates is fully justified.

SANS experimental data were fitted with the fractal model (Allen et al., 2007), that considers a smallest unit of a radius of 1.2 nm formed by tobermorite-like or jennite-like structure packed together irregularly into structures called globules with a radius of 2.5 nm approximately. These globules group to compose a volume fractal structure (mainly LD C-S-H gel) and a surface fractal structure at the top of the C-S-H surface grains. This model allows the obtainment of the fit parameters which describe the changes in the nanostructure of the C-S-H gel during dissolution: D_o increase indicates that the roughly equiaxed particles that build the C-S-H structure change their shape into sheet-like structures of increasing thickness. The obtained decrease in D_V values (≈ 2) also suggests such a structure transformation (tendency to form a sheet-like structure) as was proposed by Thomas et al. (2004) and Allen et al. (2007). D_S slightly increases indicating enhancement of surface roughness. ξ_V decrease and $\phi_{MAX}/\phi_{C\text{-}S\text{-}H}$ ratio increase indicate a loss of structural compaction and density during dissolution.

The C-S-H evolution deduced from the SANS experiments is in agreement with the ^{29}Si MAS-NMR measurements that show an increase in polymerization with C-S-H dissolution, i.e., dissolution promotes the C-S-H gel structure to tend to a more ordered tobermorite structure.

The second part of the thesis deals with the applicability of the obtained C-S-H gel dissolution rate law (1) to interpret the column experiments filled with mortar fragments under forced advective flow and (2) to study the effect that a flow of water across the mortar, induced by evaporation, exerts on the evolution of its structure and composition.

The proposed model considers a flow of water by capillarity through the walls of the cells and the corresponding temperature gradient. The mortar used in the experiments was the same that is used in El Cabril and the composition of the formed hydrate assemblage during the hydration was calculated using the GEM-Selektor (GEMS) software package (Lothenbach and Winnefeld, 2006; Lothenbach et al., 2008; De Weerdt et al.; 2011; Kulik et al., 2013; Wagner et al., 2012).

Regarding the column experiments, the columns were filled with mortar fragments of ≈ 2 mm and the experiments were carried out at room temperature under forced advective flow and under N_2 atmosphere to avoid carbonation. pH, Ca, Si, Na, K, S, Al, Fe and Mg concentrations were monitored and then, by means of implementation of the C-S-H dissolution rate law in the Crunchflow code and with addition of fitted rate constant values for ettringite, monocarboaluminate, fly ash and Si-hydrogarnet, were interpreted. Initially, a preferential dissolution of portlandite, that released a large amount of Ca in solution, only allowed slow dissolution of the C-S-H gel. The C-S-H gel with a high Ca/Si ratio started to dissolve incongruently (decalcification of the C-S-H gel). With time, portlandite kept on dissolving along the entire column, as well as the C-S-H gel with high Ca/Si ratio to form C-S-H gels with low Ca/Si ratio along the entire column. The dissolution of fly ash was uniform along the radius of the fragments as a consequence of the assumed irreversible dissolution kinetics and slowed down with time along the column. Reactivity of monocarboaluminate and Si-hydrogarnet was minor and took place along the column. Ettringite dissolved mostly at the inlet of the column, releasing S in solution that promoted ettringite precipitation in the grain surfaces at the column outlet. Quartz and hydrotalcite did not react in any significant amount. Mortar porosity increased along the column, between 40% at the inlet and 25% in the outlet.

Evaporation experiments were performed at the laboratory scale under similar conditions (although more active) to those in El Cabril and under N_2 atmosphere. The mortar was irradiated with IR light to provoke evaporation in the top of the test tube. The water used in the experiments was MilliQ water and was kept in a CO_2-free glove box. The loss of water from the reservoir was monitored. The temperature and the %RH were kept constant and monitored throughout the experiments.

Examination of the unreacted and reacted mortar samples was performed by hand lens inspection, optical microscopy and SEM. Regarding the mineralogical alterations produced by upward water flow generated by heating the top surface of the sample, no apparent changes were observed except in the 4 mm at the very bottom of the sample, where the aggregate were more visible.

Modeling of water flow and heat transport using CodeBright could reproduce the measured flow of water and temperature. The calculations predicted a completely saturated sample during all the experiment, and accordingly, evaporation only took place at the top surface. Porosity was assumed constant in this model.

1-D reactive transport simulations were performed with the coupled Retraso-CodeBright code to calculate the evolution of the mortar phases during 1460 days (4 years). The initial composition of the samples was calculated using GEMS (Lothenbach et al. 2008). The BET specific surface area of the mortar was used to calculate the reactive surface areas of the mortar phases. The C-S-H gel dissolution kinetic rate law as well as rate parameters for the mortar phases, were included in the calculations. The Retraso-CodeBright simulated water loss, taking into account porosity and permeability changes, also matched the experimental water loss.

The simulations show small variation in the content of the mortar phases over the course of the experiment (≈ 2.8 pore volumes). During the simulation, dissolution of major phases (portlandite, calcite, ettringite, fly ash and quartz) and precipitation of C-S-H gel with a Ca/Si ratio of 1.667, Si-hydrogarnet, hydrotalcite and monocarboaluminate occurs near the inlet. Along the sample, C-S-H gel (Ca/Si = 1.667), hydrotalcite, Si-hydrogarnet and monocarboaluminate precipitate all over the experiment. Precipitation of C-S-H gel with a Ca/Si ratio that varies from 1.60 to 1.667 occurs after three years and is associated to portlandite dissolution and exhaustion. Dissolution of portlandite, calcite, fly ash and quartz takes place and precipitated ettringite remains constant from the inlet to 4.5 cm. Approaching the top (up to 4.8 cm), dissolution of portlandite, calcite, ettringite, fly ash and quartz increases due to the temperature increase. Gibbsite precipitation occurs from 3 cm to the top only after 615 days. At the very top (4.9 to 5 cm), where temperature is higher (67 °C) than in the rest of the sample (53-60 °C), fast dissolution and exhaustion of calcite and ettringite originates solution supersaturation with respect to portlandite yielding portlandite precipitation. Thereafter, Ca accumulation still promotes portlandite precipitation (between 350 and 500 days). Finally, portlandite dissolves as the amount of aqueous Ca is insufficient to supersaturate the solution and is consumed by precipitation of C-S-H gel, Si-hydrogarnet and hydrotalcite. pH variation is mainly bound to portlandite dissolution. In the first 300 days, the dilution effect is caused by the inflow water, making the porewater pH reduce from 13.15 to 12.7 at the bottom. The pH increase along the sample reaches a value of 13.5 at the top by an accumulative effect. After 300 days, portlandite dissolves, and pH decreases down to 12.5 to remain fairly constant.

During the experimental run, the small changes in the volumetric fraction of the mortar phases yield small variation in porosity. The largest increase in porosity (from 12.5 % to 18 %)

is predicted to occur at the very bottom of the sample mainly due to dissolution of portlandite, quartz, calcite and ettringite. Along the sample, porosity increases with time up to around 18 % after 4 years. Near the sample top, porosity increases quickly from 15 % to 18 % due to exhaustion of ettringite, calcite and portlandite. At the very top porosity temporarily decreases to 5 % at ≈ 500 days due to large precipitation of portlandite.

The small porosity variation after 230 days, due to the small changes in the volumetric fractions of the different phases, is consistent with the negligible changes in mortar composition and texture observed by visual and SEM inspections.

References

Allen, A. J., Thomas, J. J., and Jennings, H. M. (2007). Composition and density of nanoscale calcium–silicate–hydrate in cement. *Nature Materials*, 6(4), 311-316.

De Weerdt, K., Haha, M. B., Le Saout, G., Kjellsen, K. O., Justnes, H., and Lothenbach, B. (2011). Hydration mechanisms of ternary Portland cements containing limestone powder and fly ash. *Cement and Concrete Research*, 41(3), 279-291.

Kulik, D. A., Wagner, T., Dmytrieva, S. V., Kosakowski, G., Hingerl, F. F., Chudnenko, K. V., and Berner, U. R. (2013). GEM-Selektor geochemical modeling package: revised algorithm and GEMS3K numerical kernel for coupled simulation codes. *Computational Geosciences*, 17(1), 1-24.

Kulik, D. A., Kersten, M. (2001). Aqueous solubility diagrams for cementitious waste stabilization systems: II, end-member stoichiometries of ideal calcium silicate hydrates solid solutions. *Journal of the American Ceramic Society*, 84(12), 3017-3026.

Lothenbach B., Le Saout G., Gallucci E., Scrivener K. (2008). Influence of limestone on the hydration of Portland cements. *Cement and Concrete Research*, 38(6), 848-860.

Lothenbach B., Winnefeld F. (2006). Thermodynamic modelling of the hydration of Portland cement. *Cement and Concrete Research*, 36(2), 209-226.

Thomas, J. J., Chen, J. J., Allen, A. J., and Jennings, H. M. (2004). Effects of decalcification on the microstructure and surface area of cement and tricalcium silicate pastes. *Cement and Concrete Research*, 34(12), 2297-2307.

Wagner, T., Kulik, D. A., Hingerl, F. F., Dmytrieva, S. V. (2012). GEM-Selektor geochemical modeling package: TSolMod library and data interface for multicomponent phase models. *The Canadian Mineralogist*, 50(5), 1173-1195.